



UNIVERSITY OF LIÈGE, FACULTY OF SCIENCES
CESAM RESEARCH UNIT, Q-MAT CENTER
EXPERIMENTAL PHYSICS OF NANOSTRUCTURED MATERIALS

UNIVERSITY OF ANTWERPEN, FACULTY OF SCIENCES
CONDENSED MATTER THEORY GROUP

Emergent vortex phenomena in spatially and temporally modulated superconducting condensates

Željko L. Jelić

Jury members:

Prof. Dr. N. D. NGUYEN (President)

Prof. Dr. P. SCHLAGHECK (Secretary)

Dr. C. BRUN (Paris Institute of Nanosciences CNRS and Pierre and Marie Curie
University)

Prof. Dr. J. TEMPERE (University of Antwerpen)

Prof. Dr. M. V. MILOŠEVIĆ (University of Antwerpen, promoter)

Prof. Dr. A. V. SILHANEK (Promoter)

Academic year 2017-2018

*Mojoj najdražoj Aleks,
hvala ti što si mi tolike godine bila
inspiracija i svjetlo na kraju tunela!*

Acknowledgment

This thesis, with all the results in it, would never be completed without the help of people who selflessly donated tremendous amounts of their time, and to whom I want to express my gratitude here.

First, I would never end up in Belgium if it was not for prof. Milan Tadić (University of Belgrade) and prof. François Peeters (University of Antwerpen), who recommended me for this PhD position. Iz sveg srca vam zahvaljujem and dank U veel.

I express my deepest thanks to the jury members for taking their time to review my thesis and attend the defense.

I should also acknowledge F.R.S.-FNRS, ARC SPIN TWEAKS, and COST action for funding my research and providing me with opportunity to present my findings at international scientific meetings.

To all the people who directly contributed to my work with their insightful suggestions and expertise: Toni Stanković (for saving my life when I just started PhD and helping me with illustrations, imaš moj najdublji naklon i vječnu zahvalnost), Joseph Lombardo (to him I am especially thankful for his patience with my everlasting numerical calculations), Darko Stošić (for his efforts in optimization of my code), Lise Serrier-Garcia Brinon (for her expertise in STS technique and many significant explanations), Dean Moldovan (for his insights in secrets of several programming languages and code optimization), Joris Van de Vondel (for valuable insights during our collaboration), and Yonathan Anahori (for his time and advices during our collaboration); I will forever be in their debt.

I also must mention my “brothers in arms” in Antwerp: Víctor, Lingfeng, Vladimir, Abul Hasnat, and Jesus. They have been of great help during my work. I should also thank Robbe, who helped me translate parts of the thesis in Dutch. Furthermore, to guys from Liège: Jonathan, Gorky, and Sylvain, I cannot express enough gratitude for your hospitality. Jérémy and Xavier have earned insurmountable amount of my gratitude, for extending their helping hand so many times, and especially when I needed their help in writing French parts of this thesis.

To my colleagues and friends in Antwerp: Marko, Amir, Sara, Lucia, Edith,

and Stephan; I thank you for all the lovely and fun moments. Also, without Miša all those concerts I've been to would never be so awesome. I am especially thankful to my roommates and friends, Stefan and Slaviša, for so much memorable and amazing times.

I am also very grateful for the support of my friends from Bosnia and Serbia: Igo, Rile, Siko, Stefan, Gorica, Marko, Ljubiša, Mirko, and Nemanja. Though not always scientific, their contribution to this work was crucial and much appreciated, since they remained my close friends through thick and thin. Also, to Boris, I thank you for all the genuine interest and honest enthusiasm for my research. One of the major contributions to this work was from my family, and in particular, my parents. Bez vaše podrške i neizmjerne žrtve, ovo ostvarenje nikada ne bi bilo moguće. Ne postoje riječi kojima mogu dovoljno da iskažem svoju zahvalnost na tome.

Last but not least, to my supervisors, professors Alejandro Silhanek and Milorad Milošević, I will never be able to properly express my gratitude. Their guidance and vast expertise helped me throughout these four years myriads of times, and from that experience I was able to completely redefine my views and approach to scientific methodology. I am also very thankful for their patience, and encouragement throughout my studies, and for all of those fruitful and insightful discussions that led me to many personal breakthroughs. With their help I understood that the meaning of these studies does, indeed, reflect in a fundamental understanding of an elementary phenomena of a nature around us, and that is the most important lesson I could learn.

Contents

Preface	1
Préface	5
Voorwoord	9
1 Introduction	13
1.1 History of superconductivity	13
1.2 Overview of superconducting materials	19
1.3 Superconducting electronics	23
1.4 Overview of the theories of superconductivity	25
1.4.1 Phenomenological theories	25
1.4.1.1 The London model	26
1.4.1.2 The Ginzburg-Landau model	27
1.4.2 Microscopic formalism	29
1.4.2.1 BCS theory	29
1.4.2.2 The equation of motion by Gor'kov, Eilenberger and Usadel	30
2 The generalized time-dependent Ginzburg-Landau (gTDGL) frame- work	33
2.1 gTDGL equations and their validity	33
2.1.1 Free energy functional and relaxation time of the order pa- rameter	34
2.1.2 Generalized time-dependent Ginzburg-Landau equation and the general boundary condition	36
2.1.3 Supercurrent, total current and conservation law	39
2.1.4 GL equations in steady state	41
2.1.5 Characteristic quantities and their microscopic origin	41
2.1.6 High κ regime and validity of the gTDGL equation	44

2.2	Extending the gTDGL model: Description of thermal balance in superconductors	45
2.2.1	Equation of thermal balance	46
2.2.2	Dimensionless extended gTDGL model	47
2.2.3	Discretization of the equations and numerical approach	48
2.3	Applications of the extended gTDGL model	53
2.3.1	Time-dependent thermal potential	53
2.3.2	Spatially inhomogeneous parameters of extended gTDGL theory	54
3	Basics of vortex dynamics and manipulation	57
3.1	Effect of the interplay of currents on the vortex matter	59
3.1.1	Interplay of currents in the steady state	60
3.1.2	A critical state for the onset of vortex motion	61
3.1.3	Dynamic equilibrium	62
3.2	Vortex pinning in permanent pinning landscapes	63
3.3	Individual manipulation of vortices	66
3.3.1	Scanning tunneling microscopy	66
3.3.2	Magnetic force microscopy	68
3.3.3	Scanning SQUID microscopy	70
3.3.4	Low temperature scanning laser microscopy	71
3.4	Vortex velocimetry	73
3.4.1	Transport measurements	73
3.4.2	Corbino setup	74
4	Vortex matter under current lensing	77
4.1	Geometric constriction	79
4.2	Vortex dynamics	83
4.3	Extreme vortex velocity	86
4.4	Dynamic vortex phases	89
5	Vortex matter under a dynamic pinning potential	93
5.1	Stroboscopic resonances	96
5.2	Vortex dynamics at resonances	101
5.3	Vortex velocimetry from stroboscopic resonances	104
6	Vortex matter under electronic gating	113
6.1	Superconductivity in the two-dimensional limit	114
6.2	Scanning electronic gating of the atomically thin superconductors	118

6.3	Modulation of the superconducting properties of an ultrathin Pb island via electronic gating	124
6.4	gTDGL analysis of vortex matter under electronic gating	128
7	Conclusion	137
	Appendices	141
A	Details about numerical approach	143
A.1	Euler method for temporal derivatives	143
A.2	Direct explicit solution of first gTDGL equation in arbitrary geometries	144
A.3	Crank-Nicolson method for diffusion-like equations in arbitrary geometries	145
A.4	Alternating Direction Implicit method for diffusion-like equations in arbitrary geometries	147
A.5	Fast Fourier transform for direct solution of Poisson-like equations	149
A.6	Successive over-relaxation method for iterative solution of Poisson-like equations in arbitrary geometries	152
A.7	Track and trace algorithm for simultaneous tracking of a collective of particles	152
	Bibliography	155
	Curriculum Vitae	179

Abbreviations (in alphabetical order)

1D	One dimensional
2D	Two dimensional
3D	Three dimensional
<i>ac</i>	Alternating current
ADI	Alternating direction implicit
AFM	Atomic force microscope/microscopy
ARPES	Angle-resolved photoemission spectroscopy
BCS	Bardeen-Cooper-Schrieffer
BdG	Bogolyubov-de Gennes
BEC	Bose-Einstein condensate
BSCCO	Bismuth strontium calcium copper oxide
CCD	Charged-couple device
CN	Crank-Nicolson
CPD	Cooper-pair density
<i>dc</i>	Direct current
dFT	Discrete Fourier Transform
DOS	Density of states

FET	Field-effect transistor
FFT	Fast Fourier Transform
FT	Fourier Transform
GA	Gated area
GL	Ginzburg-Landau
GM	Galvanometric mirrors
gTDGL	Generalized time-dependent Ginzburg-Landau
HTS	High temperature superconductors
IBSC	Iron-based superconductors
LBCO	Lanthanum barium copper oxide
LDOS	Local density of states
LEA	Local equilibrium approximation
LHS	Left-hand side
LK	Landau-Khalatnikov
LL	Landau-Lifshitz
LO	Larkin-Ovchinnikov
LTSLM	Low-temperature scanning laser microscopy
MFM	Magnetic force microscope/microscopy
MISFET	Metal-insulator-semiconductor FET
ML	Monolayer
MOSFET	Metal-oxide-semiconductor FET
PBS	Polarizing beam-splitter
QWS	Quantum-well state
RHS	Right-hand side

RSFQ	Rapid single-flux quantum
SEM	Scanning electron microscope/microscopy
SF	Superconductor-ferromagnet
SI	Superconductor-insulator
SIC-Pb	Striped incommensurate Pb
SN	Superconductor-normal metal
SNS	Superconductor-normal metal-superconductor
SNSPD	Superconducting nanowire single-photon detector
SOR	Successive over-relaxation
SOT	SQUID-on-tip
SS'	Superconductor-superconductor
SSPD	Superconducting single-photon detectors
STM	Scanning tunneling microscope/microscopy
STS	Scanning tunneling spectroscopy
SV	Superconductor-vacuum
SQUID	Superconducting quantum interference device
TDGL	Time-dependent Ginzburg-Landau
TS	Telecentric system
UHV	Ultra-high vacuum
YBCO	Yttrium barium copper oxide
ZBC	Zero-bias conductance

Fundamental constants

c	Velocity of light in vacuum
e	Charge of the electron
e^*	Effective charge of the Cooper pair ($2e$)
m	Mass of the electron
m^*	Effective mass of the Cooper pair ($2m$)
\hbar	Reduced Planck's constant
Φ_0	Magnetic flux quantum ($2\pi\hbar/e^*$)
k_B	Boltzmann constant
μ_0	Magnetic permeability of vacuum

Preface

Superconductivity is an *electronic state of matter* arising from the existence of a common wave function with a *coherent phase* extending on a truly *macroscopic* scale. One major manifestation of this striking quantum phenomenon is the *dissipationless transport of electrical current*, an asset deserving particular attention in the present times where the efficient energy distribution has become of utmost importance. Unfortunately, the motion of quantum units of magnetic flux (so-called vortices or fluxons), which is an unavoidable side-effect found in superconductors in the presence of transport currents and magnetic fields, severely limits the conditions to preserve dissipationless transport. This poses a challenge for achieving the functionalization of superconducting materials and threatens their spectrum of applications.

It is widely known that any inhomogeneities (either material imperfections, or ones made artificially), which locally suppress superconductivity on the scale comparable to the core of the vortex, can pin the vortex and delay the onset of the vortex motion to higher applied currents. In recent years a substantial effort has been made to minimize the effects of current-induced vortex motion by tailoring arrays of artificial pinning centers. Besides improving the critical parameters of the superconducting state, a pinning matrix can be used for the manipulation of vortex matter, thus directly affecting the vortex dynamics, such as rectification of vortex motion under an *ac* drive (vortex diode) by introducing asymmetric pinning landscapes. In the literature one can find that the realization of the anchoring of the vortices can be based on nanostructured arrays of perforations, chemically grown defects, permanent nanomagnets, or even pinning sites produced by heavy ion bombardment. All of those realizations are based on a permanent imprint on the superconductor, without any possibility for subsequent modifications in the distribution and strength of the pinning.

The principal objective of this thesis is to investigate the dynamical behavior of vortex matter under an entirely new kind of pinning landscape consisting of spatial and temporal modulation of the superconducting condensate. A particular case of spatial modulation is considered in a constricted structure where current lensing

can cause extremely high vortex velocities. Subsequently, a time-dependent thermal potential introduced to the superconducting condensate will cause stroboscopic resonances during the vortex motion - a phenomenon that cannot be observed in the systems with static pinning imprints. Finally, a study of electronic gating is presented, where the local properties of superconductor, such as mean free path, or electronic band structure in general, can be influenced electronically. This is a completely unexplored interdisciplinary research topic, which will eventually allow one to manipulate individual vortices in superconducting materials by means of spatially confined and temporally controlled thermal and electromagnetic excitations. Furthermore, such techniques can provide one fundamental insight in different states of the vortex matter with respect to variation of the transport current, highly relevant for understanding the resistive state of superconducting materials and their applications.

The thesis is organized as follows:

Chapter 1 presents a brief overview of the key historic events related to superconductivity, known classes of superconducting materials, and their applications in electronics. Further, different theoretical frameworks are presented, starting from phenomenological models of brothers London and Ginzburg and Landau, up to more sophisticated microscopic approaches, namely the Usadel theory and Bardeen-Cooper-Schrieffer model.

In **Chapter 2** the generalized time-dependent Ginzburg-Landau (gTDGL) theory, used throughout this thesis is described in detail. The central equations for order parameter and supercurrent are derived, where characteristic quantities, such as coherence length, penetration depth, critical current and inelastic scattering parameter are explained. An extension of this model with the equation of thermal balance is introduced. The second part of this Chapter discusses the extended gTDGL model in the presence of time-dependent thermal potentials and when parameters of the model are spatially inhomogeneous.

In **Chapter 3** the known behavior of the vortex matter in the presence of external magnetic field and electric current is reviewed through several direct examples, calculated using gTDGL formalism. In addition, different experimental setups used to manipulate the vortex behavior through external means are presented, where particular attention is given to design of a pinning landscape and individual vortex manipulation by a nearby magnetic or tunneling tip, or a laser beam.

In **Chapter 4** the dynamics of vortex matter under current lensing due to ge-

ometrical constriction is discussed. Vortex velocities of several tens of km/s are obtained, exceeding the pair-breaking speed limit of the Cooper-pair condensate. Coexistence of different vortex phases at high velocities are thoroughly addressed, and possible control of those phases by pinning landscapes is discussed.

In **Chapter 5** the influence of time-dependent pinning landscapes on the vortex dynamics is studied. Temporal commensurability in the form of stroboscopic resonances is found whenever the frequency of the characteristic dynamics of the condensate is matched by the frequency of the dynamic pinning landscape. These resonances persist in a broad parameter range (magnetic field, current, temperature, material parameters, etc.) and leave a clear signature in the measured voltage, which can be used for practical applications, including measurements of the vortex velocity.

Chapter 6 presents the study of vortex matter in mesoscopic superconductors under the influence of electronic gating. An extremely thin (quasi two dimensional) Pb island, exposed to an external magnetic field, was measured at INSP Paris with scanning tunneling microscope (STM) in spectroscopy regime, followed by a theoretical analysis of the experiment presented here. It was found that via the STM-induced electronic gating, the electronic band structure of an extremely thin island can be locally affected and thus its superconducting properties can be dramatically improved or suppressed as the STM tip is moved over the sample. The observed and calculated changes in the vortex matter provide a ‘smoking gun’ evidence for this gating effect.

Chapter 7 summarizes the work presented in this thesis, and offers an outlook to further possible studies.

Finally, the **Appendix** provides a brief overview of numerical methods used for simulations throughout this thesis.

Préface

La supraconductivité est un *état électronique de la matière* découlant de l'existence d'une fonction d'onde commune dotée d'une *phase cohérente* s'étendant à l'échelle *macroscopique*. Une manifestation majeure de ce phénomène quantique saisissant est le *transport sans dissipation du courant électrique*, un atout méritant une attention toute particulière à une époque où la distribution efficace de l'énergie est une préoccupation majeure. Malheureusement, le mouvement des quanta de flux magnétique (appelés vortex ou fluxons), un effet secondaire indésirable présent dans les supraconducteurs traversés par des courants et soumis à des champs magnétiques, met sérieusement en péril le transport sans dissipation. Ceci menace le spectre d'applications des matériaux supraconducteurs et constitue un challenge à relever pour quiconque désire les fonctionnaliser.

Il est bien connu que n'importe quelle inhomogénéité (des imperfections du matériau aussi bien naturelles qu'artificielles) supprimant localement la supraconductivité sur une échelle comparable à celle de la taille d'un cœur de vortex, est capable d'ancrer ledit vortex et retarder sa mise en mouvement jusqu'à des courants plus élevés. Récemment, un effort substantiel a été réalisé pour minimiser les effets du mouvement des vortex induit par un courant en confectionnant des réseaux de centres d'ancrage artificiels. En plus d'améliorer les paramètres critiques de l'état supraconducteur, une matrice d'ancrage peut être utilisée pour manipuler des vortex et donc affecter directement leur dynamique, pour induire des effets tels que la rectification de leur mouvement sous courant alternatif (diode vortex), grâce à un réseau d'ancrage asymétrique. Dans la littérature, on peut trouver des exemples d'ancrage de vortex basés sur des réseaux de perforations nanostructurées, des défauts développés chimiquement, des nano-aimants permanents ou encore créés par bombardement avec des ions lourds. Toutes ces techniques laissent une empreinte permanente sur le matériau supraconducteur, sans aucune possibilité de modifier ultérieurement la distribution ou la force de l'ancrage.

L'objectif principal de cette thèse est d'investiguer le comportement dynamique des vortex soumis à un type d'ancrage entièrement novateur consistant à moduler à la fois temporellement et spatialement le condensat supraconducteur. Un cas

particulier de la modulation spatiale est considéré dans une structure dont les dimensions se réduisent brutalement au centre et où la concentration du courant est telle qu'elle peut entrainer les vortex à des vitesses extrêmement élevées. Par la suite, un potentiel thermique dépendant du temps appliqué au condensat supraconducteur cause une résonance stroboscopique pendant le déplacement des vortex un phénomène qui ne peut pas être observé dans les systèmes dotés d'une empreinte d'ancrage statique. Finalement, une étude d'un modèle de porte électronique est présentée, où les propriétés locales du supraconducteur, telles que le libre parcours moyen ou la structure de bande électronique en général, peuvent être influencées électroniquement. Il s'agit d'un domaine de recherche interdisciplinaire complètement inexploré à l'heure actuelle, qui nous permettra in fine de manipuler des vortex de manière individuelle dans des matériaux supraconducteurs, au moyen d'excitations thermiques et électromagnétiques confinées spatialement et contrôlées temporellement. De plus, de telles techniques peuvent nous fournir des éclairages fondamentaux sur différents aspects des vortex en rapport avec la variation du courant de transport, tout à fait pertinents pour mieux comprendre l'état résistif des matériaux supraconducteurs et leurs applications.

La thèse est structurée comme suit:

Le **Chapitre 1** présente un bref aperçu des éléments historiques clés liés à la supraconductivité, les types de supraconducteurs connus et leurs applications en électronique. De plus, différents cadres théoriques sont présentés, allant des modèles phénoménologiques des frères London et de Ginzburg et Landau, jusqu'à des approches microscopiques plus sophistiquées, à savoir la théorie de Usadel et le modèle de Bardeen-Cooper-Schrieffer.

Dans le **Chapitre 2**, la théorie généralisée dépendante du temps de Ginzburg-Landau (gTDGL) est décrite. Les équations centrales pour le paramètre d'ordre et le courant supraconducteur sont dérivées et les quantités caractéristiques, telles que la longueur de cohérence, la longueur de pénétration, le courant critique et le paramètre de diffusion inélastique sont expliquées. Une extension de ce modèle incluant l'équation d'équilibre thermique est discutée.

Dans le **Chapitre 3**, le comportement (connu) des vortex en présence de champs externes et de courants électriques est présenté à travers plusieurs exemples directs, et calculé à l'aide du formalisme gTDGL. De plus, sont présentés différents dispositifs expérimentaux qui peuvent être utilisés pour manipuler le comportement des vortex de manière externe. Une attention particulière y est prêtée à la forme du potentiel d'ancrage et à la manipulation individuelle de vortex via une pointe magnétique, une pointe à effet tunnel ou un faisceau laser.

Dans le **Chapitre 4**, la dynamique des vortex est discutée lorsque des lignes de courant s'agglomèrent dû à un rétrécissement géométrique. Des vitesses de vortex de plusieurs dizaines de km/s sont obtenues, dépassant la limite de vitesse

de brisure des paires de Cooper dans le condensat. La coexistence de vortex dans différentes phases à haute vitesse est minutieusement investiguée et un possible contrôle de ces différentes phases via un potentiel d'ancrage est envisagé.

Le **Chapitre 5** est consacré à l'étude de l'influence du potentiel d'ancrage dépendant du temps sur la dynamique des vortex. La commensurabilité temporelle sous la forme de résonance stroboscopique est mise en évidence, à chaque fois que la fréquence de la dynamique caractéristique du condensat est égale à la fréquence du potentiel d'ancrage dynamique. Ces résonances persistent dans une large gamme de paramètres (champ magnétique, courant, température, paramètres propres au matériau, etc.) et laissent une signature claire dans la différence de potentiel mesurée, qui peut dès lors être utilisée pour des applications pratiques, incluant des mesures de la vitesse des vortex.

Le **Chapitre 6** présente l'étude des vortex dans des supraconducteurs mésoscopiques sous l'influence de portes électroniques. Un îlot de Pb extrêmement mince (quasi-2D), exposé à un champ magnétique externe, a été analysé à l'INSP de Paris à l'aide d'un microscope à balayage à effet tunnel (STM) en régime spectroscopique. Les résultats expérimentaux sont suivis d'une analyse théorique de l'expérience. Il a été montré que la structure électronique d'un îlot extrêmement mince peut être affectée localement si on l'observe au STM basé sur le principe de porte électronique. Ses propriétés supraconductrices peuvent donc être drastiquement améliorées ou détériorées au fur et à mesure des déplacements de la pointe STM au-dessus de l'échantillon. Les changements observés et calculés sur les vortex fournissent une preuve indiscutable de cet 'effet de porte'.

Le **Chapitre 7** résume les résultats présentés dans cette thèse et offre un aperçu des futures études possibles.

Finalement, l'**Appendice** fournit un bref aperçu des méthodes numériques utilisées dans les simulations.

Voorwoord

Supergeleiding is een *electronische toestand van materie* die ontstaat door het bestaan van een gemeenschappelijke golf functie met een *coherente fase* die zich uitspreid op een *macroscopische* schaal. Een belangrijke manifestatie van dit frappante kwantumfenomeen is het *dissipatieloze transport van elektrische stroom*, een pluspunt dat speciale aandacht verdient in huidige tijden waar efficiënte energiedistributie enorm belangrijk is geworden. De beweging van kwantumeenheden van magnetische flux (de zogenoemde vortices of fluxonen), wat een onvermijdelijk neveneffect is in supergeleiders in de aanwezigheid van transportstromen en magnetische velden, limiteert helaas de voorwaarden om dissipatieloos transport te onderhouden enorm. Dit zorgt voor een uitdaging voor het bereiken van de functionalisatie van supergeleidende materialen en bedreigt hun spectrum aan applicaties.

Het is algemeen bekend dat elke inhomogeniteit (hetzij imperfecties in het materiaal of artificieel imperfecties), die lokaal de supergeleiding onderdrukken op de schaal vergelijkbaar met de kern van de vortex, de vortex vast kan pinnen en het begin van de vortexbeweging kan vertragen tot hoger aangelegde stromen. De laatste jaren is er veel moeite gedaan om de effecten van stroom geïnduceerde vortex beweging te minimaliseren door op maat maken van roosters van artificiële pinning centers. Naast het verbeteren van de kritische parameters van de supergeleidende toestand, kan een pinning landschap gebruikt worden voor de manipulatie van de vortex dynamica, zoals bijvoorbeeld bij de rectificatie van vortex beweging onder invloed van een *ac* drive (vortex diode) door het introduceren van asymmetrische pinning centers. In de literatuur kan men vinden dat de verankering van vortices gebaseerd kan worden op nano-gestructureerde roosters van perforaties, chemisch gegroeide defecten, permanente nanomagneten, en zelfs pinning sites geproduceerd door zwaar ionen bombardement. Al deze realisaties zijn gebaseerd op een permanente verandering van de supergeleider, zonder enige mogelijkheid om achteraf modificaties in de distributie en sterkte van de pinning aan te brengen.

Het hoofddoel van deze thesis is om het dynamische gedrag van de vortex ma-

terie onder een volledig nieuw soort pinning landschap, dat bestaat uit ruimtelijke en tijdelijke modulatie van het supergeleidend condensaat, te onderzoeken. Een speciaal geval van ruimtelijke modulatie wordt overwogen in een vernauwde structuur waar stroomlensing extreem hoge vortex snelheden kan veroorzaken. Hierop volgend wordt een tijdsafhankelijke thermische potentiaal geïntroduceerd in het supergeleidende condensaat dat stoboscopische resonanties tijdens de vortexbeweging zal veroorzaken een fenomeen dat niet geobserveerd kan worden in de systemen met statische pinning landschappen. Tot slot wordt er een studie van elektronisch gating gepresenteerd, waar blijkt dat de lokale eigenschappen van de supergeleider, zoals de vrije weglengte of de elektronische bandstructuur in het algemeen, elektronisch beïnvloed kunnen worden. Dit is een volledig onontgonnen interdisciplinair onderzoeksonderwerp, dat men uiteindelijk zal toelaten om supergeleidende toestand en individuele vortices in supergeleidende materialen te manipuleren door middel van ruimtelijk ingesloten en tijdelijk gecontroleerd thermische en elektromagnetische excitaties. Voorts kunnen zulke technieken ons fundamenteel inzicht bieden in de verschillende vormen en gedrag van vortex materie in aanwezigheid van aangelegde stroom, wat zeer relevant is voor het begrijpen van de resistieve toestand van supergeleidende materialen en hun toepassingen.

De thesis is georganiseerd als volgt:

Hoofdstuk 1 presenteert een kort overzicht van de belangrijkste historische gebeurtenissen gerelateerd aan supergeleiding, gekende klassen van supergeleidende materialen, en hun toepassingen. Voorts worden verschillende theoretische modellen gepresenteerd, beginnend bij de fenomenologische modellen van de broers London en Ginzburg en Landau, tot de meer gesofisticeerde microscopische benaderingen, namelijk de Usadel theorie en de Bardeen-Cooper-Schrieffer theorie.

In **Hoofdstuk 2** wordt de gegeneraliseerde tijdsafhankelijke Ginzburg-Landau (gTDGL) theorie beschreven. De centrale vergelijkingen voor de orde parameter en superstroom worden afgeleid, waar de karakteristieke grootheden, zoals de coherentie lengte, penetratie diepte, kritische stroom en inelastische verstrooiingsparameter uitgelegd worden. Een uitbreiding van dit model met de thermische evenwichtsvergelijking wordt beschreven. Het tweede deel van dit hoofdstuk bespreekt het uitgebreide gTDGL model in de aanwezigheid van een tijdsafhankelijk thermisch potentiaal en als parameters van het model ruimtelijk inhomogeen zijn.

In **Hoofdstuk 3** wordt het gekende gedrag van de vortex materie in de aanwezigheid van een extern magneetveld en elektrische stroom besproken aan de hand van verschillende directe voorbeelden, berekend gebruik makend van het gTDGL formalisme. Verder worden verschillende experimentele opstellingen, die gebruikt kunnen worden om het gedrag van de vortex te manipuleren, besproken, speciale aandacht wordt daarbij gegeven aan het ontwerp van een pinning land-

schap of individuele vortex manipulatie door een nabij magneetveld of tunneling tip of een laserstraal.

In **Hoofstuk 4** wordt de dynamica van vortex materie onder stroom lensing door geometrische vernauwing besproken. Vortex snelheden van tientallen km/s zijn gevonden, wat de paar-breking snelheid van het Cooper-paar condensaat overschrijdt. Co-existentie van verschillende vortex fasen bij hoge snelheden worden uitgebreid aangehaald en mogelijke manieren om deze fasen te controleren door middel van pinning landschappen worden besproken.

In **Hoofstuk 5** wordt de invloed van tijdsafhankelijke pinning landschappen op de vortex dynamica bestudeerd. Tijdelijke commensurabiliteit in het gedaante van stroboscopische resonanties werd gevonden wanneer de frequentie van de karakteristieke dynamica van het condensaat overeenkomt met de frequentie van het dynamische pinning landschap. Deze resonanties blijven bestaan in een breed parameter bereik (van magnetisch veld, stroom, temperatuur, materiaal parameters, ezv.) en laten een duidelijke signaal achter in de gemeten spanning, wat gebruikt kan worden voor praktische toepassingen, inclusief metingen van de vortex snelheid.

Hoofstuk 6 presenteert de studie van vortex materie in mesoscopische supergeleiders onder invloed van de elektronische gating. Supergeleiding in een extreem dun (quasi twee dimensionaal) Pb eiland, onder een extern magnetisch veld, werd experimenteel onderzocht in INSP Parijs met een scanning tunneling microscoop (STM) in het spectroscopie regime, gevolgd door de hier gepresenteerde theoretische analyse. Er werd gevonden dat de elektronische structuur van een extreem dun eiland lokaal beïnvloed kan worden door de elektronische gating via de nabijgelegde STM naald, en dus de supergeleidende eigenschappen dramatisch verbeterd of onderdrukt kunnen worden wanneer de STM naald bewogen wordt over het staal. De geobserveerde en berekende veranderingen in de vortex materie zorgen voor het “smoking gun” bewijs voor dit gating effect.

Hoofstuk 7 vat het werk gepresenteerd in deze thesis samen en geeft een toekomstperspectief voor mogelijke verdere studies.

Tot slot wordt in de **Appendix** een korte samenvatting gegeven van de numerieke methodes die gebruikt werden voor de simulaties doorheen deze thesis.

Chapter 1

Introduction

1.1 History of superconductivity

Superconductivity was discovered in 1911 by Gilles Holst and Gerrit Jan Flim at Leiden Physics Laboratory in Netherlands [1]. The duo was working under the supervision of Heike Kamerlingh Onnes (see Fig. 1.1), who had three years earlier discovered a way to liquify helium [1, 2] (in fact, for his investigations on the properties of matter at low temperatures which led, inter alia, to the production of liquid helium, Onnes was awarded the Nobel prize in physics in 1913). Holst and Flim were investigating electrical properties of mercury with high degree of purity at the temperature of liquid helium (4.2 K). Mercury was selected since it was

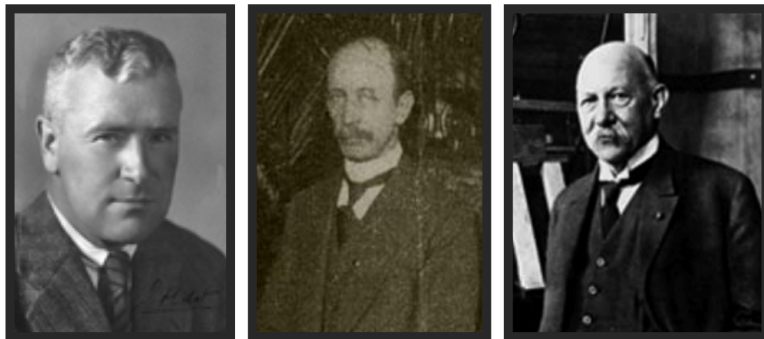


Figure 1.1: From left to right: Gilles Holst, Gerrit Jan Flim and Heike Kamerlingh Onnes.

expected to exhibit relatively high electrical resistance close to 4 K, as opposed to some other metals, like gold, whose resistance already at 13 K was below detection

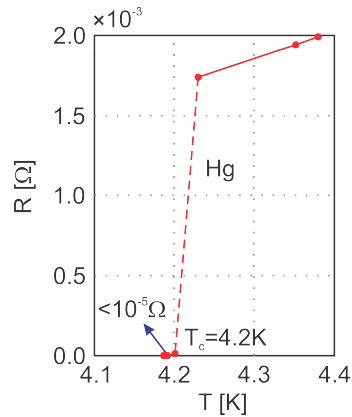


Figure 1.2: The resistance of mercury as a function of absolute temperature, reproduced from the original data obtained by Holst and Flim [3].

threshold. To their surprise, as soon as the temperature reached slightly below 4.2 K, the measured resistance abruptly dropped to zero. At first they believed a short circuit developed somewhere, but soon they learned that this short circuit would repair itself whenever the bath temperature rose above 4.2 K. Proceeding cautiously, Holst improved the resistivity measurement technique by several orders of magnitude, finding that, at 3 K, the lowest temperature he could reach, the resistivity was less than 10^{-7} of its value at room temperature. It was evident that below some temperature, denoted as *critical temperature*, material achieves a state where no electrical resistance occurs, which in turn allows dissipationless transport of electrical current (see Fig. 1.2). The result was first presented by Kamerlingh Onnes at the first Solvay Conference in Brussels [3] in 1911. As it was custom at the time, Onnes reported the work of his laboratory solely under his name, without explicitly mentioning the contribution of Holst and Flim. In the following years several other materials were found to be capable to achieve the superconducting state, namely lead and tin, while, on the other hand, some very good conductors, such as platinum and gold, have never exhibited the superconducting phase [4].

It was until 1933 that it was believed that the only landmark of superconductivity was the dissipationless transport of electrical current. At the time there were already several laboratories across the world, besides Leiden, with capability of producing liquid helium. One of them was in Berlin, under leadership of Walther Meissner, who discovered several new classes of superconducting elements, alloys and chemical compounds before he became interested in determining the nature of the flow of electrical current in superconductors [5]. In particular, he was eager to learn if the transport current flows on the surface of the superconductor, or in

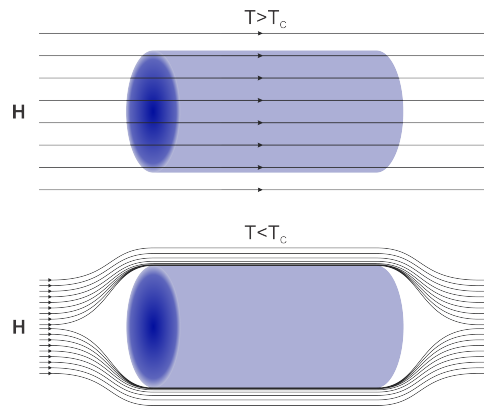


Figure 1.3: Meissner-Ochsenfeld effect in a superconducting cylinder cooled below the critical temperature in a constant external magnetic field. In the superconducting state ($T < T_c$), lines of the magnetic field are effectively expelled from the cylinder.

its bulk. Together with Robert Ochsenfeld, Meissner devised an experiment which made use of a very small coil to measure the magnetic field between two solid, current-carrying, single-crystal cylinders, made of tin. The result was unexpected: even when the tin cylinders were not carrying any current, the magnetic field between them increased when they were cooled into superconducting state, as if there was something forcing the magnetic field to be expelled out of the superconducting cylinders (see Fig. 1.3). It was clear that this effect of expulsion of applied flux is not some dynamical consequence of perfect conductivity, meaning that superconductors also exhibit *perfect diamagnetism* as a fundamental property [6]. In fact, now it is well known that this *Meissner-Ochsenfeld effect* arises because of the flow of internal currents (the so-called Meissner-Ochsenfeld currents) which generate a magnetic field inside a superconductor, equal in magnitude to the applied field, but with opposite direction so that total field is canceled out. Superconductors can remain in the state of perfect diamagnetism only up to a certain applied field, above which magnetic flux penetrates the material, and suppresses superconductivity.

The discovery of the Meissner-Ochsenfeld effect was a crucial turning point in understanding the superconductivity. Up to then, attempts to make theoretical framework that would explain superconductivity, particularly by applying quantum theory, made little progress. After the discovery of perfect diamagnetism in superconductors, even though it still yielded no ground to quantum mechanics, at least the thermodynamics of the phenomenon could be worked out. It was Paul Ehrenfest, Hendrik Casimir and Cornelius Gorter who proved that superconduc-

tivity can be treated as a *thermodynamic phase transition* [1, 7]. Very soon after a phenomenological theory was devised by brothers Fritz and Heinz London (1935) [8]. This theory regarded the local electromagnetic behaviour in superconductors, and it was not only successful in explaining the Meissner-Ochsenfeld effect, but it also provided other predictions. The London brothers claimed that if a hollow superconducting cylinder traps some magnetic flux, then the amount of the trapped flux must be exactly equal to integer multiple of one flux quantum $\frac{h}{e}$ (where h and e are Planck's constant and unit charge, respectively). It was only in 1961 that Bascom Deaver and William Fairbank experimentally confirmed the prediction that flux in superconductors is indeed quantized [9], but with a correction: it was $\Phi_0 = \frac{h}{2e}$ that was the actual flux quantum, already suggesting that charge carriers involved in the superconductivity double the charge of a free electron.

Towards the end of nineteen-thirties, and throughout nineteen-forties the Second World War interrupted the research in superconductivity. It was only in 1950 that the progress in understanding this phenomenon could be resumed. Soviet physicists, Vitaly Ginzburg and Lev Landau developed a phenomenological theory [10] (originally, their work carried the name Ψ theory, but later on, as it gained world fame, it became known simply as *Ginzburg-Landau (GL) theory*) which combined Landau's earlier analysis of second-order phase transition [11] with the important elements of Londons' ideas of superconducting electrodynamics. The final result was to represent the superconducting state very close to critical temperature, T_c , with a complex order parameter, Ψ , obtained as a solution of Schrödinger-like differential equation. The origin of the equation postulated by Ginzburg and Landau was, however, not in quantum mechanics, but in thermodynamics, i.e. the free energy functional. This magnificent tool was able to treat both thermodynamic behavior of superconductivity as it passed through its phase transition, and its spatial distribution near the superconductor-normal metal (SN) interface. The true physical meaning of wave function-like order parameter would not be explained until the microscopic theory came along towards the end of the same decade. However, even after the microscopic treatment of superconductivity was made available, the much simpler and user friendly Ginzburg-Landau model remains the most commonly used tool to analyze complex phenomena in superconductivity.

A very important contribution to the Ginzburg-Landau theory was given by Alexei Abrikosov, former student of Landau, who proposed a new class of superconducting materials, now called *type II* superconductors [12], that can have negative energy associated to a normal metal/superconductor boundary (so-called surface energy) in the presence of magnetic field (as opposed to the *type I* superconductors with positive surface energy, which were the only known superconducting materials at that time). Such state would, in principle, be unstable, and it would

require for the normal state somehow to penetrate inside the superconductor. It was again in 1955 when Abrikosov, inspired by the work of Richard Feynman on vortices in superfluids [13], realized that normal state penetrates type II superconductors in a manner of *quantized flux lines* [14] (i.e. vortices). For their work, Ginzburg and Abrikosov shared a Nobel prize in 2003, together with Anthony Leggett, for his contribution to the theory of superfluidity.

The first steps towards the formulation of a microscopic theory of superconductivity were taken already in 1950, when Herbert Frölich predicted the *isotope effect* [15]. Frölich first realized that the observation that good conductors (e.g. copper, gold) do not become superconducting might mean that superconductivity is produced by enhanced interaction between the conducting electrons and the lattice vibrations (phonons) in materials that were not good normal conductors. Later on, this assumption was experimentally confirmed by showing that the critical temperature for superconducting-normal transition is inversely proportional to the square root of the mass of the ion lattice.

It was in 1957 that the microscopic theory of superconductivity was presented by John Bardeen, Leon Cooper and Robert J. Schrieffer (nowadays known as the *BCS theory*) [16]. The trio started their work in 1955, and was competing with Richard Feynman, who was at the time also trying a way to find the quantum-mechanical explanation of superconductivity and superfluidity. Bardeen, Cooper and Schrieffer were particularly interested in studying the Fermi gas of nearly free electrons, coupled with a weak attraction to lattice phonons. In 1956, Leon Cooper succeeded in showing that the Fermi-gas ground state was unstable in the presence of even a very weak attractive interaction [17], marking the discovery of so-called Cooper pairs of electrons. Eventually, Bardeen, Cooper and Schrieffer succeeded in creating an elegant formulation in which the electrons form a coherent ground-state, acting together to occupy single-particle states in pairs (thus as bosons), so as to optimize the reduction in energy of the system afforded by the weak attractive interactions due to the phonons. The result was a gap in the energy spectrum between the ground state and the lowest-lying excited states. The trio was rewarded for their theory with a Nobel prize in 1972.

It was another student of Landau, Lev Gor'kov, who in 1959 stirred up superconducting community by revitalizing the Ginzburg-Landau theory. Gor'kov managed to prove that very close to critical temperature at which superconducting materials become normal, the microscopic theory of superconductivity, developed by Bardeen, Cooper and Schrieffer, reduces to the model devised by Ginzburg and Landau [18]. This gave complete microscopic backbone to the theory previously regarded merely as phenomenological.

The next very important discovery in superconductivity was the Cooper-pair tunneling. Brian Josephson, a graduate student at Cambridge University supervised

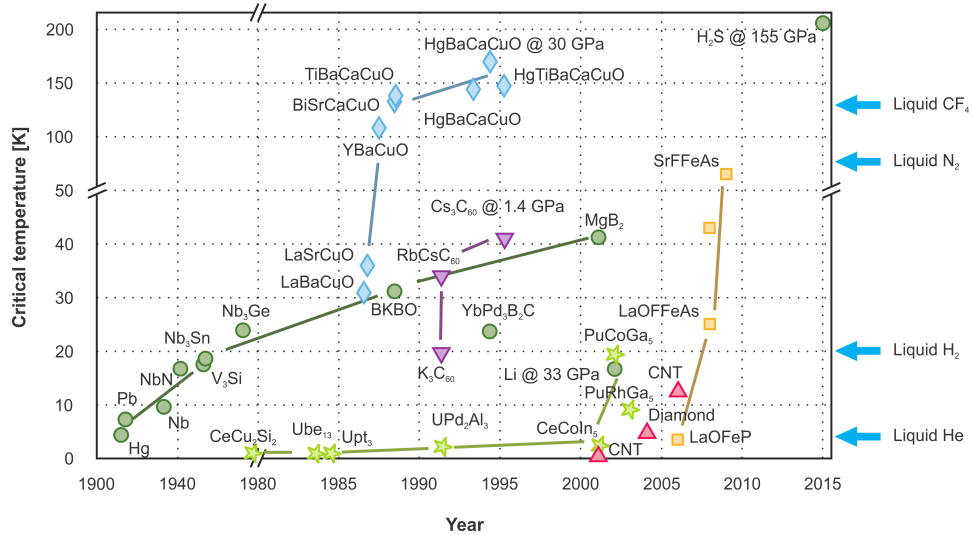


Figure 1.4: Timeline of the increase of T_c in superconductors from 1900 to 2015, according to Ref. [20].

by Sir Alfred Brian Pippard, predicted in 1961 and 1962 that the superconducting quantum liquid should be able to leak through a barrier between two superconducting samples [19]. This was verified experimentally in the following years, and in 1973 Josephson was awarded with a Nobel prize, together with Ivar Giaever and Leo Esaki, for their study of tunneling phenomena in materials. Very soon after its discovery, the tunneling phenomenon in superconductivity was labeled as the *Josephson effect*, and to date this effect has important applications (since among other things it allows for the conversion of frequency into the voltage).

Nearly two decades passed before next big step was made in the field of superconductivity. At the time, the BCS model predicted a theoretical limit between 30 K and 40 K for the critical temperature at which pair-breaking occurs. This was quite an inconvenience, since it locked the maximal working temperature for superconductors far below the room temperature. Then in 1986, Karl Alex Müller and Johannes Georg Bednorz reported a lanthanum-based perovskite ceramic superconductor (LaBaCuO or LBCO) with critical temperature of 35 K, which became known as first high T_c superconductor (HTS) [21]. Shortly after that, a couple of compounds were synthesized, one where lanthanum was replaced with yttrium [22] (so-called YBCO), and another, BiSrCaCuO [23] (BSCCO or “bisco”), with dramatic increase in critical temperature (YBCO showed T_c of 92 K, and BSCCO exhibited T_c of 107 K). Discovery of these materials sparked hope in finding the room-temperature superconductors which is often referred as the Holy Grail of

condensed matter physics (see Fig. 1.4 for evolution of T_c over recent years). Another important implication of HTS materials is that once T_c exceeds 77 K, liquid nitrogen can be used as a cooling agent. Müller and Bednorz were awarded a Nobel prize in 1987 for their ground-breaking discovery. BCS theory struggled to explain the existence of this new HTS family, which was indication that electron-phonon mechanism was not behind Cooper pairing at high temperatures. This was the reason why some new mechanisms were proposed to explain electron pairing in HTS, but to date there still exists no definite answer what yields the very high T_c values in those materials.

Following years correspond to a very turbulent period, as numerous discoveries of the superconductivity-related phenomena were reported. Mostly new materials with interesting superconducting properties were synthesized (such as MgB₂, iron-based superconductors, and carbon-based superconductors). Characteristics of some of these materials are summarized in the following Section. Moreover, ultrathin superconducting films were successfully synthesized, where it was shown that superconductivity can indeed exist in the extreme two-dimensional limit.

1.2 Overview of superconducting materials

To date, thousands of superconducting elements and compounds have been discovered. Superconductivity was first found in *elemental* materials, some of which have already been mentioned in the preceding Section. Most of the elemental superconductors can achieve superconductivity under atmospheric pressure, but others may require some special conditions [4]. Moreover, superconducting properties of bulk may be different from those found in the thin films made of same material. By looking at the periodic table of elements in Fig. 1.5, one can see that very often metals can be superconducting. Interestingly, some metals, known to be very good conductors, namely gold, platinum, copper and silver, do not exhibit the superconducting phase. One can also notice from Fig. 1.5 that all the elemental superconductors are in the low T_c regime. As bulk, most of the elemental materials are type I superconductors, while in film form they may show type II behaviour. Typically, the origin of superconductivity in elemental materials can be explained with BCS theory (electron pairing via lattice phonons), so these materials can be classified as conventional. Based on BCS theory, Cooper pairs in conventional superconductors are characterized by zero net spin and zero angular momentum (*s-wave pairing*) [4].

Clearly, the largest part of the superconducting materials are *alloys and compounds*, and it is virtually impossible to list them all in this thesis. Still, here are shortly presented some classes of superconducting compounds which are of highest im-

Chapter 1

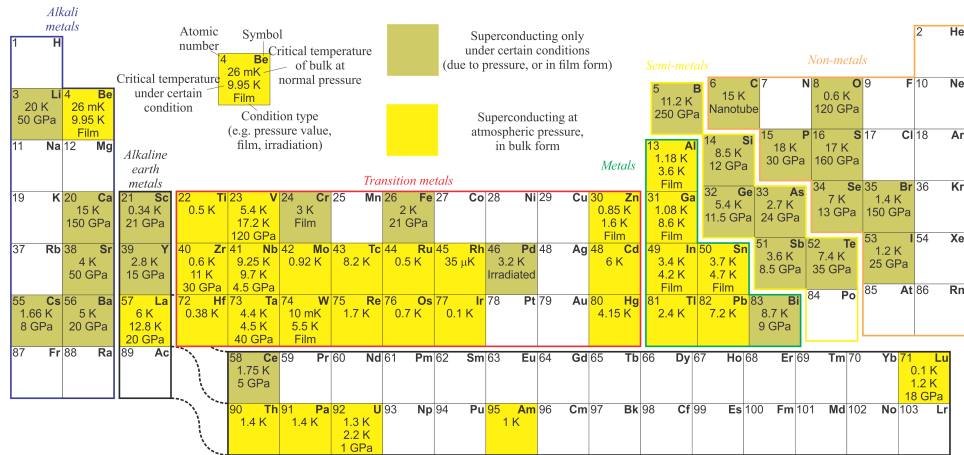


Figure 1.5: Periodic table of superconducting elements.

importance for the fundamental physics and for their technical applications.

The β -tungstens, also known as A_3B structures (where A is a transition metal and B can be any element) are the superconducting materials that have transition temperatures above 20 K at atmospheric pressure, and are capable of sustaining magnetic fields up to 20 T [24, 25, 26]. β -tungstens are mostly made as thin films, due to which they exhibit extreme type II behavior. A representative from this group, Nb_3Ge , with $T_c = 23.2$ K, was for over a decade regarded as the material with highest critical temperature. Another member of this class of alloys is Nb_3Sn , often used for manufacturing superconducting magnets.

Magnesium diboride (MgB_2) is a material with critical temperature just below 40 K, synthesised in 2001 by Jun Akimitsu and coworkers in Japan [27, 28]. MgB_2 is a conventional superconductor, in a way that the origin of its superconductivity can be explained by the electron-phonon interaction, described by BCS theory. However, superconductivity in this material is a consequence of nontrivial mixing of multiple energy bands. As a result, two separate superconducting energy gaps open in MgB_2 (one close to 2 meV and other gap near 7.5 meV) on different parts of the Fermi surface. Magnesium diboride is regarded as a type II material (although it may exhibit some intermediate behavior between type I and type II superconductors [29]), where the maximal field that MgB_2 can sustain before going to the normal state can exceed 30 T in oriented films with carbon doping [30].

Metal-hydrogen systems are the class of compounds with T_c around 10 K [31, 32]. They were intensively studied in the 1970s, prior to the discovery of HTS. One representative of this group is palladium-hydrogen, discovered in 1972. For this material, it was of particular interest which Pd-H ratio could provide highest

T_c . As this ratio approaches 1, the critical temperature is found to be around 9 K. However, by replacing hydrogen with heavier deuterium, though one would expect that T_c will be lowered due to the isotope effect, the critical temperature was found to be over 11 K at Pd-D ratio of 1. Additionally, by implementing hydrogen to the Pd-noble metal alloys, critical temperatures up to 17 K were measured [33].

Fullerene-based superconductors are derivatives of a carbon molecules, denoted as C_{60} , found in 1985. The fulleren molecules can form crystals, which, then, can be doped with different elements. In such a way one can obtain *fullerides* which in some cases can be superconducting up to very high temperatures [34]. First such fulleride was K_3C_{60} , with T_c of 20 K. Another example is Rb_3C_{60} fulleride, with T_c of almost 30 K, while the fulleride exhibiting record T_c of 40 K is Cs_3C_{60} (although such high critical temperature was obtained under the pressure of 1.4 GPa). The mentioned fullerides behave as type II superconductors that can sustain fields up to 50 T. There is overwhelming evidence that the superconductivity observed in these materials is conventional, i.e. it is based on the electron-phonon mechanism of pairing described by the BCS theory.

Chevrel phases have the composition MMo_6X_8 , where M stands for metal (for example, Pb or Sn) or rare-earth atom (e.g. Gd or Tb), and where X denotes sulfur or selenium [35]. Though the Chevrel phases are conventional superconductors, they do possess several properties which make them highly interesting. For example, $PbMo_6S_8$ has a critical temperature of 15 K, while sustaining a maximal field of 60 T. This makes $PbMo_6S_8$ very interesting for construction of magnets, but since the material is very brittle, the fabrication of wires is very difficult. Another Chevrel phase, namely $TbMo_6S_8$, where rare-earth metal is implanted, exhibits antiferromagnetic ordering in addition to superconductivity, which is then not fully destroyed, but merely weakened. It is very rare to see such a phenomenon in conventional superconductors, since any magnetic impurities tend to destroy superconductivity. Critical temperature of $TbMo_6S_8$ is 1.65 K, but the magnetic ordering occurs at 0.9 K. At the onset of magnetic order, maximal field superconductor can sustain will be reduced. Similar coexistence of antiferromagnetic ordering and superconducting state can be found in the family of *borocarbides*, such as $HoNi_2B_2C$. Moreover, a ferromagnetic ordering was found at temperatures below 0.6 K in $HoMo_6S_8$, which is superconducting up to 2 K. At the onset of ferromagnetic order, superconductivity is destroyed in $HoMo_6S_8$.

Heavy-fermion superconductors are the class of superconducting materials, where the effective mass of the electrons is several hundred times larger than the free-electron mass [36, 37, 38]. Such values of mass are due to extremely high electronic density of states at the Fermi energy, which results from the interaction between the mobile electrons and the magnetic moments localized at the lattice sites. The heavy-fermion superconductors, such as UPt_3 , UGe_2 or UBe_{13} , have

the unconventional electron pairing mechanism. Similar to the borocarbides and Chevrel phases, they also exhibit magnetic ordering in the presence of superconductivity.

Cuprates are the group of the *oxide* superconductors, renowned for their extremely high transition temperatures (in fact, they are synonymous with the high T_c superconductors). In the above text few representatives of the cuprates were already mentioned: LBCO, YBCO and BSCCO [21, 22, 23]. The cuprates are typically extreme type II superconductors. Due to their layered structure, cuprates exhibit strong anisotropy in magnetic field. The thermal fluctuations are another important factor that influences the HTS and causes particular properties unknown to the conventional superconductors. Finally, mechanism responsible for electron pairing in cuprates is still not understood. What is known is that spin state of Cooper-pairs in cuprates is singlet, with angular momentum of $2\hbar$, corresponding to the unconventional d-wave superconductivity.

Iron-based superconductors (IBSC) are iron-containing chemical compounds whose superconducting properties were discovered in 2006 [39]. This type of superconductors is based instead on conducting layers of iron and a pnictide (chemical elements in group 15 of the periodic table, here typically As and P) and seems to be the next generation of high temperature superconductors. In fact, compounds such as LaOFeAs, SmFeAsOF, and PrFeAsOF can achieve critical temperatures in range between 26 and 52 K. Similarly to superconducting cuprates, the properties of iron based superconductors change dramatically with doping. Parent compounds of FeSC are usually metals (unlike the cuprates) but, similarly to cuprates, are ordered antiferromagnetically. The superconductivity in these materials emerges upon either hole or electron doping. Iron-based superconductors have several unique properties such as robustness to impurity, high upper critical field and excellent grain boundary nature. These properties are advantageous for wire application. Recent progress in the performance of superconducting wires of IBSC is wide eyed, i.e. the maximal critical current has reached the level of commercial metal-based superconducting wires and exceeded under high magnetic field [40].

Organic superconductor [41, 42, 43] was first synthesized in 1979 by Klaus Bechgaard and coworkers, namely the $(\text{TMTSF})_2\text{PF}_6$, which exhibited T_c of 0.9 K at the pressure of 1.2 GPa. Following this, several other TMTSF-based superconductors were found, with critical temperatures not exceeding 2 K. This family of organic superconductors belongs to the type II category with anisotropic properties. The class of so-called two dimensional BEDT-TTF organic superconductors has recently been investigated, where the critical temperatures exceeding 10 K were reported. The mechanism behind the pairing in these superconductors is not entirely clear. Some of the organics show similarity with cuprates to the fact that their Cooper pairs also exhibit angular momentum of $2\hbar$.

Metallic hydrogen is a phase of hydrogen that behaves as an electrical conductor. Its existence was first predicted theoretically in 1935 [44], where it was expected that when squeezed with enough pressure inside an anvil, hydrogen should be able to conduct electricity, the hallmark of a metallic state. Unfortunately, pressure needed to achieve metallic hydrogen phase is measured in hundreds of GPa (about million times the atmospheric pressure) - a magnitude which up to now is only found in the core of the Earth. As an interesting consequence of this requirement, it is often considered that the gas-rich jovian planets, such as Jupiter, or Saturn, might have metallic hydrogen in their cores. Metallic hydrogen is hypothesized to have some peculiar properties, one being the high-temperature superconductivity. In fact, it is expected that the critical temperature for the superconducting transition of metallic hydrogen exceeds 300 K [45, 46]. Moreover, superconducting metallic hydrogen is predicted to be metastable so that it may exist at room temperature when the pressure is released [47]. Throughout the last 80 years, there have been several attempts to synthesize the metallic hydrogen, and only recently the group from Harvard University reported to be successful in exposing hydrogen to the pressure of nearly 500 GPa [48]. In general, the scientific community exerted certain amount of skepticism towards this claim, since this experiment needs to be reproduced and verified.

1.3 Superconducting electronics

Superconducting electronics (also known as *supertronics*) often utilizes the properties of the dynamic behavior of a vortex collective (so-called *fluxonics*) in a nanofabricated superconducting films, with strong emphasis on the confinement, manipulation, and motion of the vortex matter [49]. Anchoring the vortices (pinning), guided motion and rectification-based effects are among the features exploited in fluxonic devices which are based on the dynamical, the directional and the orientational control over flux quanta.

Major advantages of the supertronics when compared to semiconductor technology are found in much faster devices with decreased power demand and losses, and with the unprecedented quantum accuracy and sensitivity. Digital superconductive electronic devices featuring Josephson junctions as a principle circuit element can achieve clock frequencies of hundreds of GHz. Currently, mainstream superconducting digital technology is based on the Rapid Single-Flux Quantum (RSFQ) logic [50]. There are three main application groups for superconducting digital technology. The speed factor in combination with quantum accuracy of the digital information is essential for *telecommunications*. The low power dissipation of the superconducting circuit comes into play for large systems like *super-*

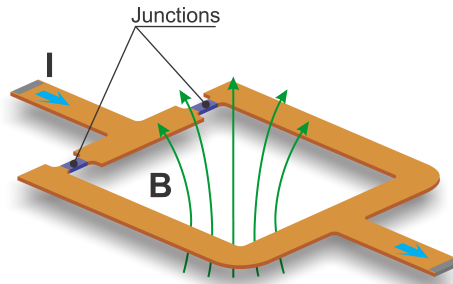


Figure 1.6: Sketch of a SQUID in magnetic field and with some applied current, where two Josephson junctions based on superconductor (orange color)-insulator (purple color)-superconductor joints are indicated.

computers and back-bone routers where integration density and parallelism of the semiconductor circuits suffer from the thermal losses. The fact that RSFQ circuits are the only complex digital circuits capable of operating below 4 K makes them a unique solution for interfacing with *cryo-sensors and superconducting quantum bits (qubits)*.

Apart from its uses for digital logic, superconductive electronics provides also the most sensitive detector of magnetic fields - the Superconducting QUantum Interference Device (shortly SQUID, see Fig. 1.6). SQUID utilizes the principle of quantum interference developed in the two superconducting electrodes separated by a very thin dielectric barrier where current tunnels (Josephson junctions). In principle, every physical quantity which can be converted into magnetic flux can be measured with SQUIDs, e.g. magnetic induction or electrical current. SQUIDs are fabricated using sophisticated thin-film deposition and patterning techniques and have to be cooled to operational temperatures of about 4 K (low T_c SQUIDs) or about 77 K (high T_c SQUIDs). SQUIDs have a number of applications, such as sensors used in medical research for detecting the delicate magnetic signals from heart and brain [51]; as sensor for geological surveying [52], and as amplifiers of electric signals.

Another important field of application is the detection of weak signals by bolometers, superconducting nanowire single-photon detectors (SNSPD), and superconductive tunnel junctions [50]. These devices can be used for detection of photons in a wide range of wavelengths (from far infrared up to gamma-ray range). When sensing occurs, temperature of the superconducting detector changes, leading to the change in electrical properties of the system. It is crucial that response time of the device is longer than the rate at which photons arrive at the detector, meaning that system is used to measure energy flux of the radiation. On the

other hand, if the detection time is shorter than the radiation rate, one speaks of a calorimeter, which can be used to measure the energy of a single particle. Since some extremely sensitive measurements must be performed at very low temperatures (<1 K), it is preferred to work with superconducting bolometers made of materials such as Al, W, or Ta, which have the critical temperature in the same range as the working temperature of the experiment. For SNSPD preferred are Nb and NbN as materials whose critical temperature does not exceed 10 K.

As stated earlier, superconducting devices have to be cooled to rather low temperatures. Whereas this was a bottleneck in the past, a huge progress with cooling techniques has been made in recent years. Very compact systems with high reliability and a wide range of cooling power are available commercially, from micro-coolers of match-box size with mW cooling power to high-reliability coolers of many watts of cooling power for applications in space. Therefore, the future for superconducting electronic devices in low-temperature applications which require very high speed, low-power consumption, extreme sensitivity or extremely high precision, looks more than promising.

1.4 Overview of the theories of superconductivity

1.4.1 Phenomenological theories

In this Section a review of the important phenomenological theories that were successful in explaining some features of superconductivity will be presented. The first of such theories was devised by brothers Fritz and Heinz London in 1935. They provided a local superconductive analogue to the Ohm's law, in order to describe the property of dissipationless transport of electrical current in superconductors. The issue with the standard Ohm's law and superconductors reflects in the fact that supercurrent flows without resistance, so one needs to establish a relation between supercurrent density \mathbf{J} and voltage U in a manner different from the case of normal metals. One more thing that London brothers had to take into account was the Meissner-Ochsenfeld effect, i.e. the property of perfect diamagnetism in superconductors.

Russian physicists Vitaly Ginzburg and Lev Landau presented in the 1950 another phenomenological theory of superconductivity based on non-local mean-field approach, which was originally called Ψ theory. Their framework later gained fame simply as the Ginzburg-Landau (GL) model. In the GL model, it is argued that thermodynamic free energy of a superconductor can be expressed in terms of a complex function Ψ , which plays the role of an order parameter in the electronic phase transition of the second kind. Moreover, nearly a decade from its first presentation GL theory gained a strong boost when it was shown that it can be derived

from the BCS microscopic theory in the limit of close proximity to the transition temperature T_c , in case of gapless superconductors.

1.4.1.1 The London model

London brothers proposed a model consisting of equations for the magnetic field \mathbf{B} and the electric field \mathbf{E} , which aimed to describe dissipationless transport of electrical current ($\frac{\partial \mathbf{B}}{\partial t} = 0$) and expulsion of magnetic field in superconductors ($\mathbf{B} = 0$) governed by the Meissner-Ochsenfeld effect [8]. Their equations read

$$\mathbf{E} = \frac{\partial}{\partial t} \left(\frac{m^*}{n_s e^{*2}} \mathbf{J}_s \right), \quad (1.1)$$

$$\mathbf{B} = -\nabla \times \left(\frac{m^*}{n_s e^{*2}} \mathbf{J}_s \right), \quad (1.2)$$

where m^* , e^* and n_s are effective superconducting electron mass, effective charge and density, respectively. Eq. 1.1 is used to describe the property of perfect conductivity, because any electric field accelerates the superconducting electrons, as opposed to Ohm's law which suggests that the electron velocity in a normal conductor is maintained constant. Perfect conductivity described by the first London equation can be achieved in the presence of any stationary fields (which can be easily verified from Faraday's law $\nabla \times \mathbf{E} = -\frac{\partial \mathbf{B}}{\partial t}$), but in order to describe the Meissner-Ochsenfeld effect, additional restriction on the magnetic field is required, namely inside the superconductor $\mathbf{B} = 0$ must be fulfilled. For this reason the second London equation was devised. When Eq. 1.2 is combined with Ampere's law ($\nabla \times \mathbf{B} = \mu_0 \mathbf{J}$) and with flux conservation ($\nabla \cdot \mathbf{B} = 0$), one obtains a differential equation

$$\nabla^2 \mathbf{B} = \frac{\mathbf{B}}{\lambda^2}, \quad (1.3)$$

which describes the penetration pattern of magnetic field inside the superconductor. The initiated reader will notice that the magnetic field inside the superconducting material decays exponentially, starting from the interface of the superconductor and its surroundings, over the length scale

$$\lambda = \sqrt{\frac{m^*}{\mu_0 n_s e^{*2}}}, \quad (1.4)$$

which is called (London) penetration depth. Therefore, within the Eq. 1.3 lies the essence of the Meissner-Ochsenfeld effect.

One should note here that a bit more compact way to represent Eq. 1.1 and 1.2 was later given by Fritz London, emphasizing the use of magnetic vector potential \mathbf{A} , as

$$\mathbf{J}_s = -\frac{n_s e^{*2}}{m^*} \mathbf{A}. \quad (1.5)$$

The Eq. 1.5 by itself is not gauge invariant, and it must be accompanied with the, so-called, London gauge, $\nabla \cdot \mathbf{A} = 0$. Though it does not explain the nature of superconductivity with the rigor of microscopic theory, the framework given by the London brothers describes very well the behavior found in superconductors with short electronic mean free path l (so-called dirty superconductors). Their theory also predicted the quantization of magnetic flux inside the superconductor, where the most profound consequence of that prediction are the point-like objects carrying quantized magnetic flux (i.e. vortices) which are characteristic of type II superconductors.

1.4.1.2 The Ginzburg-Landau model

Vitaly Ginzburg and Lev Landau devised a complex-valued quasi-classical wave function Ψ to describe the transition from the normal state ($\Psi = 0$) to higher-ordered superconducting state ($\Psi \neq 0$) [10]. In the absence of magnetic fields, this phase transition is of second order, where Ψ contains the information about an order parameter. By employing the Landau-Lifshitz theory of second-order phase transition, they were able to construct a free energy functional needed to describe the transition in superconductors. The free energy was expressed in terms of the order parameter, but only in the limiting case when the temperature of the system is close to the critical temperature T_c , at which transition occurs. From there and with the assumption of zero-field cooled system, Ginzburg and Landau expressed free energy density functional in terms of $|\Psi|^2$ (which corresponds to the density of superconducting electrons):

$$f_{S0} = f_N + a|\Psi|^2 + \frac{b}{2}|\Psi|^4 + o(|\Psi|^6). \quad (1.6)$$

f_{S0} and f_N are the free energy density of the superconductor when no external fields are present and free energy density in the normal state, respectively. The actual free energy is then obtained by integrating Eq. 1.6, $F = \int f_{S0} dV$ over some respective volume V . The parameters a and b are phenomenological expansion coefficients, which are material-dependent. Several constraints are imposed upon the terms in the free energy given by Eq. 1.6, mostly arising from the fact that f_{S0} must have a minimum (if f_{S0} has no minimum, then there is nothing preventing it from assuming arbitrarily large values). In that case, $b = \frac{\partial^2 f_{S0}}{\partial (|\Psi|^2)^2}$ must

be positive, which follows from the second derivative criterion for minima. From there, one deduces that the value of $|\Psi|^2$ for which the free energy is minimal is $\frac{-a}{b}$. It is important to notice here that the difference $f_{S0} - f_N$ at the minimum of superconducting free energy must correspond to the condensation energy of a superconductor, $-\frac{\mu_0 H_c^2}{2}$, where H_c is the thermodynamic critical field. Since below T_c the order parameter $|\Psi|^2 = \frac{-a}{b}$ must be finite (non-negative, too), and vanish at T_c , it is clear that $a = 0$ at T_c , and $a < 0$ when $T < T_c$. In the original work of Ginzburg and Landau, a was obtained close to T_c as a Taylor's series expansion up to a linear term, $a(T) \approx -a_0 \left(1 - \frac{T}{T_c}\right)$, while in the same limit $b(T) \approx b_0$ (where a_0 and b_0 are some positive coefficients). In general, both a and b should be temperature dependent [53], and in the broad range of temperatures below T_c they can be estimated as:

$$a(T) = -a_0 \frac{T_c^2 - T^2}{T_c^2 + T^2}, \quad (1.7)$$

and

$$b(T) = b_0 \frac{T_c^4}{(T_c^2 + T^2)^2}. \quad (1.8)$$

In the extreme case of $T \rightarrow T_c$ one can see that Eqs. 1.7 and 1.8 can be reduced so that $a(T) \approx -a_0(1 - \frac{T}{T_c})$ and $b(T) \propto b_0$.

In the presence of inhomogeneities Eq. 1.6 may contain additional terms. Particularly, in the presence of magnetic field the kinetic term, $\frac{1}{2m^*} |\Pi\Psi|^2$, is included in the free energy (where Π is the gauge invariant canonical momentum), together with the energy change brought by the magnetic field, $\frac{1}{2\mu_0} (\nabla \times \mathbf{A})^2$. By means of variational method one can derive the famous Ginzburg-Landau equations from the presented free energy functional, which is the central topic of Sections 2.1.1 through 2.1.4 of this thesis.

The Ginzburg-Landau theory is very general and has applications in many different areas of physics and engineering. It can be modified to describe different physical systems, including magnetism, liquid crystal phases, and even the symmetry-breaking phase transitions, which took place in the early universe as matter cooled following the Big Bang. In the field of superconductivity it brought further insights in the study of type I and type II materials, with possibility to treat vortices as realistic objects with finite size.

1.4.2 Microscopic formalism

1.4.2.1 BCS theory

BCS theory was the first successful microscopic theory of conventional superconductivity, developed by John Bardeen, Leon Cooper and Robert Schrieffer in 1957 [16, 54]. The major success of this theoretical formalism reflects in the fact that it successfully treats the general many-particle problem and provides the corresponding ground state for a many-body system in which the coupling mechanism of the electronic Cooper pairs exists [17, 54]. From the BCS theory it follows also that the superconductors must have an energy gap between the ground state and the normal state. For their work Bardeen, Cooper and Schrieffer were awarded the Nobel prize in physics in 1972.

The main task in BCS theory was to show that in the presence of some attractive potential (no matter how weak) the normal free electrons above Fermi sea will pair up. The (Cooper) pairs (being bosons) then occupy the lower energy state, namely the ground state, rendering the normal state energetically unfavorable. The electronic pairing is, of course, not unconditional. Firstly, the electron pair must have the energy above the Fermi energy, E_F . The momenta of the pair-to-be should, in general, be of equal magnitude, but opposite in direction. Finally, spins of the two electrons must be opposite. Only when these conditions are fulfilled, the electrons in the presence of an attractive potential will effectively correlate and go to the ground state as a pair.

The next task in the BCS theory was to describe the nature of the attractive potential. In a normal electron gas the predominant interaction is the repulsive Coulomb force, and in order for some attractive interaction to exist, electrons must couple with other particles or excitations, such as phonons, electrons from the other bands, spin waves in magnetic media, etc. From the earlier work of Frölich (1950), it was already known that the interaction between electrons and the atomic lattice via phonons is strongly rooted in superconductivity, so this mechanism was selected to describe the effective attraction between electron pairs. The electron-phonon interaction was incorporated into the global picture of superconductivity as follows: when two electrons are found above E_F , with the momentum and spin properties described above in the text, they move much faster than the vibrations in the crystal lattice (phonons). As the electron passes through the lattice, it will cause the polarization (accumulation of the positive ionic charge) of the lattice, similar to the wake of water behind the speed-boat. This polarization will relax over a long time period, which is more than enough for another passing electron to be caught in the “wake” of the first electron, thus effectively producing a Cooper-pair. The pair is spatially confined to a volume of radius ξ_0 , which is called the microscopic

coherence length.

After explaining the conditions for appearance of a single Cooper pair, Bardeen, Cooper and Schrieffer considered the generalized case (within a mean-field approximation) where all electrons undergo the same treatment, so the entire structure behaves as a condensate of Cooper pairs. The obtained condensate state is bosonic in nature, with total spin equal to zero. Since the condensate is in the ground state, with its energy lower than the normal state, the energy gap opens up. The gap is responsible for stabilization of Cooper pairs.

BCS theory was successful in explaining many of the phenomena found in conventional superconductors. For example, it showed that dissipationless current transport is due to the fact that in the presence of superconducting gap there will be no scattering of the electrons by the lattice atoms. Due to the condensation of the Cooper pairs into the bosonic state, the Meissner-Ochsenfeld effect naturally arises from BCS theory. The framework of Bardeen, Cooper and Schrieffer also provided the microscopic backbone to the phenomenological theory of Ginzburg and Landau. In the work of Lev Gor'kov in 1959 it was shown that close to the transition temperature, T_c , BCS wave function is equivalent to the order parameter from GL theory.

Though BCS theory was successful in explaining many phenomena regarding the conventional superconductivity, it is only applicable to the homogeneous systems without disorder. If one wants to study the systems where boundaries are imposed, or possibility of tunnel junctions, then different theoretical models must be employed. One such model is developed by Nikolay Bogolyubov and Pierre-Gilles de Gennes (*BdG model*) [55], where electron-like and hole-like fermionic quasi-particles are considered, with energies above the superconducting energy gap. The electron-like and hole-like quasi-particles are each linear combinations of the electron and hole wave functions in the normal state. However, because of the spatial dependence introduced by the boundaries, the linear combinations are in general not as simple as in the homogeneous case. BdG framework allows one to study the systems with boundaries or structures with interface between the superconducting and normal materials (SN interface). It is also used to treat clean superconductors.

1.4.2.2 The equation of motion by Gor'kov, Eilenberger and Usadel

Since the early days of the phenomenon, the out-of-equilibrium superconductivity has been attracting the attention of both experimental and theoretical solid state community. One of the reasons why this part of physics of superconductors is so renown is the extremely high degree of complexity behind it, where both the phase and the magnitude of the macroscopic wave function vary spatially and temporally. In particular, such dynamical behavior has been observed in superconducting weak

links (Josephson junctions), and phase slip centers in long superconducting filaments, both carrying transport current in excess of their respective critical currents.

One of the challenges met within theoretical descriptions of such spatially inhomogeneous and time-varying systems is the fact that one has to resort to Green's function techniques, which are a powerful but a very cumbersome toolbox. In general, Green's function is the response to the Dirac's δ distribution of a characteristic inhomogeneous differential equation, defined on a given domain, with specified initial and/or boundary conditions. Once the characteristic equation is solved for the Green's function, this solution can be related to the realistic physical environment. Within such a framework, Lev Gor'kov invented a powerful technique by constructing a set of equations of motion for the Green's functions [56, 57]. These equations couple the so-called normal and anomalous Green's functions, which are relevant for description of electron pairing into Cooper pairs. Anomalous and normal Green's functions can be used then to form a closed set of equations, the solutions of which bear all the results of the BCS theory, and moreover, can be readily extended to incorporate dirty systems with impurities (commonly, type II superconductors), as well as deal with nonlinear and dynamic phenomena. In other words, after solving such a set of equations, one essentially obtains all the relevant information about physical properties of superconductors.

Unfortunately, the model devised by Gor'kov is difficult to solve and is numerically very demanding. This was the reason why Gert Eilenberger (also Yuri Ovchinnikov and Anatoly Larkin) developed transport-like equations for a new set of Green's functions which were related to Gor'kov's formalism, where the relation between old and new Green's functions was an integration over the energy [58]. Eilenberger's set of equations was reduced, having two instead of four equations presented by Gor'kov.

The next step in this cumulative work was done by Klaus Usadel. What he learned is that for type II superconductors in the dirty limit the microscopic Green's functions introduced by Eilenberger are nearly isotropic in space [59]. From there, Usadel simplified Eilenberger's formalism to a case where diffusive motion of the Cooper pairs and normal electrons can be described. Moreover, the diffusion equation given by Usadel is much more tractable and amenable to numerical implementations, enabling realistic experimental geometries and situations to be analyzed. In particular, issues of quasi-particle injection at the normal metal-superconductor interface, non-equilibrium quasi-particle distribution, and so on, are readily computed. What is especially important for this thesis is the fact that generalized time-dependent Ginzburg-Landau equation (discussed in Section 2.1) can be obtained from the theory of Usadel, where all the phenomenological parameters now have microscopic justification.

Chapter 2

The generalized time-dependent Ginzburg-Landau (gTDGL) framework

In this Chapter the generalized time-dependent Ginzburg-Landau (gTDGL) model, used for description of the relaxation processes and dynamic behavior of dirty superconducting films, is presented. The approach in derivation of relevant equations featured throughout the thesis is phenomenological in nature, where eventually the microscopic justification for each physical quantity is given. By extending the gTDGL model with the equation of thermal balance, the thermal fluctuations that play an important role in dynamic regime are also taken into account.

2.1 gTDGL equations and their validity

Though the Ginzburg-Landau (GL) theory can be used to describe many phenomena in superconductivity, in its core form it cannot describe transitional processes nor dynamic response to the external excitations, which accompany any phase transition process. Because of this, an extension to the original work of Ginzburg and Landau, describing periodic and relaxation processes, was needed. In the pioneering work of Isaak Markovich Khalatnikov and Lev Landau [60, 61] general solution was proposed for this class of problems (the LK theory, where the superconductivity is just one particular case) in the form of relaxation time of an order parameter.

Albert Schmid [62, 63] proposed the gauge invariant version of the LK framework that provided a fundamentally important extension to the theory of superconductivity - a time-dependent GL (TDGL) model. Schmid also presented the

microscopic background to the phenomenological approach used in LK theory. On the other hand, the microscopic justification of both GL [64] and TDGL models narrowed down their applications to only gapless superconductors [65] (materials containing paramagnetic impurities which smear out a well defined energy gap).

Further modification of TDGL model that was given by Lorenz Kramer and Richard Watts-Tobin in 1978 [the generalized TDGL theory (gTDGL)] introduced for the very first time a microscopic parameter that accounts for the presence of an energy gap [66, 67]. To date, gTDGL remains one of the most versatile theoretical tools for treatment of dynamic processes in superconductivity, and it will be the main tool used to obtain results in this thesis.

2.1.1 Free energy functional and relaxation time of the order parameter

Thermodynamically, one considers superconducting state as a consequence of a phase transition. A phase transition of a system is a transformation from one state of matter to another, which in this particular case is a transition from normal state of electronic matter to a superconducting state, occurring when temperature drops below a given critical point. It is customary to say that the normal state is of higher symmetry (state occurring at higher temperatures), while the superconductivity belongs to the lower-symmetry state (occurring at lower temperatures).

To describe the properties of the system in the low symmetry state, the Helmholtz free energy F or the entropy S can serve as convenient figures of merit [68]. Since it is more natural for one to work with energies, one should then consider the free energy. Furthermore, close to the transition temperature, the free energy can be constructed as a sum of terms determined from a measure of the symmetry of the system - the complex order parameter Δ , whose magnitude is zero in higher state, and nonzero in low state of symmetry. Some properties of the order parameter can be concluded from the order of the phase transition, corresponding to the order of the derivative in the free energy with respect to some physical quantity (e.g. temperature, magnetic field, etc.) where discontinuity appears. In the absence of any external fields, superconductivity belongs to the family of the second-order phase transitions, where the order parameter must be a continuous function around T_c and must abruptly drop to zero at critical temperature. From here it follows that the physical quantity proportional to the second derivative of F with respect to the temperature must have a discontinuity at T_c , and this is, in fact, the case for the heat capacity C (indeed, the heat capacity is defined from thermodynamics as $C \propto \frac{\partial^2 F}{\partial T^2}$). Because of this one can obtain the free energy as a Taylor expansion in terms of $|\Delta|$. Additionally, the free energy is constructed in such a way that it must have a minimum, in order to prevent it from having arbitrarily large values.

Though one can expect that the expansion of the free energy in general assumes the form $F = c_0 + c_1|\Delta| + c_2|\Delta|^2 + c_3|\Delta|^3 + c_4|\Delta|^4 + o(|\Delta|^5)$, where $c_0 = F_0$ is the free energy of the higher-symmetry state, and parameters c_i (with $i = \{1, 2, 3, \dots\}$) are some material-dependent parameters, within the Landau-Lifshitz theory of phase transitions of the second kind higher-order terms are omitted from the final expression. In fact, for the second-order phase transitions, the physics is mostly well described by expansion up to the term containing $|\Psi|^4$. Regarding the restrictions on remaining coefficients, c_1 must be zero since it is impossible to have a non-zero order parameter invariant to all symmetries that would vanish during the phase transition, while $c_3 = 0$ because otherwise it would imply the first-order phase transition. Remaining coefficients c_2 and c_4 (it is customary to denote c_2 as α and c_4 as $\frac{\beta}{2}$, which is done in the rest of the thesis) were already mentioned when Eq. 1.6 was described, where $c_2 \propto a$ and $c_4 \propto b$ from Eqs. 1.7 and 1.8, respectively. Also, the function Ψ from Eq. 1.6 used as an order parameter in original GL theory carries the physical meaning of the superconducting wave-function, while Δ carries the information about the energy gap of the superconducting condensate. The relation between the two will be described later in the text, when microscopic explanation of the the phenomenological quantities is presented.

Within the GL framework in the presence of an external magnetic field \mathbf{B}_e , instead of F , the Gibbs free energy G is constructed to describe superconducting state in thermodynamic equilibrium, near critical temperature T_c , as

$$G_S^{(eq)} = G_N + \int_V \left[\alpha|\Delta|^2 + \frac{\beta}{2}|\Delta|^4 \right] dV + \int_V \gamma |(-i\hbar\nabla - e^*\mathbf{A}) \Delta|^2 dV + \int_V \frac{(\nabla \times \mathbf{A} - \mathbf{B}_e)^2}{2\mu_0} dV. \quad (2.1)$$

In Eq. 2.1 integration is performed over the volume V bounded by the oriented surface \mathbf{S} . One distinguishes the following terms in $G_S^{(eq)}$: the free energy of the normal state, G_N , the condensation energy term which accounts for the spatial variation of the order parameter, $\int_V \left[\alpha|\Delta|^2 + \frac{\beta}{2}|\Delta|^4 \right] dV$, the gauge-invariant kinetic energy term, $\int_V \left[\gamma |(-i\hbar\nabla - e^*\mathbf{A}) \Delta|^2 \right] dV$ ($\gamma > 0$ is the third phenomenological parameter that carries no thermal dependence), and the energy needed to screen the external magnetic field, $\int_V \left[\frac{(\nabla \times \mathbf{A} - \mathbf{B}_e)^2}{2\mu_0} \right] dV$.

With the free energy in equilibrium alone, one can construct stationary GL equations by varying the energy functional with respect to complex conjugate order parameter, Δ^* (it is also possible to vary the equilibrium free energy with respect to the order parameter instead, ending up with the complex conjugate of the first GL

equation), and vector potential \mathbf{A} , respectively. Since the time-dependent phenomena are of the interest here, it is necessary to accompany $G_S^{(eq)}$ with an additional term that can describe relaxation processes in the superconductor. Following the lines given in the approach of the Landau-Khalatnikov theory of superfluid helium [60], and with the Schmid's condition for gauge invariance due to temporal fluctuations [62], one can postulate a more general expression for the total free energy, G_S :

$$G_S = G_S^{(eq)} + G_S^{(relax)}, \quad (2.2)$$

where $G_S^{(relax)}$ is the relaxation term. In order to expand the scope to the temporal domain, the relaxation term is naturally introduced to the GL equations, rather than to the free energy. As such, the actual form of $G_S^{(relax)}$ can be rather complex and tedious to obtain. Moreover, the only things that carry the physical significance are the variation products of the relaxation term with respect to Δ^* ,

$$\partial G_S^{(relax)}|_{\Delta^*} = \int_V \left[\tau \left(\frac{\partial \Delta}{\partial t} + i \frac{e^*}{\hbar} \varphi \Delta \right) \right] \delta \Delta^* dV, \quad (2.3)$$

and \mathbf{A} ,

$$\partial G_S^{(relax)}|_{\mathbf{A}} = \int_V \left[\sigma_n \left(\frac{\partial \mathbf{A}}{\partial t} + \nabla \varphi \right) \delta \mathbf{A} \right] dV. \quad (2.4)$$

Here τ contains the information about the relaxation time unique for all time-dependent variables, φ is the electrostatic potential necessary for preservation of the gauge invariance due to temporal variation [62], and σ_n is the normal state conductance. The expression under the integral in Eq. 2.4, without the variation parameter $\delta \mathbf{A}$, represents the normal current density, \mathbf{J}_n , due to the externally induced electrical field, \mathbf{E} .

2.1.2 Generalized time-dependent Ginzburg-Landau equation and the general boundary condition

A generalized version of the TDGL equation was derived from the microscopic theory [67] to extend the validity of the formalism to dirty superconductors with a finite gap. Because of this, $G_S^{(relax)}$ must be modified accordingly, where the real relaxation time τ from Eq. 2.3 is exchanged with a complex quantity

$$\tilde{\tau} = \frac{u\tau_{GL}N(0)}{\sqrt{1 + \left(\frac{2\tau_i}{\hbar}|\Delta|\right)^2}} \left[1 + \frac{\left(\frac{2\tau_i}{\sqrt{2}\hbar}\right)^2 \frac{\partial |\Delta|^2}{\partial t} \Delta}{\frac{\partial \Delta}{\partial t} + i \frac{e^*}{\hbar} \varphi \Delta} \right]. \quad (2.5)$$

In $\tilde{\tau}$ several microscopic quantities appear explicitly, including density of states, $N(0)$, Ginzburg-Landau order parameter relaxation time, τ_{GL} , inelastic electron-phonon scattering time, τ_i , and parameter $u = 5.79$, which, based on microscopic theory, represents the dimensionless ratio of the relaxation times for the magnitude and the phase of the order parameter. The inelastic electron-phonon scattering time effectively influences the viscosity of the Cooper-pair condensate, and it can strongly affect the condensate dynamics. The term $\frac{2\tau_i}{\hbar} |\Delta|$ accounts for the presence of a superconducting gap.

In order to obtain gTDGL equation one starts by varying the modified version of Eq. 2.2 with respect to Δ^* ,

$$\begin{aligned} \partial G_S|_{\Delta^*} = \int_V \left\{ \frac{\tau_{GL} N(0) \left[\frac{\partial \Delta}{\partial t} + i \frac{e^*}{\hbar} \varphi \Delta + \left(\frac{2\tau_i}{\sqrt{2}\hbar} \right)^2 \frac{\partial |\Delta|^2}{\partial t} \Delta \right] u}{\sqrt{1 + \left(\frac{2\tau_i}{\hbar} |\Delta| \right)^2}} \right\} \delta \Delta^* dV \\ + \partial G_S^{(eq)}|_{\Delta^*} = 0. \end{aligned} \quad (2.6)$$

Variation of the equilibrium part of the Gibbs free energy yields

$$\begin{aligned} \partial G_S^{(eq)}|_{\Delta^*} = \int_V \{ \alpha \Delta \delta \Delta^* + \beta |\Delta|^2 \Delta \delta \Delta^* \} dV \\ + \int_V \{ \gamma [(-i\hbar \nabla - e^* \mathbf{A}) \Delta] [(i\hbar \nabla - e^* \mathbf{A}) \delta \Delta^*] \} dV. \end{aligned} \quad (2.7)$$

Since order parameter outside the volume of the superconductor (V) is zero, the integration is restricted to that volume only. By applying few simple algebraic transformations, Eq. 2.7 becomes

$$\begin{aligned} \partial G_S^{(eq)}|_{\Delta^*} = \int_V \left[(\alpha + \beta |\Delta|^2) \Delta - \gamma (\hbar \nabla - ie^* \mathbf{A})^2 \Delta \right] \delta \Delta^* dV \\ + \int_V \{ i\hbar \gamma \nabla [\delta \Delta^* (-i\hbar \nabla \Delta - e^* \mathbf{A} \Delta)] \} dV. \end{aligned} \quad (2.8)$$

The last term in Eq. 2.8 can be further transformed by applying the Gauss theorem $\int_V \nabla \mathbf{M} dV = \oint_S \mathbf{n} \mathbf{M} dS$, where S is the area encapsulating the volume V , and \mathbf{n} is the unit vector perpendicularly to the enclosed area ($\mathbf{S} = \mathbf{n} S$). Finally, one obtains

$$\begin{aligned} \partial G_S^{(eq)}|_{\Delta^*} = \int_V \left[(\alpha + \beta |\Delta|^2) \Delta - \gamma (\hbar \nabla - ie^* \mathbf{A})^2 \Delta \right] \delta \Delta^* dV \\ + \oint_S \mathbf{n} (-i\hbar \nabla \Delta - e^* \mathbf{A} \Delta) \delta \Delta^* dS. \end{aligned} \quad (2.9)$$

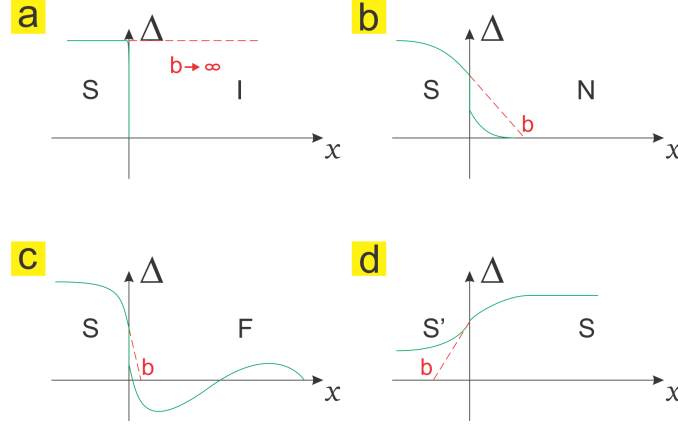


Figure 2.1: Schematic depiction of the order parameter behavior at interfaces of different types. In (a) Δ profile is shown near a superconductor-insulator (SI) boundary, in (b) near a superconductor-normal metal (SN) boundary, (c) at the superconductor-ferromagnet (SF) interface, and (d) is the junction of two superconductors (S'S).

The last term in Eq. 2.9 corresponds to the supercurrent component perpendicular to the boundary of the volume V , and it must be zero, since no supercurrent can leak outside the superconductor. This is also the boundary condition for the gT-DGL equation at the interface of a superconductor with an insulator (SI interface).

Finally, by inserting what is left from Eq. 2.9 back into Eq. 2.6, and equating everything to zero, for arbitrary $\delta\Delta^*$, one obtains the generalized TDGL equation

$$\tau_{GL}N(0)\frac{u}{\sqrt{1 + \left(\frac{2\tau_i}{\hbar}|\Delta|\right)^2}} \left[\frac{\partial\Delta}{\partial t} + i\frac{e^*}{\hbar}\varphi\Delta + \left(\frac{2\tau_i}{\sqrt{2}\hbar}\right)^2 \frac{\partial|\Delta|^2}{\partial t}\Delta \right] = -(\alpha + \beta|\Delta|^2)\Delta + \gamma(\hbar\nabla - ie^*\mathbf{A})^2\Delta. \quad (2.10)$$

One last remark here is about the generalization of the boundary condition. The boundary condition proposed by de Gennes [55]:

$$\mathbf{n}(-i\hbar\nabla - e^*\mathbf{A})\Delta|_{boundary} = \frac{i}{b}\Delta|_{boundary}, \quad (2.11)$$

introduces the extrapolation length b , which contains information about how far from the superconducting boundary the order parameter would drop to zero if it maintained the slope of decay it had at the surface of the superconductor. Usually, for insulators (or vacuum) one takes $b \rightarrow \infty$, meaning that order parameter

instantly drops to zero at the SI boundary. In the normal metals (SN interface) b is positive and large, but finite. The reason for this is that in the area of normal metal close to the SN interface some amount of Cooper pairs leaks, therefore, leading to non-zero Δ . This is called the proximity effect [70]. On the other hand, due to the leakage of superconducting electrons, in the superconductor close to the SN interface Δ weakens, and this is called inverse proximity effect [70]. In case of a superconductor-ferromagnet interface (SF), the singled Cooper-pairing and its order parameter vanish close to the border, so one adapts the boundary condition with $b \rightarrow 0$. If two superconductors with different material parameters are in contact (S'S interface), one can expect that at the boundary, finite, but negative b can be taken in the material with lower critical temperature. The schematic representation of the expected behavior of the order parameter at four discussed types of interfaces is given in Fig. 2.1.

2.1.3 Supercurrent, total current and conservation law

Next, the variation of the total free energy with respect to the vector potential is considered, in order to obtain the second TDGL equation. One starts from

$$\partial G_S|_{\mathbf{A}} = \partial G_S^{(eq)}|_{\mathbf{A}} + \partial G_S^{(relax)}|_{\mathbf{A}} = 0, \quad (2.12)$$

where $\partial G_S^{(relax)}|_{\mathbf{A}}$ was already explained in Eq. 2.4. What remains now is to resolve the expression for $\partial G_S^{(eq)}|_{\mathbf{A}}$. This term reads

$$\begin{aligned} \partial G_S^{(eq)}|_{\mathbf{A}} = & \frac{1}{\mu_0} \int_V [(\nabla \times \mathbf{A} - \mathbf{B}_e) \nabla \times \delta \mathbf{A}] dV + \\ & \int_V [\gamma (e^* \delta \mathbf{A} \Delta^*) (i\hbar \nabla + e^* \mathbf{A}) \Delta] dV - \int_V \gamma [(e^* \delta \mathbf{A} \Delta) (i\hbar \nabla - e^* \mathbf{A}) \Delta^*] dV. \end{aligned} \quad (2.13)$$

Employing vector identity $\nabla (\mathbf{M} \times \mathbf{N}) = \mathbf{N} \nabla \times \mathbf{M} - \mathbf{M} \nabla \times \mathbf{N}$, where $\mathbf{M} = \delta \mathbf{A}$ and $\mathbf{N} = \nabla \times \mathbf{A} - \mathbf{B}_e$, and after several algebraic transformations, yields

$$\begin{aligned} \partial G_S^{(eq)}|_{\mathbf{A}} = & \frac{1}{\mu_0} \int_V \{ \delta \mathbf{A} \nabla \times \nabla \times \mathbf{A} + \nabla [\delta \mathbf{A} \times (\nabla \times \mathbf{A} - \mathbf{B}_e)] \} dV + \\ & \int_V [\gamma (e^* \delta \mathbf{A} \Delta^*) (i\hbar \nabla + e^* \mathbf{A}) \Delta] dV - \int_V [\gamma (e^* \delta \mathbf{A} \Delta) + (i\hbar \nabla - e^* \mathbf{A}) \Delta^*] dV. \end{aligned} \quad (2.14)$$

With the help of Gauss theorem the term $\int_V \{ \nabla [\delta \mathbf{A} \times (\nabla \times \mathbf{A} - \mathbf{B}_e)] \} dV$ can be transformed into $\oint_S [\delta \mathbf{A} \times (\nabla \times \mathbf{A} - \mathbf{B}_e)] d\mathbf{S}$. This term is relevant only on the oriented surface \mathbf{S} encapsulating the superconductor. However, since this is the

boundary where $\nabla \times \mathbf{A} \equiv \mathbf{B}_e$, it can be concluded that this term is zero for arbitrary $\delta \mathbf{A}$.

Finally, it is possible to combine the stationary part with the relaxation part of the varied free energy, as

$$\begin{aligned} \partial G_S|_{\mathbf{A}} = & \frac{1}{\mu_0} \int_V (\nabla \times \nabla \times \mathbf{A}) \delta \mathbf{A} dV + \int_V \left(\sigma_n \nabla \varphi + \sigma_n \frac{\partial \mathbf{A}}{\partial t} \right) \delta \mathbf{A} dV - \\ & \int_V \left[2e^* \hbar \gamma \left(\frac{\Delta^* \nabla \Delta - \Delta \nabla \Delta^*}{i2} - \frac{e^*}{\hbar} |\Delta|^2 \mathbf{A} \right) \right] \delta \mathbf{A} dV = 0. \end{aligned} \quad (2.15)$$

For arbitrary $\delta \mathbf{A}$, this can be zero only if the sum of integrands is zero. If that is the case, one writes the second TDGL equation as

$$\frac{1}{\mu_0} (\nabla \times \nabla \times \mathbf{A}) = -\sigma_n \left(\nabla \varphi + \frac{\partial \mathbf{A}}{\partial t} \right) + 2e^* \hbar \gamma \left(\Im \{ \Delta^* \nabla \Delta \} - \frac{e^*}{\hbar} |\Delta|^2 \mathbf{A} \right). \quad (2.16)$$

According to the Maxwell's equation (the Ampere's law) term on the left-hand side (LHS) corresponds to the total current density \mathbf{J}

$$\mathbf{J} = \frac{1}{\mu_0} (\nabla \times \nabla \times \mathbf{A}), \quad (2.17)$$

while the first term on right-hand side (RHS) is the normal current density, \mathbf{J}_n

$$\mathbf{J}_n = -\sigma_n \left(\nabla \varphi + \frac{\partial \mathbf{A}}{\partial t} \right). \quad (2.18)$$

What remains on the RHS is the supercurrent density, \mathbf{J}_s . With the help of relation $\Delta = |\Delta| e^{i\theta}$, one can rewrite \mathbf{J}_s as

$$\mathbf{J}_s = 2e^* \hbar \gamma |\Delta|^2 \left(\nabla \theta - \frac{e^*}{\hbar} \mathbf{A} \right). \quad (2.19)$$

Up to this point first and second TDGL equations have been constructed, but an observant reader will notice that, in fact, there are three independent variables: the order parameter Δ , the vector potential \mathbf{A} , and the electrostatic potential φ . This means that an addition is needed to the existing set of equations. In order to accommodate this, the current-conservation law is called upon:

$$\nabla \mathbf{J} = \nabla (\mathbf{J}_s + \mathbf{J}_n) = \frac{\partial \rho}{\partial t}. \quad (2.20)$$

Temporal variations of the accumulated charge $\rho \propto \left(\frac{e^*}{\hbar} \varphi - \frac{\partial \theta}{\partial t} \right)$ can be neglected if the system is close to T_c ($\frac{\partial \rho}{\partial t} \rightarrow 0$) [66, 67]. Now Eq. 2.20 in combination with Eqs. 2.18 and 2.19 can be reformulated in order to obtain

$$-\nabla \mathbf{J}_n = \nabla \mathbf{J}_s. \quad (2.21)$$

In principle, Eqs. 2.10, 2.16, and 2.21 form a complete set of equations of gTDGL formalism which can be used to treat time-dependent phenomena in a wide range of systems exposed to the external magnetic and electric fields. Moreover, triplet $\{\Delta, \mathbf{A}, \varphi\}$ is gauge invariant under transformation $\{\Delta e^{i\Omega}, \mathbf{A} + \frac{\hbar}{e^*} \nabla \Omega, \varphi - \frac{\hbar}{e^*} \frac{\partial \Omega}{\partial t}\}$, where $\Omega(\mathbf{r}, t)$ is an arbitrary function that varies slowly in time compared to τ_{GL} .

2.1.4 GL equations in steady state

Here, the case when gTDGL equations reduce to stationary GL formalism is considered. One can imagine a process initiated via some *dc* external excitation applied to the superconductor in equilibrium (e.g. introducing a magnetic field and/or transport current to the system). Unless the magnitude of the excitation is strong and drives the system to the normal state or provokes the permanent oscillations in the system (for example, when large enough transport current induces the persistent and repetitive vortex motion stationary solution can not be achieved), it is reasonable to expect that after finite amount of time the system will reach a new equilibrium state. In the steady state, all temporal derivatives together with electrostatic potential can be omitted, so the GL equations governing the behavior of the system read

$$\gamma (\hbar \nabla - i e^* \mathbf{A})^2 \Delta = \alpha \Delta + \beta |\Delta|^2 \Delta, \quad (2.22)$$

$$\frac{1}{\mu_0} (\nabla \times \nabla \times \mathbf{A}) = 2 e^* \hbar \gamma |\Delta|^2 \left(\nabla \theta - \frac{e^*}{\hbar} \mathbf{A} \right), \quad (2.23)$$

with generalized boundary condition given in Eq. 2.11, which is still valid. Over the years, Eqs. 2.22 and 2.23 proved to be quite handy from the computational side. By omitting the information about the transitional processes, GL equations can be solved faster than the gTDGL and TDGL models, which enables one to assess time-independent phenomena in large-scale systems.

2.1.5 Characteristic quantities and their microscopic origin

With the appearance of gTDGL framework, microscopic explanation for all of the phenomenological parameters appearing in the Eqs. 2.10, 2.16, and 2.21 was given. In fact, Kramer and Watts-Tobin [66] obtained the gTDGL equations for dirty superconductors in the following form

$$\frac{N(0)\pi\hbar}{8k_B T u} \frac{u}{\sqrt{1 + \left(\frac{2\tau_i|\Delta|}{\hbar}\right)^2}} \left[\frac{\partial \Delta}{\partial t} + i \frac{e^*}{\hbar} \varphi \Delta + \left(\frac{2\tau_i}{\sqrt{2}\hbar}\right)^2 \frac{\partial |\Delta|^2}{\partial t} \Delta \right] = \quad (2.24)$$

$$\frac{N(0)\pi\hbar D}{8k_B T} \left(\nabla - i \frac{e^*}{\hbar} \mathbf{A} \right)^2 \Delta + \left(N(0)f(T) - g(T) \frac{N(0)\pi^2}{16uk_B^2 T^2} |\Delta|^2 \right) \Delta,$$

$$\frac{1}{\mu_0} \nabla \times \nabla \times \mathbf{A} = \sigma_n \left[\frac{\pi}{2k_B T e^*} |\Delta|^2 \left(\nabla \theta - \frac{e^*}{\hbar} \mathbf{A} \right) - \frac{\partial \mathbf{A}}{\partial t} - \nabla \varphi \right], \quad (2.25)$$

$$\begin{aligned} -\nabla \mathbf{J}_n &= \nabla \left[\sigma_n \left(\frac{\partial \mathbf{A}}{\partial t} + \nabla \varphi \right) \right] = \nabla \mathbf{J}_s = \\ &\nabla \left[\frac{\sigma_n \pi}{2k_B T e^*} |\Delta|^2 \left(\nabla \theta - \frac{e^*}{\hbar} \mathbf{A} \right) \right], \end{aligned} \quad (2.26)$$

where D is the diffusion parameter, $f(T)$ and $g(T)$ are kernel functions containing generic temperature dependence, and k_B is the Boltzmann constant. In this representation, the normal state conductance σ_n has a microscopic definition

$$\sigma_n = \frac{e^{*2} D N(0)}{2}. \quad (2.27)$$

In their work, Kramer and Watts-Tobin regarded magnitude of the order parameter $|\Delta|$ as the superconducting gap. Close to the critical temperature, T can be exchanged with T_c in all the terms of Eqs. 2.24, 2.25 and 2.26 where the temperature explicitly appears, except for the $f(T)$ and $g(T)$, which preserve the generic thermal dependence. Originally, Kramer and Watts-Tobin obtained $f(T) = \log(T_c/T)$, which close to T_c reduces to $1 - T/T_c$, while in the same limit $g(T \rightarrow T_c) \approx 1$ [66, 71]. Similar to what has been given in Eqs. 1.7 and 1.8 one can extend the precision of gTDGL model over a wider range of temperatures by modifying the expression for $f(T)$ with $\frac{T_c^2 - T^2}{T_c^2 + T^2}$, and for $g(T)$ with $\frac{T_c^4}{(T_c^2 + T^2)^2}$ [53].

By comparison with Eq. 2.10 one can finally identify the microscopic expressions for the phenomenological parameters in GL equations:

$$\alpha = -N(0)f(T) = -\alpha(0)f(T), \quad (2.28)$$

$$\beta = g(T) \frac{N(0)\pi^2}{16uk_B^2 T_c^2} = \beta(0)g(T), \quad (2.29)$$

$$\gamma = \frac{N(0)\pi D}{8k_B T_c \hbar}, \quad (2.30)$$

$$\tau_{GL} = \frac{\pi \hbar}{8k_B T_c u} = \tau_{GL}(0). \quad (2.31)$$

One can now use microscopic expressions for α , β and γ to further obtain physical quantities such as the coherence length, ξ , and magnetic field penetration depth, λ . The coherence length is the natural length scale for spatial variations of the order parameter, and it is obtained as $\xi = \sqrt{-\frac{\gamma \hbar^2}{\alpha}}$. Since α carries a thermal dependence, ξ will also be a function of the temperature. Actual representation of

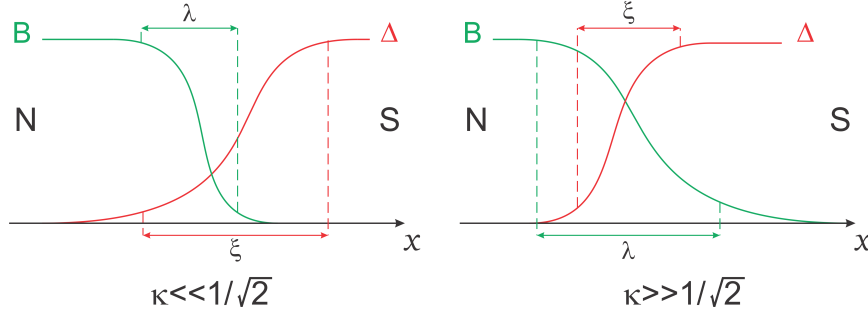


Figure 2.2: Schematic diagram of variation of \mathbf{B} and Δ at an SN interface for type I ($\kappa \ll 1/\sqrt{2}$) and type II ($\kappa \gg 1/\sqrt{2}$) materials [71].

ξ as a function of microscopic parameters depends on the purity of the material, which is hidden in the diffusion parameter D , found in parameter γ . In the case when superconductor contains a lot of impurities (dirty limit), $D = v_F l$ (where v_F is the Fermi velocity and l is the elastic mean free path). It is important to note here that in the dirty limit Cooper pairs interact with the impurities over the length of the mean free path, which is smaller than the correlation length of the Cooper pairs, $\xi_0 > l$ (ξ_0 being the BCS coherence length). However, in the clean case where mean free path greatly exceeds ξ_0 , $D = \frac{\pi \hbar v_F^2}{12 u k_B T_c}$ [72]. Based on this, it can be written

$$\xi(T) = \begin{cases} \sqrt{\frac{\hbar \pi v_F l}{8 k_B T_c f(T)}} = 0.855 \sqrt{\frac{\xi_0 l}{f(T)}}, & \text{dirty} \\ \sqrt{\frac{\hbar^2 \pi^2 v_F^2}{96 u k_B^2 T_c^2 f(T)}} = 0.74 \frac{\xi_0}{\sqrt{f(T)}}, & \text{clean} \end{cases} = \frac{\xi(0)}{\sqrt{f(T)}}. \quad (2.32)$$

Penetration depth of the magnetic field, λ , which was already introduced in the description of the London theory, is a characteristic length describing the variation of the magnetic field inside the superconductor. According to the GL theory $\lambda = \sqrt{-\frac{\beta}{2\mu_0 e^* \alpha \gamma}}$, where, due to the thermal dependence of α (and β), $\lambda = \lambda(T)$. Depending on the material purity, one obtains

$$\lambda(T) = \begin{cases} \sqrt{\frac{\pi \hbar g(T)}{4 u k_B T_c \mu_0 e^{*2} N(0) v_F l f(T)}} = \frac{\lambda(0)}{\sqrt{2}} \sqrt{\frac{\xi_0 g(T)}{1.33 l f(T)}}, & \text{dirty} \\ \sqrt{\frac{3 g(T)}{\mu_0 e^{*2} N(0) v_F^2 f(T)}} = \frac{\lambda(0)}{\sqrt{2}} \sqrt{\frac{g(T)}{f(T)}}, & \text{clean} \end{cases}. \quad (2.33)$$

Another added value of the gTDGL model is the microscopic parametrization of the dimensionless parameter κ (so-called GL parameter), defined as a ratio of λ and ξ . The importance of this parameter is reflected in the fact that it clearly

separates the magnetic behavior of superconductors into type I ($\kappa < 1/\sqrt{2}$) and type II ($\kappa > 1/\sqrt{2}$). The surface energy at the boundary between normal material and superconductor is proportional to the difference of coherence length and penetration depth, and, therefore, depends on κ . This energy changes sign at $\kappa = 1/\sqrt{2}$: in type I materials ($\kappa < 1/\sqrt{2}$) surface energy is positive, while in type II ($\kappa > 1/\sqrt{2}$) this energy is negative, which favors the formation of more superconducting-normal boundaries. As a consequence, in the presence of magnetic field the magnetic flux penetrates the superconductor in smallest units - vortices - each carrying a quantum of flux, Φ_0 . This behavior of type I and type II materials at an SN interface is illustrated in Fig. 2.2.

Finally, the $\{\Psi, \Delta\}$ dichotomy is briefly addressed. In the original work of Ginzburg and Landau Ψ was selected as an order parameter, and as such it was regarded purely phenomenologically until Gor'kov revealed the microscopic nature of Ψ [18]. Close to T_c a relationship between BCS theory and GL framework is established, where the many-body wave-function describing the distribution of Cooper pairs reduces to Ψ . According to Kopnin [72], Δ and Ψ are related as

$$\Psi = \Delta \sqrt{2m^*\gamma}. \quad (2.34)$$

Because of this, one can reconstruct gTDGL model with respect to Ψ as:

$$\begin{aligned} \tau_{GL} N(0) \frac{u}{\sqrt{1 + (\Gamma|\Psi|^2)}} \left[\frac{\partial \Psi}{\partial t} + i \frac{e^*}{\hbar} \varphi \Psi + \left(\frac{\Gamma}{\sqrt{2}} \right)^2 \frac{\partial |\Psi|^2}{\partial t} \Psi \right] = \\ - (a + b|\Psi|^2) \Psi + \frac{\hbar^2}{2m^*} (\nabla - ie^* \mathbf{A})^2 \Psi, \end{aligned} \quad (2.35)$$

$$\frac{1}{\mu_0} \nabla \times \nabla \times \mathbf{A} = \frac{e^* \hbar}{m^*} |\Psi|^2 \left(\nabla \theta - \frac{e^*}{\hbar} \mathbf{A} \right) - \sigma_n \left(\frac{\partial \mathbf{A}}{\partial t} + \nabla \varphi \right), \quad (2.36)$$

$$\nabla \left[\sigma_n \left(\frac{\partial \mathbf{A}}{\partial t} + \nabla \varphi \right) \right] = \nabla \left[\frac{e^* \hbar}{m^*} |\Psi|^2 \left(\nabla \theta - \frac{e^*}{\hbar} \mathbf{A} \right) \right], \quad (2.37)$$

where $\Gamma = \frac{2\tau_i}{\hbar\sqrt{2m^*\gamma}}$, $a = \frac{\alpha}{2m^*\gamma}$, and $b = \frac{\beta}{4m^{*2}\gamma^2}$.

2.1.6 High κ regime and validity of the gTDGL equation

In extreme type II bulk superconductors $\lambda \gg \xi$ and consequently $\kappa \gg 1$. In thin superconducting films, where thickness $d < \lambda$, ξ , current density is essentially uniform along d , so one obtains the effective GL parameter, $\kappa^* = \kappa\lambda/d$ as a descriptor of the magnetic behavior of such a superconducting film [73]. Because of $\kappa^* \propto 1/d$, thin superconducting films mostly behave as extreme type II materials,

since $\kappa^* \gg 1$. Major implication of high κ regime reflects in the fact that the magnetic response of the superconductor is negligible, and the external magnetic field penetrates the superconductor uniformly. As a consequence, one is allowed to omit Eq. 2.25 from the set of Eqs. 2.24-2.26.

The validity of the gTDGL model is addressed next. The equations of Kramer and Watts-Tobin were derived for the dirty limit under the local equilibrium approximation (LEA), reflecting in the fact that all the relevant quantities (namely Δ , \mathbf{A} , and φ) must vary slowly in time over τ_i , while their spatial variations must occur on scales larger than the inelastic diffusion length $L_i = \sqrt{D\tau_i}$. Since relevant temporal scale in gTDGL is proportional to τ_{GL} , and relevant spatial scale is ξ , one rephrases LEA as $\tau_{GL} \gg \tau_i$ and $\xi \gg L_i$. Both of these conditions can be further reduced to a single inequality

$$T_c - T \ll \frac{\pi\hbar}{8k_B\tau_i}. \quad (2.38)$$

In the literature [67] τ_i can be found for bulk Pb (20 ps), In (0.1 ns), Sn (0.3 ns) and Al (50 ns). One should keep in mind that for extremely small values of τ_i the energy gap can be smeared out from the gTDGL equations (gapless limit as $\tau_i \rightarrow 0$), which then convert into ordinary TDGL equations [62].

However, from the various successful applications of gTDGL model one can, in fact, deduce that the criterion of Eq. 2.38 is not that rigid, and that the applicable range of gTDGL theory is much broader than initially regarded. This extended range where gTDGL is successfully used, is especially observed in dirty mesoscopic superconductors.

2.2 Extending the gTDGL model: Description of thermal balance in superconductors

gTDGL theory as introduced in the text above does not take into account the thermal balance of the system. Thermal fluctuations can be a paramount factor for the behavior of current-carrying superconductors, since they affect the critical current at which the superconductor transits to the normal state. On top of that, the Joule heating from current-induced vortex motion can also raise the temperature above T_c . Superconducting systems with natural sources of heating or thermal fluctuations are capable of the most diverse behavior (e.g. can manifest nonmonotonic and stepped current-voltage characteristics, periodic or stochastic dissipative features, various unusual dynamic effects such as stochastic transitions between stable states, etc.). In order to account for this behavior, the thermal balance equation has to be included into the gTDGL model.

2.2.1 Equation of thermal balance

The equation of thermal balance was first introduced by Gurevich and Mints [74], in the form

$$C \frac{\partial T}{\partial t} = k \nabla^2 T - \frac{h}{d} (T - T_0) + V(\mathbf{r}, t). \quad (2.39)$$

Eq. 2.39 allows for the spatial and temporal monitoring of the local temperature $T(\mathbf{r}, t)$ of the system that has been cooled down to the bath temperature T_0 , where C is the heat capacity, k is the heat conductivity, h is the heat transfer coefficient, and d is the thickness of the specimen. Thermal potential $V(\mathbf{r}, t)$ in the simplest case corresponds only to the Joule heating, \mathbf{J}_n^2/σ_n . However, $V(\mathbf{r}, t)$ can contain additional terms, which are used to describe the heating of the superconductor from external sources, such as laser light or nano-heaters. Note, however, that Eq. 2.39 does not appear naturally in gTDGL formalism. In fact, this equation was constructed separately, and its sole input are the Joule losses. Fortunately, gTDGL formalism can be linked to the Joule heating in the system through calculated normal current density \mathbf{J}_n , which serves as a coupling term. After taking all of this into account, Eq. 2.39 together with Eqs. 2.24, 2.25, and 2.26 constitutes the extended gTDGL model, which can be used to describe realistic superconducting systems in the presence of applied current and magnetic field.

As a consequence of Eq. 2.39 not being native part of gTDGL model, one does not have information about C , k , and h from microscopic theory. Due to this, heat capacity, heat conductivity and heat transfer coefficient have to be obtained by different means. In general, these parameters are also functions of temperature [$C(T)$, $k(T)$, $h(T)$], being a material-dependent property. For example, from the condensation energy density of a superconductor one can estimate the heat capacity [75] as

$$C = -T \frac{\partial^2}{\partial T^2} \left[\alpha(T) |\Delta|^2 + \frac{\beta(T)}{2} |\Delta|^4 \right]. \quad (2.40)$$

Close to T_c , where $\alpha \propto 1 - \frac{T}{T_c}$ and $\beta \approx 1$, $C = C_n + T \frac{\alpha(0)^2}{\beta(0)T_c}$ ($C_n = \gamma_S T$ is the normal state heat capacity, where γ_S is the Sommerfeld constant). Moreover, if one considers gTDGL model in a wider range of temperatures, where $\alpha \propto \left[1 - (T/T_c)^2 \right] \left[1 + (T/T_c)^2 \right]^{-1}$, and $\beta \propto \left[1 + (T/T_c)^2 \right]^{-2}$, heat capacity is then given as $C = C_n + \frac{2\alpha(0)^2}{\beta(0)T_c^4} T(3T^2 - T_c^2)$.

As a rough estimate, one can use Wiedemann-Franz law to estimate heat conductivity close to T_c [76], as

$$k = \sigma_n T_c \frac{4\pi^2 k_B^2}{3e^*{}^2}. \quad (2.41)$$

In general, heat conductivity should be described by a more complex expression than the one given in Eq. 2.41, but that exceeds the needs and the scope of this thesis.

Finally, the characteristic quantities arising from the thermal balance equation are discussed. The so-called thermal healing length $\Lambda_h = \sqrt{\frac{kd}{h}}$ is the characteristic scale over which temperature varies in the sample. Diffusion of the heat is described with the ratio $\frac{k}{C}$, while removal of the heat from the system happens on the time scale $\frac{Cd}{h}$. If the influence of the surroundings needs to be taken into account, one may consider effective heat capacity, $C_{eff} = C + d_s C_s/d$ and effective heat conductivity $k_{eff} = k + d_s k_s/d$, where C_s and k_s are heat capacity and heat conductivity of the substrate, respectively, and d_s is the substrate thickness.

2.2.2 Dimensionless extended gTDGL model

The number of physical quantities considered in this thesis, such as current densities, or characteristic time and length scales, can easily vary in a wide range of magnitudes ($10^{-15} \div 10^{20}$), which can cause significant rounding errors in the numerical calculations. This is why it is a common practice to work with a dimensionless form of the extended gTDGL model. Rewritten in the dimensionless form, the extended gTDGL equations read

$$\frac{u}{\sqrt{1 + \tilde{\Gamma}^2 |\chi|^2}} \left[\frac{\partial \chi}{\partial \tilde{t}} + iV\chi + \frac{\tilde{\Gamma}^2}{2} \frac{\partial |\chi|^2}{\partial \tilde{t}} \chi \right] = (\tilde{\nabla} - i\mathbf{Q})^2 \chi + (f - g|\chi|^2)\chi, \quad (2.42)$$

$$\kappa \tilde{\nabla} \times \tilde{\nabla} \times \mathbf{Q} = |\chi|^2 (\tilde{\nabla} \theta - \mathbf{Q}) - \frac{\partial \mathbf{Q}}{\partial \tilde{t}} - \tilde{\nabla} V, \quad (2.43)$$

$$\tilde{\nabla} \left(\frac{\partial \mathbf{Q}}{\partial \tilde{t}} - \tilde{\nabla} V \right) = \tilde{\nabla} [|\chi|^2 (\tilde{\nabla} \theta - \mathbf{Q})], \quad (2.44)$$

$$\tilde{c} \frac{\partial \tilde{T}}{\partial \tilde{t}} = \tilde{k} \tilde{\nabla}^2 \tilde{T} - \tilde{h} (\tilde{T} - \tilde{T}_0) + \left(\frac{\partial \mathbf{Q}}{\partial \tilde{t}} - \tilde{\nabla} V \right)^2. \quad (2.45)$$

Here, the distances are given in units of the coherence length at zero temperature, $\xi(0) = \sqrt{\frac{\pi \hbar D}{8k_B T_c}}$ [$\tilde{\mathbf{r}} = \mathbf{r}/\xi(0)$, and the spatial derivatives $\tilde{\nabla} = \xi(0)\nabla$], the time in units of the Ginzburg-Landau relaxation time at 0K, $\tau_{GL}(0) = \frac{\pi \hbar}{8k_B T_c u}$ [$\tilde{t} = t/\tau_{GL}(0)$, and the temporal derivative $\frac{\partial}{\partial \tilde{t}} = \frac{\partial}{\partial t/\tau_{GL}(0)}$], and temperature in units of T_c ($\tilde{T} = T/T_c$). Dimensionless order parameter, χ , carries the unit

of bulk GL energy gap at zero temperature, $\Delta_{GL}(0) = \frac{4\sqrt{uk_B T_c}}{\pi}$, while the dimensionless electrostatic potential, V , is given in units of $\varphi_{GL}(0) = \frac{\hbar}{e^* \tau_{GL}(0)}$. Magnetic field is expressed in units of the second critical field at zero temperature, $B_{c2}(0) = \frac{\Phi_0}{2\pi\xi(0)^2}$ [$\tilde{\mathbf{B}} = \mathbf{B}/B_{c2}(0)$], and the dimensionless magnetic vector potential is from there obtained as $\mathbf{Q} = \mathbf{A}/B_{c2}(0)\xi(0)$. Parameter $\tilde{\Gamma}$ is a product of the inelastic phonon-electron scattering time and the bulk GL energy gap at 0K, $\tilde{\Gamma} = \frac{2\tau_i \Delta_{GL}(0)}{\hbar}$. In these units, the current density scales as $\tilde{\mathbf{J}} = \mathbf{J}/J_{GL}(0)$, where $J_{GL}(0) = \frac{\sigma_n \varphi(0)}{\xi(0)}$ is the Ginzburg-Landau current density at 0K. Dimensionless heat capacity is given as $\tilde{c} = CT_c \sigma_n / J_{GL}(0)^2 \tau_{GL}(0)$, dimensionless heat conductivity as $\tilde{k} = kT_c \sigma_n / J_{GL}(0)^2 \xi(0)^2$, and dimensionless heat transfer coefficient as $\tilde{h} = hT_c \sigma_n / J_{GL}(0)^2 d$. Parameters u, f, g and κ are by definition dimensionless, as is the phase of the order parameter, θ .

In principle, extended gTDGL model can be used to describe realistic systems where both the magnetic field and the transport current are applied. Transport current induces an electric field in the superconductor, which is a function of both the magnetic vector potential and the electrostatic scalar potential. Unfortunately, one does not work with the electric field explicitly, and, therefore, there is no way to know exactly how the applied current affects vector potential and electrostatic potential individually. In order to circumvent this inconvenience, additional gauges are introduced to relevant system of equations. There are several candidates that one can use as a gauge in the calculations [77], namely, the zero-electrostatic potential gauge $\varphi = 0$, the Coulomb gauge where $\nabla \mathbf{A} = 0$, and finally, the linear combination-based gauge, where $\varphi + \nabla \mathbf{A} = 0$. If one selects the zero-electrostatic potential gauge, Eq. 2.44 disappears. On the other hand, for the superconductors in high κ regime, where the magnetic field is uniformly distributed in the sample, it is natural to use Coulomb gauge. In this particular case, when the field is applied perpendicularly to the sample, one can define vector potential either in the so-called Landau gauge, $\mathbf{A} = (-yB_z, 0, 0)$, or the symmetric gauge, $\mathbf{A} = (-yB_z/2, xB_z/2, 0)$, both of which satisfy the condition $\nabla \mathbf{A} = 0$, and thus exclude Eq. 2.43 from calculations. The third gauge candidate, linear combination-based, is not used in this thesis.

2.2.3 Discretization of the equations and numerical approach

In order to employ the set of differential equations 2.42 - 2.45 in numerical calculations, the system is discretized on a uniform Cartesian spatial grid and transformed into a set of algebraic equations. Finite-differences method [78] is rather convenient approach here, where the maximal size of the unit cell (see Fig. 2.3) does not exceed $0.3\xi(0)$ ($\Delta x \leq 0.3\xi(0)$ and $\Delta y \leq 0.3\xi(0)$). This condition is empirically

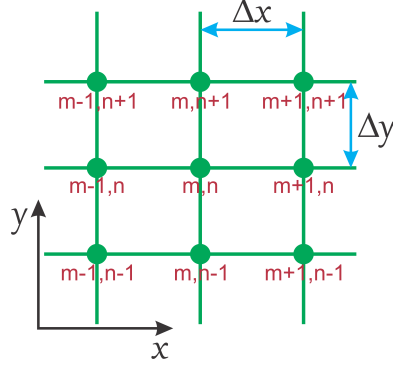


Figure 2.3: Schematic diagram of the Cartesian grid used in the numerical calculations.

instated since the relevant physical phenomena might not be captured properly on a coarser spatial grid. In this thesis mainly the thin superconducting films are considered, with thickness smaller than the characteristic lengths $\xi(0)$ and $\lambda(0)$, so the current density and the vector potential may be considered constant over the thickness of the sample [71]. Consequently, Eqs. 2.42 - 2.45 have no z component thus they can be reduced from 3D to 2D space, whilst the boundary condition 2.11 is automatically fulfilled at top and bottom surface of the superconductor.

Equations 2.42 - 2.45 with an appropriate gauge are solved in a self-consistent iterative procedure, in the presence of applied magnetic field and transport current. In order to ensure stable and fast convergence of the solution for the vector potential, the complex link variable vector is introduced

$$\mathbf{U}(\mathbf{r}_0, \mathbf{r}) = \sum_{\mu=x,y} \mathbf{e}_\mu e^{-i \int_{\mu_0}^{\mu} Q_\mu d\mu}, \quad (2.46)$$

where $\mathbf{e}_{\mu=x,y}$ correspond to the unit vectors in x and y direction, respectively, and $\mathbf{r}_0 = \sum_{\mu=x,y} \mathbf{e}_\mu \mu_0$ is some reference point. The link variables are introduced in an ad hoc fashion to restore gauge invariance, which is normally lost if the partial differential equations of the TDGL model are discretized by means of finite differences [79, 80, 81, 82, 83]. For the components of the link variable vector the following rules apply:

$$\frac{\partial U_\mu}{\partial \mu} = -i Q_\mu U_\mu, \quad (2.47)$$

$$\frac{\partial^2 U_\mu}{\partial \mu^2} = -i \frac{\partial Q_\mu}{\partial \mu} U_\mu - Q_\mu^2 U_\mu. \quad (2.48)$$

Note that $\mathbf{J}_s = |\chi|^2 (\tilde{\nabla}\theta - \mathbf{Q})$ can also be expressed as $\Im \left\{ \chi^* (\tilde{\nabla} - i\mathbf{Q}) \chi \right\}$, so that the first and the second derivative found in Eqs. 2.42 - 2.44 can be rewritten as

$$(\tilde{\nabla} - i\mathbf{Q}) \chi = \sum_{\mu=x,y} \mathbf{e}_\mu \frac{1}{U_\mu} \frac{\partial}{\partial \mu} (U_\mu \chi), \quad (2.49)$$

$$(\tilde{\nabla} - i\mathbf{Q})^2 \chi = \sum_{\mu=x,y} \frac{1}{U_\mu} \frac{\partial^2}{\partial \mu^2} (U_\mu \chi), \quad (2.50)$$

respectively. One additional transformation of Eq. 2.42 should be mentioned here, as the term $\frac{\tilde{\Gamma}^2}{2} \frac{\partial |\chi|^2}{\partial \tilde{t}} \chi$ is not convenient for numerical calculations in this form. Instead it is possible to transform it into more user-friendly term

$$\frac{\tilde{\Gamma}^2}{2} \frac{\partial |\chi|^2}{\partial \tilde{t}} \chi = \frac{\tilde{\Gamma}^2}{1 + \tilde{\Gamma}^2 |\chi|^2} \Re \left\{ \chi^* \Phi \right\} \chi, \quad (2.51)$$

where $\Phi = \sqrt{1 + \tilde{\Gamma}^2 |\chi|^2} u^{-1} \left[(\tilde{\nabla} - i\mathbf{Q})^2 \chi + (f - g|\chi|^2) \chi \right]$.

Finally, by combining Euler method [84] to discretize the temporal derivative, together with Gauss-Seidel method [85] on a rectangular box of the size $L_x \times L_y$, one obtains for the Eq. 2.42

$$\chi_{m,n}^{\tilde{t}+\Delta\tilde{t}} = \Delta\tilde{t} \left[\frac{1}{\Delta\tilde{t}} - iV_{m,n} - \frac{\tilde{\Gamma}^2}{1 + \tilde{\Gamma}^2 |\chi_{m,n}^{\tilde{t}}|^2} \Re \left\{ \chi_{m,n}^{*\tilde{t}} \Phi_{m,n}^{\tilde{t}} \right\} \right] \chi_{m,n}^{\tilde{t}} + \Delta\tilde{t} \Phi_{m,n}^{\tilde{t}}, \quad (2.52)$$

where $n = 1..N_x$ and $m = 1..N_y$ are indices in x and y direction, respectively ($N_x = \frac{L_x + \Delta_x}{\Delta_x}$ and $N_y = \frac{L_y + \Delta_y}{\Delta_y}$ are total number of gridpoints in x and y direction, respectively), and

$$\begin{aligned} \Phi_{m,n}^{\tilde{t}} = & \frac{\sqrt{1 + \tilde{\Gamma}^2 |\chi_{m,n}^{\tilde{t}}|^2}}{u} \frac{\tilde{U}_{x_{m+1,n}}^{\tilde{t}} \chi_{m+1,n}^{\tilde{t}} - 2\chi_{m,n}^{\tilde{t}} + \tilde{U}_{x_{m-1,n}}^{\tilde{t}} \chi_{m-1,n}^{\tilde{t}}}{\Delta x^2} + \\ & \frac{\sqrt{1 + \tilde{\Gamma}^2 |\chi_{m,n}^{\tilde{t}}|^2}}{u} \frac{\tilde{U}_{y_{m,n+1}}^{\tilde{t}} \chi_{m,n+1}^{\tilde{t}} - 2\chi_{m,n}^{\tilde{t}} + \tilde{U}_{y_{m,n-1}}^{\tilde{t}} \chi_{m,n-1}^{\tilde{t}}}{\Delta y^2} + \\ & \frac{\sqrt{1 + \tilde{\Gamma}^2 |\chi_{m,n}^{\tilde{t}}|^2}}{u} \left(f_{m,n} - g_{m,n} |\chi_{m,n}^{\tilde{t}}|^2 \right) \chi_{m,n}^{\tilde{t}}. \end{aligned} \quad (2.53)$$

In Eq. 2.53 somewhat different link variable is introduced. In fact, forward x and y components of the modified link variable are given as

$$\tilde{U}_{x_{m+1,n}}^{\tilde{t}} = \frac{U_{x_{m+1,n}}^{\tilde{t}}}{U_{x_{m,n}}^{\tilde{t}}} = \frac{e^{-i \int_{x_0}^{x_0+(m+1)\Delta x} Q_x dx}}{e^{-i \int_{x_0}^{x_0+m\Delta x} Q_x dx}} \approx e^{-i Q_{x_{m+1,n}} \Delta x}, \quad (2.54)$$

$$\tilde{U}_{y_{m,n+1}}^t = \frac{U_{y_{m,n+1}}^t}{U_{y_{m,n}}^t} = \frac{e^{-i \int_{y_0}^{y=(n+1)\Delta y} Q_y dy}}{e^{-i \int_{y_0}^{y=n\Delta y} Q_y dy}} \approx e^{-i Q_{y_{m,n+1}} \Delta y}, \quad (2.55)$$

while the backward components are

$$\tilde{U}_{x_{m-1,n}}^t = \frac{U_{x_{m-1,n}}^t}{U_{x_{m,n}}^t} = \frac{e^{-i \int_{x_0}^{x=(m-1)\Delta x} Q_x dx}}{e^{-i \int_{x_0}^{x=m\Delta x} Q_x dx}} \approx e^{i Q_{x_{m,n}} \Delta x}, \quad (2.56)$$

$$\tilde{U}_{y_{m,n-1}}^t = \frac{U_{y_{m,n-1}}^t}{U_{y_{m,n}}^t} = \frac{e^{-i \int_{y_0}^{y=(n-1)\Delta y} Q_y dy}}{e^{-i \int_{y_0}^{y=n\Delta y} Q_y dy}} \approx e^{i Q_{y_{m,n}} \Delta y}. \quad (2.57)$$

In case of the SI boundary, the conditions $U_{x_{m\pm 1,n}}^t \chi_{m\pm 1,n}^t = \chi_{m,n}^t |_{m=m_{boundary}}$ and $U_{y_{m,n\pm 1}}^t \chi_{m,n\pm 1}^t = \chi_{m,n}^t |_{n=n_{boundary}}$ must be fulfilled ($m_{boundary} = 1, N_x$ and $n_{boundary} = 1, N_y$). At the SN boundary, no order parameter is present, hence $\chi_{m,n}^t |_{m=m_{boundary}} = 0$, and $\chi_{m,n}^t |_{n=n_{boundary}} = 0$.

In the zero-electrostatic potential gauge ($V = 0$), the Eq. 2.44 is omitted and vector Eq. 2.43 is split into two scalar equations [86]

$$\tilde{U}_{\mu_{m,n}}^{t+\Delta t} = \left(\frac{1}{\Delta t} - i \Delta t \mathfrak{S} \left\{ \mathcal{F}_{\mu_{m,n}}^t \right\} \right) \tilde{U}_{\mu_{m,n}}^t, \quad (2.58)$$

where

$$\mathcal{F}_{x_{m,n}}^t = \kappa^2 \frac{\tilde{U}_{x_{m,n+1}}^{*t} \tilde{U}_{y_{m,n}}^{*t} \tilde{U}_{x_{m,n}}^t \tilde{U}_{y_{m+1,n}}^t - \tilde{U}_{x_{m,n}}^{*t} \tilde{U}_{y_{m,n-1}}^{*t} \tilde{U}_{x_{m,n-1}}^t \tilde{U}_{y_{m+1,n-1}}^t}{\Delta y^2} + \tilde{U}_{x_{m,n}}^t \chi_{m,n}^{*t} \chi_{m+1,n}^t, \quad (2.59)$$

and

$$\mathcal{F}_{y_{m,n}}^t = \kappa^2 \frac{\tilde{U}_{x_{m-1,n+1}}^{*t} \tilde{U}_{y_{m-1,n}}^{*t} \tilde{U}_{x_{m-1,n}}^t \tilde{U}_{y_{m,n}}^t - \tilde{U}_{x_{m,n+1}}^{*t} \tilde{U}_{y_{m,n}}^{*t} \tilde{U}_{x_{m,n}}^t \tilde{U}_{y_{m+1,n}}^t}{\Delta x^2} + \tilde{U}_{x_{m,n}}^t \chi_{m,n}^{*t} \chi_{m,n+1}^t. \quad (2.60)$$

In order to solve the diffusion Eq. 2.58, the Crank-Nicolson implicit (CN) method [87] is used, which speeds up the convergence of the solution, while preserving the great degree of stability. Regarding the boundary conditions, at the edge of the simulated area (where $m = m_{boundary}$ or $n = n_{boundary}$) the connection between the external magnetic field, \tilde{B}_{ext} , and the link variables is given as

$$\tilde{B}_{ext} = \frac{1 - \tilde{U}_{x_{m,n+1}}^{*t} \tilde{U}_{y_{m,n}}^{*t} \tilde{U}_{x_{m,n}}^t \tilde{U}_{y_{m+1,n}}^t}{i \Delta x \Delta y}.$$

In case when one employs the Coulomb gauge ($\tilde{\nabla} \mathbf{Q} = 0$), in the high κ regime where field in the specimen is spatially homogeneous and temporally invariable (with the corresponding stationary vector potential in the symmetric gauge, $\mathbf{Q} = [-\frac{1}{2}\tilde{y}\tilde{B}_{ext}, \frac{1}{2}\tilde{x}\tilde{B}_{ext}, 0]$), then the Eq. 2.43 disappears, and the Eq. 2.44 is discretized as

$$\begin{aligned} \frac{V_{m+1,n} - 2V_{m,n} + V_{m-1,n}}{\Delta x^2} + \frac{V_{m,n+1} - 2V_{m,n} + V_{m,n-1}}{\Delta y^2} = \\ \frac{J_{S_{x_{m+1,n}}} - J_{S_{x_{m-1,n}}}}{2\Delta x} + \frac{J_{S_{y_{m,n+1}}} - J_{S_{y_{m,n-1}}}}{2\Delta y}, \end{aligned} \quad (2.61)$$

where supercurrent components are given as

$$J_{S_{x_{m,n}}} = \Im \left\{ \chi_{m,n}^{*\tilde{t}} \frac{\chi_{m+1,n}^{\tilde{t}} \tilde{U}_{x_{m+1,n}}^{\tilde{t}} - \chi_{m,n}^{\tilde{t}}}{\Delta x} \right\}, \quad (2.62)$$

$$J_{S_{y_{m,n}}} = \Im \left\{ \chi_{m,n}^{*\tilde{t}} \frac{\chi_{m,n+1}^{\tilde{t}} \tilde{U}_{x_{m,n+1}}^{\tilde{t}} - \chi_{m,n}^{\tilde{t}}}{\Delta y} \right\}. \quad (2.63)$$

In order to solve numerically Eq 2.61, one can use either Fast Fourier Transform (FFT) algorithm [88], if the geometry of the specimen is uniformly rectangular, or Successive Over-Relaxation method (SOR) [89] for arbitrary geometries. At the SI interface there is no flow of the component of normal current perpendicular to that boundary (in other words, $\mathbf{n}_{SI} \tilde{\nabla} V = 0$, where \mathbf{n}_{SI} is the unit vector perpendicular to the SI interface, which translates into the discrete space as $V_{m\pm 1,n} = V_{m,n}|_{m=m_{boundary}}$ and $V_{m,n\pm 1} = V_{m,n}|_{n=n_{boundary}}$). At the metallic contacts (SN interface), the transport current is applied, for which it is assumed to be completely transformed into normal current component perpendicular to the SN boundary ($\mathbf{n}_{SN} \tilde{\nabla} V = \mathbf{J}_a$, or given in the discrete space $V_{m\pm 1,n} = V_{m,n} \pm \tilde{J}_a \Delta x|_{m=m_{boundary}}$ and $V_{m,n\pm 1} = V_{m,n} \pm \tilde{J}_a \Delta y|_{n=n_{boundary}}$). This unfortunate selection of all-Neumann boundary conditions leads to the scenario where it is not possible to find the unique solution of the Poisson-like Eq. 2.61. One can then either impose an additional condition so the solution is artificially made unique (for example, one can always select such value of electrostatic potential so that $\langle V \rangle = 0$, which will not affect the physical quantities of interest, since they depend only on the potential difference - the voltage U), or instead of transport current one can apply external potential difference, so the boundary conditions change to $V_{m,n} = V_{ext}|_{m=m_{boundary}}$ and $V_{m,n} = V_{ext}|_{n=n_{boundary}}$.

The general form of discretized equation of thermal balance is obtained as

$$\begin{aligned} \tilde{T}_{m,n}^{t+\Delta\tilde{t}} = \tilde{T}_{m,n}^t - \Delta\tilde{t} \left(\tilde{T}_{m,n}^t - \tilde{T}_0 \right) \frac{\tilde{h}}{\tilde{c}} + \frac{\Delta\tilde{t}}{\tilde{c}} \tilde{\mathbf{J}}_{nm,n}^t + \\ \Delta\tilde{t} \left(\frac{\tilde{T}_{m+1,n}^t - 2\tilde{T}_{m,n}^t + \tilde{T}_{m-1,n}^t}{\Delta x^2} + \frac{\tilde{T}_{m,n+1}^t - 2\tilde{T}_{m,n}^t + \tilde{T}_{m,n-1}^t}{\Delta y^2} \right) \frac{\tilde{k}}{\tilde{c}}. \end{aligned} \quad (2.64)$$

This parabolic differential equation is solved with alternating direction implicit (ADI) method [90]. The boundary conditions used to solve this equation are a mixture of Neumann and Dirichlet conditions, where at the SI interface the Neumann boundaries are imposed ($\nabla\tilde{T} = 0$, corresponding to the open flow of the heat through the system) and at the SN interface the Dirichlet boundaries allow that the temperature at the metallic contacts is set above the critical temperature ($\tilde{T} \geq 1$). Further details about numerical calculations, including the model for the arbitrary geometries, are discussed in Appendix A.

2.3 Applications of the extended gTDGL model

It was already stated in this thesis that the main advantage of time-dependent formalism lies in the fact that it can describe dynamic processes that underpin a plethora of novel physical phenomena. As such, extended gTDGL model can be used not only to describe the non-equilibrium processes in the superconducting condensate due to the presence of external electric and magnetic fields, but also to describe the systems where external local probing of the condensate is performed, such as scanning tunneling microscopy, magnetic force microscopy, SQUID microscopy, etc. Since extended gTDGL theory provides an insight into the thermal balance of the system, then the effects of thermally-invasive microscopy techniques can be studied, as well (e.g. low temperature scanning laser microscopy). In the following Section some of the possible additions to the presented theoretical model, which one can use in order to simulate the realistic experimental setups, are discussed.

2.3.1 Time-dependent thermal potential

Externally induced local changes in the temperature of the system, which are not a simple consequence of the interplay of the applied currents in the presence of geometrical lensing, often strongly contribute to the overall behavior of the superconducting condensates and can even be the cause of the studied phenomena. This can be useful systems where dynamical properties of the superconducting condensate are studied, e.g. for realization of dynamic pinning mechanisms, or individual

manipulation of magnetic flux quanta. Examples of such a setup can be found in the low-temperature scanning electron microscopy, laser microscopy, or setups with nano-heaters. Monitoring the local heat distribution has a crucial role in the superconducting single-photon detectors (SSPD), where the incident light creates hot spots which trigger transition to the normal state so that an impact of a photon can be detected. In all of the mentioned cases, one is faced with external potential $\nu^{(ext)}(\mathbf{r}, t)$ that repetitively suppresses and recovers superconductivity in a specific region of the specimen via controlled thermal modulation. The parameters characterizing this potential are: the frequency of the oscillations $\omega^{(s)}$ (if periodic), the intensity of the suppression ν_0 , and size and shape of the hot-spot. Since one is constrained to the gTDGL framework, the parameters in question must be explained with respect to the important physical quantities defined already for the extended gTDGL model.

The frequency of oscillations can be translated to period $\tau^{(s)} = \frac{2\pi}{\omega^{(s)}}$, which, in principle, must always respect the restriction $\tau^{(s)} > \tau_{GL}(0)$, so that validity of gTDGL theory is preserved. In other words, the period of oscillations has a lower limit, which for materials such as Al, Pb, or NbN ranges from several ps to hundreds of ns (translating into highest frequencies close to 1 THz). Besides the scenario where the local temperature in the hot-spot is raised and superconductivity is suppressed (or even fully depleted, if $T(\mathbf{r}, t) \geq T_c$), cooling of the condensate is also possible, so the superconducting properties are enhanced under the spot. In general, intensity modulation achieved at the external source defines the temporal profile of the magnitude of the thermal potential. Radius of the spot, R , should follow the condition $R > \xi(0)$, for the result of gTDGL theory to remain meaningful. In the realistic systems, the shape of the hot spot is usually obtained from the diffraction pattern, which allows one to create stripes, circular spots, rings, or even periodic lattices of hot spots.

2.3.2 Spatially inhomogeneous parameters of extended gTDGL theory

The gTDGL equations are used in their dimensionless form where the characteristics of the material, as well as the universal constants, are included in the dimensionless variables, making the formalism more convenient for analysis and computations. In realistic cases material inhomogeneities are always present, and in order for one to perform a reliable theoretical analysis and reproduce the essential physical phenomena in the studied system, these inhomogeneities must be described and included in the theoretical model. In this Section it is explained how the inhomogeneities in the superconductors can be taken into account, provided that the scale of the inhomogeneities is comparable to the coherence length. This model can also

be used to treat the specimen composed of an assembly of different materials, as in the case of superconducting junctions.

If one recalls Eqs. 2.24, 2.25, 2.26, and 2.39

$$\begin{aligned} & \frac{N(0)\pi\hbar}{8k_B T_c u} \frac{u}{\sqrt{1 + \left(\frac{2\tau_i|\Delta|}{\hbar}\right)^2}} \left[\frac{\partial\Delta}{\partial t} + i\frac{e^*}{\hbar}\varphi\Delta + \left(\frac{2\tau_i}{\sqrt{2}\hbar}\right)^2 \frac{\partial|\Delta|^2}{\partial t}\Delta \right] = \\ & \frac{N(0)\pi\hbar D}{8k_B T_c} \left(\nabla - i\frac{e^*}{\hbar}\mathbf{A} \right)^2 \Delta + \left(N(0)f(T) - g(T) \frac{N(0)\pi^2}{16uk_B^2 T_c^2} |\Delta|^2 \right) \Delta, \\ & \frac{1}{\mu_0} \nabla \times \nabla \times \mathbf{A} = \sigma_n \left[\frac{\pi}{2k_B T_c e^*} |\Delta|^2 \left(\nabla\theta - \frac{e^*}{\hbar}\mathbf{A} \right) - \frac{\partial\mathbf{A}}{\partial t} - \nabla\varphi \right], \\ & -\nabla\mathbf{J}_n = \nabla \left[\sigma_n \left(\frac{\partial\mathbf{A}}{\partial t} + \nabla\varphi \right) \right] = \nabla\mathbf{J}_s = \\ & \quad \nabla \left[\frac{\sigma_n\pi}{2k_B T_c e^*} |\Delta|^2 \left(\nabla\theta - \frac{e^*}{\hbar}\mathbf{A} \right) \right], \\ & c \frac{\partial T}{\partial t} = k\nabla^2 T - \frac{h}{d} (T - T_0) + V(\mathbf{r}, t), \end{aligned}$$

respectively, one should note that the values of the parameters T_c , $N(0)$, τ_i , D , σ_n , c , k , and h are characteristics of the material. Therefore, in the case of an inhomogeneous sample, these quantities are no longer simple coefficients, but instead have spatial distribution. Material parameters can also depend on some external quantity, such as temperature, which can vary with time. Thus, in this situation one can postulate

$$\begin{aligned} T_c(\mathbf{r}, t) &= T_c^{(0)} p_{T_c}(\mathbf{r}, t), \\ N(0)(\mathbf{r}, t) &= N(0)^{(0)} p_{N(0)}(\mathbf{r}, t), \\ \tau_i(\mathbf{r}, t) &= \tau_i^{(0)} p_{\tau_i}(\mathbf{r}, t), \\ D(\mathbf{r}, t) &= D^{(0)} p_D(\mathbf{r}, t), \\ \sigma_n(\mathbf{r}, t) &= \sigma_n^{(0)} p_{\sigma_n}(\mathbf{r}, t), \\ c[T(\mathbf{r}, t)] &= c^{(0)} p_c(\mathbf{r}, t), \\ k[T(\mathbf{r}, t)] &= k^{(0)} p_k(\mathbf{r}, t), \\ h[T(\mathbf{r}, t)] &= h^{(0)} p_h(\mathbf{r}, t), \end{aligned}$$

where $T_c^{(0)}$, $N(0)^{(0)}$, $\tau_i^{(0)}$, $D^{(0)}$, $\sigma_n^{(0)}$, $c^{(0)}$, $k^{(0)}$, and $h^{(0)}$ are some reference values, while $p_{T_c}(\mathbf{r}, t)$, $p_{N(0)}(\mathbf{r}, t)$, $p_{\tau_i}(\mathbf{r}, t)$, $p_D(\mathbf{r}, t)$, $p_{\sigma_n}(\mathbf{r}, t)$, $p_c(\mathbf{r}, t)$, $p_k(\mathbf{r}, t)$, and $p_h(\mathbf{r}, t)$ are dimensionless kernels containing generic spatial and temporal dependence.

As stated before, the dimensionless parameter u is originally obtained to have value of 5.79 ($u = \pi^4/14\zeta(3)$, where $\zeta(3)$ is Riemann zeta function), but estimates from microscopic theories state that u can go as high as 12 [91, 92].

Finally, even in thin films (2D structures), variations in the thickness of the sample [$d(\mathbf{r}) = d^{(0)}p_d(\mathbf{r})$] can play an important role in emergent physics. In order to account for the influence of the nonuniform thickness, Eq. 2.24 should be modified by including the additional term $\frac{N(0)\pi\hbar D}{8k_B T_c} (\nabla - i\frac{e^*}{\hbar}\mathbf{A}) \Delta \frac{\nabla p_d}{p_d}$. Furthermore, current densities \mathbf{J}_s and \mathbf{J}_n in Eqs. 2.25, 2.26 should be exchanged with $\mathbf{J}_s p_d$ and $\mathbf{J}_n p_d$, respectively. Finally, the set of dimensionless extended gTDGL equations accounting for the inhomogeneous material parameters, with thickness variation included, reads

$$\frac{u}{\sqrt{1 + (\tilde{\Gamma} p_{\tau_i} |\chi|)^2}} \left[\frac{\partial \chi}{\partial \tilde{t}} + iV\chi + \frac{(\tilde{\Gamma} p_{\tau_i})^2}{2} \frac{\partial |\chi|^2}{\partial \tilde{t}} \chi \right] = \quad (2.65)$$

$$p_D (\tilde{\nabla} - i\mathbf{Q})^2 \chi + \left(p_{T_c} f - \frac{g|\chi|^2}{p_{T_c}} \right) \chi + p_D (\tilde{\nabla} - i\mathbf{Q}) \chi \frac{\nabla p_d}{p_d},$$

$$\frac{\kappa^2}{p_d} \tilde{\nabla} \times \tilde{\nabla} \times \mathbf{Q} = p_{\sigma_n} \left[\frac{|\chi|^2}{p_{T_c}} (\tilde{\nabla} \theta - \mathbf{Q}) - \frac{\partial \mathbf{Q}}{\partial \tilde{t}} - \tilde{\nabla} V \right], \quad (2.66)$$

$$\tilde{\nabla} \left(p_{\sigma_n} \frac{\partial \mathbf{Q}}{\partial \tilde{t}} - p_{\sigma_n} \tilde{\nabla} V \right) = \tilde{\nabla} \left[\frac{p_{\sigma_n}}{p_{T_c}} |\chi|^2 (\tilde{\nabla} \theta - \mathbf{Q}) \right], \quad (2.67)$$

$$\tilde{c} p_c \frac{\partial \tilde{T}}{\partial \tilde{t}} = \tilde{k} p_k \tilde{\nabla}^2 \tilde{T} - \frac{\tilde{\hbar} p_h}{p_d} (\tilde{T} - \tilde{T}_0) + \frac{p_d^2}{p_{\sigma_n}} \left(\frac{\partial \mathbf{Q}}{\partial \tilde{t}} - \tilde{\nabla} V \right)^2. \quad (2.68)$$

Chapter 3

Basics of vortex dynamics and manipulation

Bulk type II superconductors exhibit the so-called Shubnikov (or mixed) phase for a certain range of magnetic fields, where superconducting and normal state can spatially coexist. When the magnetic field is sufficiently high for a superconductor to reach the Shubnikov state, the field overcomes the Meissner-Ochsenfeld barrier and penetrates in the system. The penetrating flux is quantized, where each flux quantum Φ_0 is enclosed with a whirling current. Such physical construct is called a vortex. A region of radius ξ around the vortex core is nearly free of superconducting carriers, and exhibits a singularity at the vortex center $\Delta(\mathbf{r} \rightarrow 0) \rightarrow 0$. Furthermore, vortex carries a 2π winding in phase of the order parameter, θ . Different properties of the vortex (e.g. magnetic field, current profile, $|\Delta|^2$ and θ distribution) are shown in Fig. 3.1(a)-(d). In large superconducting systems one typically finds a bundle of vortices, which, due to vortex-vortex interaction and interaction of vortices with the geometric boundaries, is arranged into a lattice. Abrikosov, who was first to theorize the existence of vortices, calculated that the vortex matter should be arranged in a square lattice in bulk superconductors [see Fig. 3.1(e)], where the distance between nearest neighbours is given as $a_{\square} = \sqrt{\frac{\Phi_0}{B}}$. However, it soon turned out from the experimental observation [93] and subsequent calculations that the triangular arrangement of the vortex lattice is slightly more favorable [shown in Fig. 3.1(f)], with lattice constant given as $a_{\Delta} = 1.075\sqrt{\frac{\Phi_0}{B}}$.

In most of their applications, type II superconductors are used to carry electrical current. It is not seldom that superconducting current carriers are exposed to the external magnetic field, due to which dissipative effects emerge. This is mostly because transport current together with magnetic field gives rise to a Lorentz-like

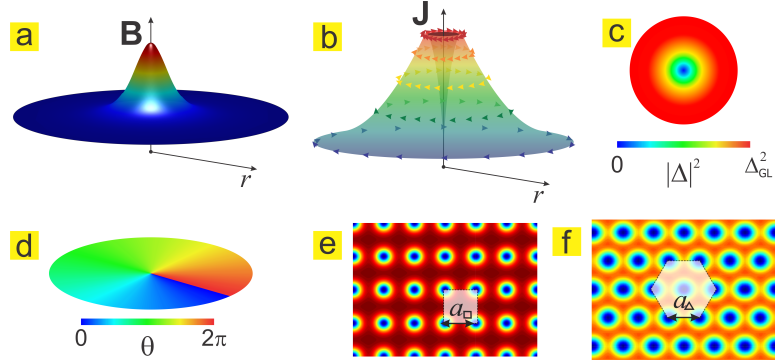


Figure 3.1: Properties of a superconducting vortex: (a) The magnetic field of a single vortex. (b) The current enclosing the vortex (note that supercurrent drops to zero in vortex core). In (c) and (d) profiles of the Cooper-pair density and phase of a vortex are given, respectively. (e) shows square vortex lattice with lattice constant a_{\square} , where the unit cell is marked with the transparent white square. In (f) the triangular vortex lattice with lattice constant a_{Δ} is given, where hexagonal unit cell is indicated by transparent white area.

driving force ($\mathbf{J} \times \mathbf{B}$), which acts on vortices in the direction perpendicular to the flow of current. In homogeneous superconductors, without any defects to anchor the vortices, the sole opposition to the driving force is the viscous drag. However, if the applied current is high enough, the driving force will overpower the viscous force, and vortices will be set in motion. Since each moving vortex carries magnetic flux, the dynamic behavior of the condensate leads to redistribution of the overall magnetic flux of the system as a function of time. These temporal variations of the magnetic flux will cause a finite voltage U in the system (thus the non-zero resistance), which can be translated directly to the Joule losses ($P = IU$). Moreover, with further increase of the applied current, transitions to higher resistive states are bound to happen due to rearrangement of the vortex lattice [94]. Such transitions lead to an increase in the slope of the voltage, which can readily be seen in the current density-voltage characteristic, the example of which is given in Fig. 3.2. This characteristic was obtained by solving Eqs. 2.42 and 2.44 (with Coulomb gauge) for the thin film in extreme type II regime, where the specimen size was $150\xi(0) \times 75\xi(0)$, the bath temperature $T_0 = 0.9T_c$, and the applied magnetic field was $0.5B_{c2}(0)$. The changes of the voltage slope correspond to the changes in the dynamic resistivity of the specimen, which can be very subtle. For this reason the zoomed-in inset of the current-voltage characteristic is also given in

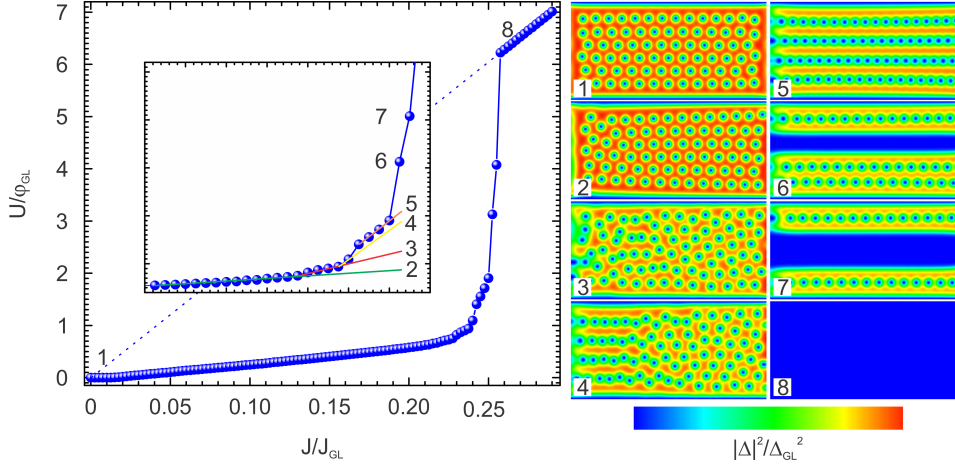


Figure 3.2: The current density-voltage characteristic of a superconducting stripe, exposed to perpendicular magnetic field. The inset depicts the zoomed-in part of the characteristic, where the slope is changed due to the rearrangements in the vortex lattice (points 1-8). As a guide to the eye, solid lines of different colors are introduced in the inset to point out the changes in the slope of the voltage. Dashed line in the main panel indicates the slope of the voltage exhibited as the system reaches the normal state, at high currents. Snapshots of the Cooper-pair density 1-8 show the evolution of the vortex matter in the superconductor when the current is increased, corresponding to each slope change.

Fig. 3.2, where the subtle variations in dynamic resistivity are easier to spot. Each change in the slope is complemented with the snapshot of the Cooper-pair density (CPD) profile, from which it can be verified that rearrangement of the vortex lattices takes place each time a change in voltage slope is seen.

In this chapter common behavior of the superconducting condensate exposed to external magnetic field and applied electric current is overviewed within gTDGL framework. Moreover, several experimental techniques for manipulation of the vortex behavior through external means were described.

3.1 Effect of the interplay of currents on the vortex matter

In this Section gTDGL theory is used to explain how the interplay of transport currents and the magnetic field-induced screening currents may lead to the dynamical behavior of the superconducting condensate. This interplay is first discussed for

the case of the steady state, after which the condition for the critical state for the onset of vortex motion is described. Finally, an overview of the dynamic behavior of the superconducting condensate is given.

3.1.1 Interplay of currents in the steady state

As stated earlier in the text, whenever a superconductor is exposed to an external magnetic field, due to the Meissner-Ochsenfeld effect, a screening supercurrent will arise which in turn induce a magnetic field opposing the applied one. In this way a barrier is created for applied magnetic field that prevents its penetration inside the superconductor. The response of the superconductor to increasing applied magnetic fields leads to induction of stronger Meissner-Ochsenfeld currents, J_M . This is shown in Fig. 3.3(a), where an evolution of line profiles of Meissner-Ochsenfeld current density across the sample is seen for different magnetic fields. These curves were obtained, once again, by solving Eqs. 2.42 and 2.44 in Coulomb gauge, for a thin film in extreme type II regime, for a sample size $45\xi(0) \times 22.5\xi(0)$, and working temperature $T_0 = 0.9T_c$. From Fig. 3.3(a) one can see that the highest Meissner-Ochsenfeld currents are at the sample edges. The supercurrent that grows with the increasing magnetic field is limited by the depairing current, J_{DP} , at which the Cooper pairs are destroyed. The depairing current is given by

$$J_{DP} = \frac{2}{3\sqrt{3}} \frac{e^* \Delta_{GL}^2 N(0) \pi D}{4k_B T_c \xi} = \frac{2}{3\sqrt{3}} J_{GL}. \quad (3.1)$$

When the Meissner-Ochsenfeld currents at the edges of the sample reach J_{DP} , a vortex will nucleate at the border of the sample.

On the other hand, if some current density J_a is applied, the situation is somewhat different. In the absence of magnetic field the evolution of the line profiles of the transport current density is shown in Fig. 3.3(b), where one sees a nearly flat profile of current density across the sample. However, if there is some finite magnetic field present as well, the total current density will be the superposition of the Meissner-Ochsenfeld and the transport current densities. In such a case, transport current density enhances the Meissner-Ochsenfeld current density at one edge of the sample ($J = J_a + J_M$), while suppressing it on the other edge ($J = J_a - J_M$). For illustration, Fig. 3.3(c) shows this evolution of the total current density in the case when different transport currents are applied to the system exposed to the external magnetic field.

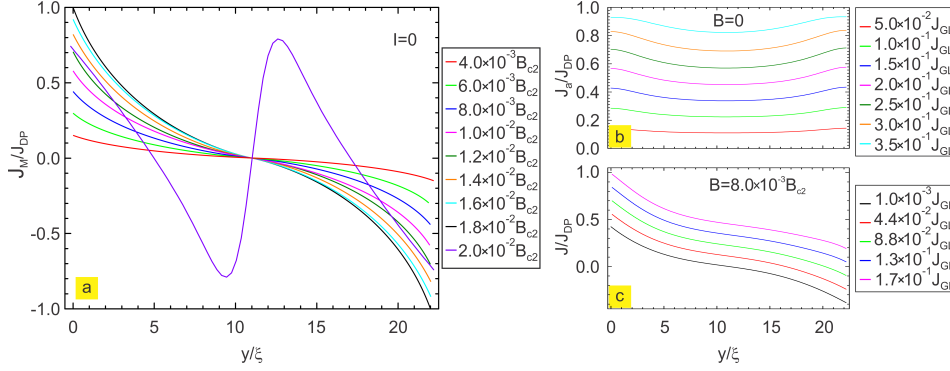


Figure 3.3: (a) Evolution of the Meissner-Ochsenfeld currents in a superconducting stripe (of size $45\xi(0) \times 22.5\xi(0)$) with respect to the applied perpendicular magnetic field, in the absence of applied current. (b) Profiles of supercurrent response to several values of applied current, in the absence of magnetic field. (c) Total supercurrent which is obtained from superposition of Meissner-Ochsenfeld current for a single value of magnetic field and several different applied currents.

3.1.2 A critical state for the onset of vortex motion

In the previous Section the situation is discussed where the superconductor is exposed to some external field and transport current. However, in the superconducting state, one cannot increase the applied current to arbitrarily large values. In fact, the maximal value that limits the total supercurrent density, J , is the depairing current. If J locally reaches J_{DP} , nucleation of a vortex will occur. When vortex appears in the specimen, currents associated to it compensate the Meissner-Ochsenfeld currents. In principle, vortex will remain trapped in the sample if the barrier for vortex exit is too high. In this case more applied current is needed to lower the exit barrier and push the vortex outside, so that the critical state for the onset of permanent vortex motion is reached. Based on the same representative sample as in previous Section, in Fig. 3.4(a) is shown the profile of the total supercurrent across the sample, corresponding to the critical condition just before vortices start to move. This is complemented with a Cooper-pair density (CPD) snapshot showing the vortices on the verge of exiting the specimen, as the current density at the exit boundary is nearly zero. In general, a good way to obtain information about dynamical phenomena in a superconductor is to track the associated voltage in real time. In Fig. 3.4(b) this voltage is shown in two cases, namely just below the critical current (blue line) and at the onset of the resistive state (red line). One can notice that when vortices start to move, real-time voltage profile exhibits

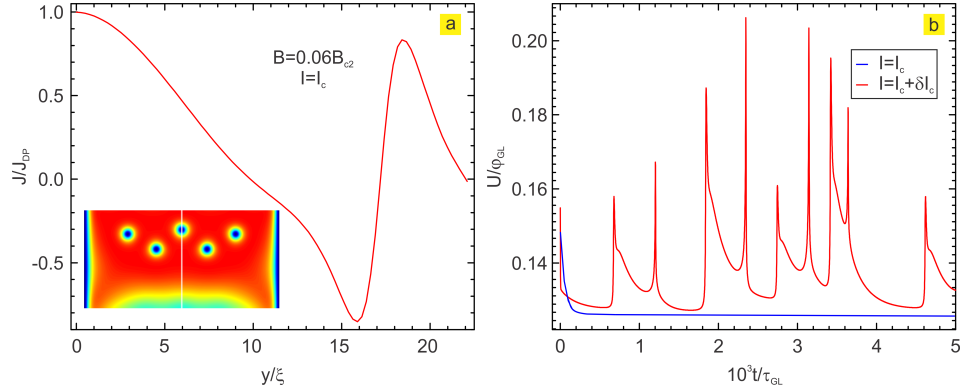


Figure 3.4: (a) Supercurrent profile in the critical state for the onset of the resistive state. Snapshot of Cooper-pair density (CPD) depicts vortices pushed towards the edge of the sample. The line across the CPD inset indicates where the current density profile was taken. (b) Time-dependent profile of the calculated voltage before (blue line) and just after the critical state (red line), when dynamic regime is instated.

multiple peaks with time, which are signatures of vortices entering and exiting the specimen.

The critical applied current, I_c , at which the transition from stationary to a dynamical state occurs, represents a very important parameter for any superconducting system. In particular, the control of I_c is crucial when designing the systems where losses are crucial (e.g. superconducting cables), or where the onset of resistance serves as a quantum switch (such as Josephson junctions). The critical current depends on most properties of the system, including geometry of the specimen, disorder (its nature and distribution), artificial pinning sites for vortices, magnetic field, temperature, etc.

3.1.3 Dynamic equilibrium

Once the motion of vortices commences, with all the properties of the system fixed (applied current, magnetic field, temperature, etc.), the initial response of the system may be seemingly chaotic, but over the course of time, the system relaxes into a periodically oscillating state. This oscillatory behavior in which vortex motion becomes fully periodic is called dynamic equilibrium. Relaxation times needed for the system to reach dynamic equilibrium are usually not longer than several nanoseconds, while most of the relevant experimental measurements are performed

on much longer time scales (minutes, or even hours). However, for numerical simulations, where longest considered times hardly exceed one microsecond, the task of reaching periodic oscillations in the system can prove to be quite challenging on occasion, especially in larger samples, or when dynamics of flux quanta is complex, since extensive computational time and resources are required.

The voltage evolution in real time can be used to represent the condensate dynamics, but only if its characteristic features can be recognized and understood. Figure 3.5 shows a characteristic sequence of the system once it has relaxed into the fully periodic oscillatory state. There, the temporal dependence of the voltage, spanning over three periods of characteristic dynamics, where the magnetic field, applied current, and bath temperature remain unchanged, is shown. During one period Δt eight instances are selected to point out interesting features, manifesting themselves through voltage maxima and minima. The cycle begins with the entrance of a vortex into the system already containing four vortices (CPD snapshot 1 in Fig. 3.5). As this vortex progresses deeper in the specimen (snapshot 2), two vortices closest to the sample edge are pushed outside simultaneously (snapshot 3). The condensate then remains with only four vortices present (snapshot 4) until two more flux quanta penetrate the sample (snapshot 5). As these new vortices take their place in the triangular lattice (snapshot 6), single vortex closest to the edge exits the sample (snapshot 7). The system then remains in this state (snapshot 8) until the cycle ends and a new one starts.

Variation in some of the properties of the system can lead to more complex dynamics (e.g. in Fig. 3.2, inset 4 shows a rather complex condensate behavior at high currents). For example, at higher currents more features within characteristic cycles should be expected, since vortex motion can be affected by additional phenomena such as Larkin-Ovchinnikov instabilities, or where due to fast motion, vortices slipstream each other inside the channels of permanently suppressed superconductivity [94].

3.2 Vortex pinning in permanent pinning landscapes

A long-standing challenge on the path to superconducting applications of type II materials is the unwanted motion of vortices [95]. A vortex can be pinned in a superconductor by collocating its energetically costly core within a preexisting defect where superconductivity is already suppressed. The strength of the pinning dictates the maximal current at a given magnetic field which can be applied without vortex motion and, consequently, dissipation (in other words, the magnitude of pinning force is roughly determined by the product $I_c B$). Superconductors usually possess intrinsic random pinning due to material impurities, disorder, or low

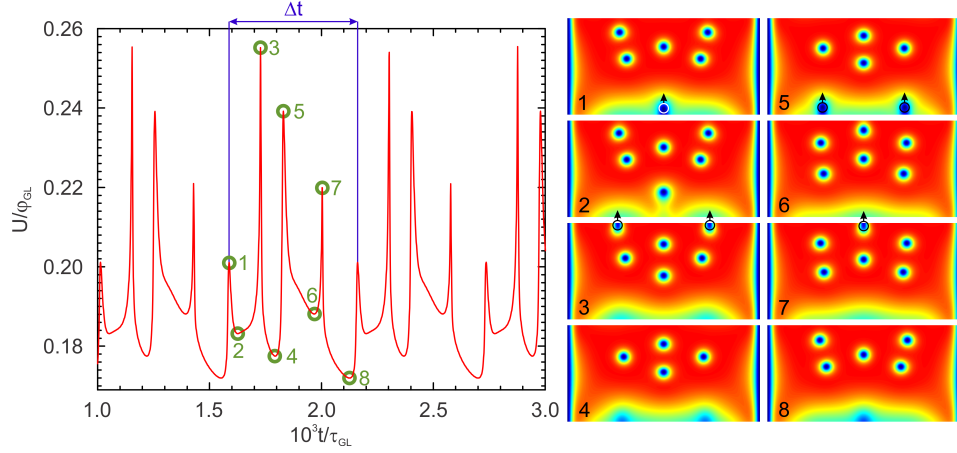


Figure 3.5: Exhibited voltage oscillations of the system in dynamic equilibrium. Period of oscillations is denoted with Δt . Snapshots of the CPD at instances 1-8 illustrate the characteristic behavior of the condensate during one period. Black arrows and hollow rings in snapshots 1, 3, 5, and 7 indicate vortices entering and exiting the system.

crystallographic quality of the material. This type of pinning does not yield high critical currents, as the onset of vortex motion can be easily activated. To improve the functionality of superconductors so they can sustain strong transport currents while maintaining low dissipation, many artificial pinning mechanisms were engineered over the last several decades. For example, through the introduction of nano-particles by means of irradiation of superconducting films can produce randomly distributed pinning sites [96, 97], which can have different pinning energies. Other fabrication techniques, such as chemically grown defects [98], nanostructured perforations [99], or patterning with permanent nanomagnets [100], allow precise design of pinning centers in mesoscopic samples, with precise control of their shape, size, and arrangement. This allows one to impose periodic arrangement of the pinning sites, which gives rise to commensurability phenomena between the vortex lattice and the pinning potential. In particular, whenever the pinning landscape matches the otherwise stable vortex configuration, a strong enhancement in the critical current at a given field can be observed, as shown in Fig. 3.6, for an Al bridge, patterned with periodic array of triangular holes. Note that in absence of pinning, critical current exhibits monotonic decrease when magnetic field is increased. These enhanced values of the critical current occur at the integer multiples of the first matching field, $B = nB_m$ (see Fig. 3.6), which is defined as the field

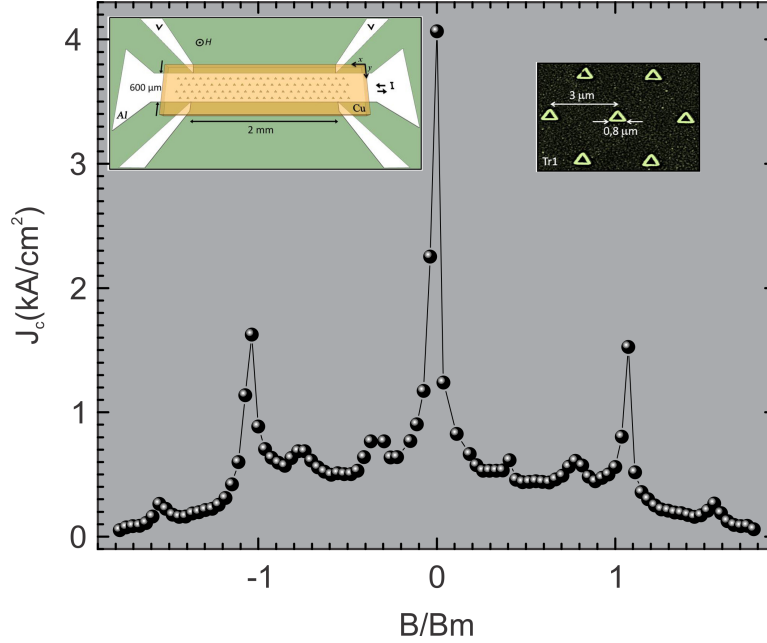


Figure 3.6: The critical current versus magnetic field characteristic of a 50 nm thick Al film patterned with triangular pinning array of triangular holes with lattice parameter and size of pinning sites shown in inset on the left (from Ref. [101]). Inset on the right is the image of the system, obtained by scanning electron microscopy.

at which the density of vortices equals the density of pinning sites. Interestingly, it has been observed that at the rational multiples of B_m noticeable enhancement of the critical current can occur, due to formation of fractional sublattices at interstitial sites of the pinning lattice.

The maximal number of vortices that can occupy one pinning site, n_s , can roughly be estimated as a ratio of the size of the pinning site and the radius of the vortex core (i.e. ξ). If the field is high enough to induce more vortices per pinning site than n_s , then some vortices will be located at the interstitial positions, in between the holes. High mobility of interstitial vortices can then cause a decrease in the critical current. Furthermore, the shape of the pinning can impose a preferential direction for vortices to move (so-called rectification effect, where an *ac* current drive in such a case leads to a net *dc* voltage). This is frequently seen in asymmetric pinning potentials, such as the one with triangular holes shown on the inset in Fig. 3.6, and can also be used for enhancement of critical current for a particular direction of the driving force.

3.3 Individual manipulation of vortices

In the previous Section the pinning mechanism that affects the behavior of vortex lattice, with the task of preventing the unwanted motion of the flux quanta was discussed. Continued reduction in uncontrolled vortex motion is beneficial for applications, both for reduced noise in superconducting circuits for sensing and communication, and for dissipationless utilization of large currents in high-field magnets and power distribution.

On the other hand, many superconducting devices operate based on a single-vortex manipulation [102]. Controlled vortex motion can serve as a rectifier [103], clocked logic [104], or to control spins in an adjacent diluted magnetic semiconductor [105], while vortices neighbouring an electron gas in a quantum-Hall state may support creation of exotic quantum states [106]. Vortex matter is of theoretical interest for its own sake [107, 108], as crucial evidence for underlying mechanisms of superconductivity [109, 110], as analogues for interacting bosons [111], or as model systems for soft condensed matter [108]. In the following text some state of the art experimental techniques for detection and manipulation of single vortices will be briefly summarized.

3.3.1 Scanning tunneling microscopy

Tunneling spectroscopy has developed into a field of intense research since its first application to superconductors by Giaever [112, 113] in 1961. Subsequently, it was extended to surface studies, mainly through inelastic tunneling spectroscopy [114]. Seminal advance to this field was made by Gert Binnig and Heinrich Rohrer who developed the scanning tunneling microscope (STM) in 1981, and who were awarded the Nobel prize in physics in 1986 for this endeavour [115, 116] (note: The designation “STM” is subsequently used interchangeably to denote “scanning tunneling microscope” and “scanning tunneling microscopy”). Image acquisition with STM technique introduces resolutions up to 0.1 nm in lateral direction and up to 10 pm of high resolution [117], which makes scanning tunneling microscope an excellent tool for visualizing surfaces at the atomic level, where also individual atoms at the surface of the material can be manipulated. Further advantages of STM include the fact that it can be used in a wide temperature range (from nearly 0 K up to over 1000 K) and it works in different ambients, such as ultra-high vacuum, air, water, various liquids and gasses.

Scanning tunneling microscope consists of a sharp conducting tip, whose apex can be a single atom, mounted on a piezoelectric tube. The tip is in charge of image acquisition pixel by pixel, where piezoelectric stylus, biased from external voltage source, is responsible for shifting the tip from one pixel to another in ex-

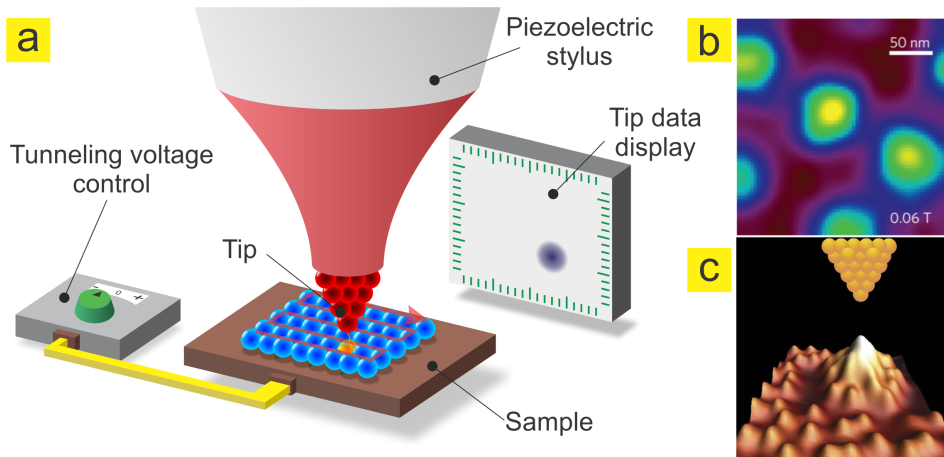


Figure 3.7: Scanning tunneling microscope (STM). (a) Schematic description of the STM. A tip with an apex of a single atom width is mounted on a piezoelectric stylus which scans the sample. Tunneling current is controlled with external voltage, and the output signal is shown on the display. (b) Image of the vortices in a superconducting film obtained by STM (figure taken from Ref. [118]). (c) Manipulation of the vortices with an STM tip, where vortex clustering is caused by local heating due to tunneling current (figure taken from Ref. [119]).

tremely subtle and accurate manner [shown in Fig. 3.7(a)]. The piezo-tube also controls the distance between the tip and the surface of the material, and it can be used for scanning in so-called constant height mode, appropriate for atomically flat surfaces. The underlying physical basis of the STM is electron tunneling occurring between the apex of the conducting tip of the microscope (first electrode) and the conducting surface of the material (second electrode), separated by sufficiently thin insulating layer, or in physical terms, potential barrier. Fundamental to the operation of the STM is the extreme sensitivity to tip-surface distance of the tunneling current. The tunneling current decreases by roughly an order of magnitude for every increase in height of 0.1 nm, in which case the effective diameter of the filament through which the current tunnels decreases to atomic scales [120]. In this way individual atoms of the material surface can be resolved and displayed, so that the material landscape is recorded and reconstructed in an image of an atomistic precision. Moreover, STM can scan the sample in constant current mode, where, while scanning the surface, the height of the tip is adjusted in such a way that the tunneling current is maintained constant. As the current is proportional to the local density of states, the tip follows a contour of a constant density of states during

scanning. A kind of a topographic image of the surface is generated by recording the vertical position of the tip. However, STM images do not only display the geometric structure of the surface, but also depend on the electronic density of states in the specimen, as well as on characteristic interactions between the tip and the sample which are not completely explained to date.

In superconductivity, STM can provide high-resolution imaging of vortex matter, where the output signal displays the contrast between normal electrons and Cooper pairs, as is shown in Fig. 3.7(b) (figure taken from Ref [118]). In this manner, the position of vortex cores can be easily seen. Additionally, scanning tunneling spectroscopy can be utilized to influence the individual vortices. By sweeping the external voltage, tunneling current can be used to locally suppress or recover superconductivity, and thus pin/depin the vortex, as shown in Fig. 3.7(c) (figure taken from Ref. [119]). In this way, one can create a dynamic pinning landscape, which can be utilized to manipulate the motion of individual vortices.

3.3.2 Magnetic force microscopy

The study of magnetic forces at the nanometer scale has long been of interest to investigators of magnetic recording materials, superconductors, and magnetic nanoparticles, among others. The magnetic force microscope (MFM) is a device where a sharp magnetized tip picks-up the magnetic signal of a specimen. During this procedure the tip-sample magnetic interactions are detected and used to reconstruct the magnetic structure of the sample surface. This imaging technique can achieve spatial resolution of the order of few tenths of nanometers. Image acquisition with MFM usually requires sample-tip separation larger than several nm, otherwise atomic forces become an important factor during the scanning procedure.

Scanning the sample is performed with piezoelectric tubes, that move either the sample below the tip or the tip above the sample, in all three spatial dimensions. External voltage is used to control the movement, and usually 1 V of potential difference is enough to create displacement under 10 nm. Full image is obtained by slowly scanning the surface of the specimen in a raster fashion. The tip itself is located on one end of the cantilever, which is usually made of single-crystalline silicon, silicon dioxide, or silicon nitride. The tip is coated with a thin film (of thickness less than 50 nm) of magnetic material, as a form of shielding, so that the magnetic state of the tip does not change during the imaging. As the sample below the tip moves, its local magnetic landscape causes the cantilever to deflect in lateral and vertical direction. An overview of this system is shown in Fig. 3.8(a). The deflection of the cantilever is then measured and can be displayed for further analysis and characterization.

Since the stray magnetic field from the sample can affect the magnetic state

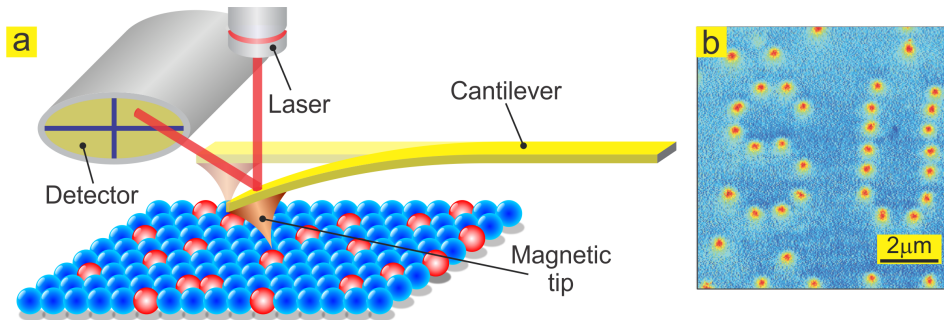


Figure 3.8: Magnetic force microscope (MFM). (a) Magnetic tip attached on one end of the cantilever scans the magnetic landscape of the specimen. Motion of the tip causes elastic deformation of the cantilever. Laser light is used to illuminate the tip-carrying end of the cantilever. Deformation of the cantilever causes the light to refract under a different direction, which is then detected on a photodetector. After being detected, signal is processed and recorded on an external device. (b) Image of vortex manipulation via MFM, where magnetic tip of the MFM is used to arrange vortices into letters S and U (image taken from Ref. [102]).

of the tip, and vice versa, interpretation of the MFM measurement is not always straightforward. For this reason it is quintessential to know all properties of the tip with its exact geometry. An image taken with a magnetic tip contains information about both the topography and the magnetic properties of a surface of the sample. Which effect dominates depends on the distance of the tip from the surface, because the interatomic magnetic force persists for greater tip-to-sample separations than the van der Waals force. If the tip is close to the surface, in the region where atomic forces are dominant, the image will be predominantly topographic (AFM mode). As the separation between the tip and the sample increases, magnetic effects become apparent (MFM mode). Collecting a series of images at different tip heights is one way to separate magnetic from topographic effects.

The MFM can be used to image various magnetic structures including domain walls, closure domains, recorded magnetic bits, etc. Furthermore, the motion of domain walls can also be studied in an external magnetic field. The popularity of MFM originates from several reasons. For one, the sample does not need to be electrically conductive. Measurement can be performed at ambient temperature, in ultra-high vacuum (UHV), in liquid environment, at different temperatures, and in the presence of variable external magnetic fields. Measurement is not invasive to the crystal lattice or structure. Long-range magnetic interactions are not sensitive to surface contamination. No special surface preparation or coating is required.

Deposition of thin non-magnetic layers on the sample does not alter the results.

Since vortices in type II superconductors carry magnetic field in their cores, MFM can be used to image them, but also to influence their behavior due to the magnetic interaction with the tip. In combination with imaging of the magnetic landscape created by the vortices in superconductor, one can use magnetic tip of the MFM to depin and drive individual vortices through the material, as shown in Fig. 3.8(b) [102, 121]. Imaging the vortices before, during, and after the depinning has great prospects for correlating pinning with topography, for determining the pinning landscape directly, and for studying single-vortex dynamics.

3.3.3 Scanning SQUID microscopy

In the previous Section the magnetic force microscope which is capable of producing images of magnetic field on a microscopic scale was discussed. Magnetic images can reveal, for example, the location of electric currents flowing in a sample or spatial variations in magnetic susceptibility. To be of general use, the microscope must be capable of sensing very weak magnetic fields: most materials exhibit only a weak magnetic susceptibility and many technologically interesting samples, such as microelectronic circuits, carry relatively small currents [122]. The most sensitive systems in the field of magnetometry make use of a low noise superconducting quantum interference device (SQUID) [123, 124, 125]. Since SQUIDs are by far the most sensitive detectors of magnetic flux and thus provide the best product of spatial resolution and field sensitivity, they are a natural choice as a sensor for a magnetic microscope. Though SQUID microscopy dates back to 1980, the first scanning SQUID microscope was developed only in 1992 by Randall C. Black *et al.* at the University of Maryland [122].

As the SQUID material must be superconducting, measurements must be performed at low temperatures (typically 4.2 K, corresponding to liquid helium). However, advances in fabrication of thin film high-temperature superconductors have allowed relatively inexpensive liquid nitrogen cooling to be used instead. It is even possible to measure room-temperature samples by cooling only high- T_c SQUID and maintaining thermal separation with the sample [126]. The SQUID itself is mounted onto a cantilever and operated just above the sample surface. The position of the SQUID is usually controlled by some form of electric step-motor. Operation of a scanning SQUID microscope consists of simply cooling down the probe (and sample), and rastering the tip across the area where measurements are desired. Detected field strength is then recorded by a system that also keeps track of the position of the probe.

After its development, numerous applications for scanning SQUID microscopy have appeared. In particular, scanning SQUID microscope can be used in the field

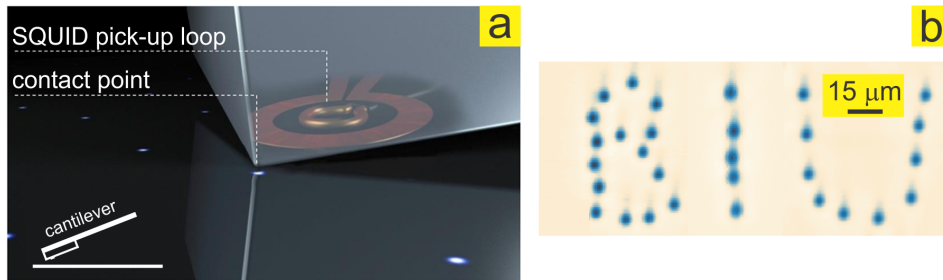


Figure 3.9: Scanning SQUID microscope. (a) Experimental configuration of the scanning SQUID microscope, taken from Ref. [127]. (b) Inset depicting vortices arranged into capital letters B, I, and U. Vortices are attracted by the stress applied with the tip of the SQUID by pushing the cantilever into the sample using scanning SQUID microscope (data taken from Ref. [127]).

of superconductivity for both imaging of the magnetic landscapes of the vortex matter and the mechanical control of individual flux quanta [127]. In the latter case, by applying local vertical stress with the tip of the sensor, vortices can be attached to the contact point, relocated, and stabilized at new position. In this way, mechanical manipulation of vortices provides a local view of the interaction between strain and nanomagnetic objects as well as controllable, effective, and reproducible manipulation technique.

3.3.4 Low temperature scanning laser microscopy

Techniques that provide insight in spatial distribution of superconducting properties in thin superconducting films are pivotal for both fundamental and applied science. Probing on such level provides the means for studying the resistive state of superconducting films, and as well the control of the operation of superconductive circuits and devices. With discovery of high T_c superconductors significance of these techniques has rapidly grown, since the properties of such materials often show inhomogeneous nature. One such technique is the low-temperature scanning laser microscopy (LTSLM) [128, 129]. LTSLM can be readily used at high magnetic fields.

The technique is based on a simple principle of scanning a sample with a laser beam (probe) focused on a sample surface, with a simultaneous recording of the response of the specimen (shown in Fig. 3.10(a)). A change in any characteristic of the sample or the probe, arising as a result of their local interaction, may serve as a response signal. In the case of a current-carrying superconducting film it is

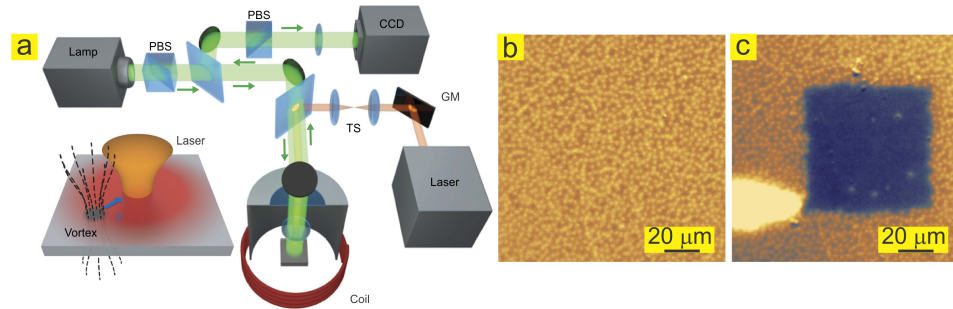


Figure 3.10: Low temperature scanning laser microscopy (LTSLM). (a) The concept of vortex attraction in a thermal gradient induced by a laser spot is illustrated, based on Ref. [130]. Magneto-optical imaging of individual vortices is based on the Faraday rotation of light polarization (PBS - polarizing beam-splitter, CCD - charge-coupled device). Local heating of the film is performed with a tightly focused continuous wave laser. Vortex imaging is performed by moving the laser beam with galvanometric mirrors (GM) placed in a telecentric system (TS). Example of vortex manipulation by LTSLM: (b) Distribution of vortices prior to LTSLM. (c) Final vortex distribution, after the manipulation by LTSLM. Dark blue square area is the part of the sample where the vortices were removed from by the laser. Bright yellow spot represents vortices that vacated the square area.

convenient to choose as a response signal the change in the voltage drop across the sample that arises due to the change in the resistance at the irradiated spot. The voltage response dependence on the probe coordinates at the sample surface can be visually represented as a two-dimensional image of resistive domains.

The change in voltage due to the illumination of a current-loaded superconductor is caused by a considerable number of mechanisms which can be divided into two classes: equilibrium (bolometric) and nonequilibrium (nonbolometric) mechanisms. The effects of the first class are displayed in the resistance change due to the lattice heating, mainly caused by low-energy phonons. Non-equilibrium mechanisms are related to the pair-breaking process by photons. This process is accompanied by high energy quasi-particle formation and involves non-equilibrium effects produced by electrons, phonons and Josephson effects at grain boundaries in the film.

LTSLM provides the opportunity to carry out the spatial resolved measurements of the superconducting films and phase transitions in high magnetic fields, or to investigate a local pinning and photo-induced creep of magnetic flux (deter-

mining the current-carrying capacity of superconductors) which is very important for the power applications. LTSLM in nonbolometric regime can be used also for dynamical manipulation of individual vortices [130]. In this mode a tightly focused laser beam induces a strong thermal gradient that can be used to manipulate single flux quanta [see Fig. 3.10(b) and (c)]. The laser locally heats the superconductor and creates a hot-spot of the size comparable to the vortex core, with a temperature rise in the Kelvin range, while keeping the temperature below T_c . The large thermal gradient can easily be tuned with laser power, so that the generated thermal force overcomes the pinning potential and induces a vortex motion towards the laser focus. Therefore, the laser beam acts as an optical tweezers that capture and can move single flux quanta to any new desired position in a disordered superconductor.

3.4 Vortex velocimetry

An important development of recent years has been the investigation of the dynamic behavior of magnetic flux structures and the discovery of the intimate connection between vortex motion and the transport properties of superconductors [131]. Usually, the experimentally studied device consists of a superconducting film with a magnetic field applied perpendicular to broad surfaces. Motion of the flux quanta can be induced by the driving force of an electric current. The dynamics of flux quanta becomes important in various technological applications of superconductivity. Pertinent to the dynamics of type II superconductors is the velocity at which flux quanta move, since it often must be parametrized in fluxonic devices, and is directly related to power dissipation. There are several available methods used to estimate vortex velocity, and in the following text some of them are briefly summarized.

3.4.1 Transport measurements

The transport measurements in superconductivity consist of a set of techniques used for quantification of superconducting properties in the presence of electrical current. Such techniques include measuring the normal state resistance as a function of the temperature, measurement of superconducting-normal state phase boundary, the magneto-resistance characteristic and the current-voltage characteristic. In the presence of magnetic field, transport measurements can be useful for characterization of vortex velocities. From measurement of the average voltage (the current-voltage characteristic), for example, one can extract the information about the average vortex velocity, as $v = U/BL$ (L being the distance between

the contacts where the voltage U is measured) [132]. In order for this voltage-velocity conversion to be justified, several conditions must be considered, all of which guarantee uniform distribution of local vortex velocity [133]. First of all, only the rectangular and square geometries should be taken into account for the velocity measurements, since any constriction that can cause current-crowding in the sample will lead to a velocity gradient, which can significantly deviate from the average value. Furthermore, specimen must exhibit weak intrinsic pinning, where the pinning density gradient can be neglected. Finally, linear voltage-velocity relation is only applicable in the regime of flux flow, found in a certain range of low currents, and which breaks down at the onset of higher dissipative states. From this type of velocity measurements, it can be concluded that during the flux flow Abrikosov vortices move with average velocities of the order of few hundreds of m/s [134].

3.4.2 Corbino setup

The Corbino configuration is a type of transport measurement where a superconducting disk is exposed to electric current injected at the center of the disk and removed at the perimeter [135]. If magnetic field is applied perpendicularly to the sample surface, due to the azimuthal direction of the driving force, vortices will move in concentric circles of radii r , with common axis located in the center of the disk. A schematic of this setup is shown in Fig. 3.11. Due to the geometry of the setup, radial current density, J , decays as $1/r$. In the absence of in-plane vortex-vortex correlations each vortex moves independently with a radial velocity proportional to the radial current density, $v \propto J \propto 1/r$. However, if over some length scale the in-plane vortex motion is correlated, one expects to detect a deviation from the $1/r$ velocity distribution. To spatially resolve the radial dependence of the vortex velocity and the length scale of the vortex-vortex correlation, multiple voltage contacts are typically introduced into the sample, at equidistant intervals along the disk radius. Note that these voltage contacts are used to obtain the information about local vortex velocity in the same fashion as done in the transport measurements for vortices collectively in the flux-flow regime (see Section 3.3.1). In this way, the control of the driving force gradient and the measurement of the spatial dependence of the velocity response provide a uniquely powerful combination for measuring fundamental properties as the shear modulus of the solid, the shear viscosity of the liquid, and the nature of plastic motion. Moreover, due to the gradient of the current density, one should expect the appearance of different vortex phases (including structures with a characteristic core elongation of vortices, usually observed at higher dissipative states, where such phenomena as Larkin-Ovchinnikov instabilities dominate [136]). Therefore, the Corbino setup allows

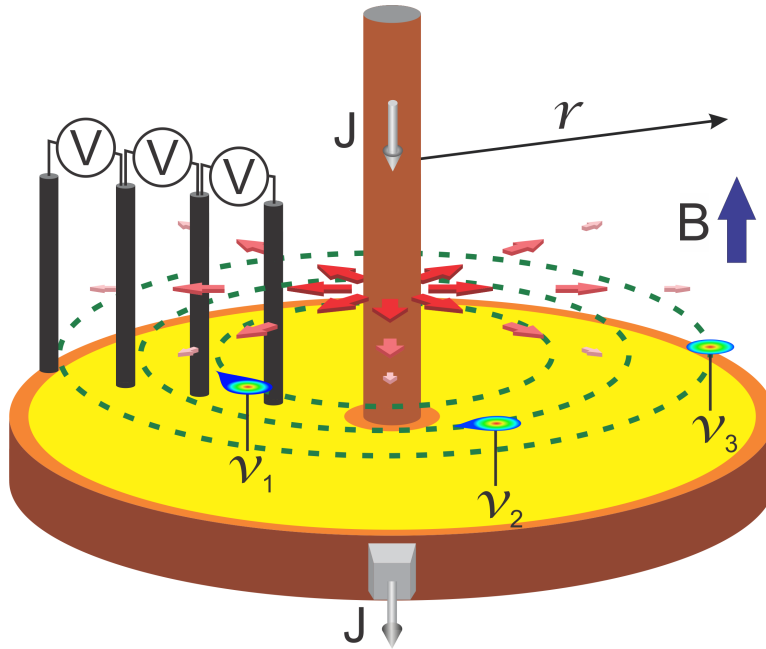


Figure 3.11: Corbino setup. Disk-shaped superconductor of radius r is exposed to magnetic field, B , perpendicular to the sample surface, and to transport current density, J , injected at the center of the disk and removed at the perimeter. Current density weakens radially from the center, which is indicated by arrows of decreasing size and with red color gradient. Such configuration forces the vortices present in the sample to move in circular orbits (indicated with green dashed lines), but with a gradient of velocities (v_1 , v_2 , and v_3). Voltage measurement contacts are introduced in the sample, so the distribution of vortex velocities could be measured.

one to measure relative vortex velocities, thus giving deeper insights into vortex zoology, without direct imaging of the vortex matter.

Chapter 4

Vortex matter under current lensing

The exact dynamics of current-driven vortex matter is of major importance both for the comprehension of the fundamental collective behavior of strongly interacting vortices and for attaining high non-dissipative currents in superconductors for applications. Materials advances in e.g. incorporating artificial pinning centers that immobilize vortices, particularly oxide nanoprecipitates in cuprates, have enhanced the critical current densities J_c between 10 and 20 percent of the depairing current density J_{DP} at which the superconducting state breaks down [96, 137, 138]. At such high current densities J , once a vortex gets depinned from a defect, it can move with high velocity v and dissipate heat. Understanding the details of this process is critical for many applications, such as high-field magnets [139], superconducting digital memory, and qubits [140], THz radiation sources [141], or resonator cavities for particle accelerators [142]. Yet, little is known about what happens to a vortex driven by very strong currents at the depairing limit $J \propto J_{DP}$ and what is the maximal terminal velocity a vortex can reach. Moreover, the fundamental question as to whether the notion of a moving vortex as a stable topological defect [72, 107] remains applicable at ultrahigh velocities has not been explored.

At high current densities with $J \gg J_c$ the effect of the disorder-induced pinning force diminishes and the resulting velocity of a vortex v is mainly determined by the balance of the driving force per vortex unit length ($\propto \Phi_0 J$) and the viscous drag force, $F_d = \eta(v)v$ [72, 107, 144]. At small v the viscous Bardeen-Stephen drag coefficient, $\eta_0 \propto \Phi_0^2 \sigma_n / 2\pi \xi^2$, results from dissipation in a circular, non-superconducting vortex core of radius $r \approx \xi$. Since the current density is limited by the depairing value given in Eq. 3.1, at which the speed of the superconducting condensate reaches the pair-breaking velocity $v_{DP} = \hbar / \pi m^* \xi$ [72], the maximal

vortex velocity can be extrapolated to $v_c = \Phi_0 J_{DP} / \eta_0 = \xi / 2\mu_0 \lambda^2 \sigma_n$ [142]. For a Pb film with $\lambda = 96$ nm and $\xi = 46$ nm at $T = 4.2$ K, and $\sigma_n \approx 50$ MS/m [143], one obtains $v_{DP} = 0.4$ km/s and $v_c \approx 40$ km/s, which suggests that the vortex could move at a velocity that is two orders of magnitude higher than the maximal drift velocity of the Cooper-pair condensate. A vortex moving much faster than the perpendicular current superflow which drives it raises many fundamental issues. What is the maximal terminal velocity that a single vortex can actually reach and what are the mechanisms that set this limit? Does a vortex remain a well defined topological defect even under the extreme conditions of the strongest possible current drive? Does the superfast vortex matter form dynamic patterns qualitatively different from the conventional flux flow at low velocities? Some of these issues have been studied theoretically, in a limiting case for temperatures very close to T_c [94, 132, 144, 145, 146, 147]. Since suitable theoretical frameworks for exploring the extreme dynamics of superfast vortices at low temperature have not yet been developed, the role of the experiment becomes paramount. However, addressing the physics of fast vortices experimentally is extremely challenging. For instance, inferring the terminal velocity v_c from the conventional measurements of dc voltage-current characteristics [132, 147, 148, 149] is rather indirect because it assumes that all vortices move with the same constant velocity, which is not the case, as will be shown later in this Chapter. Therefore, a local probe capable of tracing vortices moving at supersonic velocities is required. A number of methods, including STM [150, 151, 152], MFM [121, 153], magneto-optical imaging [154], SQUID microscopy [127], and scanning Hall magnetometry [155, 156, 157] have been employed to image slowly moving vortex structures, but none of them could resolve the properties of high-speed vortices.

In this Chapter the gTDGL framework was employed to treat the superfast vortex matter under current lensing in the specimen with a geometrical constriction [158]. In order to achieve thorough understanding, this theoretical treatment was supplemented by a novel experimental approach based on SQUID on tip (SOT) technique, where a nano-scale SQUID resides on the apex of a sharp tip [159], thus providing with high spatial resolution magnetic imaging [160, 161], reaching single-spin sensitivity [159] and enabling detection of sub-nanometer vortex displacements [143]. In this work the theoretical gTDGL framework succeeds in interpreting the first direct microscopic imaging of superfast vortices under current densities approaching the depairing limit. Results of the numerical simulations not only successfully reproduce the experimentally revealed vortex velocities up to tens of km/s, cascades of striking branching instabilities, and dynamic transitions in the moving vortex matter, but also surpass the limit of the current experiment and predict some more subtle states of the vortex matter. Comprehension of the fundamental vortex properties under these extreme, previously unexplored condi-

tions may have implication beyond academic curiosity as a source of low-power high-frequency electromagnetic waves.

4.1 Geometric constriction

The geometry of the specimen plays a crucial role in the overall interplay of present currents and the dynamics of the superconducting condensate. In Chapter 3 the behavior of the supercurrent density J resulting from the combination of screening and bias currents was discussed (Fig. 3.3). Since the superconducting bridge considered there was uniform and rectangular, anywhere along the specimen (but far away from the contacts where the current is injected) the transport current density profile taken across the sample remains the same and homogeneous. Homogeneity of the current density profile somewhat changes in the presence of magnetic field, which induces the circular Meissner-Ochsenfeld currents that break the symmetry in the profile of J measured across the bridge.

However, if the geometry of a specimen is no longer uniform, and a constriction is introduced so that a current flow experiences a bottleneck, subsequent change in the distribution of the current density dramatically modifies the behavior of the condensate. Since the continuity of the current flow cannot be violated, one concludes that as the current approaches closer to the bottleneck, its density must increase, with the peak in the narrowest point of the isthmus. This causes the current streamlines to crowd (therefore the name of the effect as *current crowding* [162]), as illustrated in Fig. 4.1. Current crowding is not exclusively related to superconductors, since it arises in every current-carrying system with inhomogeneous distribution of current density. It is usually regarded as detrimental effect, due to the limits it imposes in the efficiency of an electrical device, causing unwanted heating in the system and thus faster deterioration of the material [163].

One should bear in mind, however, that current crowding is not necessarily a problem. Especially in superconductors, current crowding translates into an inhomogeneous current density distribution, bound to lead to a plethora of novel effects. In particular, one can consider how the current lensing due to geometrical features affects the motion of the vortices. For this purpose, a sample of length $5.7 \mu\text{m}$ and width $5 \mu\text{m}$, with a central constriction of width $2.8 \mu\text{m}$ [see Fig. 4.2(a)] is simulated. The course of the simulations goes hand-in-hand with the experiment performed on the Pb film with thickness $d = 75 \text{ nm}$ and $T_c = 7.2 \text{ K}$, patterned into a $10 \mu\text{m}$ -wide microbridge with a central constriction of width $w = 5.7 \mu\text{m}$ [see Fig. 4.2 (b)]. Although the simulated specimen was taken twice smaller than the experimental one, it still represents a formidable numerical effort on a $\propto 10^3 \times 10^3$ two-dimensional spatial mesh. Full form of the model used for this theoretical

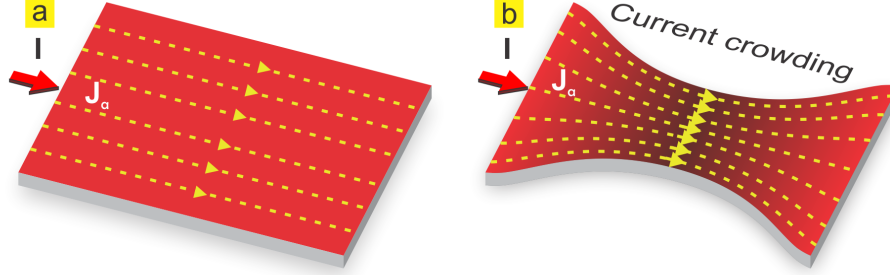


Figure 4.1: Current crowding. In (a) a rectangular superconducting bridge is shown, where the current I is applied from left to right side of the specimen. Since no constriction is imposed upon such geometry, current density J_a is homogeneous, with straight current streamlines, denoted with dashed yellow lines. However, if a constriction is made, as shown in (b), J_a attains inhomogeneous distribution, indicated by color gradient. Furthermore, current streamlines (yellow dashed lines) crowd inside the constriction, with highest density of crowding at the isthmus of the bridge.

treatment consists of Eqs. 2.42, 2.44, and 2.45 (with corresponding boundary conditions at SI and SN interfaces described in Section 2.2.3). The simulated system was treated in the high- κ regime. Because of this, the gauge $\nabla\mathbf{Q} = 0$ is selected for Eqs. 2.42 and 2.44. The parameter $\tilde{\Gamma}$ is set to 100 as an order of magnitude estimate for Pb, which was the material used in the experiment. The simulations were implemented using a finite-difference method, on a Cartesian map with a dense grid spacing of $0.1 \xi(0)$, where the geometry of the experimental specimen is reproduced based on the SEM image. The gTDGL simulations are taken in the limit of a model of superfast vortices driven by strong current densities $J \gg J_c$, for which the disorder is neglected. In what follows, the experimental data is presented first, in order to set the direction for the simulations.

In the selected geometry and perpendicular magnetic field, vortices only penetrate in the narrowest part of the bridge, which greatly reduces heating. Imaging of the local magnetic field B above the film surface at 4.2 K was done using a 228 nm diameter SOT incorporated into a scanning probe microscope. Figure 4.3(a)-(d) [where panel (a) corresponds to a zoom-in of the vortex region in a three-dimensional representation shown in the panel (b)] shows the distribution of vortices in the strip after field-cooling in $B_a = 2.7, 5.4,$ and 9.0 mT, which display a disordered vortex structure pinned by material defects. The observed vor-

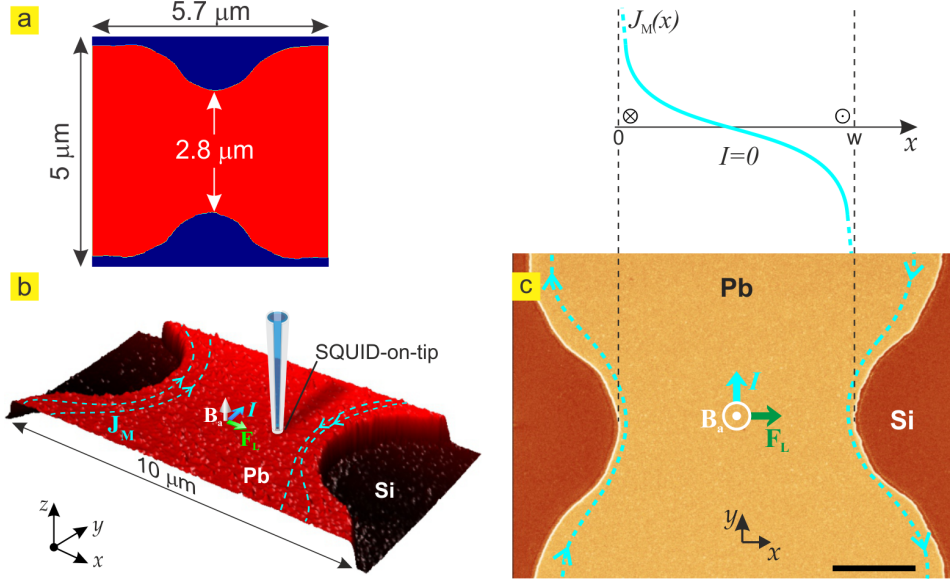


Figure 4.2: Overview of the system. (a) Simulated specimen of the size $5.7 \times 5 \mu\text{m}^2$ with a $2.8 \mu\text{m}$ wide constriction. (b) 3D representation of a $10 \times 5 \mu\text{m}^2$ AFM scan of the 75 nm -thick Pb film patterned into a $10 \mu\text{m}$ -wide strip with a $5.7 \mu\text{m}$ wide constriction. Indicated are the directions of the applied magnetic field B_a , current I , the driving Lorentz force acting on vortices F_L , and the screening current density J_M that is maximal along the edges. (c) SEM image of the same sample with corresponding distribution of the Meissner current $J_M(x)$ across the constriction, in absence of vortices and applied current. Scale bar is $2 \mu\text{m}$.

tex density is not uniform, as one may expect under field-cooling conditions, but has a dome-shaped profile with a maximum in the center surrounded by vortex-free bands along the edges. This is the result of the geometrical barrier [164], which is strikingly demonstrated here with single-vortex resolution. Unlike a bulk superconductor in which the screening currents flow in a narrow layer of thickness λ at the surface, in a thin film strip of width $0 < x < w$ and thickness $d \ll w$ in perpendicular field B_a , the shielding current density in the Meissner state $J_M(x) = B_a(w - 2x)/(d\mu_0\sqrt{x(w-x)})$ varies over much larger scales and decreases slowly as $J_M(x) \propto x^{-1/2}$ and $J_M(x) \propto -(w-x)^{-1/2}$ away from the left and right edges, respectively [Fig. 4.2(c)]. These currents push vortices into the central part of the strip, where they form a magnetic flux dome surrounded by vortex-free regions [164, 165, 166]. The vortex-free region shrinks with B_a as seen

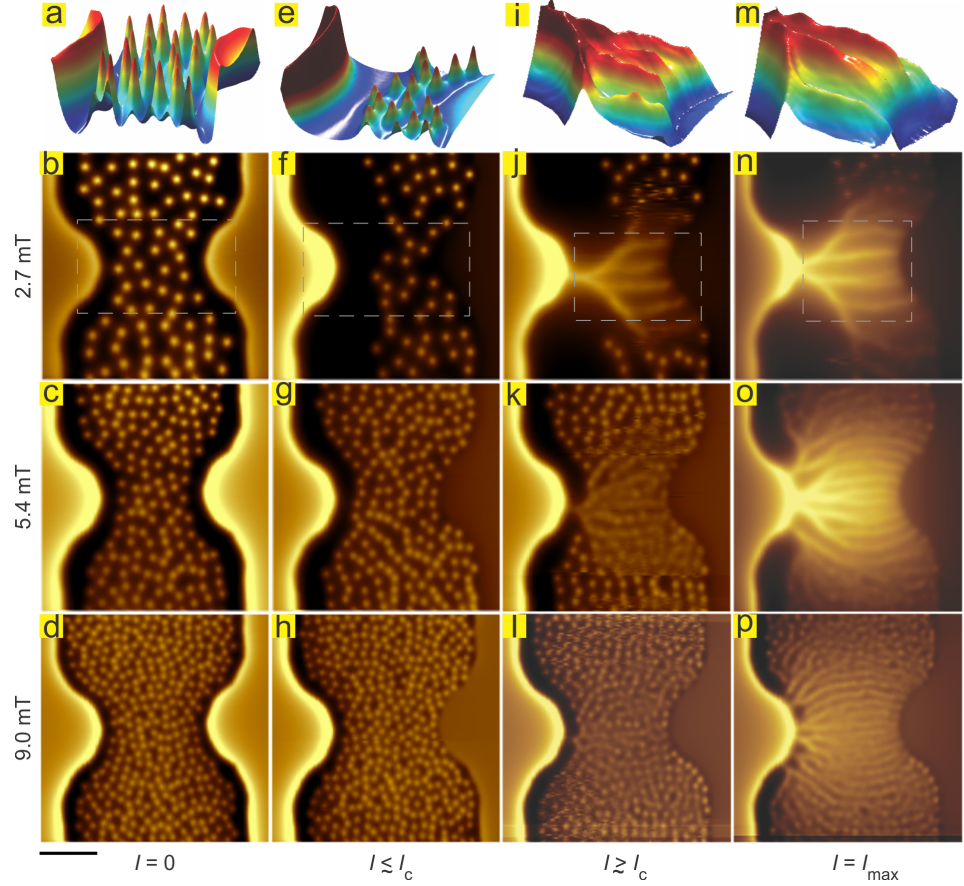


Figure 4.3: Magnetic imaging of stationary and fast moving vortices in Pb film at 4.2 K. (a)-(d) $B(x, y)$ SQUID-on-tip images of vortex configurations at $I = 0$ for different values of applied field $B_a = 2.7$ (a),(b); 5.4 (c); and 9.0 mT (d). (e)-(h) Images acquired at the verge of vortex motion at $I \lesssim I_c$, at $B_a = 2.7$ mT and $I = 16$ mA (e),(f); $B_a = 5.4$ mT, $I = 12.2$ mA (g); and $B_a = 9.0$ mT, $I = 6.0$ mA (h). (i)(l) Images of onset of vortex flow at $I \gtrsim I_c$ at $B_a = 2.7$ mT, $I = 18.9$ mA (i),(j); $B_a = 5.4$ mT, $I = 12.4$ mA (k); and $B_a = 9.0$ mT, $I = 9.1$ mA (l). (m)(p) Vortex flow patterns at the highest sustainable current with $B_a = 2.7$ mT, $I = 20.9$ mA (m),(n); $B_a = 5.4$ mT, $I = 16.2$ mA (o); and $B_a = 9.0$ mT, $I = 11.8$ mA (p). The color scale represents the out-of-plane field $B(x, y)$ with span of 1.8 (b), 2.5 (c), 3.0 (d), 2.9 (f), 3.2 (g), 3.4 (h), 3.1 (j), 3.4 (k), 3.4 (l), 3.1 (n), 3.6 (o), and 2.8 mT (p). All 2D images are $12 \times 12 \mu\text{m}^2$, with pixel size of 40 nm, and acquisition time is 240 s/image. The scale bar is $3 \mu\text{m}$. The top row shows zoomed-in 3D representation of $B(x, y)$ in the corresponding dashed areas marked in the second row.

in Fig. 4.3.

4.2 Vortex dynamics

The vortex-free regions observed in Fig. 4.3(a)-(d) have important effect on vortex dynamics in the presence of transport current. As the applied current I is increased, the sum of transport and shielding current densities $J(x)$ increases at the left edge ($x = 0$) and decreases at the right edge ($x = w$). As a result, the vortex dome shifts towards the right edge and the vortex-free region at the left edge expands [164, 167], as shown in Fig. 4.3(e)-(h) [where panel (e) is, once again, a 3D zoom-in of the vortex region shown in the panel (f)] for $I \leq I_c$. At the critical current $I = I_c$, the current density at the left edge approaches the depairing limit $J(x = 0) = J_{DP}$, and the flux dome reaches the right edge where $J(x)$ vanishes, so that the conditions for the onset of vortex motion are met. Here, the critical state, revealed with a single-vortex resolution, is dominated by the geometrical and extended surface barriers [164, 165, 166, 167, 168], and has two essential differences as compared to the continuum, pinning-dominated Bean critical state [169, 170]. First, unlike the Bean state in which the vortex density is highest at the penetration edge of the sample, Fig. 4.3(e)-(h) shows zero vortex density at the penetration side (left). Second and most importantly, in the Bean model at $I = I_c$ the current density equals J_c across the entire sample, whereas this thin film bridge is separated into two distinct regions clearly seen in Fig. 4.3(f). In the left vortex free region, J significantly exceeds the critical current density, $J_c < J < J_{DP}$, and no stationary vortices can be present [164, 165, 166, 167]. In the right half where $0 < J \leq J_c$ vortices are pinned. It is this unique inhomogeneous current state which allows one to investigate dynamics of superfast vortices driven by high local current densities, that cannot be done by global transport measurement in bulk samples. Here, the penetrating vortices can be subjected locally to extremely high current densities $J \gg J_c$ at the edges while the net current is only slightly above the critical, $I \geq I_c$ and heating is weak.

The stationary pattern of vortex channels shown in Fig. 4.3 seems counterintuitive since vortices repel each other and should therefore disperse over the film. Moreover, each stem grows into a tree through a series of subsequent bifurcations but the branches of different trees do not merge. In order to keep vortices within each channel a mechanism for dynamic alignment of fast moving vortices must be present. One such mechanism is that a rapidly moving vortex leaves behind a wake of reduced order parameter which attracts the following vortex. As a result, a confined chain of vortices in a self-induced channel of reduced superfluid density can be formed, as it was observed previously in numerical TDGL simulations [94, 132]

at high currents, $J \sim J_{DP}$, and $T \approx T_c$. As discussed below, this mechanism apparently becomes dominant at velocities substantially higher than those accessible in our experiment.

At this point the experimental results are complemented with the gTDGL simulations in the very limit of a model to address superfast vortices emerging at current densities above J_c . The simulated Cooper-pair density $|\chi(x, y)|^2$ shown in Fig. 4.4(a) reproduces the main features of the SOT images at $I \leq I_c$, namely vortices displaced to the right edge and a pronounced vortex-free region along the left edge. Notice that in the absence of disorder, the stationary vortices in Fig. 4.4(a) form an ordered structure within a smooth confining potential of the geometrical barrier, in contrast to Fig. 4.3(f) which shows a disordered vortex configuration determined by pinning in the right-hand side of the sample where $J < J_c$. At $I = I_c$ the calculated current density $J(x)$ shown in Fig. 4.4(b) reaches the depairing limit J_{DP} at the left edge of the constriction and vanishes at the opposite edge.

At $I > I_c$ vortices start penetrating through the left edge and move along a network of preferable paths forming a branching tree with an overall shape determined by the bridge geometry. The vortex chains are curved on larger scales [Fig. 4.4(e)] due to the lensing effect of the current distribution in the constriction, which tends to orient the vortex chains perpendicular to the local current $J(x, y)$. The calculated vortex flow pattern is similar to the SOT image in Fig. 4.3(j) and also exhibits the coexistence of moving and stationary vortices as observed in Fig. 4.3, where bulk pinning further hampers the motion of remote vortices. The Copper-pair density averaged over the simulated period of time shows a non-uniform distribution along the vortex channels [Fig. 4.4(c) and (e)], with distinct bright spots of reduced Cooper-pair density indicating that the vortex velocity varies non-monotonically along the channels. The bright spots describe the regions where the vortices slow down or even stop momentarily, giving rise to vortex crowding. Similar features of the magnetic field along the channels are observed in Fig. 4.3(i)-(p). Such vortex “traffic jams” can be understood as follows. A vortex penetrating from the left edge slows down as it moves along the channel since the driving current $J(x, y)$ decreases across the strip. The subsequent penetrating vortices move along the same trajectory, causing jamming in the regions where vortices slow down. The resulting mutual repulsion of vortices either pushes them further along the channel, where vortices speed up due to attraction to the right edge of the strip, or causes bifurcation of the channel into branches.

The fact that there is a single entry point for a vortex and several exit points implies that the penetration frequency per stem is higher than the exit frequency per channel. Figure 4.4(d),(f) shows snapshots of vortex motion at different applied currents, with arrows proportional to the instantaneous velocities of vortices right after penetration of a new vortex. One finds that the periodically-entering vor-

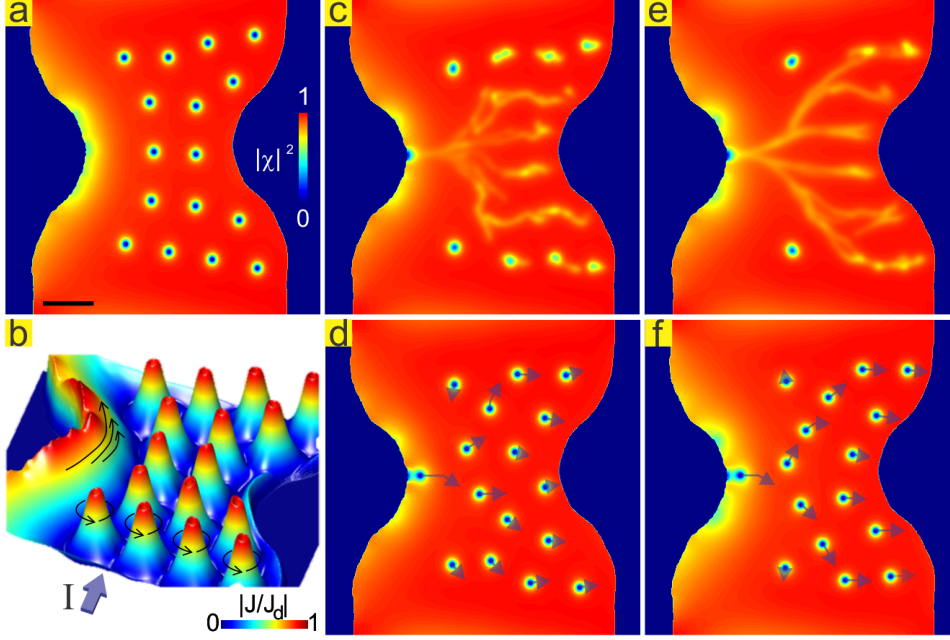


Figure 4.4: TDGL simulations of stationary and fast moving vortices at the experimentally accessible velocities. (a) Calculated Cooper-pair density $|\chi(x, y)|^2$ of a stationary vortex configuration at applied current density and magnetic field corresponding to the experimental conditions in Fig. 4.3(f). (b) Corresponding distribution of the supercurrent density $|J(x, y)/J_{DP}|$ in the sample showing edge currents in the constriction reaching J_{DP} at the verge of vortex penetration. The black arrows point to the local direction of the current. (c) Time-average of the Cooper-pair density over $5 \times 10^4 \tau_{GL}$ at $I = 1.05 I_c$, revealing branching vortex trajectories coexisting with adjacent stationary vortices. (d) Snapshot of moving vortices in (c) with arrows denoting the relative displacement of each vortex following an entry of a new vortex into the sample. (e),(f) Same as (c),(d) but at highest applied current before an additional stem is formed. The scale bar in a is $1 \mu\text{m}$.

tices take alternating routes at the bifurcation points due to interactions with other vortices, which slow down further after the bifurcation.

4.3 Extreme vortex velocity

The precise information about the velocity of individual vortices seen in Fig. 4.4(d), (f) can be obtained from the simulations, from the calculated evolution of the Cooper-pair density in time. For this purpose one must devise a particle-tracking algorithm, where the position of the vortex core center in an arbitrary geometry can be detected as a function of time (see Appendix A for additional explanation of the algorithm). Recording of the velocity was performed over a long time exposition [$5 \times 10^4 \tau_{GL}(0)$], which guaranteed that multiple vortices pass through the same stem ($N_{vortices} \approx 100$), and thus provide enough statistical data. These results are presented in Fig. 4.5(a).

In the experiment, the velocity was obtained from simultaneous measurement of the voltage-current characteristics and state of the art SOT imaging. At a given magnetic field, the onset of finite voltage coincides with the appearance of the first vortex channel as the current exceeds a critical value I_c that decreases with the magnetic field. Figure 4.5(b) shows the measured voltage drop on the bridge (left axis) along with the number of vortex stems n observed by SOT imaging (right axis) vs. current at 2.7 mT. The appearance of each subsequent stem in Fig. 4.5(b) matches a step in the voltage and a change in the differential resistance dU/dI . Linear fits to the data (dashed) show a roughly twofold increase in dU/dI , from 13.9 m Ω for one stem to 25.1 m Ω for two stems. For a given number of stems n , the vortex penetration frequency f in each stem is given by the Faraday law, $f = U/n\Phi_0$. Figure 4.5(c) shows that the penetration frequency jumps from zero to 3.7 GHz at the formation of the first stem. As the applied current increases, f rises to 15.3 GHz and then drops abruptly to 9.1 GHz upon the formation of the second stem.

Vortex conservation requires that $f = U/n\Phi_0$ remains constant along the stem up to the bifurcation point, so that the vortex velocity along the stem is given by $v(x) = fa(x)$, where $a(x)$ is the local average intervortex distance. The average field along a chain of vortices separated by $a(x)$ is given by $B_{av} = \int_{-\infty}^{\infty} B_v(u)du/a(x)$, where $B_v(u)$ is the magnetic field profile of an individual vortex. By measuring $B_{av}(x)$ along the stem and $B_v(x)$ across an isolated stationary vortex, one thus obtains $a(x)$ along a single stem, which is presented in Fig. 4.5(d). Taking the penetration rate f from Fig. 4.5(c), one obtains the corresponding vortex velocity $v(x)$ as shown in Fig. 4.5(e). The remarkable findings seen here, both in the theoretical and experimental data, are the extreme values of

vortex velocities of 10-20 km/s, much larger than the depairing superfluid velocity $v_{DP} = 0.4$ km/s estimated above.

These very high velocities measured in the experiment are attained at $0.5 < x < 1.5 \mu\text{m}$ where the estimated current density is between $0.2J_{DP}$ and $0.6J_{DP}$. In the region $x < 0.5 \mu\text{m}$ at the film edge, where even higher currents and vortex velocities are possible, the utilized SOT technique cannot resolve the actual $v(x)$ as the vortex field $Bv(x)$ close to the edge becomes partly extinguished by the image vortex imposed by the boundary conditions [171]. In the simulations the region where the velocity is measured is $0.25 < x < 1.5 \mu\text{m}$, due to the fact that already at $x = 0.25 \mu\text{m}$ vortex core becomes unambiguously distinguishable. The average vortex velocity in the stem can be estimated independently of the above analysis by assuming the distance between the moving vortices to be of the order of their mean stationary distance $a = 1 \mu\text{m}$ from Fig. 4.3b (which is close to $a = (2\Phi_0/\sqrt{3}B_a)^{1/2} = 0.94 \mu\text{m}$) and taking the highest frequency of 15 GHz from Fig. 4.5(c). This yields $v = fa \approx 15$ km/s which is consistent with the measured vortex velocities in both Fig. 4.5(a) and (d).

The mesoscopic chains of single vortices moving along stationary channels under a *dc* drive are fundamentally different from transient dendritic flux avalanches observed by magneto-optical imaging in increasing magnetic fields [172, 173, 174, 175, 176]. Those macroscopic filaments of magnetic flux focused in regions overheated above T_c can propagate with velocities as high as 150 km/s in $\text{YBa}_2\text{Cu}_3\text{O}_7$ films at 10 K [174] or 360 km/s in $\text{YNi}_2\text{B}_2\text{C}$ at 4.6 K [175]. Such thermomagnetic avalanches are driven not by the motion of single vortices but by strong inductive overheating caused by the fast-propagating stray electromagnetic fields outside the film [176], unlike the correlated flow of quantized vortices revealed by here presented SOT imaging under nearly isothermal conditions. The mechanisms of channeling and branching of fast vortices in our viscosity-dominated regime at $J \gg J_c$ are also different from the disorder-driven formation of networks of slower vortices near the depinning transition observed in numerical simulations [177, 178].

Using the current density $J(x)$ obtained from the simulations and $v(x)$ extracted from the experimental data, one can obtain the vortex viscous drag coefficient $\eta = 2.6 \times 10^{-8} \text{ kgm}^{-1}\text{s}^{-1}$. This value of η is of the order of $\eta_0 = \Phi_0^2\sigma_n/2\pi\xi^2 = 10^{-8} \text{ kgm}^{-1}\text{s}^{-1}$ of the Bardeen-Stephen model, which indicates no excessive changes in the structure of the Abrikosov vortex core even at velocities of the order of 10 km/s. This conclusion is corroborated by the gTDGL simulations in Fig. 4.5, which reproduce the channel bifurcations due to vortex repulsion and the variation of the magnetic field along the channels due to variations in vortex velocity induced by disorder and vortex-vortex interactions. The totality of the presented SOT and gTDGL results indicate that vortices maintain their integrity as stable topological defects even at the observed extreme veloci-

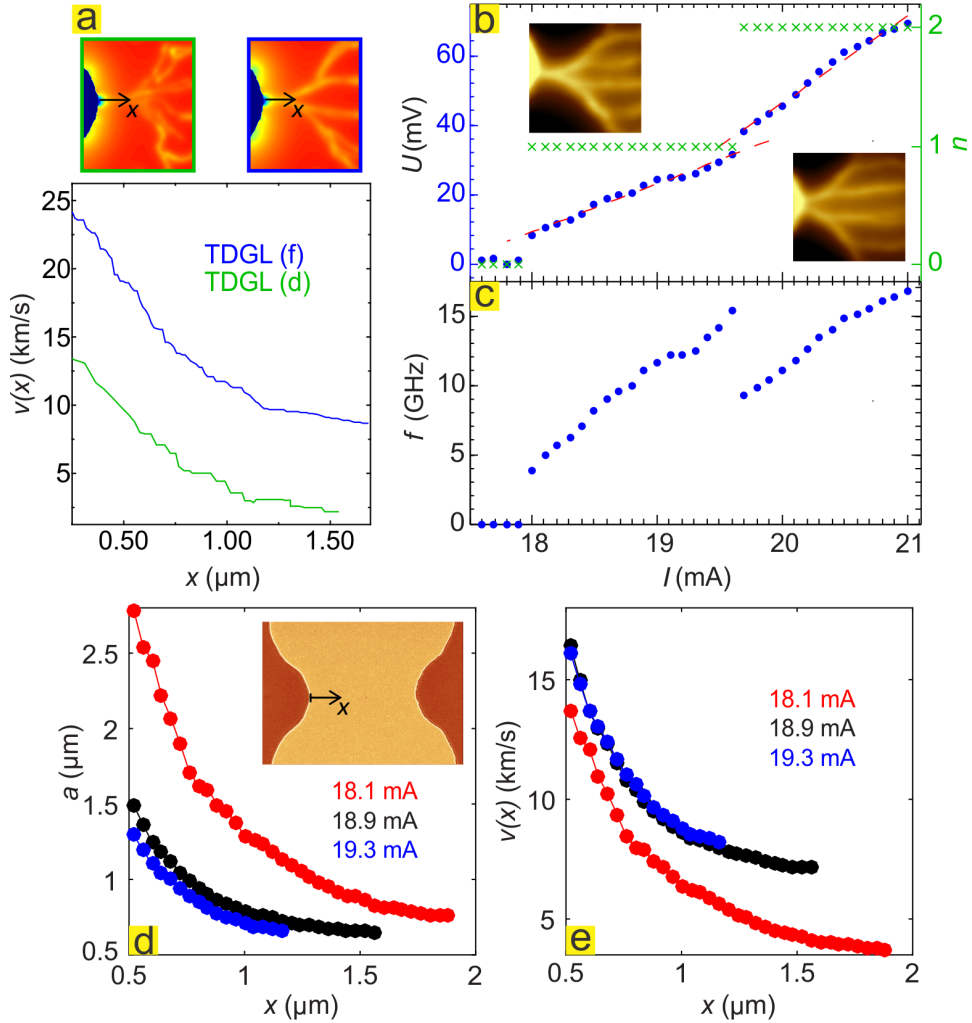


Figure 4.5: Ultrafast vortex velocity. (a) Vortex velocity from the simulations, corresponding to Fig. 4.4(d) (green line) and (f) (blue line). Vortex velocity is measured from the point $x = 0.25 \mu\text{m}$. Insets of the time-averaged Cooper-pair density are provided with marked x axis to indicate along which line the vortex velocity is measured. (b) Voltage across the bridge (blue) and the number of vortex stems n (green) as a function of current at 2.7 mT. The red dashed lines are linear fits with $dU/dI = 13.9 \text{ m}\Omega$ in the single stem and $25.1 \text{ m}\Omega$ in double stem regions. The insets show zoomed-in SOT images of single stem and double stem vortex flow. (c) Vortex penetration rate f per stem vs. current I . (d) Spacing between successive vortices $a(x)$ along the stem from $x = 0.5 \mu\text{m}$ up to the bifurcation point at 2.7 mT at various indicated currents. Inset: SEM image of the sample with marked x axis. (e) Corresponding vortex velocities $v(x)$ along the stem, from $x = 0.5 \mu\text{m}$ up to the bifurcation point. 88

ties, i.e. the magnetic field of a moving vortex does not deviate substantially from that of a stationary Abrikosov vortex. In particular, one observes no evidence of the transition of Abrikosov vortices into Josephson-like phase slip lines [179, 180] extending across the bridge.

4.4 Dynamic vortex phases

Within the framework of gTDGL theory one can analyze even faster vortices, beyond the experimentally accessible range of parameters, for which a significant change in the internal vortex structure is expected. For instance, nonequilibrium effects can give rise to a velocity dependence of $\eta(v)$ and to the Larkin-Ovchinnikov (LO) instability caused by diffusion of quasi-particles between the vortex cores [136]. The LO instability results in jumps in the vortex velocity above $J > J_{LO} \approx \eta_0 v_0 / 2\Phi_0$ for which the force balance $\Phi_0 J = \eta(v)v$ at $v > v_0$ is not satisfied because $\eta(v) = \eta_0 / (1 + v^2/v_0^2)$ decreases with v [136]. The LO or overheating instabilities [74, 181], have been observed on various superconductors with v_0 ranging from 1 to 10 km/s [147, 148, 149].

Presented gTDGL calculations at twice higher current and field as compared to those shown in Fig. 4.5 reveal three different types of vortices described in Fig. 4.6. Far from the constriction region, J is lower and the moving vortices [red dot in Fig. 4.6(a)] have a regular, nearly isotropic shape with no wake of reduced order parameter behind them. Closer to the constriction, a chain of vortices [marked by a black dot in Fig. 4.6(a)] is confined in a channel of reduced order parameter. These faster-moving vortices are slipstreaming one another because their velocity v exceeds a/τ_χ , where $\tau_\chi = \pi\hbar\sqrt{1 + \tilde{\Gamma}^2|\chi|^2/8k_B(T_c - T)}$ is a recovery time of the superconducting order parameter in the wake of the moving vortex. The gTDGL simulations show that these vortices, moving in channels, have elongated cores along the direction of motion, and their drag coefficient can be approximated by the LO dependence $\eta_{LO}(v) = \eta_0 / (1 + v^2/v_0^2) + \eta_i$ with $\eta_i \approx 0.25\eta_0$ and $v_0 \approx \xi/\tau_\chi \approx 20$ km/s for the given sample parameters, even though the slipstreaming is not based on the quasi-particle tunneling at the base of the LO effect. These anisotropic slip-streamed vortices can undergo a kinematic transition to conventional vortices upon stem bifurcation which leads to additional vortex slowdown, as marked by a blue dot in Fig. 4.6(a).

The most radical change in the structure of moving vortices occurs in the narrowest part of the constriction, where J is maximal. Here, a channel with a significant reduction of the mean superfluid density appears, in which ultrafast vortices [green dot in Fig. 4.6(a)] are moving with velocities that are 35 times higher than the speed of slipstreamed vortices, as shown in Fig. 4.6(c). The ultrafast vortices in

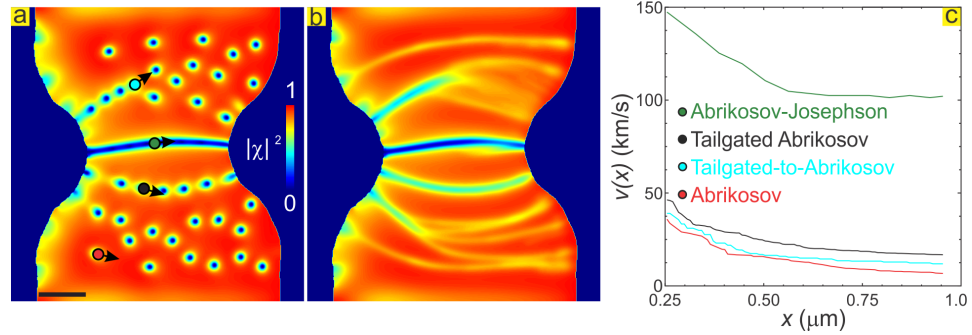


Figure 4.6: Different morphologies of ultra-fast vortices at velocities significantly higher than observed in the experiment. (a),(b) A snapshot (a) and time-averaged Cooper-pair density $|\chi(x, y)|^2$ (b) as in Fig. 4.4, but for twice higher applied field and twice the current. Three vortex phases are found with distinctly different core structure, level of quasi-particle tailgating, velocities and resulting kinematic trajectories, namely the extremely fast Abrikosov-Josephson vortices (marked by green dot), the ultrafast slipstreamed vortices (black dot), and conventional Abrikosov moving vortices (red dot). (c) Spatial profiles of vortex velocities $v(x)$ for the three main vortex phases, and for one detected branch of vortices going through an in-motion transition [dynamic transition from slipstreamed vortices to conventional Abrikosov vortices, identified by a blue dot in (a)]. The scale bar in (a) is $1 \mu\text{m}$.

the central channel can be regarded as mixed Abrikosov-Josephson vortices similar to vortices at grain boundaries [182, 183], in high-critical-current planar junctions [184], or S/S'/S weak links [185]. The gTDGL results shown in Fig. 4.6(c) suggest that Josephson-like vortices in these channels can move with velocities as high as $\sim 100 \text{ km/s}$, because the viscous drag coefficient $\eta(v)$ in the channel is reduced to just a few percent of η_0 due to strongly elongated and overlapping vortex cores. Spatial modulation of the order parameter between these vortices is rather weak and effectively the channel behaves as a self-induced Josephson junction, which appears without material's weak link. Similar flux channels in thin films were previously interpreted in terms of phase-slip lines [179, 180]. In the case of strong suppression of the order parameter and weak repulsion of Josephson vortices which extend over lengths exceeding $2\lambda^2/d$, the channel does not bifurcate as shown in Fig. 4.6(a) and the magnetic field along the channel is nearly uniform. This feature of Josephson-like vortices appears inconsistent with the SOT observations of vortex channels which always bifurcate and show noticeable variations of the mag-

netic field along the channels. The SOT results thus indicate an essential effect of intervortex repulsions and weak suppression of the order parameter along the channel, consistent with the dynamics of Abrikosov vortices shown in Fig. 4.5.

Another interesting SOT observation shown in Fig. 4.3(n)–(p) is the nucleation of additional stems of vortices as current increases. This effect can be understood as follows. The first stem appears at $I = I_c$ as the local current density J at the edge of the constriction reaches J_{DP} . As I increases above I_c , vortices start penetrating at the narrowest part of the constriction in such a way that a counterflow of circulating currents produced by a chain of vortices moving in the central channel maintains the current density $J(y) < J_{DP}$ everywhere along the curved edge of the film except for the vortex entry point. This condition defines the spacing $a(I)$ between the vortices in the chain. However, above a certain current $I > I_1$, a single chain of vortices can no longer maintain $J(y) < J_{DP}$ along the rest of the constriction edge, leading to nucleation of an additional stem as seen in Fig. 4.3(n). In addition, the edge roughness can affect the location and the dynamics of stem evolution, favoring stem nucleation at points of local edge protuberances. Actual details of the edge shape of experimental sample derived from the SEM image have been incorporated into the gTDGL simulations, resulting in the observed asymmetry between the vortex channels in the upper and lower parts of Fig. 4.6(a),(b).

As the magnetic field increases, the width of the vortex-free region near the edges and vortex velocities decrease. Figure 4.3 shows how dissipative vortex structures evolve from a few mesoscopic chains and branches sustaining extremely high vortex velocities at low field [Fig. 4.3(j), (n)] to a multi-chain structure with much lower vortex velocities at higher fields [Fig. 4.3(l), (p)]. Remarkably, the vortex channeling is preserved even at high fields that would usually be associated with the conventional flux flow of the Abrikosov lattice. The dynamic structure revealed in Fig. 4.3(p), in which vortices move in parallel channels, appears consistent with the predictions of the moving Bragg glass theory [186], thus providing microscopic evidence with a single vortex resolution for the existence of this dynamic phase.

In conclusion, this work uncovers the rich physics of ultrafast vortices in superconducting films and offers a broad outlook for further experimental and theoretical investigations. By proper sample design and improved heat removal it should be possible to reach even higher velocities for investigation of non-equilibrium instabilities [74, 136, 147, 148, 181, 187]. Our detection of vortices moving at velocities of up to 20 km/s, significantly faster than previously reported, strengthens the recently renewed appeal of vortex-based cryogenic electronics [188]. The observed frequencies of penetration of vortices in excess of 10 GHz may be pushed to the much technologically desired THz gap in the case of dynamic Abrikosov-

Josephson vortex phases. This work shows that the SOT technique can address some outstanding problems of nonequilibrium superconductivity and ultrafast vortices in type II superconductors as well as dynamics of the intermediate state in type I superconductors on the nanoscale. These issues can also be essential for further development of superconducting electronics, opening new challenges for theories and experiments in the yet unexplored range of very high electromagnetic fields and currents.

The results of this Chapter were published in Ref. [158].

Chapter 5

Vortex matter under a dynamic pinning potential

As stated in previous Chapters, a type-II superconductor can allow penetration of external magnetic field in terms of quantized filaments of magnetic flux inside which superconductivity is locally depleted, namely vortices. The whirl of superconducting current around this topological defect interacts with an applied electric current causing the motion of vortices in a manner analogous to the Lorentz force [189]. Unfortunately, this dissipative motion results in progressive Joule heating and quenching of superconductivity.

Over the past decades, the main strategy to prevent (or at least decrease) the described energy dissipation was to artificially anchor the vortices, using specifically designed arrays of pinning centers. In that respect, many alternatives were employed - e.g. pinning centers produced by irradiation with heavy ions [96], chemically grown defects [98], nanostructured perforations [99], or permanent nanomagnets [100]. Regardless of the exact nature of pinning, the common idea has always been to create a spatial inhomogeneity in the superconducting condensate, i.e. locally suppress superconductivity on a scale comparable to the size of the vortex core. If then a periodic arrangement of the pinning centers is made, the superconductor can sustain a particularly high critical current at so-called matching fields, where the ideally homogeneous lattice of vortices is interlocked with the periodic lattice of the pinning centers [190, 191]. Properties of such periodical pinning landscapes have been extensively investigated in the literature, with particular attention on the appearance of resonant features in the presence of the *ac* force [192, 193, 194, 195, 196].

Previously, all used pinning strategies involved an energy landscape imposed on permanent basis - i.e. neither its intensity nor its spatial distribution could be

further modified. The question arises - how would a dynamic pinning landscape affect the superconducting properties? Clearly, the added degrees of freedom in terms of frequency and strength of the pinning, as well as its possible mobility and speed, next to its spatial geometry, could trigger new phenomena unattainable with static pinning. Such a study is not only interesting but also timely, since dynamic and highly controllable pinning potential can now be achieved, for instance, by inhomogeneous light distribution (created by arrays of lasers [197] or plasmonic nanostructures [198, 199, 200]) or by intensity modulation of the laser light.

Since several different phases of a resistive state of superconducting thin films in an external magnetic field and applied transport current can arise due to dissipative motion of vortices [201, 202], one finds that it is paramount to study more carefully the dynamic phenomena in type II superconductors. While the Abrikosov vortices retain their cylindrical core [see, for example, Fig. 4.4(d),(f)], it has been theoretically shown that vortices traveling at high velocities exhibit core deformation and tailgating of quasi-particles (for recent studies of the behavior of vortex core quasi-particles under applied current see Refs. [203, 204]), due to which moving vortices tend to align and connect to the wake of the preceding vortex [94]. As seen in Fig. 4.6, several types of elongated vortices may exist, where most notorious are the vortices with extreme core elongation (where the full channel-like suppression of the order parameter arises), often referred to as Abrikosov-Josephson, resembling the ones found at step-edges and grain boundaries [180, 184, 205, 206, 207]. Their further acceleration in increasing current leads to the formation of a phase-slip [179], a line of fully suppressed superconductivity across which the phase of the superconducting order parameter changes by 2π , and along which phase singularities move with extremely high velocity. Those coreless yet moving singularities are often referred to as Josephson vortices (in analogy to those in S-N-S junctions [208, 209, 210]).

Real-time observations of the vortex motion are notoriously difficult to achieve, because vortex velocity in the condensate largely exceeds the sweeping rate in most of the scanning probe techniques and the time between two consecutive frames in snapshot techniques [174, 211]. Estimates of the average vortex velocity reported in literature have been mainly obtained from transport measurements [132, 212, 213]. Relative vortex velocity, and vortex-vortex interaction within the dynamic regime have also been studied in the past, using the Corbino setup [135]. Even the dispersion of the vortex velocities has been measured [214]. All of the obtained results concurred that the speed of the Abrikosov vortices can be as high as several km/s, while the velocity of Josephson vortices can rise to 100 km/s [215]. In Chapter 4 it was shown that Abrikosov vortices in Pb can achieve the velocity of 10-20 km/s, even though they could not be directly seen in experiment (but rather their averaged trajectory).

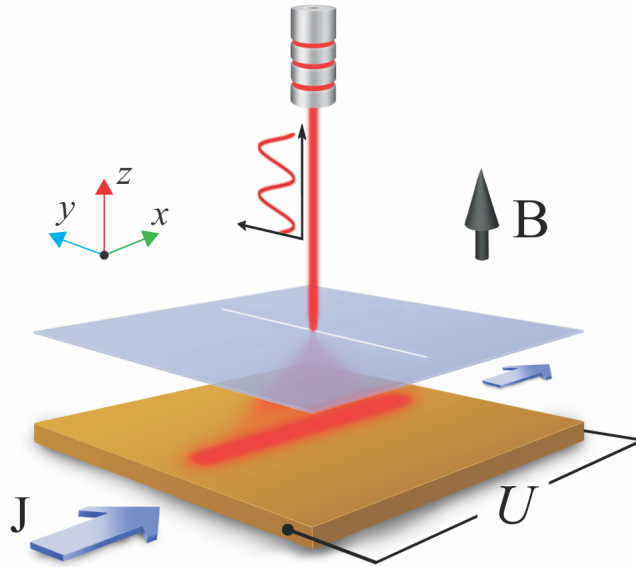


Figure 5.1: Possible experimental setup corresponding for dynamic pinning, by using a laser light at the far field passing through a metallic mask to create time-dependent and spatially modulated depletion of the superconducting condensate.

The interaction of light with superconductivity has been of interest for decades, and it is now very well established that in most cases it leads to local heating and depletion of the superconducting condensate (a feature employed in superconducting single-photon detectors [216, 217, 218, 219, 220]), as illustrated in Fig. 5.1, though at frequencies close to the superconducting gap light can interfere with the recombination of Cooper-pairs and even enhance superconductivity [221]. Interaction of laser light with vortices has also been studied, to form the base of the modern imaging technique of low-temperature laser scanning microscopy (LTLSM) [128]. For example, mode-locked solid-state lasers can emit pulse repetition rates between 50 MHz and a few gigahertz [222] (in extreme cases above 100 GHz), and can modulate the superconducting condensate by localized heating. Note that in order to confine light to few tens of nm (which is comparable to the radius of the vortex core in many type II superconductors), one can envisage to use nanoscale metallic waveguides which transform the long wavelength incoming light into surface plasmon polaritons able to be focused down to the required scales [223]. However,

light as a source of a time-dependent pinning potential in superconductors has not been explored to date, although it has been utilized for dynamic optical scanning in Bose-Einstein condensates (BECs) [224], and for flashing ratchets in colloidal systems [225, 226, 227, 228, 229, 230, 231]. On the other hand, there are other ways to achieve the time-periodic potential. Moreover, a submicron nano-heating source has also been recently demonstrated [232], using a single Ag nanowire as resistive nano-heater, where possible bandwidth can be tuned by the pulsed current. Alternatively, one can envisage the use of low-temperature scanning electron microscopy [233], operating down to 4 K, where electron beam sizes of few tens of nm are equipped with fast electrostatic beam blankers with rising time of sub-ns and repetition rate of 300 MHz.

In this Chapter, detailed study of the interaction between the temporally periodic thermal potential and superconducting condensate is presented. The Chapter consists of two parts, where in the first part fundamental effects of the oscillating thermal potential on the behavior of the resistive state of the type II superconductors are studied, while in the second part the novel velocimetry technique based on the latter effects is presented and discussed.

5.1 Stroboscopic resonances

In this Section, the fundamental consequences of a temporally periodic pinning landscape imprinted on a superconducting condensate are investigated. Here, as a simple but exemplary case, a superconducting stripe, of the size $L \times W = 300 \times 100$ nm², with the parameters of NbN is considered [$\xi(0) = 4.2$ nm, $T_c = 12.7$ K, with bath temperature $T_0 = 0.9T_c$, and the normal state conductivity $\sigma_n = 4241$ S/cm [234]], with longitudinally applied current, in magnetic field perpendicular to its plane, and with an oscillating depletion line. The oscillating depletion line has width of $2\xi = 26.5$ nm [where $\xi = \xi(0)/\sqrt{1 - T_0/T_c}$ is the coherence length at bath temperature] and it is positioned along the middle of the sample, perpendicular to direction of the motion of the vortices, as shown in Fig. 5.2. The sample is periodic in L , so the appropriate boundary conditions for order parameter [$\chi(x = 0) = \chi(x = L)$] and vector potential [$\mathbf{Q}(x = 0) = \mathbf{Q}(x = L)$] must be instated in the corresponding direction. The transport current was introduced via the boundary condition for the vector potential in the y direction: $\tilde{\nabla} \times \mathbf{Q}|_z(y = 0, W) = \tilde{B} \pm \tilde{B}_I$, where $\tilde{B}_I = I \cdot \text{const}$ is the magnetic field induced by the current I . The focus is placed on the range of currents and fields where vortex motion induces a resistive state [235, 236, 237], and exhibits the rich emergent phenomena as a function of the frequency of the pinning landscape. Theoretical model used for this analysis consists of Eqs. 2.42 and 2.43, with the zero electrostatic potential gauge. The

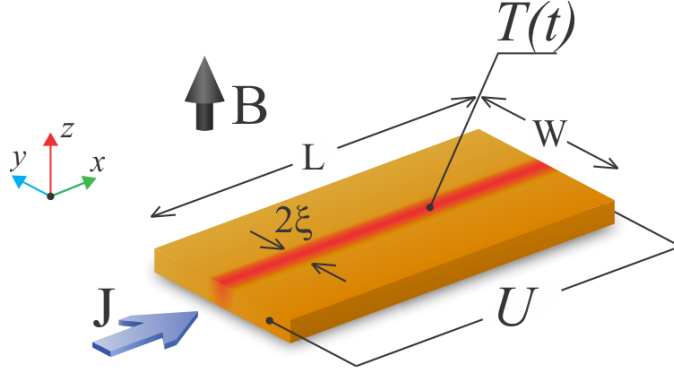


Figure 5.2: Layout of the studied system. A superconducting stripe of width W with a central, time-dependent, pinning line of width comparable to the vortex size (ξ is the superconducting coherence length at a given temperature), and a 4-point probe-bridge to apply dc current (with density J), and measure voltage (U , at contacts separated by distance L). A depletion region is simulated as sinusoidally oscillating local heating up to the critical temperature T_c and back to working temperature, with period τ .

system described in this part of the Chapter corresponds to the situation where heat removal is very efficient due to the negligible heat diffusion within the sample, so the Eq. 2.45 is omitted from calculations. Furthermore, the overheating due to the temporally periodic thermal potential is included directly into Eq. 2.42 through function f , which is defined as

$$f(t, \mathbf{r}) = \begin{cases} 1 - \frac{T_0}{T_c}, & \text{out of depletion region,} \\ \frac{1}{2} \left(1 - \frac{T_0}{T_c}\right) \left(1 - \cos \frac{2\pi t}{\tau}\right), & \text{in depletion region,} \end{cases} \quad (5.1)$$

while the other thermal kernel is taken as $g = 1$ due to the fact that bath temperature is close to T_c . Quantity τ in Eq. 5.1 represents the period of the oscillations.

What phenomenology should one expect from the frequency dependence of the pinning landscape? Clearly, if the change between ON and OFF state of the pinning potential (further denoted as period τ) is faster than the characteristic relaxation time of the superconducting order parameter (i.e. $\tau \leq \tau_{GL}$, where $\tau_{GL} = \tau_{GL}(0)/(1 - T_0/T_c)$ is the Ginzburg-Landau relaxation time at T_0), then a recovery of the superconducting condensate is not possible - leading to permanent depletion and effectively static pinning. When the frequency of pinning oscillations

is below this ultrafast limit, but still faster than the vortex velocity (or in terms of the characteristic time scales, $\tau_{GL} \ll \tau < \tau_{cross}$, where τ_{cross} is the average time needed for a vortex to cross the pinning-free sample at certain magnetic field and applied current), there will be a noticeable change. Even though superconductivity has sufficient time to fully recover over one pinning cycle, the duration of the ON state is still not long enough to fully trap the moving vortex, hence the interaction between the flux quanta and the dynamic pinning can be considered weak (this regime is referred to as ‘vortex tapping’). At further decreased pinning frequencies, where τ becomes comparable with τ_{cross} , one reaches the ‘vortex pinning’ regime where the motion of the flux quanta is greatly influenced by the variations in the pinning landscape. This is the richest part of the frequency phase diagram, and the main focus of this study. Finally, in the limit where $\tau \rightarrow \infty$, the system becomes a simple alternation of two long-lasting states: the one where the pinning is OFF and the structure behaves as the pinning-free sample, and the second one with the pinning ON behaving as the static case extensively studied in literature.

In what follows, the regimes where pinning landscape and moving vortices interact most are discussed in detail. In Fig. 5.3, the diagram of the calculated voltage on the sample as a function of the period of the pinning oscillations τ , varied between 10^3 and $10^4 \tau_{GL}(0)$ is presented. The voltage can be obtained from the vector potential by using the relation $U = \frac{\partial}{\partial t} \int \mathbf{Q} d\mathbf{l}$, where the voltage represents a measure of dissipation for the given current, hence is intimately related to the vortex motion. Fig. 5.3(a) reveals clear indications of resonant behavior, namely, all $U(\tau)$ characteristics show well-defined occurrence of extendedly stable states perfectly and continuously linking the curves for different applied currents. This resonant behavior at different currents is highlighted by black lines in Fig. 5.3(a), and follows $1/\tau$ dependence as evidenced in Fig. 5.3(b). To see the origin of this behavior, we chose one point on the curve [for $\tau = 3 \times 10^3 \tau_{GL}(0)$ and applied current density $J = 2.1 \times 10^{-3} J_{GL}(0)$] and monitored the vortex motion $y(\hat{t})$ and voltage as a function of time [shown in Fig. 5.4(a),(b)]. For the chosen length of the simulation region L and the considered magnetic field, we actually had $N_v = 6$ parallel vortices simultaneously moving in a single row, as shown in the contour-plots of the Cooper-pair density in the right panel of Fig. 5.4. There, points 1-5 are used to denote one period of the vortex dynamics, marking the characteristic instances: the entry of a new vortex row (beginning of the cycle - 1), the exit of a single row of the previously present vortices (2), the trapping of the vortex row in the depletion region, together with remaining preexisting vortices (3), the depinning of the second row of the previously present vortices from the depletion region (4), and finally, the exit of the last preexisting vortices (5). As one can observe in Fig. 5.4, at the chosen resonance the frequency of pinning is exactly synchronized with the vortex motion - the period of the pinning matches exactly the period of the

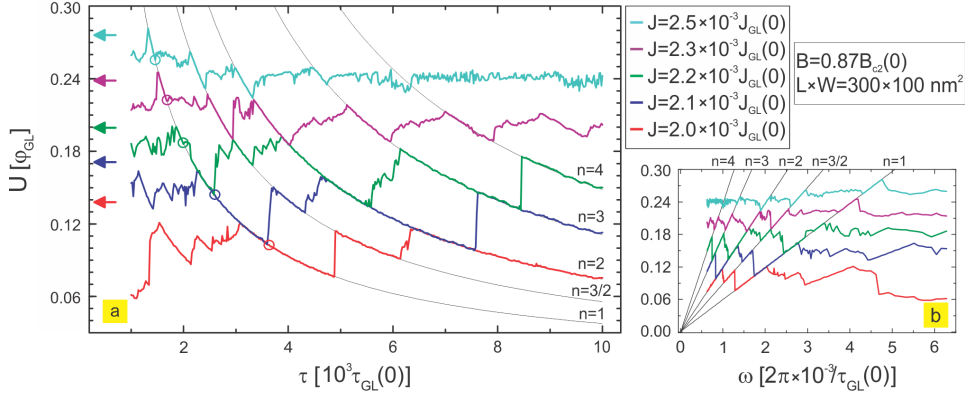


Figure 5.3: Stroboscopic voltage resonances. (a) Voltage is plotted versus the period τ of the oscillating pinning landscape shown in Fig. 5.2, for a given sample size and magnetic field, and for five different values of the applied current. Arrows indicate the voltage in absence of pinning for the corresponding current, while dots indicate the transition between two dynamic regimes: vortex tapping at low τ and vortex pinning at high τ . The black lines highlight the resonances where $U \propto \frac{1}{\tau}$ as further shown in (b) where voltage is plotted against pinning frequency $\omega = 2\pi/\tau$, and clearly shows a linear dependence when resonance conditions are met.

measured voltage [see Fig. 5.4(b)], and during one period effectively one vortex row crosses the sample from one edge to another, while one vortex row remains pinned all the time [see Fig. 5.4(a)], or in words of Faraday's law - the voltage corresponds to the change of magnetic flux over period τ of exactly one flux quantum, multiplied by N_v .

Therefore, a temporal matching effect is revealed here, which is in essence stroboscopic, i.e. caused by synchronization between pinning and vortex dynamics. Multiple resonances are possible, depending on the number of vortices that participate in the characteristic dynamics during one period of the pinning oscillations (further denoted by n). Every integer number n leaves the resonant fingerprint on the $U(\tau)$ characteristics, but also fractional resonances are possible - for example for $n = 3/2$, where 3 magnetic flux quanta (Φ_0) cross the sample over a period of 2τ (per vortex row). At all resonances, the voltage exhibits $U \propto 1/\tau$ behavior (specifically $U_n = nN_v\Phi_0/\tau$, i.e. $U_n = 2\pi nN_v/\tau = nU_0$ in dimensionless units), hence it has linear dependence on pinning frequency, as shown directly in Fig. 5.3(b). Please note that in realistic experimental conditions, and significantly longer samples than the one in our simulation, the number N_v of simultaneously

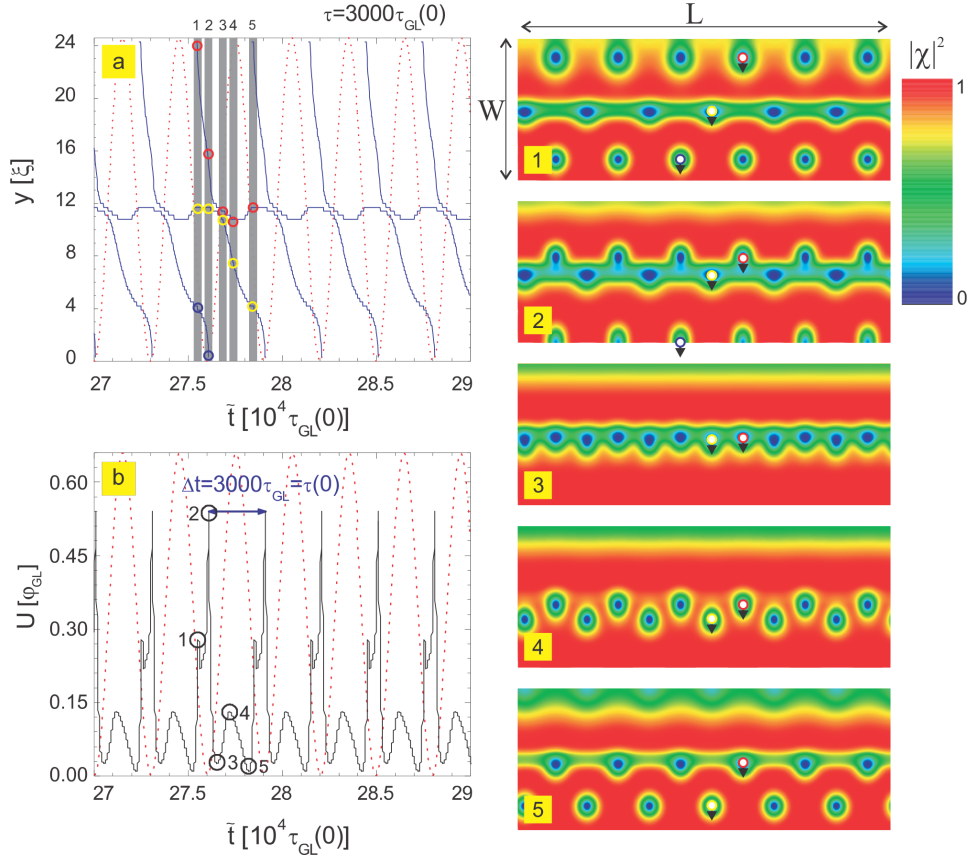


Figure 5.4: Vortex trajectory and temporal voltage response at the first resonance. The location of the vortex core traveling across the sample as a function of time (a), and the corresponding change in the voltage (b), for one example of the system at the first resonance (in particular, for $2.1 \times 10^{-3} J_{GL}(0)$ and $\tau = 3000 \tau_{GL}(0)$, see Fig. 5.3). Dotted lines show the profile of the time-dependent pinning potential, where minima of the dotted lines represent the ON state of the pinning, and the maxima represent the OFF state. Points 1-5 denote one cycle of the vortex dynamics, marking the instances when the new vortex row enters (cycle begins) (1), some of the the previously existing vortices exit (2), the vortex row is trapped in the depletion region (3), the remaining preexisting vortices are depinned from the depletion region (4), and the remaining previously existing vortices exit the sample (5). Corresponding snapshots of the Cooper-pair density for states 1-5 are given in the right panel, showing rows containing six vortices in parallel and simultaneous motion. The resulting periodicity of the voltage during vortex motion exactly matches the period of the pinning, and entering/exiting vortices provide a flux change of exactly one flux-quantum per vortex row during that period.

moving vortex rows at the resonance will be larger, hence the measured voltage at resonance will be proportionally larger than shown in these results - which facilitates the observation of the reported phenomenon.

The initiated reader will immediately notice the resemblance of this temporal matching events to the spatial commensurability phenomena employed in the past to enhance the critical parameters of superconductors. In the particular case presented in this Section, the system is always in a dynamic regime, but matching effects in resonances do decrease the voltage, hence also decrease the overall dissipation. Looking at the $n = 1$ resonance in Fig. 5.3, we note the possible tuning of resistance in a very broad range by simultaneous adjustment of τ and applied current - both externally controllable parameters.

5.2 Vortex dynamics at resonances

Another careful look at the resonances shown in Fig. 5.3 reveals more important details. Particularly, we observe that voltage curves obtained for different currents can overlap at certain pinning periods. In other words, for specific τ the system can exhibit identical voltage at two different bias currents. One of such cases is examined in Fig. 5.5, where we constructed the current-voltage $U(J)$ characteristics for $\tau = 3600\tau_{GL}(0)$. For $J = 2 \times 10^{-3} - 2.1 \times 10^{-3} J_{GL}(0)$ the system remains in the same $n = 1$ resonance, as seen in Fig. 5.3, and consequently $U(J)$ characteristics show a Shapiro step at these currents. At larger currents more Shapiro steps are found, corresponding to higher resonances and exhibiting *exactly quantized voltages* - equal to nU_0 , thus tunable by τ .

It is a well-known fact that when a superconductor in the presence of a periodic potential is driven with the superimposed dc and ac force, Shapiro steps can be experimentally found in the $U(I)$ characteristics [238, 239, 240, 241]. In this case Shapiro steps appear due to the fact that dc Lorentz force is applied via magnetic field and current, and on the other side the time-dependent pinning potential is contributing with the ac component. The presence of the pinning potential reflects in the variation of the superconducting order parameter, which then translates in the ac variation of the supercurrent. In addition, due to the stripe-like profile of the depletion region, our structure is a time-dependent Josephson junction ($S - N(t) - S$ junction), hence the relevance of Shapiro physics is clear.

Interestingly, in the reported investigation we observe Shapiro steps not only in current-voltage characteristics, but also with varying practically any parameter instead of current. An analogy can be drawn here with the case of static periodic pinning and an ac excitation (both for superconducting vortices and colloids), for which resonant features have been reported [192, 194, 196, 225]. In our case, the

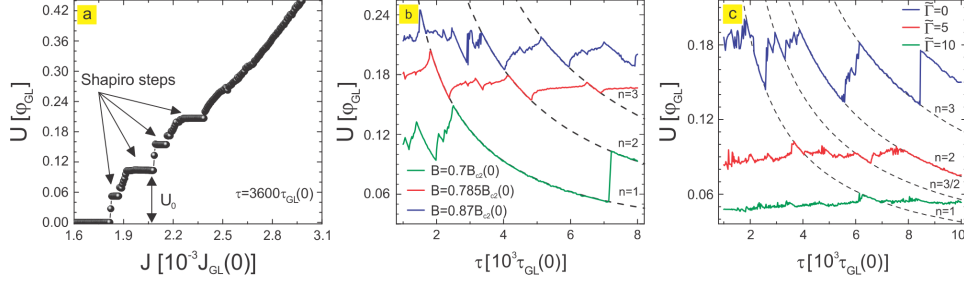


Figure 5.5: Shapiro steps. (a) The Shapiro steps in $U(J)$ characteristics for the pinning period of $3600\tau_{GL}(0)$. U_0 indicates the Shapiro step at first resonance. (b) The resonant behavior in $U(\tau)$ for different values of magnetic field indicates possible Shapiro steps in magnetoresistivity. (c) The resonant behavior in $U(\tau)$ is also found for varied disorder, i.e. varied inelastic phonon-electron scattering time, with effective influence on the viscosity of the superconducting condensate.

reason is that the origin of the stroboscopic phenomenon is the synchronization of vortex motion and time-dependent pinning, and vortex motion can be influenced in more ways than just by current. In Fig. 5.5(b) we demonstrate the dependence of the $U(\tau)$ characteristics on the applied magnetic field, for fixed applied current. We again note the presence of the resonances, which obey the exact same $1/\tau$ behavior as in Fig. 5.3(a). This leads us to the conclusion that Shapiro steps should also be expected in $U(B)$ characteristics, i.e. in magnetoresistance. For additional check, we conducted simulations for varied inelastic phonon-electron scattering time of the superconductor, such that the effective viscosity for vortex motion changes. Even then resonances are observed to follow the same $1/\tau$ behavior and where, with increased viscosity (parameter $\tilde{\Gamma}$ in the theory), the vortices slow down, and voltage slides down on the resonant curve [see Fig. 5.5(c)]. Further relations between vortex velocity and voltage will be explored in the next Section.

In a region where there is no interconversion between supercurrent and normal current densities (i.e., wherever $\nabla \mathbf{J}_s = 0$, thus well outside moving vortex cores) the electric field \mathbf{E} and the gauge-invariant vector potential \mathbf{Q}_s are related by the simple gauge-independent equation

$$\mathbf{E} = -\frac{\partial \mathbf{Q}_s}{\partial t} = -\frac{\partial}{\partial t}(\mathbf{Q} + \tilde{\nabla}\theta), \quad (5.2)$$

where \mathbf{Q} is the vector potential within a chosen gauge, and θ is the phase of the order parameter in the same gauge. Our calculations show that the contribution of $\tilde{\nabla}\theta$ to \mathbf{Q}_s is far larger than that due to \mathbf{Q} . This argument arises from the fact that the

magnetic-flux contributions can be neglected relative to kinetic-energy contributions when the linear dimensions of the nanocircuits under consideration are small by comparison with the Pearl length [242]. For this reason, at least for relatively narrow nanocircuits it is an excellent approximation to write

$$\mathbf{E} = -\frac{\partial}{\partial \tilde{t}}(\tilde{\nabla}\theta), \quad (5.3)$$

hence

$$U_{ab}(t) = \frac{\partial}{\partial \tilde{t}} [\theta_b(\tilde{t}) - \theta_a(\tilde{t})], \quad (5.4)$$

which is the standard Josephson relation between voltage and phase (a and b being the arbitrary points between which the voltage is measured). For additional check, we plotted in Fig. 5.6 the change of phase $\theta_{12} = \theta_2 - \theta_1$ between the points where the voltage is measured, together with the time derivative of θ_{12} , and confirmed that $\bar{U}|_{\tau} = nN_v \frac{\Delta\theta_{12}}{\tau}$, as stipulated by Eq. (5.4). As also shown in e.g. Ref. [243], the dc average of $\bar{U}(t)$ during vortex crossing will be $U_{dc} = \Phi_0 R$, where R is the rate of vortex crossings. The latter corresponds exactly to our resonant conditions.

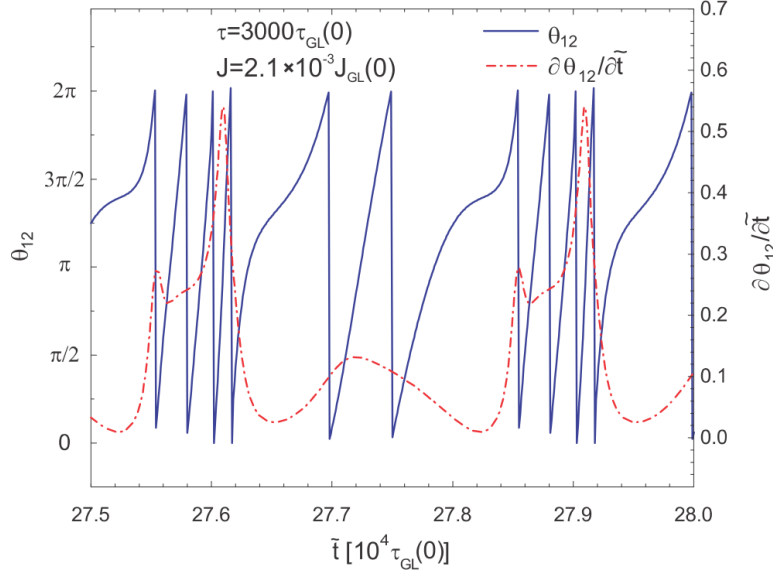


Figure 5.6: Relation of voltage to phase. The temporal evolution of the phase difference (blue line) and the temporal derivative of the phase difference (red dash-dots) measured between the voltage contacts, for the situation corresponding to Fig. 5.4.

Finally, we take a step back to the case of faster oscillations of the pinning, the so called ‘tapping’ mode. The reason is that a careful look at Fig. 5.3(a) reveals the possibility of having a *larger* voltage at the resonance (see beginning of the $n = 1$ curve) than in the case without any pinning in the sample (indicated by an arrow in the vertical axis). This is highly counterintuitive, as adding pinning to superconductors is supposed to anchor vortices and decrease dissipation. This unusual feature is only possible in the tapping regime (see the dots separating the tapping from the pinning regime in Fig. 5.3). Namely, the conditions to obtain this phenomenon are such that when the vortex enters the sample, the pinning is at its maximum, but weakens as vortex approaches. Therefore, the attractive force between the vortex and the depletion region will accelerate the vortex, only to tap it and release as if there is no pinning. Hence the average vortex velocity is expected to be larger than in the case without pinning, which is a unique case of pinning-enhanced dissipation.

5.3 Vortex velocimetry from stroboscopic resonances

In this Section we devise a novel concept for vortex velocity measurement stemming from the frequency-dependent phenomena in a superconductor with a dynamic pinning landscape. Here, a sample of finite size $L \times W = 400 \times 100 \text{ nm}^2$ was considered, once again with parameters of NbN, at bath temperature $T_0 = 0.9T_c$, with longitudinally applied current, in magnetic field perpendicular to its plane, but with an oscillating channel of the width $W_{ch} = 26.5 \text{ nm}$, positioned *across* the middle of the specimen (as shown in Fig. 5.7). For this purpose, a more realistic theoretical framework was employed, consisting of Eqs. 2.42, 2.44 and 2.45, where the calculations were done in the Coulomb gauge and extreme type II regime. The added value of upgraded theoretical model reflects in the fact that the external thermal potential $\nu^{(ext)}(t, \mathbf{r})$ is now included directly in the equation of the thermal balance

$$\tilde{c} \frac{\partial \tilde{T}}{\partial t} = \tilde{k} \tilde{\nabla}^2 \tilde{T} - \tilde{h} (\tilde{T} - \tilde{T}_0) + (\tilde{\nabla} V)^2 + \nu^{(ext)}(t, \mathbf{r}), \quad (5.5)$$

where the profile of the thermal potential in the channel is given as

$$\nu^{(ext)}(t, \mathbf{r}) = 0.5 \tilde{h} \frac{T_c - T_0}{T_c} \left(1 - \sin \frac{2\pi t}{\tau} \right), \quad (5.6)$$

while vanishing everywhere outside the channel. Within such approach, in which one accounts for spatial and temporal heat dissipation, one is able to precisely capture vortex velocities, even very high ones, and thereby discern different vortex

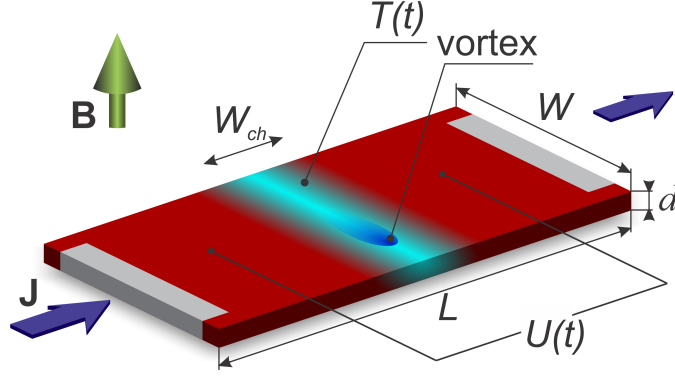


Figure 5.7: The oblique view of the investigated system. Superconducting bridge (of size $L \times W$) is exposed to perpendicular magnetic field \mathbf{B} and longitudinal transport current density \mathbf{J} . In the center of the bridge a channel of depleted superconductivity (of width W_{ch}) is created by local heating, and varies over time. Time-dependent voltage $U(t)$ is measured across the channel.

phases at the crossover from Abrikosov to Josephson ones, each of which are tunable either by external modulation, or by temperature, current, or magnetic field.

In this upgraded model, behavior of the condensate during transitions between hot (ON) and cold (off) states of the channel, and vice versa, is no longer determined only by τ_{GL} and period of the pinning, since thermal processes also occur on some competing time scale. In fact, the response of the condensate in the channel depends on the thermal diffusion of the heat supplied by the time-dependent pinning potential. The time over which the thermal diffusion becomes relevant is proportional to the ratio of the \tilde{c} and \tilde{k} in Eq. 5.5. In principle, the parameters used to calculate heat diffusion (thermal capacity, conductivity and heat transfer coefficient) are temperature dependent [244] and also depend on the substrate properties (e.g. thickness of the substrate d_s , heat capacity c_s , and heat conductivity k_s of the substrate), as was explained in Section 2.2.1. However, it is their respective ratio's that determine the equilibration of temperature in the system, and since the temperature dependence of individual parameters is not generic (or known) for all materials, this analysis is restricted to few characteristic parametric choices, known in literature and covering the regimes of both slow and fast heat diffusion in the system. Mainly for the computational convenience, we use $\tilde{c} = 0.03$ (which corresponds to the real-unit heat capacity of the film $c_f = 0.15$ mJ/cm³K), $\tilde{k} = 0.06$ (with corresponding heat conductivity of the film in real units $k_f = 1.33$ mW/cmK), and $\tilde{h} = 2 \times 10^{-4}$ (the real-unit heat transfer coefficient of

the film $h_f = 16.94 \text{ W/cm}^2\text{K}$ [76, 145, 245, 246]. We note, however, that if only temperature-independent thermal parameters of the superconducting film close to T_c are taken into account, one can use Wiedemann-Franz law to estimate the dimensionless heat capacity $\tilde{c} = 0.65$ ($c_f = 3.25 \text{ mJ/cm}^3\text{K}$) and heat conductivity $\tilde{k} = 0.06$ ($k_f = 1.33 \text{ mW/cmK}$) independently of the considered material. In reality the substrate influence can hardly be neglected, and for example, in NbN films considered in Ref. [247] effective heat capacity was $d_s c_s/d + c_f = 2.4 \text{ mJ/cm}^3\text{K}$, total heat conductivity $d_s k_s/d + k_f = 1.1 \text{ mW/cmK}$, and $h_f = 56.5 \text{ W/cm}^2\text{K}$. Thus, for either set of parameters the thermalization time τ_{th} defined by the ratio \tilde{c}/\tilde{k} does not exceed $100\tau_{GL}(0)$, which is considerably shorter than the period τ of the thermal potential $\nu^{(ext)}(t, \mathbf{r})$ used in this work. A case of \tilde{c} and \tilde{k} leading to a thermalization time τ_{th} exceeding the period of the pinning potential τ would lead to heat accumulation in the channel due to the ineffective heat removal via diffusion, causing full depletion of superconductivity (i.e. forming a permanent Josephson junction, and completely suppressing stroboscopic effects, which is not of interest in the present analysis). Additionally, we estimate the time needed for a vortex to cross the considered sample, τ_{cross} , to be of the order of $1000\tau_{GL}(0)$. When τ is in the range $(\tau_{th}, \tau_{cross})$, the effective heat removal is established, causing the distinct ON and OFF states in the channel, but there exists no synchronized vortex motion in the sample, and thus no characteristic dynamics is found. Only when $\tau \gtrsim \tau_{cross}$ vortex motion in the channel will be completely governed by switching between ON and OFF states, causing the particular stroboscopic behavior of the condensate.

In Fig. 5.8 one can find once again stroboscopic resonances in $U(\tau)$ characteristics, for several different values of the applied current. As expected, in the regime $\tau > \tau_{cross}$ a synchronization between the vortex motion and the flashing channel will arise whenever the flashing period is long enough for an integer number of vortices to cross the sample along the depletion region, i.e. $\tau = n\tau_{cross}$. During the synchronization, stroboscopic effect appears and manifests as recurring voltage drops in the $U(\tau)$. Quasi-periodic behavior of the $U(\tau)$ characteristics shown in Fig. 5.8 corroborates that, where in each consecutive stroboscopic state an additional vortex participates in the dynamics, relating the order of the resonance n exactly to the number of crossing vortices while the channel is open. In other words, the shift in the period τ between the subsequent resonances exactly corresponds to the average crossing time of one vortex, τ_{cross} . This enables one to extract the average vortex velocity from the (experimentally accessible) voltage characteristics shown in Fig. 5.8 (as W/τ_{cross}). During each resonance, the average voltage of the system follows a $1/\tau$ functional dependence (specifically $U_n = 2\pi n/\tau$), which is indicated by dotted lines in Fig. 5.8. To emphasize again, the drops in $U(\tau)$ ex-

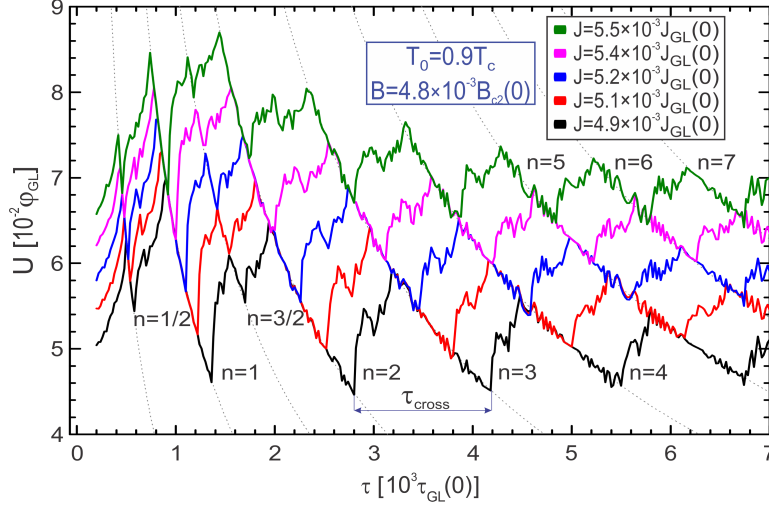


Figure 5.8: Quasi-periodic voltage plotted versus period τ of the oscillating thermal channel shown in Fig. 5.7, for given magnetic field and temperature, and for five different values of the applied current. The inter-resonance period is denoted as τ_{cross} . Dotted lines indicate the $1/\tau$ profile of the voltage during the resonances. Numbers $n = 1 - 7$ indicate the order of the resonance. Fractional resonances are also visible, and denoted by fractional n numbers.

hibit periodicity which is exactly equal to the τ_{cross} . One should however note the fractional resonances in Fig. 5.8 [e.g. around $\tau = 600\tau_{GL}(0)$ and $1600\tau_{GL}(0)$, for $J = 4.9 \times 10^{-3} J_{GL}(0)$], where over the pulse duration of 2τ odd number of vortices traverse the channel. With prolonged flashing the occurrence of fractional resonances diminishes. By taking the above mentioned parameters of NbN, one can estimate the frequency ($1/\tau$) presented in Fig. 5.8 to be in the range 4 GHz to 120 GHz [222, 248], which is still below the gap frequency of NbN ($\nu_{gap} \approx 1$ THz). The same values yield $\tau_{cross} \approx 40$ ps, vortex velocity $W/\tau_{cross} \simeq 2.5$ km/s, and observed voltage drops during the resonances ≈ 0.5 mV. The required pinning frequency to properly observe the resonances must be higher than $1/\tau_{cross}$ (≈ 25 GHz). It is possible to lower $1/\tau_{cross}$ by selecting a material with larger $\tau_{GL}(0)$ or shorter inelastic scattering time, as seen in Fig. 5.5(c). Alternatively, one can force vortices to travel longer distances by making the samples wider, thereby proportionally increasing τ_{cross} . Additionally, we note here that all superconducting and vortex-related time-scales become longer if the temperature is lowered, without any qualitative changes to the reported stroboscopic behavior of the superconduct-

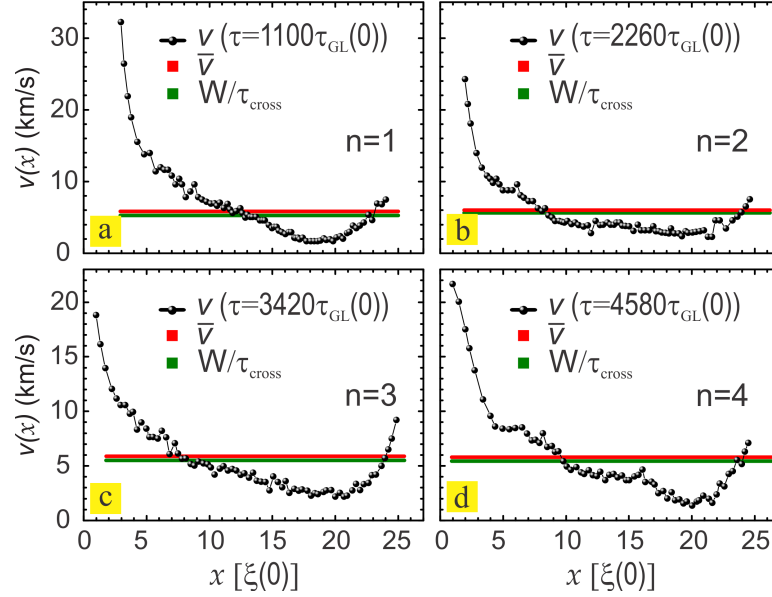


Figure 5.9: Vortex velocities. (a)-(d) Spatial distribution of the vortex velocity along the pinning channel during first four resonances. The black points show the instantaneous vortex velocities, directly measured in the simulations. Average vortex velocity (red line) compares well to W/τ_{cross} (green line).

ing condensate, which is seemingly more convenient for practical realization of our predictions. However, since the specific heat, the thermal conductivity, and the heat transfer coefficient decrease with decreasing temperature, the heating becomes more localized - which may lead to heat accumulation so that periodic oscillations of the order parameter may no longer be achieved [249]. Note that this problem of local periodic heating and continuous cooling has been addressed in Ref. [250] in the context of current driven phase slips in superconducting nanowires.

Typically in experiments the vortex velocity can only be reliably estimated at high magnetic fields, since vortex-vortex interaction dominates over vortex-pinning and therefore the velocity distribution function is very narrow [133]. As discussed above, stroboscopic resonances occur with periodicity that matches the crossing time of one additional vortex (τ_{cross}) from which one can determine the average vortex velocity during the resonance. To verify this, in our numerical simulations we directly tracked the velocities of individual vortices as they pass along the channel, by developing a software (see Appendix A for details) capable of mapping the vortex trajectory in real time (shown in Fig. 5.9, for

one value of applied current). The obtained velocity profiles resemble the velocity profiles measured in Ref. [251]. From this distribution of instantaneous vortex velocities we can compute the average vortex velocity (red line) which indeed matches the ratio of the channel length W and the corresponding $U(\tau)$ resonance period, τ_{cross} (green line), as predicted in the above analysis. Furthermore, by substituting the characteristic values of $\xi(0)$ and T_c for different materials one can easily compare the vortex velocities to be expected. Using the parameters of Al [$\xi(0) = 90$ nm, $\tau_{GL}(0) = 0.38$ ps, $T_c = 1.37$ K [109]] and Pb [$\xi(0) = 33$ nm, $\tau_{GL}(0) = 72$ fs, $T_c = 7.2$ K [252]], one obtains the velocity multiplier ratios: $M^{Al} = \xi^{Al}(0)\tau_{GL}^{NbN}(0)/\xi^{NbN}(0)\tau_{GL}^{Al}(0) = 2.3$ and $M^{Pb} = \xi^{Pb}(0)\tau_{GL}^{NbN}(0)/\xi^{NbN}(0)\tau_{GL}^{Pb}(0) = 4.5$, estimating expected velocity for Abrikosov vortices to be significantly larger than in NbN.

In what follows, we discuss the thermal effects related to the resonances and the vortex behavior through $U(\tau)$ characteristics shown in Fig. 5.10 for the same current used in Fig. 5.9, in the case when: (a) bath temperature is varied and (b) maximal temperature in the channel is varied. From Fig. 5.10(a) one can conclude that the resonant states are well preserved at low bath temperatures ($T_0 \leq 0.9T_c$), and that their behavior follows the trend exhibited in Fig. 5.8, where all vortices traverse the sample in a single line along the channel [snapshot (1) in Fig. 5.10(a)]. Especially for the lowest considered bath temperature $T_0 = 0.86T_c$, stroboscopic states appear at integer resonances, without exhibiting fractional resonances. Clear stroboscopic states persist up to a bath temperature exceeding $0.9T_c$, after which four additional crossing channels appear next to the pinning channel, along which vortices traverse with mismatched velocities. This excess vortex motion outside the pinning channel causes a jump to the higher dissipative state [snapshot (2) in Fig. 5.10(a), corresponding to $T_0 = 0.92T_c$]. In principle, stroboscopic resonances in the $U(\tau)$ characteristic still exist in the higher dissipative state, but are concealed and heavily smeared by the voltage harmonics produced from freely moving vortices out of the depletion region.

As a consequence of an external potential modulation, heat released in the channel varies, which affects the vortex motion in the channel. In Fig. 5.10(b) we show how the $U(\tau)$ characteristics change with increase of the thermal potential amplitude, $\nu_{max}^{(ext)}$. For a weak amplitude [$\nu_{max}^{(ext)} \leq 0.2\tilde{h}(T_c - T_0)/T_c$] non-invasive regime is instated, where the vortex motion is barely affected, due to which the resonances are accompanied by very weak voltage oscillations. These oscillations become more visible as the amplitude is increased [$0.2\tilde{h}(T_c - T_0)/T_c < \nu_{max}^{(ext)} \leq 0.6\tilde{h}(T_c - T_0)/T_c$], and we have resonant states comparable to results in Fig. 5.8. For further increased amplitude, more and more vortices pass through the channel during the resonance, so the $U(\tau)$ shifts to the left. For the selected value of the

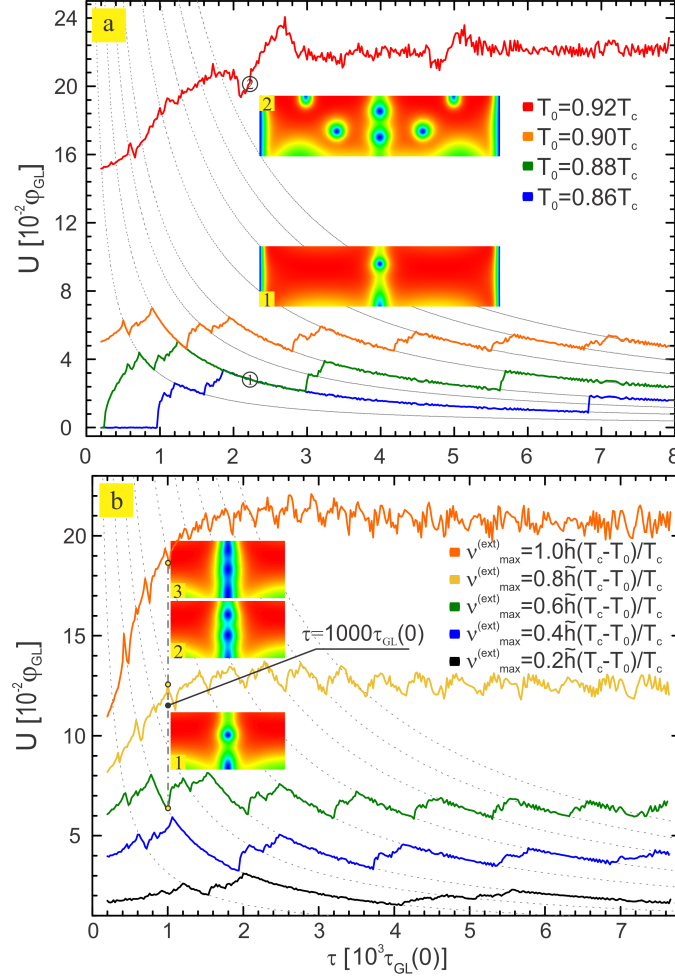


Figure 5.10: The resonant behavior in $U(\tau)$ for different bath temperatures (a), and for varied maximal temperature in the channel (b). (a) With increasing the bath temperature, a transition to a higher dissipative state may occur, where additional vortices move outside of the channel, thus creating additional harmonics that will smear out the average voltage from the $1/\tau$ behavior [depicted by Cooper-pair density snapshots (1) for observable resonances and (2) for smeared resonances]. (b) By varying the maximal temperature in the channel, one may selectively switch between different vortex phases, from Abrikosov vortex, transitional state between Abrikosov and Josephson vortex, and to Josephson vortex [depicted by Cooper-pair density snapshots (1)-(3), respectively, at $\tau = 1000\tau_{GL}(0)$].

flashing period $\tau = 1000\tau_{GL}(0)$, we show that by simple tuning of $\nu_{max}^{(ext)}$ in the range $[0.6\tilde{h}(T_c - T_0)/T_c, \tilde{h}(T_c - T_0)/T_c]$ one can switch between different resonant states and thereby manipulate the vortex velocity in the channel, thus entering the invasive mode. Moreover, the obtained results show that by varying the heat released in the channel, one can even controllably switch between different vortex phases and study them in more detail. Snapshots of the Cooper-pair density in Fig. 5.10(b) indicate that the vortex core deforms progressively with increasing heating, so that the found vortex phase at the same resonance for sequentially increasing $\nu_{max}^{(ext)}$ can change from the Abrikosov vortex (1), to Abrikosov-Josephson transition (2), and then Josephson vortex (3) [94, 182, 205, 253, 254]. The accompanying change in τ_{cross} indicates that vortex velocity multiply increases during the transition between these vortex phases. Finally we emphasize that for any given applied magnetic field (of magnitude lower than B_{c2}), one can tune either the current or the local temperature in order to switch between different resonances and study different types of vortices with core deformation.

In summary, the very first consideration of the effects of dynamic pinning landscape on resistive state in superconductors was presented in this Chapter. For a pinning channel placed orthogonally to the direction of vortex motion, stroboscopic matching between vortex dynamics and pinning oscillations was revealed, which leaves unexpected signature as resonances in the measured voltage versus the period of the pinning, continuous in wider parameter space (for different applied current, magnetic field, microscopic sample parameters). Most of these parameters are externally variable, hence system can be easily tuned along the resonant condition, to achieve beneficial resistive conditions, Shapiro physics without any nanostructuring, or advanced control of flux quanta, all of which deserve further experimental and theoretical pursuit. For an altered geometry and a dynamic pinning channel placed along the direction of vortex motion, stroboscopic synchronization between the vortex dynamics and the thermal oscillations in the channel was again found, but now the shift between the subsequent resonances in the measured voltage versus the flashing period is directly linked to the time needed for one additional vortex to traverse the channel. As a consequence, the voltage characteristic versus the period of the pinning potential provides a direct and reliable measure of the vortex velocity, and that in a broad range of velocities, from slow Abrikosov vortices, to tenfold faster Josephson ones. Presented velocimetry method therefore enables experimental confirmation of the limits of vortex velocity and the realistic characterization of the speed of the emerging vortex-based devices and technology [146, 188, 255, 256] and nicely corroborates the findings presented in Chapter 4.

The main results shown in this Chapter were published in Refs. [257] and [258].

Chapter 6

Vortex matter under electronic gating

Superconductivity is known to occur not only in metals but also in doped semiconductors. The latter started to be of interest in relation to SrTiO_3 and $\text{Ba}(\text{Bi,Pb})\text{O}_3$ in the 1960s and 1970s and became firmly established after the discovery of cuprate high-temperature superconductors in the 1980s [259]. Carrier doping into parent materials, which are usually insulators, could produce a variety of superconductors, in which the carrier density is approximately one order of magnitude smaller than that in metal superconductors. An important aspect of these low-carrier-density superconductors is that critical temperature is strongly dependent on the carrier density. In addition, carrier doping in insulators is a versatile and powerful route towards new superconductors.

Carrier doping is usually performed by chemical means that inherently involve randomness or disorder, such as substitution and intercalation; it is thus believed that chemical carrier doping negatively impacts superconductivity. As a cleaner solution for desired changing of the electronic structure of the superconductor with high degree of tunability, electric field-based superconducting devices have been proposed, mostly around the concept behind field-effect transistors (FETs) [259]. FET technology eventually evolved into metal-oxide semiconductor FET (MOSFET) devices with an insulated gate, whose voltage determines the conductivity of the entire device. Another variation of this device is metal-insulator-semiconductor FET (MISFET). Using a capacitor-like MOS (MIS) configuration, charge carriers can be accumulated at the semiconductor channel through the application of gate voltage, allowing one to change the channel conductivity between the source and drain electrodes. It is expected that with the help of such devices the carrier density and thus the transition temperature of low-carrier-density superconductors can be

modified simply by changing the voltage, without inducing any chemical disorder. First such successful experiment where the superconductivity was manipulated by an external electric field was performed in 1960 [260], where a capacitor electrode of MOSFET was replaced by a superconductor, yielding a slight improvement in T_c (from 4 K, the critical temperature was increased by $70 \mu\text{K}$) [259, 260].

From there on, electric-field control of superconductivity came under spotlight [261, 262]. Especially after the discovery of high- T_c superconductors, the idea of electronic gating started looking more realistic. To date, most successful examples are based on channel materials that are in the vicinity of insulator-superconductor transition, so that superconductivity can be modulated by an electric field. Contemporary field-induced devices utilize surface-confined superconductivity where two-dimensional electron gas is formed, and the gate is located within several nm distance (for example electric double layer transistor) [259]. Such two-dimensional architecture is justified by the fact that significantly smaller electrical fields are needed for the gating effect, where the bulk superconductors are impractical. Since in the last couple of decades 2D superconductors have attracted much attention, electronic gating could impose itself as a crucial technique in their analysis, characterization, and manipulation, with strong emphasis of improvement of the superconducting properties. In the ultrathin and atomically flat structures where local probing via electronic contact is a standardized procedure, a scanning tunneling spectroscopy arises as a viable electronic gating technique for manipulation of superconductivity.

6.1 Superconductivity in the two-dimensional limit

Superconductivity as an electronic state of matter exhibits robustness in the bulk materials (specimens where all three spatial dimensions are much larger than both coherence length and penetration depth). However, systems with reduced dimensionality, such as thin films and nanowires, behave differently due to the spatial confinement, and are more susceptible to thermal and quantum fluctuations. Superconducting films have been thoroughly studied for decades now, which yielded a significant number of superconducting devices, with a wide range of applications. In this process, one particular question gained on significance - is there a limit imposed on the thickness of the film below which superconductivity cannot survive? And if so, what changes does the superconductivity suffer while approaching this limiting case? Answer to the first question lies in the recent experimental evidence which revealed that surface-confined superconductivity can span through as little as several atomic layers (monolayers) [263, 264, 265, 266, 267, 268, 269, 270] with recent verification that it can even be preserved in one-atomic-layer metal

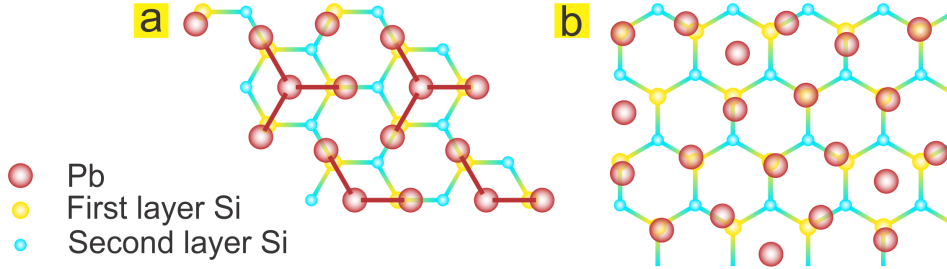


Figure 6.1: Schematic structure representation of the one-atomic-layer superconducting metal films of Pb grown on Si(111), taken from Ref. [118]. Panel (a) shows a striped incommensurate (SIC) phase, which has a Pb coverage of $4/3$ monolayers. Here, three of the four Pb atoms each form a covalent bond with an underlying Si atom, with one Pb atom unbound to the Si substrate. (b) shows the so-called $\sqrt{7} \times \sqrt{3}$ -Pb phase with a smaller coverage of $6/5$ monolayers, where there are six Pb atoms per five surface Si atoms. Circles with red outline represent Pb atoms, while the ones with yellow and blue outline correspond to the first and the second layer of Si, respectively.

films [118]. Another class of 2D superconductors have been proposed, based on interface-confined films, buried below the surface of the structure [271]. However, in that case one cannot use the surface-sensitive techniques like angular-resolved photoemission spectroscopy (ARPES) or scanning tunneling spectroscopy (STS) to probe the local superconducting properties and to characterize the electronic band-structure. This is especially important for gated devices, where far stronger electrical fields are necessary in order to reach and control the buried interfaces. Note also that with high electric field dielectric breakdown becomes a very plausible scenario. Therefore, the surface-confined systems became a benchmarking etalon for studying the emerging phenomena in ultimately thin superconducting films.

There are several types of surface-confined superconductors that have been reported over time, such as granular superconducting films [271, 272], or disordered homogeneous superconducting films [273, 274, 275, 276]. Arguably the most important class, that became available over the last decade are the crystalline ultrathin superconducting films [267, 269, 271, 277, 278, 279]. The thickness of such films can be controlled at atomic level yielding high quality, laterally macroscopic, single-crystals. As a consequence, crystalline films behave as very weakly disordered diffusive thin films hosting a perfect crystalline structure. For a given thickness their superconducting properties are thus homogeneous, and as shown in

Ref. [271], the quantum-size effects are present and evidenced, leading to resonant behavior of the critical temperature as a function of film thickness.

Out of the group of crystalline ultrathin superconductors, In and Pb films grown on silicon Si(111) substrate in UHV have initially attracted most attention. In such combination, a very clean interface with Si(111) can be made, allowing for the atomically smooth Pb and In films to be grown with a single-monolayer precision. Moreover, in Ref. [118] two different Pb/Si(111) superconducting monolayer structures have been reported, the so-called striped incommensurate phase (SIC-Pb) and the $\sqrt{7} \times \sqrt{3}$ -Pb phase. In a unit cell of the SIC-Pb phase, there are four Pb atoms per three surface Si atoms. Three of the four Pb atoms each form a covalent bond with an underlying Si atom, leaving one Pb atom without bonding to the Si substrate. Besides the covalent bonds with the Si substrate, the metal atoms also form metallic bonds within the metal overlayer. In a unit cell of the $\sqrt{7} \times \sqrt{3}$ -Pb phase, there are six Pb atoms per five surface Si atoms. Five of the six Pb atoms each form a covalent bond with an underlying Si atom, leaving one Pb atom without bonding to the Si substrate. Schematic representations of these Pb phases are shown in Fig. 6.1.

Peculiar characteristics of ultrathin metallic films (when compared to bulk materials) are mostly due to the effects of electron confinement in the film, and the influence of the film-substrate and the film-vacuum interfaces. This confinement manifests itself in the formation of quantum wells with discrete energy spectrum [280], whose influence can be traced, for example, in the observed oscillations of the critical temperature [281, 282]. Furthermore, better understanding of fundamental properties of metals, like electron-phonon coupling, was possible from confinement studies in 2D films [283]. In such films, electron motion is only confined in the direction normal to the surface, which allows one to describe emerging quantum wells with dispersion relation $E(k_{\parallel})$ for the component of electron wave vector k_{\parallel} along the directions parallel to the film. Effective masses m_{eff} are used to describe the dispersion with the parallel component of the wave vector k_{\parallel} , $E = \hbar^2 k_{\parallel}^2 / 2m_{eff}$. As determined experimentally from ARPES, measured dispersion relations generally agree well with those from theoretical calculations based on free-standing films [281].

To date, STS, magnetometry and electrical transport measurements conducted on surface-confined superconducting properties of Pb/Si(111) nano-islands have revealed that both the critical temperature and the gap diminish with decreasing film thickness. The presence of vortices has been reported in ultrathin Pb/Si(111) films under perpendicular applied magnetic field [118, 263, 284, 285]. Due to the confinement in nano-islands, stable vortex arrangements, other than the triangular lattice, are expected to emerge. Giant vortex - a single vortex core, comprising of multiple flux quanta (having an integer winding number $L > 1$ of 2π

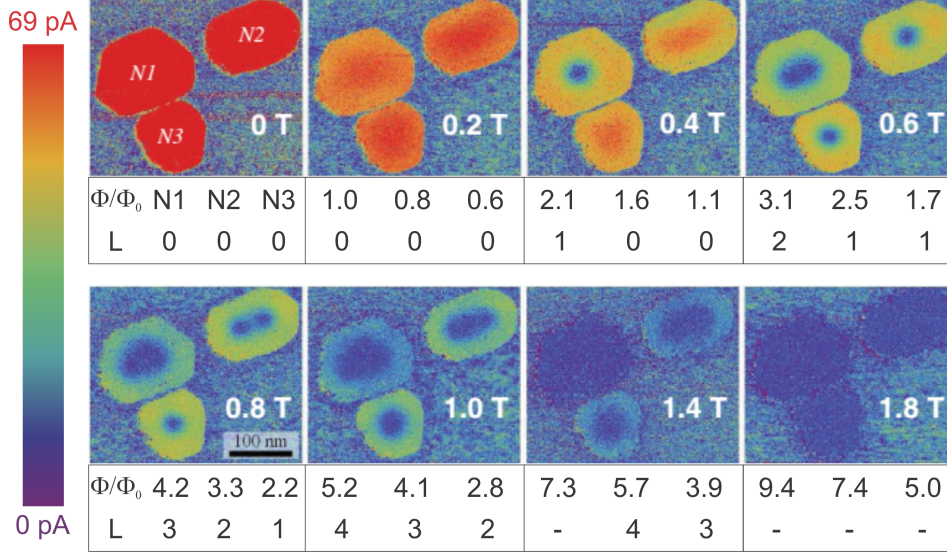


Figure 6.2: Evolution of the confined condensates in magnetic field, measured by STS in Ref. [286]. Three islands of different geometries are denoted with Ni , where $i = 1, 2, 3$. The thicknesses of the islands are between 2.3 nm (N2 and N3) and 2.8 nm (N1), with 8 and 10 single atomic layers of Pb, respectively. The magnetic flux Φ threading each island (in units of Φ_0) and the vorticity L are given for each value of the applied magnetic field. The measurements were performed at 320 mK.

phase changes) is one of these stable states reported in Pb/Si(111) islands [286]. As an exemplary case, in Fig. 6.2 we show experimental data from Ref. [286], where it is clearly seen how the confinement affects the vortex arrangement in three Pb/Si(111) nano-islands of different geometry.

The first manipulation of the vortex states in ultrathin Pb films using STS probe, accompanied by a brief theoretical analysis was performed in Ref. [287]. In this case, a large tunneling current was used as a local source of heating, attracting vortices, with a conclusion that geometrical barrier for vortex penetration (exit) can be efficiently influenced only in the case of rather extreme suppression of the superconducting state. However, the question remained if more subtle electronic (not thermal) excitations can induce noticeable changes in these delicate surface-confined superconducting condensates, and with what consequences.

6.2 Scanning electronic gating of the atomically thin superconductors

Due to its indispensable role in the characterization of 2D superconductors, the STM technique has gained a privileged position in the field. On the other hand, STM could prove very useful as a potential candidate for electronic gating in which superconductivity is modified via electric field. Already in Chapter 3 the main features and operation principles of the STM technique were outlined. Scanning tunneling spectroscopy is a regime of STM where the tunneling current is measured between a sharp metallic tip and a conducting sample separated by a thin insulating barrier, generally vacuum. The ability to control the spacing between the tip and the sample, as well as of the lateral position of the tip, using piezoelectric transducers with extremely high precision, brought additional degree of freedom to the well-established point-contact tunneling spectroscopy. In addition to imaging the surface topography with atomic-scale resolution, it allows one to probe the electronic local density of states (LDOS) with exceptional spatial resolution and well-controlled tunneling barriers. The tunneling regime is defined by a set of three inter-dependent parameters: the electrode spacing z , the tunneling current I , and the bias voltage U . To study intrinsic sample properties with lowest degree of invasion, it is preferable to use tips with a featureless density of states and a well-defined Fermi surface. The metals most commonly used for the tip are Au, W, Ir, and PtIr.

Locally-resolved electron spectroscopy is probably the most sophisticated application of STM. The electronic density of states can be accessed by recording the tunneling current $I(U)$ while the bias voltage is swept with the tip held at a fixed vertical position. If a positive bias voltage U is applied to the sample, electrons will tunnel into unoccupied states, whereas at negative bias they will tunnel out of occupied states. Although the interpretation of spectra can be quite complex, it can be shown that in ideal conditions the tunneling conductance $dI/dU(U)$ provides a valid measurement of the sample LDOS (general dependence of the tunneling conductance and LDOS can be found, for example, in Ref. [288]). dI/dU spectra can be obtained either as a derivative of $I(U)$ curves with respect to the voltage or directly by using an oscillatory excitation of small amplitude and recording the response with a lock-in amplifier.

STS measurements proved to be indispensable in the analysis of ultrathin superconducting Pb islands, in particular when one aims to determine the energy gap and LDOS of the structure. Figure 6.3(a) shows the characteristic profile of the conductance, obtained from STS. Presented results are taken from Ref. [284] and correspond to the hexagonal Pb island of the thickness of 5.5 nm (see inset) in the

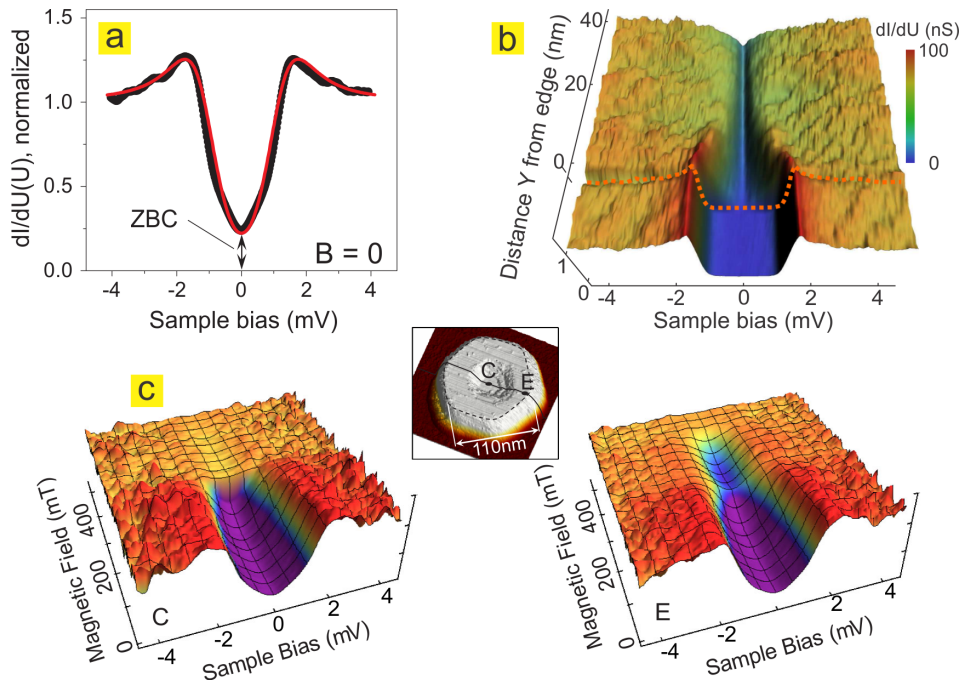


Figure 6.3: (a) Characteristic normalized local tunneling conductance spectrum $dI/dU(U)$ of a Pb island at $B = 0$ T (circles) and the best fit using standard BCS DOS with $\Delta = 1.12$ meV, $T = 4.3$ K (red line). Zero-bias conductance is indicated with an arrow. Data taken from Ref. [284]. (b) Spatial variations of the local dI/dU spectra (the conductance varies from 0 to 100 nS) as a function of the distance from an island edge. Data taken from Ref. [289]. (c) Evolution of the local tunneling dI/dU spectra in the magnetic field, according to Ref. [284]. The central inset shows a topographic image of the islands, while left and right bottom graphs represent $dI/dU(U, B)$ measured at points C and E, respectively.

absence of magnetic field. The minimal value of the conductance found at zero bias voltage [the zero-bias conductance (ZBC)] occurs due to the presence of the superconducting state. Maxima occur when the tunneling current destroys superconductivity, and the structure goes to the normal state. In order to obtain the value of the superconducting gap, one usually needs to fit $dI/dU(U)$ curve with DOS calculated from BCS theory. From this fit, one extracts the information about the superconducting gap as the voltage distance between the two maxima in the conductance. This measurement can be taken at different locations in the sample, or even over the entire specimen. For example, in the analysis of the proximity effect in the Pb islands, the spatial distribution of $dI/dU(U)$ is proved to be very useful. Such data is presented in Fig. 6.3(b), taken from Ref. [289], where it was found that due to proximity effect superconductivity can survive in the amorphous Pb monolayer relatively far outside the superconducting island. Conductance can also be measured in the presence of magnetic field, as is shown in Fig. 6.3(c). This image comes from Ref. [284], where the influence of confinement of the Pb island on the vortex matter was studied. In that case, while scanning with the tip, detailed information about vortex structure can be obtained.

However, ZBC maps represent a handy tool for imaging the vortex matter in real space. Since ZBC value changes with respect to the magnetic field (see Fig. 6.4(a), taken from Ref. [286]), measurement of ZBC at every point of the island can be used for unambiguous mapping of the vortex distribution, as it was done in Ref. [286], with examples shown in Fig. 6.4(b) for four different values of the magnetic field.

One important ingredient that needs to be mentioned here is the influence of the relative work function existing between the tip and the island. Work function represents the minimal energy needed to remove an electron from a solid to a point in the nearby vacuum. Since each material is characterized with a specific work function, and since in general the materials used to make the tip and the island do not have to be the same, a difference in their respective work functions can induce a finite voltage. For example, if STS is performed with an IrPt tip on the Pb island, where the tip and the island are comparable in size, a difference in their respectable work functions can induce a voltage of the order of several mV. This voltage is not supposed to strongly affect superconductivity in the island, as additional evidence suggests that in mesoscopic superconductors position-dependent STS at much higher biases is needed to locally deplete superconductivity due to local pair-breaking [287]. Nevertheless, since the additional energy added through the work function is not negligible neither compared to the superconducting gap, nor compared to the electronic levels in the island [290], thus some effects are expected to emerge due to such interaction.

Recently, the analysis of the confinement effects on vortices in ultrathin Pb

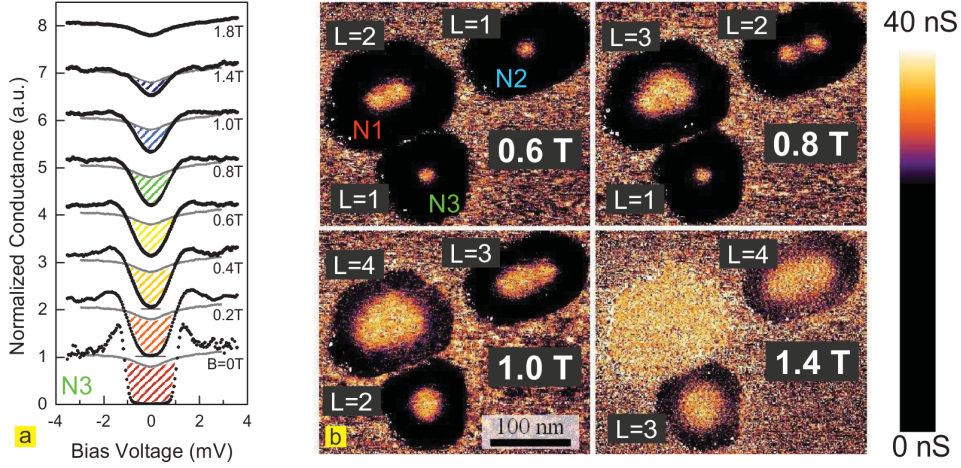


Figure 6.4: (a) Local tunneling conductance spectra $dI/dU(U)$ (black lines) acquired at the periphery of the smallest crystal N3 of (b) at different magnetic fields. Gray line correspond to the normal state spectrum. The spectra are presented normalized to unity at 50 nS. (b) ZBC maps of three Pb islands, (denoted as N1, N2 and N3) revealing the extension of the vortex cores at four different values of magnetic field. The locations characterized by a superconducting gap are intentionally saturated in black; the cores of individual vortices appear as small bright spots (see the color bar). With the same contrast, the $L > 2$ phases are revealed as extended regions. Data taken from Ref. [286].

islands was performed via STS, when moving the tip across the island [286]. The resulting diagram of measured ZBC for different positions of the tip, as a function of magnetic field, is shown in Fig. 6.5(a), taken for the island N3 presented in Fig. 6.4(b). From the diagram one sees a series of sharp transition lines, each corresponding to a threshold field between the states with different vorticity. One can notice there that at around 0.6 T the first vortex enters the sample and sits in the center [see also snapshot of the ZBC of the island N3 in Fig. 6.4(b), taken at 0.6 T]. At 0.9 T vorticity is changed to $L = 2$, and this state is maintained until 1.3 T. From the snapshot taken at 1 T in Fig. 6.4(b), one sees clearly a single round object located at the sample center, instead of two individual vortices. This state corresponds to $L = 2$ giant vortex. Even for $L = 3$ state first occurring around 1.3 T, similar phenomenon is visible, corresponding to a giant vortex. From the flat and symmetric transition lines between different vortex states regardless of the position of the tip, one concludes that all ZBC measurements performed on this

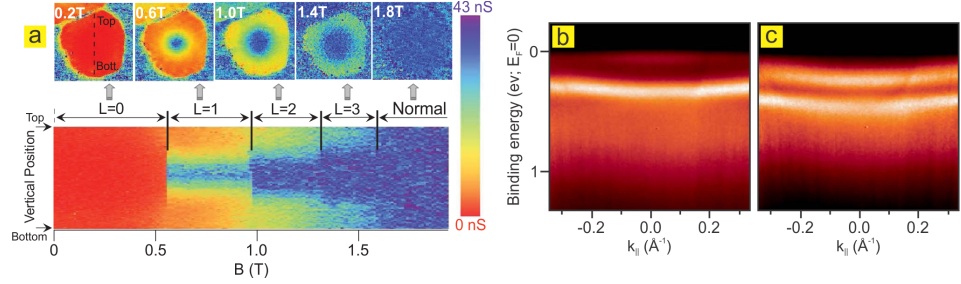


Figure 6.5: (a) Vorticity phase diagram from [286]. Top: ZBC maps of corresponding vortex configurations. Dashed line: The scanning line along which the ZBC-field diagram was acquired. Bottom: Color-coded diagram of ZBC values vs magnetic field, taken over the dashed line crossing the island. Abrupt transitions separate the phases of different vorticity L . (b,c) In-plane dispersion of QWS for 17 and 22 ML of Pb on Si(111), respectively, obtained by ARPES in Ref. [281].

island were non-invasive to the superconducting state.

However, in ultrathin superconductors it is expected that quantization of the electron motion in the direction normal to the film results in the formation of so-called quantum-well states (QWS), and the band structure of the single-electron states splits in a series of two-dimensional parabolic sub-bands [291]. These QWS are able to move up or down in energy through electrostatic gating. When a QWS passes the Fermi level, a new sub-band becomes relevant to superconductivity, as this passage should be accompanied by a significant change of the density of single-electron states near the Fermi level. In ultrathin Pb islands, due to the inherent crystal configuration, QWS are rather flat, which can be seen from ARPES images shown in Fig. 6.5(b) and (c), taken from Ref. [281]. On the other hand, the exact energy position of QWS strongly depend on the island thickness, and, in fact, QWS move down in energy with increasing the film thickness [291]. Consequently, the electronic properties of a thin metallic film will be greatly modulated by varying its thickness at nanoscale. This indicates that the direct effect of gating should actually be dependent on the number of atomic layers in the island. In Ref. [267] the dependence on sample thickness of the energy levels of QWS with respect to the Fermi level was studied for ultrathin Pb islands using STS, and their most relevant data is presented in Fig. 6.6(a). Here it is visible that only for specific thicknesses certain energy levels lie in close vicinity of the Fermi level. By checking the composition of the islands N1, N2, and N3 from Ref. [286] [Fig. 6.4(b)], which are 10, 8 and 8 atomic layers thick, respectively (including the wetting layer), and comparing to the measurements of Ref. [267] shown in Fig. 6.5(b)

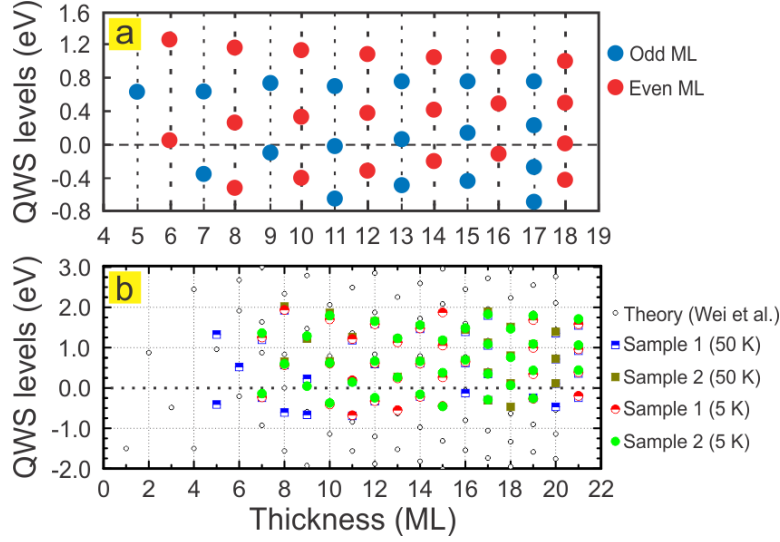


Figure 6.6: (a) Display of the locations of the quantum-well states for Pb islands of various thicknesses [given in monolayers (ML)], as reported by Eom *et al.* in Ref. [267]. The red color is for even number of MLs and the blue is for odd number of MLs. Measurement of the energy levels was done by STS. (b) Locations of quantum-well states (QWS) for Pb islands of various thicknesses obtained by ARPES. Sample 1 is an annealed Pb island, and Sample 2 is unannealed Pb island, in both of which the QWS were measured at 5 and 50 K. Experimental data is taken from Ref. [292]. Theoretical calculations of QWS levels from Ref. [290] are shown as well.

for 8 and 10 monolayers, one sees that there are no QWS close to the Fermi energy in those three islands. Therefore, any gating effect can hardly be relevant in that case. On the other hand, data shown in Fig. 6.6(a) indicate that in the case of islands that are 6, 9, 11, 13, 16, and 18 monolayers thick one should have an energy level sufficiently close to the Fermi level, on which the effects of the STS-based gating might become significant. Comparing these energy levels to the ARPES data in Fig. 6.6(b) some definite difference can be seen. We recall that results of Eom *et al.* in Ref. [267] are obtained by STS, which inherently already contains gating contribution. Fortunately, ARPES measurements of QWS energy levels in islands of different thickness done in Ref. [292] and presented in Fig. 6.6(b) are free of such an influence. From ARPES data one sees that the thicknesses in atomic layers closest to the Fermi energy are 7, 9, 11, 14, 18, 20 ML, and are expected to be most susceptible to STS gating. In fact, one could say that Fig. 6.6(b) and (a)

summarize the change in electronic structure before and after (i.e. during) gating, respectively. Depending on the position of the energy state (below or above the Fermi level), the presence of STS gating is expected to enhance superconductivity (energy state is above E_F and gating drags it below the Fermi energy) or to suppress it (energy level is below E_F and gating drags it above the Fermi energy).

6.3 Modulation of the superconducting properties of an ultrathin Pb island via electronic gating

The suggestion that only the Pb islands of specific thickness are feasible for electronic gating implores for more detailed exploration of such samples. The first experimental attempt was performed recently in the Institut des Nanosciences de Paris (France) [293] where the 9 ML Pb crystal was *in situ* grown on Si(111), and the experiment was performed in UHV ($P < 10^{-10}$ mbar) [284, 286]. PtIr tips were used for spectroscopy, and in order to resolve fine spectroscopic features, the STS was performed at $T = 300$ mK.

The effective diameter of the studied Pb island was estimated as $D_{eff} \approx 120$ nm, and its thickness as $d \approx 2.2$ nm, corresponding to 9 single atomic layers of Pb in (111) direction (including the presence of wetting layer which forms at the entire Pb/Si interface). An overview of the sample is shown in Fig. 6.7(a). In such a system, it is expected that the atomic lattices of Si and Pb are mismatched, introducing disorder at the Pb/Si interface, which therefore limits the electron mean free path in Pb island to $\ell \approx 2d = 4.4$ nm [269], and plays a role in its superconducting properties. For such thin films in dirty limit, by taking into account that BCS coherence length for bulk Pb is $\xi_0^{(Pb)} = 83$ nm, and the London penetration depth of bulk Pb is $\lambda_L^{(Pb)} = 37$ nm, one can estimate the effective coherence length as $\xi_{eff}(0K) = 0.855\sqrt{\xi_0^{(Pb)}\ell} = 16.34$ nm and the effective penetration depth as $\Lambda_{eff}(0K) \approx 0.752\lambda_L^{(Pb)^2}\xi_0^{(Pb)}\ell^{-2} = 4.41$ μm , according to Eqs. 2.32 and 2.33, respectively. These estimates indicate that one deals with extreme type II superconductor in this ($\ell \ll \xi_{eff} \ll \Lambda_{eff}$) diffusive limit, with $\kappa^* = \Lambda_{eff}/\xi_{eff} \approx 270$. It is, therefore, reasonable to assume that the magnetic field fully penetrates the sample ($d \ll D_{eff} \ll \Lambda_{eff}$), as the Meissner-Ochsenfeld effect is negligible. Based on the ratio of the effective island diameter and the effective coherence length, $D_{eff}/\xi_{eff} \approx 7 \ll \Lambda_{eff}$, one expects a strong influence of confinement.

ZBC as a function of the magnetic field was first recorded at a particular position indicated by a dark spot in Fig. 6.7(a). The sample was zero-field-cooled, and the magnetic field was slowly increased until superconductivity was destroyed, followed by a downward field sweep (i.e. from normal state, field is slowly decreased

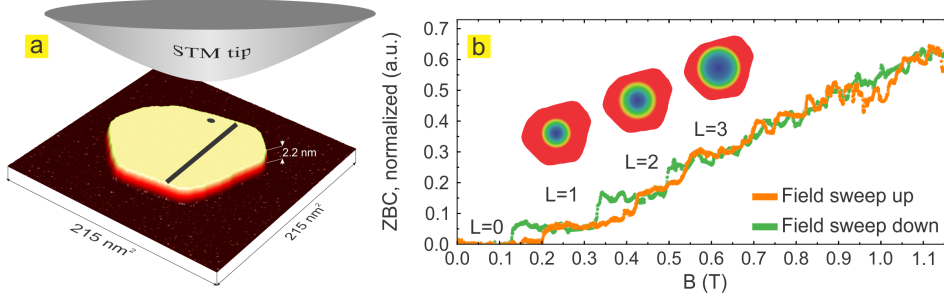


Figure 6.7: (a) Oblique view of the studied Pb island under the STM tip, with thickness of 2.2 nm (9 ML). Dark spot marks the position at which tip was located when ZBC vs magnetic field curves were obtained, shown in (b). Black line indicates the trajectory over which the tip was moved in order to obtain the ZBC phase diagram shown in Fig. 6.8. (b) ZBC as a function of magnetic field taken at the dark spot seen in (a), recorded when field was measured from zero-field cooled state (orange curve) and when field was decreased from larger value (green curve). Insets show the illustration of vortex ($L = 1$) and giant vortices for the states $L = 2$ and 3.

to zero), both at a rate of 4.45×10^{-5} T/s. The results are shown in Fig. 6.7(b). Out of the visible noise, plateaus can be recognized in the measured conductance, corresponding to states with different vorticities. During the upward sweep of the magnetic field signs of transitions in between different states L can be seen around 0.20 T, 0.43 T, 0.55 T, while in the downward sweep the switch between plateaus occurs at 0.13 T, 0.32 T, 0.50 T. In both cases, at larger magnetic field it becomes harder to distinguish the transitions. Provided snapshots in Fig. 6.7(b) help one to correlate the changes in $dI/dU(U = 0, B)$ seen in ZBC to states $L = 1, 2$, and 3, the latter two in the giant-vortex form.

In the second phase of the experiment the diagram of ZBC versus magnetic field (swept up and down) was taken as the tip was moved across the island, slightly off-center [along the line depicted in Fig. 6.7(a)]. The results is shown in Fig. 6.8. Unlike what was found in Fig. 6.5(a), here some of the transition lines between different vortex states are curved, a phenomenon that becomes more and more pronounced as the magnetic field is increased. To highlight this behavior, simplified color-coded diagram is also provided in Fig. 6.8. There the measured spatial profiles of ZBC for states $L = 1$ and $L = 2$ are also shown, indicating that giant vortex is formed at higher vorticities. Initially, at the very first transition from $L = 0$ to 1, just a straight delimiting line is seen in the diagram. However, when $L = 1$ switches to $L = 2$, mild curving in the transition lines for both upward and down-

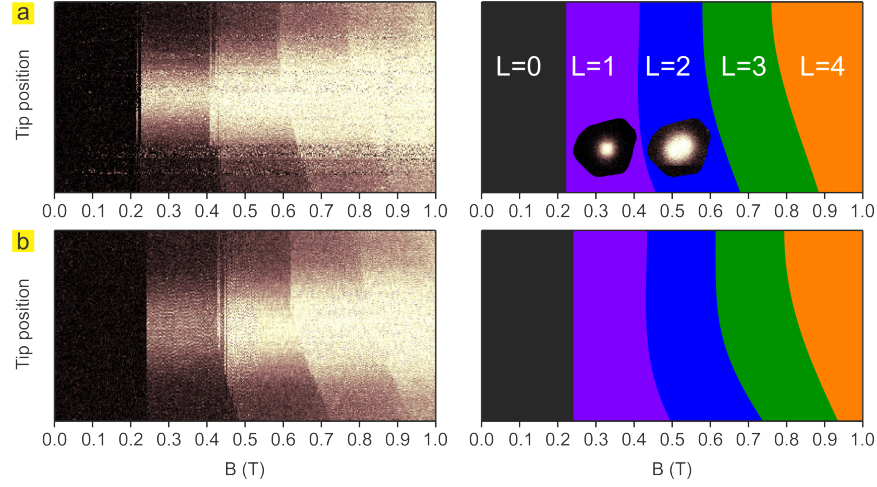


Figure 6.8: Phase diagrams (on the left) of the measured ZBC as a function of magnetic field, taken as the tip is moved along the black line in Fig. 6.7(a). Diagrams were recorded for field swept up (a) and down (b). On the right side are the corresponding simplified color-coded versions of the same diagrams, to highlight the transitions. ZBC maps of the island for states $L = 1$ and $L = 2$ shown as insets indicate that at higher vorticities the giant vortex state forms.

ward field sweep can be seen. When states change from $L = 2$ to 3, a curvature in the transition line is seen until deep into the sample. Even more obvious manifestation of the phenomenon is seen at $L = 3$ to 4 transition. The unique features of this phase diagram are qualitatively well preserved regardless of the direction of sweep of the magnetic field, even though a mild hysteresis can be observed between Figs. 6.8(a) and (b).

Finally, one may be led to conclude that the anomalous behavior seen in ZBC is a direct consequence of an invasive interaction between the STS tip and the island. As reported in this experiment, superconductivity is not destroyed during the spectroscopy, meaning that some intrinsic and subtle relation between the island and the tip is responsible for the observed behavior. Another argument in favor of this interpretation is the fact that during the performed spectroscopy the bias voltage is swept between a positive and a negative value of the same magnitude, and therefore any subsequent influence of that bias is expected to be cancelled out. Therefore, the observed behavior must be caused by other alternative mechanism. We recall the fact that the considered Pb island of 9 ML thickness has an energy level very close to the Fermi energy [see Fig. 6.6(b)], suggesting that this level can

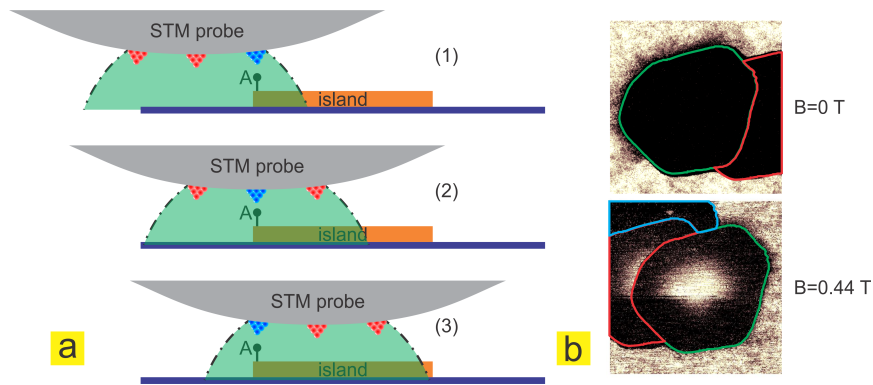


Figure 6.9: (a) STM probe with multiple tips. Depending on which tip the measurement at point A is performed, the work function of the probe may affect different portions of the island underneath. Sketches illustrate the scenario's corresponding to the case when the active tip (depicted in blue) is at the front edge of the probe, so most of the island is not affected by the gating produced by the high electrostatic potential region (green region) (1), case with the active tip in the middle of the probe, causing partial gating in the island while imaging only point A (2), and the worst case scenario, where active tip is at the back edge of the probe, leading to a major part of the island being gated (3). Regions affected by gating are denoted by green color. (b) Artifacts in ZBC map due to multiple-tip imaging. Insets taken in the absence of magnetic field where the tip doubling effect is evident (green and red contours), and at 0.44 T, where the tip tripling is evidenced by red, green and blue contours of the same island.

be easily influenced by the contribution of the work function of the tip above the island, regardless of it performing spectroscopy or not.

Further, we note the problem of multiple tips, arising in realistic STS probes. Due to the local clustering of atoms at the surface of the probe, it is possible to have more than one tip through which the tunneling is performed, causing several distinct features. First, the actual position of the active tip on the surface of the probe remains unknown and therefore it is not possible to know where exactly the spatial scope of influence of the gating in the island begins and where it ends, with respect to the position of the tunneling tip. This is illustrated in Fig. 6.9(a), where the recorded measurement of ZBC in point A depends on the position of the active tip (blue) on the probe surface. Since there is more than one atomic cluster on the probe that can be used for imaging, depending on which of them is currently active (blue), the work function may exert gating in a narrow section (1), significant part

(2), or almost entire (3) island. Additionally, more than one tip can be active at the same time, due to which artifacts may appear in the final image, as shown in Fig. 6.9(b) in the absence of magnetic field and at 0.44 T. Both of these issues may lead to some ambiguities in the interpretation of experimental results, as will be more obvious in the discussion below. In the following Section the gTDGL framework is employed to provide further insights in the behavior of vortex matter in the studied island in the presence of local electronic gating, taking into account above caveats.

6.4 gTDGL analysis of vortex matter under electronic gating

Based on the AFM image from the experiment, a map of the area $13.2\xi_{eff}(0K) \times 13.2\xi_{eff}(0K)$ ($215 \times 215 \text{ nm}^2$), shown in Fig. 6.10(a), was prepared for numerical simulations using gTDGL model, so that all the geometrical features of the realistic Pb island are preserved. In this case, only the gTDGL equation for the order parameter is relevant, since in this extreme type-II ultrathin island the magnetic field is homogeneous and there is no applied current. Since only the experimental ZBC was used to build up the phase diagrams shown in Fig. 6.8, in the following simulations no spectroscopy is considered, so the entire theoretical analysis addresses the mere presence of the STM probe above the island and the ambiguity over the exact position of the tip on the surface of the probe. Moreover, it is estimated in the experiment that the diameter of the curvature of the probe is comparable to (and may even exceed) the size of the island. Based on the evidence that can be found in the literature [294], which substantiate this claim, we show the image of the PtIr STM tip obtained by transmission electron microscopy (TEM) in Fig. 6.10(b). During the scanning, due to the differences in the work functions between the STM probe and the island the electric field is generated over a region of a finite size, and this is where the effect of gating is relevant. Therefore, by taking into account size comparison between the STM probe and the Pb island, it is reasonable to assume that only the part of the island that is currently covered by the electric field effect of the probe is affected by the gating. Depending on the position of the tip on the probe, as the tip is moved while scanning [along the line shown in Fig. 6.10(a)], different percentage of the total surface of the island will be exposed to gating. To make this more clear, we stress again the different scenarios of gating while scanning, which are illustrated in Fig. 6.10(c). In the case (1) the tip is located at the front of the STM probe, and as the probe moves between points A and B, tip only measures ZBC in the part of the island which is not yet fully affected by the gating (green area). Intermediate case (2) corresponds to the situation where the tip is located at the center of the surface of the probe, so that during the gating, in

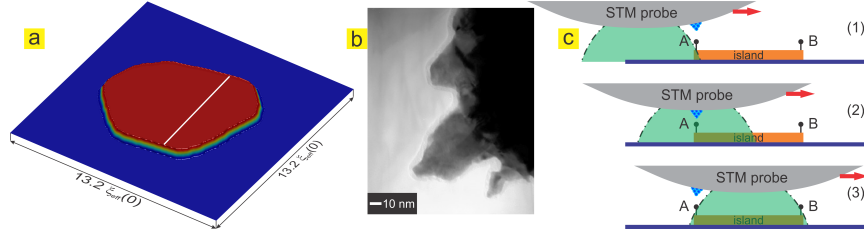


Figure 6.10: (a) Oblique view of the considered sample, in a simulation area $13.2\xi_{eff}(0K) \times 13.2\xi_{eff}(0K)$. White line marks the trajectory along which the tip motion is simulated. (b) Transmission electron microscopy image of the STM tip, taken from Ref [294] (c) Schematic representation of the STM probe scanning the area between the points A and B, when the tip is located at the front of the probe (1), at the middle of the probe (2), and at the back of the probe.

the island exist both the area affected by the gating, and the pristine one, and the tip probes within the fully gated area. In the last scenario (3), the position of the tip is at the back side of the probe, so as it moves it always measures ZBC in the sample as it recovers from gating effect.

In order to reproduce the main features of the phase diagram from Fig. 6.8, one must evaluate which superconducting properties are affected by the gating effect, and if those properties are accessible within the gTDGL model. Previous reports on the influence of the STS probe on the superconducting condensate were primarily focused on thermal effects [119, 287]. In addition to possible local heating, it is also reasonable to suspect that gating-induced changes in the electronic structure of the ultrathin material can cause the fundamental superconducting properties to be locally modified as well. However, gTDGL theory does not provide the complete microscopic description of superconductivity. Instead, the only accessible parameters are seen in Eq. 2.65, namely the critical temperature, inelastic electron-phonon scattering time, and diffusion parameter, which is governed by the product of the electronic mean free path and the Fermi velocity. The inelastic electron-phonon scattering time only plays a role in dynamical processes when the system is driven out of the equilibrium, so one can neglect its contribution in this particular case, since the duration of experimental measurements takes sufficiently long time for one to assume that all detected states are in equilibrium. The density of states is also featured in the gTDGL model (see, for example, Eq. 2.24), however, it affects all the terms in the relevant equation in the same way, so the obtained vortex state for a given magnetic field would not change if only the density of states changes. Based on these arguments, gTDGL can primarily account for the influence of local

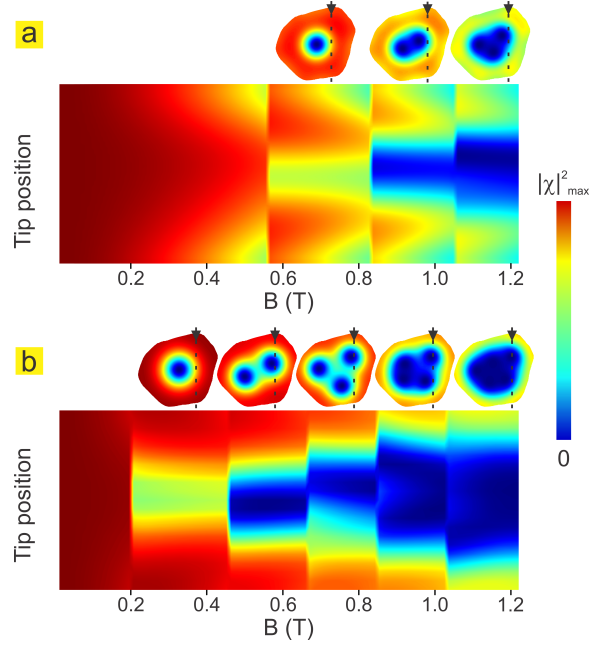


Figure 6.11: (a,b) Phase diagrams of the value of Cooper-pair density (CPD) under the tip as a function of magnetic field, obtained as the tip is moved along the line indicated in Fig. 6.10(a), and taken during sweep up and down of the magnetic field, respectively, for a pristine Pb island in the absence of any heating or gating by the tip. Each vorticity state is accompanied by the corresponding inset showing spatial distribution of CPD, where the dashed lines indicate the line along which the phase diagram was recorded, and the arrows indicate the direction of the tip motion.

gating through heating and/or changes in T_c [$T(\mathbf{r}, t)$], as well as the change in diffusivity through the mean free path [$\ell(\mathbf{r}, t)$] and the Fermi velocity [$v_F(\mathbf{r}, t)$] of the pairing electrons. For this purpose Eq. 2.65 is applicable for describing the spatial variations in the mean free path, the Fermi velocity, and T_c while the pure heating effects can be considered through thermal kernels f and g . The temperature of the sample in simulations is taken the same as in the experiment ($T_0 = 300$ mK), with the critical temperature of the pristine Pb island taken as $T_c^{(pristine)} = 7.2$ K. The parameter $\tilde{\Gamma}$ has the value 10. In order to directly compare the results with the experiment, we follow the analogous behavior of the square modulus of the order parameter ($|\chi|^2$) and ZBC.

As a reference, we first present the phase diagram of $|\chi|^2$ under the tip in the

pristine Pb island (in absence of any gating or heating by the tip) in Fig. 6.11(a) (magnetic field swept up) and Fig. 6.11(b) (magnetic field swept down), taken as the tip is moved down along the line shown in Fig. 6.10(a). In this island scanning is completely non-invasive, and similarly to the diagram in Fig. 6.5(a), one notices that transitions between states of different vorticity are described with straight vertical, symmetric lines. For such a sample, an hysteresis is also noticeable, where the corresponding transitions in vorticity [see insets in (c)] occurring at 0.56 T ($L = 0$ to 1), 0.83 T ($L = 1$ to 2), and 1.7 T ($L = 2$ to 3) during field swept up, occur at 0.2 T, 0.45 T, and 0.65 T during sweep down of the magnetic field [see Cooper-pair density (CPD) plots of the states with $L = 1, 2,$ and 3 in (d)]. Moreover, during the sweep down of the magnetic field transitions between states with even higher vorticities are found at 0.85 T ($L = 3$ to 4), and 1.04 T ($L = 4$ to 5) [see CPD plots of the states with $L = 4$ and 5 in (d)]. These results serve as a reference for the following discussion, where the heating and/or gating by the tip are considered.

Let us first present the study of a purely thermal influence of the tip on the condensate, where the presence of the STM tip and its tunneling current leads to a local hot spot, i.e. distribution of T/T_c ratio as

$$\frac{T}{T_c} = \begin{cases} \tilde{T}(\mathbf{r}, t), & \text{under the tip,} \\ \frac{T_0}{T_c^{(pristine)}} = 0.042, & \text{everywhere else.} \end{cases} \quad (6.1)$$

The ratio $\tilde{T}(\mathbf{r}, t)$ can take any value from the interval $(0, 1)$, and is further used in the thermal kernels f and g in Eq. 2.65. From there, the phase diagram of $|\chi|^2$ under the tip is recorded as a function of magnetic field and the position of the tip. For each value of magnetic field, the tip scans the island in every point of the designated trajectory, forward and backward, over a sufficiently long simulation time for the vortex state to equilibrate for every position of the tip. Snapshots depicting the distribution of Cooper-pair density (CPD) in the island for different positions of the tip are shown in Fig. 6.12(a), when the thermal coefficient of the area under the tip is taken as $\tilde{T}(\mathbf{r}, t) = 0.1$. The corresponding phase diagram is given in Fig. 6.12(b), and from it one notices that transitions between vortex states occur at lower magnetic fields, when compared to the ones seen in Fig. 6.11(a). There are still very subtle kinks in the transition lines between states with different vorticities, however no particular curvature is detected here. The same character of the phase diagram perseveres when the heating under the tip is further enhanced. In particular, when the thermal ratio $\tilde{T}(\mathbf{r}, t)$ is increased to 0.3, the corresponding phase diagram shown in Fig. 6.12(c) reveals no drastic change in the transitions between found states. Here, the transitions occur at even lower magnetic fields,

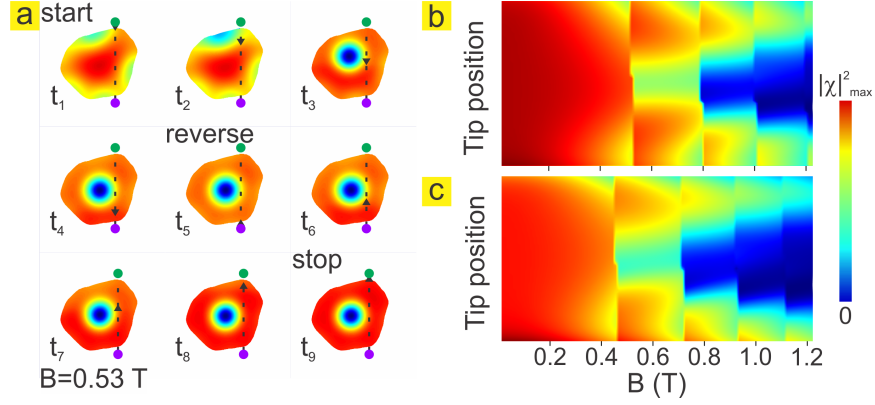


Figure 6.12: (a) Snapshots of the superconducting condensate in equilibrium at $B = 0.53$ T (transition from $L = 0$ to $L = 1$ state), taken at nine different locations, as the tip performs the scan across the island. Scanning trajectory is denoted with dashed line, and it starts from the green dot (t_1). As the tip moves further (instances $t_2 - t_4$), the part of the island under it experiences the increase in temperature to $T = 0.1T_c$, which allows the vortex to penetrate inside the island. At the instance t_5 the tip reaches the purple dot, and it reverses its motion back to green dot (instances $t_6 - t_9$). In the final snapshot, the vortex remains in the island, as a stable state. (b) Diagram of $|\chi|^2$ under the tip taken as the tip moves along the dashed line in (a), versus the magnetic field, corresponding to the tip-induced local increase of temperature to $0.1T_c$, where no curved transition lines are found in the diagram. (c) The phase diagram obtained in the same way as the one in (b), with increased tip-induced heating ($T = 0.3T_c$). Once again, no pronounced curved transitions between states of different vorticity are found.

with visible small kinks at every transition line, and again without any special curvature in those lines. Therefore, one can conclude that the observed behavior, which is purely due to thermal effects, cannot be responsible for the phenomenon seen in experiment and shown in Fig. 6.8. The tip-induced thermal influence considered in the simulations (up to 30 percent of the critical temperature) can even be considered greatly exaggerated, since during the experimental measurement the temperature of the island was directly measured, and never exceeded 350 mK ($\tilde{T} \approx 0.05$) [295].

Therefore, in what follows we turn our attention to the possible gating effects of the tip on the island. As a consequence of the additional electronic band crossing the Fermi level produced by the electrostatic gating, one may expect that the STM

probe changes the critical temperature of the gated part of the island. However, it was found in Ref. [296] that the Pb islands with thickness of 9 ML (where gating is relevant) exhibited a minimal change in T_c compared to the 8 ML islands (where gating is not relevant), so we can safely exclude at this stage the contribution of changing T_c from the explanation of the observed effects in experiment.

The only remaining parameter to consider as a variable in gTDGL model is the diffusivity, which may indeed change due to the presence of the STM tip. The main constituents of the diffusivity, namely the mean free path and the Fermi velocity, are directly affected by the additional energy level introduced to the superconducting state via gating. In ultrathin Pb, the energy bands in question are fairly flat [281] and carry large density of states, hence can cause considerable change in the average mean free path and the Fermi velocity of electrons participating in the Cooper pairing. Though the experimental data shown in Fig. 6.6(a,b) lead one to conclude that the gating-induced electronic-band-crossing would enhance the overall superconducting properties of the island in question, it is however not trivial to directly quantify the resulting enhancement. That is why, similarly to the case of heating, we model the change in diffusivity as

$$\frac{D(\mathbf{r}, t)}{D(\text{pristine})} = \begin{cases} p_D(\mathbf{r}, t), & \text{under the tip,} \\ 1, & \text{everywhere else,} \end{cases} \quad (6.2)$$

where, in general, $p_D(\mathbf{r}, t)$ takes values below 1 in case of enhanced superconductivity, and above 1 in case of suppressed superconductivity. Moreover, one should also keep in mind the possible ambiguity in the interpretation of the experimental results regarding the actual position of the tip on the STM probe, as illustrated in Fig. 6.10(c). Under the assumption that the total area of the electric field effect of the probe (i. e. where the gating is relevant) is comparable to the size of the Pb island under investigation, we consider two possible cases: (i) case where the tip is located at the frontal part of the probe moving across the island [as in inset (1) in Fig. 6.10(c)], and scans the part of the island that is being affected by the gating, and case (ii) where the tip is at the back of the moving probe [as depicted in inset (3) in Fig. 6.10(c)], so it scans the gated part of the island that is about to be recovered to the pristine state. For multiple values of parameter p_D we conducted simulations in which due to the presence of the tip, gating enhances superconducting properties, and the clearly noticeable change in the system occurs when $p_D \leq 0.5$. We present the phase diagrams in Fig. 6.13 for $p_D = 0.3$, where panel (a) corresponds to the case (i) and panel (b) to case (ii) regarding the location of the tip on the probe. In these diagrams, transitions between the states of different vorticity are clearly curved, with curvatures becoming more pronounced at higher

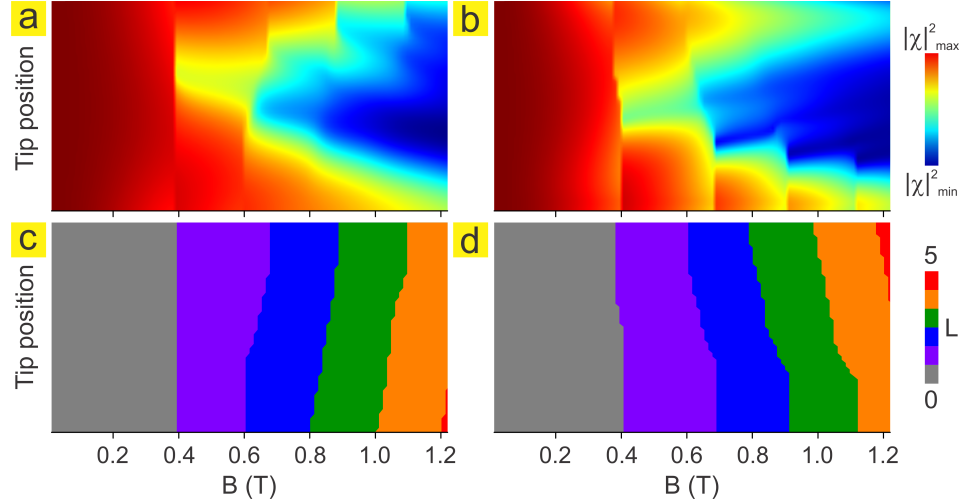


Figure 6.13: (a,b) Phase diagrams of the value of the order parameter under the tip as a function of magnetic field, obtained when the tip is located at the front of the STM probe [see Fig. 6.10(c), inset (1)], or in the back of the STM probe [as depicted in inset (3) in Fig. 6.10(c)], respectively, and moves along the line indicated in Fig. 6.10(a). (c,d) Vorticity diagrams corresponding to (a) and (b), respectively, obtained by detecting the number of vortices in the island for every tip position and each value of the applied magnetic field.

magnetic fields. In order to make it easier to distinguish the transitions between the different states, we also provide the matching diagrams of the vorticity in the island in panels (c) and (d) of the Fig. 6.13, corresponding to cases (i) and (ii), respectively. For each position of the tip and for each value of the magnetic field, the vorticity diagrams were obtained by inspecting the phase of the order parameter in the entire island. It turns out from these diagrams that the gating in setup (i) (panels (a) and (c) in Fig. 6.13) causes the curvatures in the transition lines to be in the opposite direction compared to the experimental data in Fig. 6.8. On the other hand, simulation of the gating based on the setup (ii) [see Fig. 6.13(b,d)] qualitatively reproduces the experimental results seen in Fig. 6.8.

As the diagrams in Fig. 6.13(a,c) suggest [case (i)], while the gating becomes relevant in the larger area of the island during the scanning, manifested through the local decrease of the diffusivity, vortices can be driven out of the island due to the enhancement of superconductivity. At lower magnetic fields it is necessary for the tip to gate more of the island in order to expel vortices, however, as the mag-

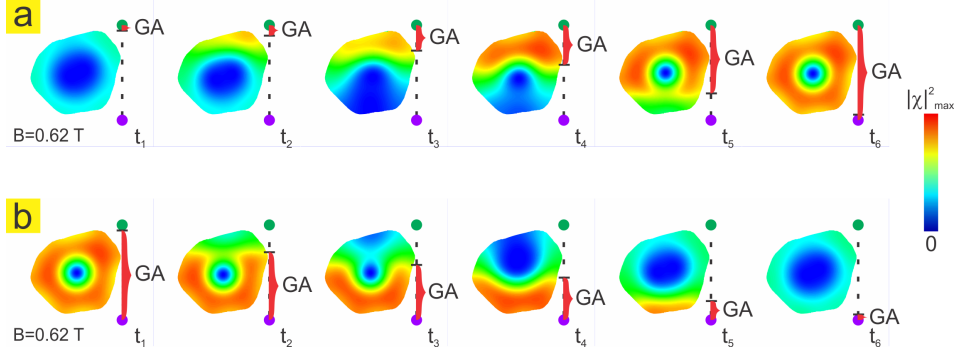


Figure 6.14: Sequence of the gating procedure as the tip moves across the Pb island at $B = 0.62$ T, when the tip is located in the front of the STM probe (a), or in the back of the STM probe (b). As reflected through the Cooper-pair density plots at six characteristic instances, the tip is driven across the island (top to bottom in the images). The correspondingly gated area (GA) is denoted by the stretching red band on the right, where superconductivity is enhanced.

netic field increases and the states of higher vorticities are stabilized, it becomes easier to drive the vortices outside the island. As an illustration, for the magnetic field of 0.62 T, we display the behavior of the superconducting condensate through six-instances-long sequence of the gating in Fig. 6.14(a). From there, it is clear that when the tip progresses further into the island [so that the gated area (GA) is increased], instead of the two vortices being present in the sample, as prior to the gating (t_1 and t_2), one of them will be pushed out (t_3 and t_4), finally leaving the island with only one vortex present (t_5 and t_6).

If the situation is reversed [case (ii)], so that superconductivity recovers from the enhancement as the tip moves deeper in the island, vortex entry is facilitated, increasingly more with increase of the magnetic field. For such a scenario we also provided insets of the CPD in Fig. 6.14(b) during the gating at $B = 0.62$ T. From the insets it is visible that now the gated area (GA) decreases as the tip progresses further into the island, which allows entry of an additional vortex into the island. Due to the qualitative agreement between the phase diagrams in Figs. 6.8(a) and 6.13(b), one can argue that this is likely the behavior occurring in the experiment.

This analysis of the observed gating effect points out the change in the particular superconducting properties, expected to occur in the ultrathin crystalline films whose thickness imposes specific conditions on the electronic structure. gT-DGL theory nicely reproduces the main features seen in experiment, based on local change in electronic properties and not the thermal ones. However, in order to fully

Chapter 6

grasp the phenomenon presented here, or reach better quantitative agreement between theory and the experiment one must enter the domain of the microscopic theory of superconductivity, which is out of the scope of this thesis.

Chapter 7

Conclusion

The principal objective of this thesis was to study the novel effects emerging in vortex matter, in mesoscopic superconducting condensates under externally-controlled temporal and spatial variations. Since the presence of vortices is of great importance in both fundamental scientific research of superconductors and practical applications, where their dissipative motion can be either detrimental or beneficial (depending on how the working principles of device are postulated), it is of paramount value to understand how can one manipulate vortices with precision, yet in a variety of ways. The overall behavior of vortices depends on a multitude of conditions (i.e. spatial and temporal confinement, inherent and externally added disorder, permanent or dynamic artificial pinning landscapes with stationary or varying intensity and distribution), so their efficient manipulation can be a difficult task. Here, different approaches in control of vortex matter have been shown, starting from systems where current lensing arising due to geometric features of the sample causes vortex motion with extremely high velocities, over superconducting systems with dynamic pinning landscapes in which the stroboscopic resonances arise, to finally ultrathin crystalline superconducting structures under the influence of electronic gating that can locally change the superconducting properties of the sample.

Common properties of the dynamic behavior of the superconducting condensate and the vortex matter arising from the presence of the magnetic field and the transport electric current can be very conveniently and accurately described by generalized time-dependent Ginzburg-Landau (gTDGL) theory. On the basis of the gTDGL model we developed a powerful theoretical simulation tool, capable of treating superconductivity in samples of arbitrary geometry, and in the presence of external temporally and spatially dependent potentials used to manipulate the vortex matter. Substantiated with the microscopic justification, the model detailed and

used in this thesis accounts for the possible inhomogeneities in the material parameters, while the inclusion of the equation of thermal balance in the model provided the means to address the ever-present self-heating effects of the system, which, finally, allows one to theoretically treat even more complex realistic systems.

The first major success of our gTDGL model was to capture the relevant phenomena regarding the ultrafast vortex matter, which was evidenced for the very first time in the group of prof. Eli Zeldov at Weizmann Institute of Science in Israel. Using a nanoscale SQUID with unprecedented spatial resolution and sensitivity, they were able to image for the first time vortices penetrating into a superconducting microbridge at rates of tens of GHz and moving with super-fast velocities up to tens of km/s. Such velocities exceed the pair-breaking speed limit of the Cooper-pair condensate by two orders of magnitude, a phenomenon that our simulations were able to capture as well. This study, based on both experimental and theoretical analysis, revealed striking metamorphosis of vortices at such extreme velocities, including unconventional dynamic states comprising cascades of bifurcations of vortex channels as the current and magnetic field are increased. Moreover, our work brings about the fundamental issue of whether the notion of a vortex as a stable topological defect remains applicable at such extreme velocities. We presented our study of the actual evolution of vortex patterns and discussion of the underlying physics in a clear and visually self-explanatory way in order to reach out a broad scientific audience. The physics of superfast vortex matter may have far-reaching interdisciplinary implications in such seemingly different fields as dynamics of supersonic dislocations, particles motion in viscous media, or general pattern formations out of equilibrium.

Another important aspect of this thesis concerns the dynamic landscape used to control the motion of vortex matter in superconducting condensates. There, we explored the temporal matching phenomena of the characteristic vortex dynamics under applied current and magnetic field, to a specially designed time-dependent thermal pinning landscape, in order to develop an innovative method for experimental monitoring, reliable measurement, and tuning of the vortex velocity. We not only propose a novel technique, but also analyze its sensitivity to the relevant experimental factors, and discuss the high vortex velocities for different superconducting materials of current interest (also for potential applications). On fundamental end, we discuss the ability of the method to probe the mobility of different kinds of vortices (Abrikosov to Josephson) encountered on the path to the Larkin-Ovchinnikov instability at ultrahigh vortex velocity. Understanding the kinematics of those vortices and their properties is very important for mastering the dissipation in superconductors at high driving currents and hence is of technological relevance as well.

External modulation of the superconducting condensate can be observed in ul-

trathin islands, where strong quantum confinement exists, so the quantization of the electron motion emerges, resulting in the formation of electronic quantum-well states. It was noticed that in the samples of specific thickness these quantum wells are very sensitive to external modulation via STM probe by changing the electronic structure of the superconductor. In this study, where experimental data from the research group at INSP Paris are complemented by our theoretical analysis, evidences for electronic gating were found. The shown gTDGL simulations exclude the local heating as the source of experimentally observed phenomena, and reproduce a very peculiar experimentally recorded phase diagram when assuming a purely electronic effect of the tip on the superconducting condensate. Considering that gTDGL theory successfully captured all the key features seen in experimental phase diagram, further simulations of particular vortex devices are foreseen (such as quantum switches where the tunneling conductance through the vortex is manipulated by electronically changing its vorticity [297], or transport switches where for fixed applied current the vortex flow is turned on-off by the gating, or the dynamic resistivity is tuned in desired range - of potential use for adjusting the sensitivity of crystalline superconducting single-photon detectors), where local gating can be of particular use.

Although we provided thorough theoretical analysis of novel phenomena arising from manipulation of vortex matter, still more work needs to be done in this field. For example, the mere existence of above mentioned ultrafast vortices raises many questions, both from fundamental science and possible application standpoints (high-field magnets, superconducting digital memory and qubits, THz radiation sources, to name a few).

Though the presented gTDGL model proved to be a powerful asset in the analysis of realistic systems, there is still room for improvement. One of the most frequent criticisms directed towards gTDGL theory is the fact that it is trustworthy only at the temperatures close to the critical one. Even though some empirical solutions have been proposed, the actual expansion of the theory to wider temperature ranges must be provided in the microscopic framework (such as BCS theory), which is far from a trivial task. Moreover, since the significant computational resources are needed for simulations of the large-scale superconducting structures, such as circuitry consisting of a multiple superconducting devices, an innovative approach in the development of the optimal equation solvers must be employed, where advanced algorithms for resource management are utilized. Finally, the all-inclusive gTDGL model, which solves all of the Eqs. 2.65-2.68 simultaneously, without simplifications through usage of additional gauges, is needed in order to maximize the reliability when studying the realistic systems.

Appendices

Appendix A

Details about numerical approach

A.1 Euler method for temporal derivatives

Euler method is a computational algorithm employed for solving the first-order differential equations of the form

$$\frac{d\chi}{d\tilde{t}} = P(\chi, \tilde{t}), \quad (\text{A.1})$$

defined with a corresponding initial guess $\chi(\tilde{t} = \tilde{t}_0) = \chi_0$. Function $P(\chi, \tilde{t})$ contains some known dependence on quantities χ and \tilde{t} , and it also can include spatial derivatives of χ . On a finite and discrete interval, $[\tilde{t}_0, \tilde{t}_T]$, where \tilde{t}_k and \tilde{t}_{k+1} are two adjacent instances ($\tilde{t}_0 \leq \tilde{t}_k < \tilde{t}_{k+1} \leq \tilde{t}_T$, and $\Delta\tilde{t} = \tilde{t}_{k+1} - \tilde{t}_k$), within the forward finite difference representation one can exchange Eq. A.1 with an approximate expression

$$\frac{\chi(\tilde{t}_{k+1}) - \chi(\tilde{t}_k)}{\Delta\tilde{t}} = \frac{\chi^{(k+1)} - \chi^{(k)}}{\Delta\tilde{t}} = P[\chi(\tilde{t}_k), \tilde{t}_k] = P^{(k)}, \quad (\text{A.2})$$

for every instance $\tilde{t}_k \in [\tilde{t}_0, \tilde{t}_T]$. This is, in essence, the Euler method. From here it is easy to obtain updated value of χ at instance \tilde{t}_{k+1} , as

$$\chi^{(k+1)} = \chi^{(k)} + \Delta\tilde{t}f^{(k)}. \quad (\text{A.3})$$

One can notice here that Eq. A.3 has exactly the same form of Eq. 2.52 from Chapter 2. The Euler method is a first-order method, which means that the local error (error per step) is proportional to the square of the step size, and the global error (error at a given time) is proportional to the step size. In this thesis, Euler method is used in combination with direct explicit approach for solving partial differential equation (first gTDGL equation), which imposes some constraints on the time step, $\Delta\tilde{t}$. This will be explained in the following Section.

A.2 Direct explicit solution of first gTDGL equation in arbitrary geometries

First gTDGL equation in this work is solved with the combination of Euler method and direct explicit solver. The form of this equation is given in Eqs. 2.52 and 2.53. However, in order to determine the spatio-temporal behavior of complex order parameter χ in arbitrary geometries, one must somehow introduce the geometry into the equation itself. This is done through the boundary conditions. For the first gTDGL equation, there are two possible boundary conditions considered in this thesis: superconductor-insulator (vacuum) interface [SI(V)], and superconductor-normal metal interface (SN).

First boundary condition prohibits the flow of supercurrent component perpendicular to the interface $\left[(\tilde{\nabla} - i\mathbf{Q}) \chi|_{SI(V)} = 0 \right]$, and second condition imposes vanishing order parameter ($\chi|_{SN} = 0$). Since all the nonuniform geometries considered in this thesis exhibit nonuniformity only through SI(V) boundary, one can devise a simple way to include these boundary conditions inside Eq. 2.52 by introducing a map L of the 2D geometry, constructed upon a rectangle of the size $L_x \times L_y$ (with a corresponding number of gridpoints $N_x \times N_y$, where the size of each unit cell is $\Delta x \times \Delta y$), where superconducting area at some point is denoted by $L_{m,n} = 1$, and insulator (vacuum) in another point is denoted by value 0. Within finite-difference representation and link-variable method, these boundary conditions are implemented in the following way:

$$\begin{aligned} \chi_{m,n}^{(k+1)} &= \chi_{m,n}^{(k)} + \Delta \tilde{t} f_{m,n}^{(k)} L_{m,n} = \chi_{m,n}^{(k)} + \Delta \tilde{t} \Phi_{m,n}^{(k)} L_{m,n} - \\ &\Delta \tilde{t} \left[iV_{m,n} + \frac{\tilde{\Gamma}^2}{1 + \tilde{\Gamma}^2 |\chi_{m,n}^{(k)}|^2} \Re \left\{ \chi_{m,n}^{(k)*} \Phi_{m,n}^{(k)} \right\} \right] \chi_{m,n}^{(k)} L_{m,n}, \end{aligned} \quad (\text{A.4})$$

and

$$\begin{aligned} \Phi_{m,n}^{(k)} &= \Theta \frac{\left(\tilde{U}_{x_{m+1,n}}^{(k)} \chi_{m+1,n}^{(k)} - \chi_{m,n}^{(k)} \right) L_{m+1,n}}{\Delta x^2} + \\ &\Theta \frac{\left(\tilde{U}_{x_{m-1,n}}^{(k)} \chi_{m-1,n}^{(k)} - \chi_{m,n}^{(k)} \right) L_{m-1,n}}{\Delta x^2} + \\ &\Theta \frac{\left(\tilde{U}_{y_{m,n+1}}^{(k)} \chi_{m,n+1}^{(k)} - \chi_{m,n}^{(k)} \right) L_{m,n+1}}{\Delta y^2} + \\ &\Theta \frac{\left(\tilde{U}_{y_{m,n-1}}^{(k)} \chi_{m,n-1}^{(k)} - \chi_{m,n}^{(k)} \right) L_{m,n-1}}{\Delta y^2} + \Theta \left(f_{m,n}^{(k)} - g_{m,n}^{(k)} |\chi_{m,n}^{(k)}|^2 \right) \chi_{m,n}^{(k)}, \end{aligned} \quad (\text{A.5})$$

where $\Theta = \frac{\sqrt{1+\tilde{\Gamma}^2|\chi_{m,n}^{(k)}|^2}}{u}$. Notice how the second-order derivatives (i.e. kinetic term) in Eq. A.5 are now split, so they explicitly contain two components each - forward and backward finite difference representation of first-order derivatives, which are exactly the boundary conditions for the supercurrent left, right, up and down from the given point (m, n) . If any of the neighboring points is outside of the superconducting region, components of the map parameter, $L_{m+1,n}$, $L_{m-1,n}$, $L_{m,n+1}$, or $L_{m,n-1}$ are going to impose the boundary condition and set the component of the second-order derivative to zero. On the other hand, if the current point (m, n) is already outside of the superconductor, map parameter $L_{m,n} = 0$ prohibits any survival of the order parameter there.

Solving the first gTDGL equation is done in an iterative manner, where the iterations are performed within the interval $[\tilde{t}_0, \tilde{t}_T]$, with each iteration done over time $\Delta\tilde{t}$. Since this equation is solved with direct explicit solver in combination with Euler method, the solution will be conditionally stable, i.e. a relation between $\Delta\tilde{t}$, Δx , and Δy exists. Since usually Δx and Δy are predefined, then limitations are imposed upon $\Delta\tilde{t}$ from being arbitrarily large. Further limitations on $\Delta\tilde{t}$ can be empirically found with increase of $\tilde{\Gamma}$, which can dramatically slow down the performance of the simulations in case of realistic materials with large $\tilde{\Gamma}$.

A.3 Crank-Nicolson method for diffusion-like equations in arbitrary geometries

Direct explicit solvers for diffusion-like equations (e.g. first and second gTDGL equation, or equation of thermal balance) impose quite a limitation on the performance of the simulation, which develops into a nuisance especially when one works with large and realistic systems. For this reason, more stable algorithms have been developed. *Crank-Nicolson* algorithm (CN) is one of them, which is a second-order implicit method in time.

CN scheme for the diffusion-like differential equation can be written as

$$\frac{\tilde{u}^{(k+1)} - \tilde{u}^{(k)}}{\Delta\tilde{t}} = \frac{1}{2} \left[P^{(k+1)}(\tilde{u}) + P^{(k)}(\tilde{u}) \right], \quad (\text{A.6})$$

where the solution of the next iteration, $\tilde{u}^{(k+1)}$, must be solved implicitly from the system of algebraic equations. If the partial differential equation is nonlinear, the discretization in \tilde{t} will also be nonlinear so that advancing in time will involve the solution of a system of nonlinear algebraic equations, though linearizations are possible. In many problems, especially linear diffusion, the algebraic problem is tridiagonal and may be efficiently solved with the tridiagonal matrix algorithm,

which gives a fast $\mathcal{O}(n)$ direct solution as opposed to the usual $\mathcal{O}(n^3)$ for a full matrix. For example, one can rewrite first gTDGL equation (A.4) in this way, in order to increase the stability of temporal convergence. Another equation that can be solved this way is the second gTDGL equation (Eq. 2.58). In order to do so, one must first transform Eq. 2.58 into a more user-friendly diffusion-like equation, as was done in Ref. [298],

$$\begin{aligned} \frac{\tilde{u}_{\mu m,n}^{(k+1)} - \tilde{u}_{\mu m,n}^{(k)}}{\Delta \tilde{t}} = \Im \left\{ e^{-i\tilde{u}_{\mu m,n}^{(k)}} \chi_{m,n}^{(k)*} \chi_{m+1,n}^{(k)} \right\} L_{m+1,n} L_{m,n} + \\ \frac{\kappa^2 L_{m,n}}{\Delta(\mu+1)^2} \left[\left(\tilde{u}_{\mu m,n+1}^{(k)} - \tilde{u}_{\mu m,n}^{(k)} \right) L_{m,n+1} + \left(\tilde{u}_{\mu m,n-1}^{(k)} - \tilde{u}_{\mu m,n}^{(k)} \right) L_{m,n-1} \right] + \\ \tilde{P} \left(\tilde{u}_{\mu+1 m,n}^{(k)} \right). \end{aligned} \quad (\text{A.7})$$

In order to derive Eq. A.7 from 2.58, μ -th component of the link variable $\tilde{U}_{\mu m,n}$ ($\mu = x, y$, with cyclic permutation for $\mu = x$ given as $\mu + 1 = y$, and for $\mu = y$ given as $\mu + 1 = x$) needs to be represented as $e^{-i\tilde{u}_{\mu m,n}^{(k)}}$, where $\tilde{u}_{\mu m,n}^{(k)}$ is a real function, directly proportional to the μ -th component of the vector potential. Order parameter here is denoted once again with χ , and function \tilde{P} contains remaining terms from Eq. 2.58, independent of \tilde{u}_{μ} . Equation A.7 now has a form of diffusion equation

$$\frac{\partial \tilde{u}_{\mu}(\mathbf{r}, \tilde{t})}{\partial \tilde{t}} = P(\tilde{u}_{\mu}) + \tilde{P}, \quad (\text{A.8})$$

and CN method can be implemented on it as

$$\begin{aligned} \tilde{u}_{\mu m,n}^{(k+1)} - \frac{\Delta \tilde{t}}{2} \Im \left\{ e^{-i\tilde{u}_{\mu m,n}^{(k+1)}} \chi_{m,n}^{(k+1)*} \chi_{m+1,n}^{(k+1)} \right\} L_{m+1,n} L_{m,n} + \\ \frac{\Delta \tilde{t} \kappa^2}{2\Delta(\mu+1)^2} \left(\tilde{u}_{\mu m,n+1}^{(k+1)} - \tilde{u}_{\mu m,n}^{(k+1)} \right) L_{m,n+1} L_{m,n} + \\ \frac{\Delta \tilde{t} \kappa^2}{2\Delta(\mu+1)^2} \left(\tilde{u}_{\mu m,n-1}^{(k+1)} - \tilde{u}_{\mu m,n}^{(k+1)} \right) L_{m,n-1} L_{m,n} + \frac{\Delta \tilde{t}}{2} \tilde{P} \left(\tilde{u}_{\mu+1 m,n}^{(k+1)} \right) = \\ \tilde{u}_{\mu m,n}^{(k)} - \frac{\Delta \tilde{t}}{2} \Im \left\{ e^{-i\tilde{u}_{\mu m,n}^{(k)}} \chi_{m,n}^{(k)*} \chi_{m+1,n}^{(k)} \right\} L_{m+1,n} L_{m,n} + \\ \frac{\Delta \tilde{t} \kappa^2}{2\Delta(\mu+1)^2} \left(\tilde{u}_{\mu m,n+1}^{(k)} - \tilde{u}_{\mu m,n}^{(k)} \right) L_{m,n+1} L_{m,n} + \\ \frac{\Delta \tilde{t} \kappa^2}{2\Delta(\mu+1)^2} \left(\tilde{u}_{\mu m,n-1}^{(k)} - \tilde{u}_{\mu m,n}^{(k)} \right) L_{m,n-1} L_{m,n} + \frac{\Delta \tilde{t}}{2} \tilde{P} \left(\tilde{u}_{\mu+1 m,n}^{(k)} \right). \end{aligned} \quad (\text{A.9})$$

If one considers only the behavior of a superconducting film in the presence of magnetic field, and in the absence of transport current, a unique boundary condition

can be imposed on the vector potential, $\tilde{\nabla} \times \mathbf{Q} = \tilde{\mathbf{B}}_{ext}$, stating that at the edge of simulated area, all magnetic field must be equal to the applied external magnetic field. One can also consider (infinitely) long current-carrying filaments within this treatment, but then, periodic boundary conditions [$\mathbf{Q}(\mathbf{r}, t) = \mathbf{Q}(\mathbf{r} + L, t)$, where L is the spatial period] must be provided in the direction of the dominant size of the specimen. Then the current induced magnetic field contribution is added to the remaining boundary condition at SI(V) interface as $\tilde{\nabla} \times \mathbf{Q} = \tilde{\mathbf{B}}_{ext} + \tilde{\mathbf{B}}_I$, where the magnitude of $\tilde{\mathbf{B}}_I$ is approximated as linear function of the applied current. The orientation of the current-induced magnetic field must match the orientation of the applied field at one side of the sample, while opposing it at the facing side. One should also notice that within this approach, no nonuniformity, such as pinning centers or constrictions, can be correctly included in the superconducting filaments.

A.4 Alternating Direction Implicit method for diffusion-like equations in arbitrary geometries

Though it comes with an improved stability, CN scheme exploits excessive computational resources, and thus can be very cumbersome for solving. The main disadvantage of the CN method lies in the fact that the matrices in the above equations are banded, with a band width that is generally quite large. This makes direct solution of the system of linear equations quite costly (although efficient approximate solutions exist, for example using the conjugate-gradient method preconditioned with incomplete Cholesky factorization). However, CN algorithm can be further modified in such a manner that the spatial operators are separated, thus providing equation of simpler form. This approach is called *alternating direction implicit method* (ADI), and in that case the equations that have to be solved in each step have a less complex structure and can be solved efficiently with the tridiagonal matrix algorithm (Gaussian elimination). As an introductory example, one can consider diffusion-like kernel, written such that both spatial and temporal derivatives are given explicitly

$$\frac{\partial \tilde{u}}{\partial t} = \frac{\partial^2 \tilde{u}}{\partial x^2} + \frac{\partial^2 \tilde{u}}{\partial y^2} + P(\tilde{u}). \quad (\text{A.10})$$

The idea behind the ADI method here is to split Eq. A.10 into two CN-like equations, one with the x derivative taken implicitly and the other with the y derivative taken implicitly,

$$\frac{\tilde{u}^{(k+1/2)} - \tilde{u}^{(k)}}{\Delta \tilde{t}} = \frac{1}{2} \left[\frac{\partial^2 \tilde{u}}{\partial x^2} + P(\tilde{u}) \right]^{(k+1/2)} + \frac{1}{2} \left[\frac{\partial^2 \tilde{u}}{\partial y^2} + P(\tilde{u}) \right]^{(k)}, \quad (\text{A.11})$$

Appendix A

$$\frac{\tilde{u}^{(k+1)} - \tilde{u}^{(k+1/2)}}{\Delta \tilde{t}} = \frac{1}{2} \left[\frac{\partial^2 \tilde{u}}{\partial y^2} + P(\tilde{u}) \right]^{(k+1)} + \frac{1}{2} \left[\frac{\partial^2 \tilde{u}}{\partial x^2} + P(\tilde{u}) \right]^{(k+1/2)}. \quad (\text{A.12})$$

Notice that the separation of the operators revolves around virtual instance $\tilde{t}_{k+1/2}$, at which Eq. A.11 is solved.

In the thesis, ADI method was used to solve Eq. 2.64 for both spatial and temporal evolution of the temperature in arbitrary geometries. As just shown on a simpler example, one first needs to start from discretized CN scheme for arbitrary geometries, which takes the form

$$\begin{aligned} & \tilde{T}_{m,n}^{(k+1)} - \frac{\Delta \tilde{t}}{2\tilde{c}} \left[\left(\tilde{T}_{m,n}^{(k+1)} - \tilde{T}_0 \right) \tilde{h} + \tilde{\mathbf{J}}_{nm,n}^{(k+1)^2} \right] L_{m,n} + \\ & \frac{\Delta \tilde{t}}{2} \left(\frac{\tilde{T}_{m+1,n}^{(k+1)} - \tilde{T}_{m,n}^{(k+1)}}{\Delta x^2} L_{m+1,n} + \frac{\tilde{T}_{m-1,n}^{(k+1)} - \tilde{T}_{m,n}^{(k+1)}}{\Delta x^2} L_{m-1,n} \right) \frac{\tilde{k}}{\tilde{c}} L_{m,n} + \\ & \frac{\Delta \tilde{t}}{2} \left(\frac{\tilde{T}_{m,n+1}^{(k+1)} - \tilde{T}_{m,n}^{(k+1)}}{\Delta y^2} L_{m,n+1} + \frac{\tilde{T}_{m,n-1}^{(k+1)} - \tilde{T}_{m,n}^{(k+1)}}{\Delta y^2} L_{m,n-1} \right) \frac{\tilde{k}}{\tilde{c}} L_{m,n} = \\ & \tilde{T}_{m,n}^{(k)} - \frac{\Delta \tilde{t}}{2\tilde{c}} \left[\left(\tilde{T}_{m,n}^{(k)} - \tilde{T}_0 \right) \tilde{h} + \tilde{\mathbf{J}}_{nm,n}^{(k)^2} \right] L_{m,n} + \\ & \frac{\Delta \tilde{t}}{2} \left(\frac{\tilde{T}_{m+1,n}^{(k)} - \tilde{T}_{m,n}^{(k)}}{\Delta x^2} L_{m+1,n} + \frac{\tilde{T}_{m-1,n}^{(k)} - \tilde{T}_{m,n}^{(k)}}{\Delta x^2} L_{m-1,n} \right) \frac{\tilde{k}}{\tilde{c}} L_{m,n} + \\ & \frac{\Delta \tilde{t}}{2} \left(\frac{\tilde{T}_{m,n+1}^{(k)} - \tilde{T}_{m,n}^{(k)}}{\Delta y^2} L_{m,n+1} + \frac{\tilde{T}_{m,n-1}^{(k)} - \tilde{T}_{m,n}^{(k)}}{\Delta y^2} L_{m,n-1} \right) \frac{\tilde{k}}{\tilde{c}} L_{m,n}, \end{aligned} \quad (\text{A.13})$$

where the corresponding boundary condition $\tilde{\nabla} \tilde{T} = 0$ along the SI(V) interface is implemented internally, with help of the map L . At the SN interface the Dirichlet boundary condition is imposed, so in those points the value of $\tilde{T}(r)$ is implicitly inherited from the user-defined initial solution for the temperature.

Under the assumption that spatial operators are independent, one can split Eq.

A.13 into two simpler equations

$$\begin{aligned}
 & \tilde{T}_{m,n}^{(k+1/2)} - \frac{\Delta \tilde{t}}{2\tilde{c}} \left[\left(\tilde{T}_{m,n}^{(k+1/2)} - \tilde{T}_0 \right) \tilde{h} + \tilde{\mathbf{J}}_{n_{m,n}}^{(k+1/2)^2} \right] L_{m,n} + \\
 & \frac{\Delta \tilde{t}}{2} \left(\frac{\tilde{T}_{m+1,n}^{(k+1/2)} - \tilde{T}_{m,n}^{(k+1/2)}}{\Delta x^2} L_{m+1,n} + \frac{\tilde{T}_{m-1,n}^{(k+1/2)} - \tilde{T}_{m,n}^{(k+1/2)}}{\Delta x^2} L_{m-1,n} \right) \frac{\tilde{k}}{\tilde{c}} L_{m,n} = \\
 & \tilde{T}_{m,n}^{(k)} - \frac{\Delta \tilde{t}}{2\tilde{c}} \left[\left(\tilde{T}_{m,n}^{(k)} - \tilde{T}_0 \right) \tilde{h} + \tilde{\mathbf{J}}_{n_{m,n}}^{(k)^2} \right] L_{m,n} + \\
 & \frac{\Delta \tilde{t}}{2} \left(\frac{\tilde{T}_{m,n+1}^{(k)} - \tilde{T}_{m,n}^{(k)}}{\Delta y^2} L_{m,n+1} + \frac{\tilde{T}_{m,n-1}^{(k)} - \tilde{T}_{m,n}^{(k)}}{\Delta y^2} L_{m,n-1} \right) \frac{\tilde{k}}{\tilde{c}} L_{m,n},
 \end{aligned} \tag{A.14}$$

and

$$\begin{aligned}
 & \tilde{T}_{m,n}^{(k+1)} - \frac{\Delta \tilde{t}}{2\tilde{c}} \left[\left(\tilde{T}_{m,n}^{(k+1)} - \tilde{T}_0 \right) \tilde{h} + \tilde{\mathbf{J}}_{n_{m,n}}^{(k+1)^2} \right] L_{m,n} + \\
 & \frac{\Delta \tilde{t}}{2} \left(\frac{\tilde{T}_{m,n+1}^{(k+1)} - \tilde{T}_{m,n}^{(k+1)}}{\Delta y^2} L_{m,n+1} + \frac{\tilde{T}_{m,n-1}^{(k+1)} - \tilde{T}_{m,n}^{(k+1)}}{\Delta y^2} L_{m,n-1} \right) \frac{\tilde{k}}{\tilde{c}} L_{m,n} = \\
 & \tilde{T}_{m,n}^{(k+1/2)} - \frac{\Delta \tilde{t}}{2\tilde{c}} \left[\left(\tilde{T}_{m,n}^{(k+1/2)} - \tilde{T}_0 \right) \tilde{h} + \tilde{\mathbf{J}}_{n_{m,n}}^{(k+1/2)^2} \right] L_{m,n} + \\
 & \frac{\Delta \tilde{t}}{2} \left(\frac{\tilde{T}_{m+1,n}^{(k+1/2)} - \tilde{T}_{m,n}^{(k+1/2)}}{\Delta x^2} L_{m+1,n} + \frac{\tilde{T}_{m-1,n}^{(k+1/2)} - \tilde{T}_{m,n}^{(k+1/2)}}{\Delta x^2} L_{m-1,n} \right) \frac{\tilde{k}}{\tilde{c}} L_{m,n}.
 \end{aligned} \tag{A.15}$$

The system of involved equations is symmetric and tridiagonal, and is typically solved using tridiagonal matrix algorithm. It can be shown that this method is unconditionally stable and second-order in time and space [299]. There are more refined ADI methods such as the methods of Douglas [300], or the f-factor method [301] which can be used for three or more dimensions.

A.5 Fast Fourier transform for direct solution of Poisson-like equations

Fourier transform (FT) is a procedure in which a signal (a physical quantity) is converted into a type of frequency domain. Besides the fact that such transformation reveals certain properties of the observed quantity, otherwise inaccessible, one can use Fourier transformation to solve differential equations. The convenience arising

from FT is that in the frequency domain differential equations can turn into algebraic equations, thus making them much easier to solve. Following the solution in frequency domain, one just needs to apply inverse FT in order to get real-time and/or real-space distribution of the signal. When dealing with numerical calculations, discrete form of FT comes into play (dFT), and very reliable algorithm for performing dFT of a discrete signal is fast FT (FFT). FFT method rapidly computes signal transformations by factorizing the dFT matrix into a product of sparse factors. As a result, it manages to reduce the complexity of computing the dFT from $\mathcal{O}(n^2)$, which arises if one simply applies the definition of dFT, to $\mathcal{O}(n \log n)$, where n is the data size. FFT of a physical quantity f is obtained according to

$$\hat{f}_{i,j} = \sum_{m=0}^{N_x} \sum_{n=0}^{N_y} f_{m,n} \cos \frac{\pi j m}{N_x} \frac{\pi i n}{N_y}, \quad (\text{A.16})$$

while the inverse FFT of a given quantity is

$$f_{m,n} = \frac{2}{N_x} \frac{2}{N_y} \sum_{i=0}^{N_x} \sum_{j=0}^{N_y} \hat{f}_{i,j} \cos \frac{\pi j m}{N_x} \frac{\pi i n}{N_y}. \quad (\text{A.17})$$

Perfect example where FFT algorithm can be applied is Poisson-like differential equation, into which Eq. 2.44 transforms for extreme type II superconductors, in the London gauge, $\tilde{\nabla} \mathbf{Q} = 0$. Equation 2.44 is solved in a region with Neumann boundary conditions for electrostatic potential ($\tilde{\nabla} V = 0$ at SI(V) boundary and $\tilde{\nabla} V = \mathbf{J}_a$ at SN boundary), arising from the fact that at SI(V) interface no current density perpendicular to the boundary can exist, while at SN boundary all applied current transforms into normal current density. Once the definition of the system is done, the following prescription is followed in order to solve Poisson equation: first, the boundary conditions which connect applied current density with the electrostatic potential ($\tilde{\nabla} V = \mathbf{J}_a$) are moved to the RHS of the equation Eq. 2.44, so they form a unique quantity together with the divergence of the supercurrent:

$$\tilde{\nabla}^2 V = \tilde{\nabla} \tilde{\mathbf{J}}_s - \tilde{\nabla} \tilde{\mathbf{J}}_a = R. \quad (\text{A.18})$$

From there, one takes the FFT of RHS of Eq. 2.44 according to Eq. A.16. Equation 2.44 can still be preserved in the real space, but it should be rewritten so that it is discretized (as in Eq. 2.61) and each quantity in it is described through corre-

spending inverse FFT as

$$\begin{aligned}
 & \frac{4\Delta y^2}{N_x N_y} \sum_{i=0}^{N_x} \sum_{j=0}^{N_y} \widehat{V}_{i,j} \left[\cos \frac{\pi i(m+1)}{N_x} - 2\cos \frac{\pi im}{N_x} + \cos \frac{\pi i(m-1)}{N_x} \right] \cos \frac{\pi jn}{N_y} + \\
 & \frac{4\Delta x^2}{N_x N_y} \sum_{i=0}^{N_x} \sum_{j=0}^{N_y} \widehat{V}_{i,j} \left[\cos \frac{\pi j(n+1)}{N_y} - 2\cos \frac{\pi jn}{N_y} + \cos \frac{\pi j(n-1)}{N_y} \right] \cos \frac{\pi im}{N_x} = \\
 & \frac{\Delta x \Delta y}{N_x N_y} \sum_{i=0}^{N_x} \sum_{j=0}^{N_y} \widehat{R}_{i,j} \cos \frac{\pi im}{N_x} \cos \frac{\pi jn}{N_y}.
 \end{aligned} \tag{A.19}$$

In this form, since every operation occurs under a same sum, sums can be omitted, so, therefore, one can express the unknown \widehat{V} as a function of \widehat{R} and remaining cosines, for every point i and j . What remains now is just to apply inverse FFT from Eq. A.17 onto \widehat{V} in order to obtain real-space electrostatic potential V .

Due to the all-Neumann boundary conditions, solution $V_{Poisson}$ of the Poisson-like equation can only be determined up to an arbitrary constant, $V_{Poisson} = V_{true} + C$. Usually, the electrostatic potential does not play an important role, and instead one uses difference of electrostatic potential between two points, so the arbitrary constant presents no problem. However, within the gTDGL framework, exactly the electrostatic potential is related with the phase of the order parameter. Though phase itself does not carry much of a physical significance (instead gradient of the phase is directly proportional to the current density), the arbitrary constant inherited from electrostatic potential can dramatically slow down the convergence of the numerical procedure. For this reason one can renormalize the solution of the Poisson equation in such a way that, for example, $V_{renormalized} = V_{Poisson} - \langle V_{Poisson} \rangle$. Such renormalized electrostatic potential in principle stabilizes the convergence procedure.

Another important note here regards the geometries in which FFT can be applied. Unfortunately, **presented FFT method cannot be used to solve Poisson equation in nonuniform geometries, and as such it should be only utilized in the case of specimens defined on a rectangular box**. For arbitrary geometries, one must employ different kind of numerical solver, based on algorithms such as successive over-relaxation method or multigrid method. One can also impose virtual relaxation time for electrostatic potential [302] and then solve diffusion-like equation with one of the methods described in previous Sections.

A.6 Successive over-relaxation method for iterative solution of Poisson-like equations in arbitrary geometries

The *Successive Over-Relaxation* method (SOR) is an algorithm used for solving linear system of equations. It is derived from the *Gauss-Seidel* method, where an over-relaxation factor ω was introduced in order to over-correct the solution, and thus to speed-up the convergence of the procedure. SOR is an iterative method where update of the solution throughout the iteration is performed in the following way

$$V_{m,n}^{(k+1)} = V_{m,n}^{(k)} - \omega R_{m,n}^{(k)}, \quad (\text{A.20})$$

where index k now counts the iterations of the procedure, and R is the residual. The procedure is convergent only for $\omega \in (0, 2)$, where if $\omega < 1$ under-relaxation occurs, while over-relaxation takes place for $\omega > 1$. If $\omega = 1$ method is reduced to Gauss-Seidel algorithm. In general, it is not possible to compute in advance the value of ω that will maximize the rate of convergence of SOR. Frequently, some heuristic estimate is used, like the one based in Chebyshev acceleration, $\omega^{(k+1)} = (1 - \rho^2 \omega^{(k)} / 4)^{-1}$. Radius of convergence is defined on a rectangular mesh with a grid cell of size $\Delta x \times \Delta y$, as

$$\rho = \frac{\Delta y^2 \cos \frac{\pi}{N_x} + \Delta x^2 \cos \frac{\pi}{N_y}}{\Delta x^2 + \Delta y^2}. \quad (\text{A.21})$$

One of the advantages of SOR is that it can treat the systems with nonuniform geometries. In order to do so, one just needs to set the proper form of the residual, and in the case of Eq. 2.44 this is determined as

$$R_{m,n}^{(k)} = \frac{aV_{m,n}^{(k)} + bV_{m+1,n}^{(k)} + cV_{m-1,n}^{(k)} + dV_{m,n+1}^{(k)} + eV_{m,n-1}^{(k)} - f}{a}, \quad (\text{A.22})$$

where terms $a = -[\Delta y^2 (L_{m+1,n} + L_{m-1,n}) + \Delta x^2 (L_{m,n+1} + L_{m,n-1})] L_{m,n}$, $b = \Delta y^2 L_{m+1,n} L_{m,n}$, $c = \Delta y^2 L_{m-1,n} L_{m,n}$, $d = \Delta x^2 L_{m,n+1} L_{m,n}$, and $e = \Delta x^2 L_{m,n-1} L_{m,n}$. The remaining term f contains the right hand side of the Eq. 2.61, which is a divergence of the supercurrent multiplied with factor $\Delta x^2 \Delta y^2$.

A.7 Track and trace algorithm for simultaneous tracking of a collective of particles

Moving superconducting vortices can serve as a basis for a number of super-fast devices, and as such the need arises for precise description of their motion. As discussed in Chapters 4 and 5, direct measurement of the individual vortex velocity

proves to be a difficult task for both theory and experiment, mostly because information obtained from a superconducting system is encoded by the contribution from the entire condensate. Most frequently, one can indirectly obtain the average vortex velocity from the voltage of the system in a narrow range of applied currents, where linear dependence between the voltage and vortex velocity exists.

However, if due to inhomogeneities in the system different vortex types coexist together at the same time (as seen in Chapter 4), due to the averaging, such details will be overlooked, and the velocity estimate from the voltage will not correspond to reality. Moreover, such approach also fails to characterize vortex dynamics at higher dissipative states. Within gTDGL framework, one can only reproduce the experimental environment, and, thus, estimate the velocity from calculated voltage in the system, since no quantity obtained from this theoretical model can be used to fully characterize the dynamics of an individual vortex in real time.

On the other hand, if the snapshots of the condensate dynamics with distinguishable vortex cores could be obtained fast enough (e.g. on a scale $\propto \tau_{GL}$), one could, in principle, measure the displacement of every vortex between each frame, and thus monitor the dynamic behavior in details. This was a motivation for development of one such tool, that, when provided with a series of images of the dynamical behavior as an input, recognizes and traces the particles across multiple frames, while gathering the information about the position of each particle in real time. This software was developed under the name “Track & Trace”, and it can be used to track down individual particles in any collective, bounded by an arbitrary geometry.

As an input, series of images are prepared in form of frames, where each frame corresponds to the snapshot of the system at a given instance. Software then reads each of the images, and finds the points of highest contrast (local minima and maxima) in every frame. After the inspection, every two consecutive images are compared in order to calculate the displacement between the positions of local extrema. Comparison is done in the following way: after one frame was scanned for points of contrast, these locations are stored separately, and preserved until the scanning of next frame was done. Then regions with a user-defined radius are scanned in the second image, with origin at the points of the local extrema from the first image. If any of the local extrema lies within the scanning region in both frames, such event corresponds to a displacement of the same particle. This is how particles are recognized and traced. Some processing of the data is also performed here in order to account for the geometry and pinning. Program also needs to be able to distinguish the new particles in the system, as well as terminate the data collection for particles that exited the system. If more than one particle moves in the system in such a way that there exists the distribution of velocities, then the radius of the search area will have to be adapted. After successfully tracing all

Appendix A

the particles throughout the entire range of provided images, this tool can provide several insights. Besides the detailed description of the motion of each particle (real time coordinate tracking, determination of the components of the velocity, together with the spatio-temporal velocity distribution), statistical analysis can be performed. One can readily obtain the spatial distribution of velocity averaged for a specific type of particles, temporally and/or spatially averaged velocity for each particle, and an average displacement between particles following the same trajectory.

This software was mostly used to characterize the behavior of superconducting vortices, but, in principle its application can be found in a broader area of research, wherever one needs to characterize the “particle in a plane” system (with small modifications, such software can be adapted to work with three dimensional systems, as well). Finally, as an evidence of its functionality, all the theoretical results in Chapter 4 and Chapter 5 regarding the velocity measurements were calculated by this tool.

Bibliography

- [1] Goodstein, D., & Goodstein, J. *Richard Feynman and the History of Superconductivity*. Physics in Perspective **2**, 30-47 (2000).
- [2] Onnes, H. K. *Sur les résistances électriques*. Communications from the Physical Laboratory of the University of Leiden **29**, 111 (1911).
- [3] Straumann, N. *On the first Solvay Congress in 1911*. arXiv 1109.3785v2 (2011).
- [4] Buckel, W., & Kleiner, R. *Superconductivity - Fundamentals and applications*. Wiley-VCH Verlag GmbH & Co. KGaA (2004).
- [5] Dahl, P. F. *Superconductivity after World War I and Circumstances Surrounding the Discovery of a State $B = 0$* . Historical Studies in the Physical and Biological Sciences **16**, 1-58 (1986).
- [6] Meissner, W., & Ochsenfeld, R. *Ein neuer Effekt bei Eintritt der Supraleitfähigkeit*. Die Naturwissenschaften **21**, 787-788 (1933).
- [7] Gorter, C. J., & Casimir, H. *On supraconductivity I*. Physica **1**, 306-320 (1934).
- [8] London, F., & London, H. *The Electromagnetic Equations of the Supraconductor*. Proceedings of the Royal Society A: Mathematical, Physical and Engineering Sciences **149**, 866 (1935).
- [9] Deaver, B. C., & Fairbank, W. M. *Experimental Evidence for Quantized Flux in Superconducting Cylinders*. Physical Review Letters **7**, 43-43 (1961).
- [10] Ginzburg, V. L., & Landau, L. D. *On the theory of superconductivity*. Journal of Experimental and Theoretical Physics **20**, 1064 (1950).
- [11] Landau, L. D. *On the theory of phase transitions*. Journal of Experimental and Theoretical Physics **7**, 19-32 (1937).

Bibliography

- [12] Abrikosov, A. A. *Influence of dimensions on the critical field of superconductors of the second group*. Doklady Akademii Nauk SSSR **86**, 489-492 (1954).
- [13] Feynman, R. P. *Application of quantum mechanics to liquid helium*. Progress in Low Temperature Physics **1**, 17-53 (1955).
- [14] Abrikosov, A. A. *On the Magnetic Properties of Superconductors of the Second Group*. Journal of Experimental and Theoretical Physics **5**, 1174-1182 (1957).
- [15] Frölich, H. *Theory of the Superconducting State. I. The Ground State at the Absolute Zero of Temperature*. Physical Review **79**, 845-856 (1950).
- [16] Bardeen, J., Cooper, L., & Schrieffer, J. R. *Microscopic Theory of Superconductivity*. Physical Review **106**, 162-164 (1957).
- [17] Cooper, L. *Bound electron pairs in a degenerate Fermi gas*. Physical Review **104**, 1189-1190 (1956).
- [18] Gor'kov, L. P. *Microscopic derivation of the Ginzburg-Landau equations in the theory of superconductivity*. Journal of Experimental and Theoretical Physics **36**, 1364-1367 (1959).
- [19] Josephson, B. D. *Possible new effects in superconductive tunneling*. Physics Letters **1**, 251-253 (1962).
- [20] Ray, P. J. *Structural investigation of $La_{2-x}Sr_xCuO_{4+y}$ - Following staging as a function of temperature*. Master's thesis, Niels Bohr Institute, Faculty of Science, University of Copenhagen, Denmark (2015).
- [21] Bednorz, J. G. & Müller, K. A. *Possible high T_c superconductivity in the Ba-La-Cu-O system*. Zeitschrift für Physik B **64**, 189-193 (1986).
- [22] Wu, M. K. et al. *Superconductivity at 93 K in a new mixed-phase Y-Ba-Cu-O compound system at ambient pressure*. Physical Review Letters **58**, 908-910 (1987).
- [23] Maeda, H., Tanaka, Y., Fukutomi, M., & Asano, T. *A New High- T_c Oxide Superconductor without a Rare Earth Element*. Japanese Journal of Applied Physics **27**, 209-210 (1988).
- [24] Testardi, L. R., Wernick, J. H., & Royer, W. A. *Superconductivity with onset above 23 K in Nb_3Ge sputtered films*. Solid State Communications **15**, 1-4 (1974).

-
- [25] Testardi, L. R. *Structural instability and superconductivity in A-15 compounds*. Reviews of Modern Physics **47**, 637-648 (1975).
- [26] Muller, J. *A15-type superconductors*. Reports in Progress in Physics **43**, 641-687 (1980).
- [27] Nagamatsu, J., Nakagawa, N., Muranaka, T., Zenitani, Y., & Akimitsu, J. *Superconductivity at 39 K in magnesium diboride*. Nature **410**, 63-64 (2001).
- [28] Buzea, C. & Yamashita, T. *Review of the superconducting properties of MgB₂*. Superconductor Science and Technology **14**, R115-R146 (2001).
- [29] Moshchalkov, V. V. et al. *Type-1.5 Superconductivity*. Physical Review Letters **102**, 117001 (2009).
- [30] Senkowicz, B. J., Giencke, J. E., Patnaik, S., Eom, C. B., Hellstrom, E. E., & Larbalestier, D. C. *Improved upper critical field in bulk-form magnesium diboride by mechanical alloying with carbon*. Applied Physics Letters **86**, 202502 (2005).
- [31] Skoskiewicz, T. *Superconductivity in the palladium-hydrogen and palladium-nickel-hydrogen systems*. Physica Status Solidi A **11**, K123-K126 (1972).
- [32] Stritzker, B., & Buckel, W. *Superconductivity in the palladium-hydrogen and the palladium-deuterium systems*. Zeitschrift für Physik **257**, 1-8 (1972).
- [33] Kalsi, S. S. et al. *HTS SMES magnet design and test results*. IEEE Transactions on Applied Superconductivity **7**, 971-976 (1997).
- [34] Hebard, A. et al. *Superconductivity at 18 K in potassium-doped C₆₀*. Nature **350**, 600-601 (1991).
- [35] Birrer, P. et al. *Magnetic penetration depth in the Chevrel-phase superconductors SnMo₆S_{8-x}Se_x and PbMo₆S_{8-x}Se_x*. Physical Review B **48**, 16589 (1993).
- [36] Steglich, F. et al. *Superconductivity in the Presence of Strong Pauli Paramagnetism: CeCu₂Si₂*. Physical Review Letters **43**, 1892-1896 (1979).
- [37] Heffner, R. H., & Norman, M. R. *Heavy Fermion Superconductivity*. Comments Condensed Matter Physics **17**, 361 (1996).
- [38] Thalmeier, P., Jourdan, M., & Huth, M. *Unkonventionelle Supraleitung*. Physik Journal **6**, 51 (2002).

Bibliography

- [39] Yoichi, K. et al. *Iron-Based Layered Superconductor: LaOFeP*. Journal of the American Chemical Society **128**, 10012-10013 (2006).
- [40] Hosono, H., & Kuroki, K. *Iron-based superconductors: Current status of materials and pairing mechanism*. Physica C **514**, 399-422 (2015).
- [41] Little, W. A. *Possibility of Synthesizing an Organic Superconductor*. Physical Review **143A**, 1416 (1964).
- [42] Jérôme, D., Mazaud, A., Ribault, M., & Bechgaard, K. Comptes rendus hebdomadaires des séances de l'Académie des Sciences B **290**, 27 (1980).
- [43] Bechgaard, K., Carneiro, K., Olsen, M., Rasmussen, R. B., & Jacobsen, C. B. *Zero-Pressure Organic Superconductor: Di-(Tetramethyltetraselenafulvalenium)-Perchlorate [(TMTSF)₂ClO₄]*. Physical Review Letters **46**, 852-855 (1981).
- [44] Wigner, E., & Huntington, H. B. *On the possibility of a metallic modification of hydrogen*. Journal of Chemical Physics **6**, 764-770 (1935).
- [45] Ashcroft, N. W. *Metallic Hydrogen: A High-Temperature Superconductor?* Physical Review Letters **21**, 1748-1749 (1968).
- [46] Richardson, C. F., & Ashcroft, N. W. *High Temperature Superconductivity in Metallic Hydrogen: Electron-Electron Enhancements* Physical Review Letters **78**, 118-121 (1997).
- [47] Baer, B. J., Chang, M. E., & Evans, M. J. *Raman shift of stressed diamond anvils: Pressure calibration and culet geometry dependence*. Journal of Applied Physics **104**, 034504 (2008).
- [48] Dias, R., & Silvera, I. F. *Observation of the Wigner-Huntington Transition to Solid Metallic Hydrogen*. arXiv 1610.01634 (2016).
- [49] Dobrovolskiy, O. V. *Abrikosov fluxonics in washboard nanolandscapes*. arXiv 1510.06872v1 (2015).
- [50] Anders, S. et al. *European roadmap on superconductive electronics status and perspectives*. Physica C **470**, 2079-2126 (2010).
- [51] Swithenby, S. J. *SQUID Magnetometers: Uses in Medicine*. Physics in Technology **18**, 17-24 (1987).
- [52] Clarke, J. *Geophysical Applications of SQUIDs*. IEEE Transactions on Magnetics **19**, 288-294 (1983).

-
- [53] Stenuit, G., Michotte, S., Govaerts, J., & Piraux, L. *Temperature dependence of penetration and coherence lengths in lead nanowires*. Superconductor Science and Technology **18**, 174-182 (2005).
- [54] Bardeen, J., Cooper, L., & Schrieffer, J. R. *Theory of Superconductivity*. Physical Review **108**, 1175-1204 (1957).
- [55] de Gennes, P. G. *Superconductivity of Metals and Alloys*. Westview Press (1999).
- [56] Altomare, F., & Chang, A. M. *One-Dimensional Superconductivity in Nanowires*. Wiley-VCH Verlag GmbH & Co. KGaA (2013).
- [57] Gor'kov, L. P. *Theory of Superconducting Alloys in a Strong Magnetic Field near the Critical Temperature*. Journal of Experimental and Theoretical Physics **10**, 998-1004 (1960).
- [58] Eilenberger, G. *Transformation of Gorkov's Equation for Type II Superconductors into Transport-Like Equations*. Zeitschrift für Physik **214**, 195-213 (1968).
- [59] Usadel, K. D. *Generalized diffusion equation for superconducting alloys*. Physical Review Letters **25**, 507-509 (1970).
- [60] Landau, L. D., & Khalatnikov, I. M. *Collected Papers of L. D. Landau*. Gordon and Breach (1965).
- [61] Landau, L. D., & Khalatnikov, I. M. *On the anomalous absorption of sound near a second order phase transition point*. Doklady Akademii Nauk SSSR **96**, 469-472 (1954).
- [62] Schmid, A. *A time dependent Ginzburg-Landau equation and its application to the problem of resistivity in the mixed state*. Physik der Kondensierten Materie **5**, 302-317 (1966).
- [63] Schmid, A., & Schön, G. *Linearized Kinetic Equations and Relaxation Processes of a Superconductor near T_c* . Journal of Low Temperature Physics **20**, 207-227 (1975).
- [64] Abrikosov, A. A., & Gor'kov, L. P. *On the problem of knight shift in superconductors*. Journal of Experimental and Theoretical Physics **39**, 1781-1784 (1960).
- [65] Phillips, J. C. *Gapless superconductivity*. Physical Review Letters **10**, 96-98 (1963).

Bibliography

- [66] Kramer, L., & Watts-Tobin, R. J. *Theory of Dissipative Current-Carrying States in Superconducting Filaments*. Physical Review Letters **40**, 1041-1044 (1978).
- [67] Watts-Tobin, R. J., Krähenbühl, Y., & Kramer, L. *Nonequilibrium Theory of Dirty, Current-Carrying Superconductors: Phase-Slip Oscillators in Narrow Filaments Near T_c* . Journal of Low Temperature Physics **42**, 459-501 (1981).
- [68] Lifshitz, E. M., & Landau, L. D. *Course of Theoretical Physics, Vol. 5: Statistical Physics*. Pergamon Press (1970).
- [69] de Gennes, P. G. *Boundary Effects in Superconductors*. Reviews of Modern Physics **36**, 225-237 (1964).
- [70] Buzdin, A. I. *Proximity effects in superconductor-ferromagnet heterostructures*. Reviews of Modern Physics **77**, 935-976 (2005).
- [71] Tinkham, M. *Introduction to superconductivity*. McGraw-Hill, Inc. (1996).
- [72] Kopnin, N. *Theory of Nonequilibrium Superconductivity*. Oxford University Press (2001).
- [73] Pearl, J. *Current distribution in superconducting films carrying quantized fluxoids*. Applied Physics Letters **5**, 65-66 (1964).
- [74] Gurevich, A. V., & Mints, R. G. *Self-heating in normal metals and superconductors*. Reviews of Modern Physics **59**, 941-1000 (1987).
- [75] Annett, J. F. *Superconductivity, Superfluids, and Condensates*. Oxford University Press (2003).
- [76] Vodolazov, D. Y., Peeters, F. M., Morelle, M., & Moshchalkov, V. V. *Masking effect of heat dissipation on the current-voltage characteristics of a mesoscopic superconducting sample with leads*. Physical Review B **71**, 184502 (2005).
- [77] Fleckinger-Pellé, J. & Kaper, H. G. *Gauges for the Ginzburg-Landau Equations of Superconductivity*. Zeitschrift für Angewandte Mathematik und Mechanik **76**, 345-348 (1996).
- [78] LeVeque, R. J. *Finite Difference Methods for Ordinary and Partial Differential Equations*. SIAM (2007).

-
- [79] Groppe, W. D., Kaper, H. G., Leaf, G. K., Levine, D. M., Palumbo, M., & Vinokur, V. M. *Numerical Simulation of Vortex Dynamics in Type-II Superconductors*. Journal of Computational Physics **129**, 254-266 (1996).
- [80] Moriarty, K. J. M., Myers, E., & Rebbi, C. *A vector code for the numerical simulation of cosmic strings and flux vortices in superconductors on the ETA-10*. Computer Physics Communications **54**, 273-294 (1989).
- [81] Frahm, H., Ullah, S., & Dorsey, A. T. *Flux dynamics and the growth of the superconducting phase*. Physical Review Letters **66**, 3067-3072 (1991).
- [82] Adler, S. L., & Piran, T. *Relaxation methods for gauge field equilibrium equations*. Reviews of Modern Physics **56**, 1-40 (1984).
- [83] Doria, M. M., Gubernatis, J. E., & Rainer, D. *Solving the Ginzburg-Landau equations by simulated annealing*. Physical Review B **41**, 6335-6341 (1990).
- [84] Atkinson, K. *An Introduction to Numerical Analysis*. John Wiley & Sons (1989).
- [85] Isaacson, E., & Keller, H. B. *Analysis of Numerical Methods*. Dover Publications Inc. (1993).
- [86] Winiiecki, T., & Adams, C. S. *A Fast Semi-Implicit Finite-Difference Method for the TDGL Equations*. Journal of Computational Physics **179**, 127-139 (2002).
- [87] Crank, J., & Nicolson, P. *A practical method for numerical evaluation of solutions of partial differential equations of the heat-conduction type*. Advances in Computational Mathematics **6**, 207-226 (1996).
- [88] Rao, K. R., Kim, D. N., & Hwang, J. J. *Fast Fourier Transform: Algorithms and Applications*. Springer (2010).
- [89] Press, W. H., Teukolsky, S. A., Vetterling, W. T., & Flannery, B. P. *Numerical Recipes*. Cambridge University Press (2007).
- [90] Peaceman, D. W., & Rachford, H. H. *The numerical solution of parabolic and elliptic differential equations*. Journal of the Society for Industrial and Applied Mathematics **3**, 28-41 (1955).
- [91] Likharev, K. K. *Superconducting weak links*. Reviews of Modern Physics **51**, 101-159 (1979).

Bibliography

- [92] Gor'kov, L. P., & Eliashberg, G. M. *Generalization of Ginzburg-Landau Equations for Non-Stationary Problems in the Case of Alloys with Paramagnetic Impurities*. Journal of Experimental and Theoretical Physics **27**, 328-334 (1968).
- [93] Essmann, U., & Träuble, H. *The direct observation of individual flux lines in type II superconductors*. Physics Letters A **24**, 526-527 (1967).
- [94] Vodolazov, D. Y., & Peeters, F. M. *Rearrangement of the vortex lattice due to instabilities of vortex flow*. Physical Review B **76**, 014521 (2007).
- [95] Zhang, J. T. et al. *Single-vortex pinning and penetration depth in superconducting $NdFeAsO_{1-x}F_x$* . Physical Review B **92**, 134509 (2015).
- [96] Maiorov, B. et al. *Synergetic combination of different types of defect to optimize pinning landscape using $BaZrO_3$ -doped $YBa_2Cu_3O_7$* . Nature Materials **8**, 389-404 (2009).
- [97] Silhanek, A. V. et al. *Evidence for vortex staircases in the whole angular range due to competing correlated pinning mechanisms*. Physical Review B **59**, 13620 (1999).
- [98] MacManus-Driscoll, J. L. et al. *Strongly enhanced current densities in superconducting coated conductors of $YBa_2Cu_3O_{7-x} + BaZrO_3$* . Nature Materials **3**, 439443 (2004).
- [99] Editors: Moshchalkov, V. V., Woerdenweber, R., & Lang, W. *Nanoscience and Engineering in Superconductivity*. Springer (2010).
- [100] Kramer, R. B. G., Silhanek, A. V., Gillijns, W., & Moshchalkov, V. V. *Imaging the Statics and Dynamics of Superconducting Vortices and Antivortices Induced by Magnetic Microdisks*. Physical Review X **1**, 021004 (2011).
- [101] Adami, O. A. et al. *Onset, evolution, and magnetic braking of vortex lattice instabilities in nanostructured superconducting films*. Physical Review B **92**, 134506 (2015).
- [102] Straver, E. W. J., Hoffman, J. E., Auslaender, O. M., Rugar, D., & Moler, K. A. *Controlled Manipulation of Individual Vortices in a Superconductor*. Applied Physics Letters **93**, 172514 (2008).
- [103] Villegas, J. E. et al. *A superconducting reversible rectifier that controls the motion of magnetic flux quanta*. Science **302**, 1188-1191 (2003).

- [104] Hastings, M. B., Reichhardt, C. J. O., & Reichhardt, C. *Ratchet Cellular Automata*. Physical Review Letters **90**, 247004 (2003).
- [105] Berciu, M., Rappoport, T. G., & Boldizs'ar, J. *Manipulating spin and charge in magnetic semiconductors using superconducting vortices*. Nature **435**, 71-75 (2005).
- [106] Weeks, C., Rosenberg, G., Seradjeh, B., & Franz, M. *Anyons in a weakly interacting system*. Nature Physics **3**, 796-801 (2007).
- [107] Blatter, G., Feigel'man, M. V., Geshkenbein, V. B., Larkin, A. I., & Vinokur, V. M. *Vortices in high-temperature superconductors*. Reviews of Modern Physics **66**, 1125-1388 (1994).
- [108] Nelson, D. R. *Defects and Geometry in Condensed Matter Physics*. Cambridge University Press (2002).
- [109] Wynn, J. C. et al. *Limits on Spin-Charge Separation from $h/2e$ Fluxoids in Very Underdoped $YBa_2Cu_3O_{6+x}$* . Physical Review Letters **87**, 197002 (2001).
- [110] Hoffman, J. E. et al. *A Four Unit Cell Periodic Pattern of Quasi-Particle States Surrounding Vortex Cores in $Bi_2Sr_2CaCu_2O_{8+\delta}$* . Science **295**, 466-469 (2002).
- [111] Kafri, Y., Nelson, D. R., & Polkovnikov, A. *Unzipping Vortices in Type-II Superconductors*. Physical Review B **76**, 144501 (2007).
- [112] Binnig, G., & Rohrer, H. *Scanning Tunneling Microscopy*. Surface Science **126**, 236-244 (1983).
- [113] Giaever, I. *Energy Gap in Superconductors Measured by Electron Tunneling*. Physical Review Letters **5**, 147-148 (1960).
- [114] Wolfram, T. *Inelastic Electron Tunneling Spectroscopy: Springer Series in Solid State Sciences - Vol. 4*. Springer (1978).
- [115] Binnig, G., Rohrer, H., Gerber, C., & Weibel, E. *Surface Studies by Scanning Tunneling Microscopy*. Physical Review Letters **49**, 57-61 (1982).
- [116] Binnig, G., Rohrer, H., Gerber, C., & Weibel, E. *Tunneling through a controllable vacuum gap*. Applied Physics Letters **40**, 178-180 (1982).
- [117] Chen, C. J. *Origin of atomic resolution on metal surfaces in scanning tunneling microscopy*. Physical Review Letters **65**, 448-451 (1990).

Bibliography

- [118] Zhang, T. et al. *Superconductivity in one-atomic-layer metal films grown on Si(111)*. Nature Physics **6**, 104-108 (2010).
- [119] Ge, J. Y. et al. *Nanoscale assembly of superconducting vortices with scanning tunnelling microscope tip*. Nature Communications **7**, 13880 (2016).
- [120] Binning, G., & Rohrer, H. *Scanning Tunneling Microscopy*. IBM Journal of Research and Development **30**, 279-293 (1986).
- [121] Auslaender, O. M. et al. *Mechanics of individual isolated vortices in a cuprate superconductor*. Nature Physics **5**, 35-39 (2009).
- [122] Black, R. C. et al. *Magnetic microscopy using a liquid nitrogen cooled $YBa_2Cu_3O_7$ superconducting quantum interference device*. Applied Physics Letters **62**, 2128-2130 (1993).
- [123] Mathai, A., Song, D., Gim, Y., & Wellstood, F. C. *One dimensional magnetic flux microscope based on the dc superconducting quantum interference device*. Applied Physics Letters **61**, 598-600 (1989).
- [124] Geng, Q., Minami, H., Chihara, K., Yuyama, J., & Goto, E. *Technique for measuring absolute intensity of weak magnetic fields by a SQUID pickup coil system*. Review of Scientific Instruments **63**, 3972-3977 (1992).
- [125] Buchanan D. S., Crum, D. B., Cox, D., & Wikswo, J. P. *Advances in Bio-magnetism*. Plenum, New York (1989).
- [126] Lee, T. S., Chemla, Y. R., Dantsker, E., & Clarke, J. *High- T_c SQUID microscope for room temperature samples*. IEEE Transactions on Applied Superconductivity **7**, 3147 - 3150 (1997).
- [127] Kremen, A., Wissberg, S., Haham, N., Persky, E., Frenkel, Y., & Kalisky, B. *Mechanical Control of Individual Superconducting Vortices*. Nano Letters **16**, 1626-1630 (2016).
- [128] Sivakov, A. G., Zhuravel', A. P., Turutanov, O. G., & Dmitrenko, I. M. *Spatially resolved characterization of superconducting films and cryoelectronic devices by means of low temperature scanning laser microscope*. Applied surface science **106**, 390-395 (1996).
- [129] Zhuravel', A. P., Sivakov, A. G., Lukashenko, A. V., & Dmitrenko, I. M. *Low temperature scanning laser microscope for studies in high magnetic fields*. Proceedings of the 21st International Conference on Low Temperature Physics (1996).

-
- [130] Veshchunov, I. S. et al. *Optical manipulation of single flux quanta*. Nature Communications **7**, 12801 (2016).
- [131] Huebener, R. P. **Magnetic flux structures in superconductors**. Springer-Verlag Berlin Heidelberg GmbH (1979).
- [132] Grimaldi, G. et al. *Speed limit to the Abrikosov lattice in mesoscopic superconductors*. Physical Review B **92** 024513 (2015).
- [133] Silhanek, A. V. et al. *Influence of artificial pinning on vortex lattice instability in superconducting films*. New Journal of Physics **14**, 053006 (2012).
- [134] Grimaldi, G. et al. *Evidence for low-field crossover in the vortex critical velocity of type-II superconducting thin films*. Physical Review B **82**, 024512 (2010).
- [135] López, D. et al. *Spatially Resolved Dynamic Correlation in the Vortex State of High Temperature Superconductors*. Physical Review Letters **82**, 1277-1280 (1999).
- [136] Larkin, A. I., & Ovchinnikov, Y. N. *Nonlinear conductivity of superconductors in the mixed state*. Journal of Experimental and Theoretical Physics **41**, 960-965 (1975).
- [137] Kang, S. et al. *High-performance high- T_c superconducting wires*. Science **311**, 1911-1914 (2006).
- [138] Gutiérrez, J. et al. *Strong isotropic flux pinning in solution-derived $YBa_2Cu_3O_{7-x}$ nanocomposite superconductor films*. Nature Materials **6**, 367-373 (2007).
- [139] Si, W. et al. *High current superconductivity in $FeSe_{0.5}Te_{0.5}$ -coated conductors at 30 tesla*. Nature Communications **4**, 1347 (2013).
- [140] Devoret, M. H., & Schoelkopf, R. J. *Superconducting circuits for quantum information: an outlook*. Science **339**, 1169-1174 (2013).
- [141] Welp, U., Kadowaki, K., & Kleiner, R. *Superconducting emitters of THz radiation*. Nature Photonics **7**, 702-710 (2013).
- [142] Gurevich, A., & Ciovati, G. *Dynamics of vortex penetration, jumpwise instabilities, and nonlinear surface resistance of type-II superconductors in strong rf fields*. Physical Review B **77**, 104501 (2008).

Bibliography

- [143] Embon, L. et al. *Probing dynamics and pinning of single vortices in superconductors at nanometer scales*. Scientific Reports **5**, 7598 (2015).
- [144] Kwok, W. K. et al. *Vortices in high-performance high-temperature superconductors*. Reports on Progress in Physics **79**, 116501 (2016).
- [145] Berdiyrov, G. R. et al. *Large magnetoresistance oscillations in mesoscopic superconductors due to current-excited moving vortices*. Physical Review Letters **109**, 057004 (2012).
- [146] Milošević, M. V., Berdiyrov, G. R., & Peeters, F. M. *Fluxonic cellular automata*. Applied Physics Letters **91**, 212501 (2007).
- [147] Klein, W., Huebener, R. P., Gauss, S., & Parisi, J. *Nonlinearity in the flux-flow behavior of thin-film superconductors*. Journal of Low Temperature Physics **61**, 413432 (1985).
- [148] Doettinger, S. G. et al. *Electronic instability at high flux-flow velocities in high- T_c superconducting films*. Physical Review Letters **73**, 16911694 (1994).
- [149] Samoilov, A. V., Konczykowski, M., Yeh, N. C., Berry, S., & Tsuei, C. C. *Electric-field-induced electronic instability in amorphous Mo_3Si superconducting films*. Physical Review Letters **75**, 41184121 (1995).
- [150] Troyanovski, A. M., Aarts, J., & Kes, P. H. *Collective and plastic vortex motion in superconductors at high flux densities*. Nature **399**, 665668 (1999).
- [151] Lee, J., Wang, H., Dreyer, M., Berger, H., & Barker, B. I. *Nonuniform and coherent motion of superconducting vortices in the picometer-per-second regime*. Physical Review B **84**, 060515 (2011).
- [152] Timmermans, M., Samuely, T., Raes, B., Van de Vondel, J., & Moshchalkov, V. V. *Dynamic visualization of nanoscale vortex orbits*. ACS Nano **8**, 27822787 (2014).
- [153] Keay, J. C. et al. *Sequential vortex hopping in an array of artificial pinning centers*. Physical Review B **80**, 165421 (2009).
- [154] Goa, P. E. et al. *Real-time magneto-optical imaging of vortices in superconducting $NbSe_2$* . Superconductor Science and Technology **14**, 729731 (2001).
- [155] Raes, B. et al. *Local mapping of dissipative vortex motion*. Physical Review B **86**, 064522 (2012).

-
- [156] Kalisky, B. et al. *Dynamics of single vortices in grain boundaries: I-V characteristics on the femtovolt scale*. Applied Physics Letters **94**, 202504 (2009).
- [157] Cole, D. et al. *Ratchet without spatial asymmetry for controlling the motion of magnetic flux quanta using time-asymmetric drives*. Nature Materials **5**, 305311 (2006).
- [158] Embon, L. et al. *Imaging of super-fast dynamics and flow instabilities of superconducting vortices*. Nature Communications **8**, 85 (2017).
- [159] Vasyukov, D. et al. *A scanning superconducting quantum interference device with single electron spin sensitivity*. Nature Nanotechnology **8**, 639644 (2013).
- [160] Lachman, E. O. et al. *Visualization of superparamagnetic dynamics in magnetic topological insulators*. Science Advances **1**, e1500740 (2015).
- [161] Anahory, Y. et al. *Emergent nanoscale superparamagnetism at oxide interfaces*. Nature Communications **7**, 12566 (2016).
- [162] Clem, J. R., Mawatari, Y., Berdiyrov, G. R., & Peeters, F. M. *Predicted field-dependent increase of critical currents in asymmetric superconducting nanocircuits*. Physical Review B **85**, 144511 (2012).
- [163] Adami, O. A. *Electric current crowding effects in microstructured superconductors*. PhD thesis, Faculty of Science, University of Liège, Belgium (2016).
- [164] Zeldov, E. et al. *Geometrical barriers in high-temperature superconductors*. Physical Review Letters **73**, 1428-1431 (1994).
- [165] Brandt, E. H. *Geometric barrier and current string in type-II superconductors obtained from continuum electrodynamics*. Physical Review B **59**, 33693372 (1999).
- [166] Brandt, E. H., Mikitik, G. P., & Zeldov, E. *Two regimes of vortex penetration into platelet-shaped type-II superconductors*. Journal of Experimental and Theoretical Physics **117**, 439448 (2013).
- [167] Benkraouda, M., & Clem, J. R. *Critical current from surface barriers in type-II superconducting strips*. Physical Review B **58**, 1510315107 (1998).
- [168] Burlachkov, L., Geshkenbein, V. B., Koshelev, A. E., Larkin, A. I., & Vinokur, V. M. *Giant flux creep through surface barriers and the irreversibility*

Bibliography

- line in hightemperature superconductors*. Physical Review B **50**, 1677016773 (1994).
- [169] Brandt, E. H., & Indenbom, M. *Type-II-superconductor strip with current in a perpendicular magnetic field*. Physical Review B **48**, 1289312906 (1993).
- [170] Zeldov, E., Clem, J. R., McElfresh, M., & Darwin, M. *Magnetization and transport currents in thin superconducting films*. Physical Review B **49**, 98029822 (1994).
- [171] Kogan, V. G. *Pearl's vortex near the film edge*. Physical Review B **49**, 1587415878 (1994).
- [172] Albrecht, J. et al. *Dramatic role of critical current anisotropy on flux avalanches in MgB₂ films*. Physical Review Letters **98**, 117001 (2007).
- [173] Mikheenko, P., Johansen, T. H., Chaudhuri, S., Maasilta, I. J., & Galperin, Y. M. *Ray optics behavior of flux avalanche propagation in superconducting films*. Physical Review B **91**, 060507 (2015).
- [174] Bolz, U., Biehler, B., Schmidt, D., Runge, B. U., & Leiderer, P. *Dynamics of the dendritic flux instability in YBa₂Cu₃O_{7δ} films*. Europhysics Letters **64**, 517523 (2003).
- [175] Biehler, B., Runge, B. U., Wimbush, S. C., Holzapfel, B., & Leiderer, P. *Velocity measurements of the dendritic instability in YNi₂B₂*. Superconductor Science and Technology **18**, 385387 (2005).
- [176] Aranson, I. S. et al. *Dendritic flux avalanches and nonlocal electrodynamicics in thin superconducting films*. Physical Review Letters **94**, 037002 (2005).
- [177] Olson, C. J., Reichhardt, C., & Nori, F. *Superconducting vortex avalanches, voltage bursts, and vortex plastic flow: effect of the microscopic pinning landscape on the macroscopic properties*. Physical Review B **56**, 61756194 (1997).
- [178] Olson, C. J., Reichhardt, C., & Nori, F. *Fractal networks, braiding channels, and voltage noise in intermittently flowing rivers of quantized magnetic flux*. Physical Review Letters **80**, 21972200 (1998).
- [179] Sivakov, A. G. et al. *Josephson behavior of phase-slip lines in wide superconducting strips*. Physical Review Letters **91**, 267001 (2003).

-
- [180] Andronov, A., Gordion, I., Kurin, V., Nefedov, I., & Shereshevsky, I. *Kinematic vortices and phase slip lines in the dynamics of the resistive state of narrow superconductive thin film channels*. Physica C **213**, 193199 (1993).
- [181] Kunchur, M. N. *Unstable flux flow due to heated electrons in superconducting films*. Physical Review Letters **89**, 137005 (2002).
- [182] Gurevich, A. V. et al. *Flux flow of Abrikosov-Josephson vortices along grain boundaries in high-temperature superconductors*. Physical Review Letters **88**, 097001 (2002).
- [183] Cedergren, K. et al. *Interplay between static and dynamic properties of semifluxons in $YBa_2Cu_3O_{7\delta}$ $0 - \pi$ Josephson junctions*. Physical Review Letters **104**, 177003 (2010).
- [184] Roditchev, D. et al. *Direct observation of Josephson vortex cores*. Nature Physics **11**, 332337 (2015).
- [185] Carapella, G., Sabatino, P., Barone, C., Pagano, S., & Gombos, M. *Current driven transition from Abrikosov-Josephson to Josephson-like vortex in mesoscopic lateral S/S/S superconducting weak links*. Scientific Reports **6**, 35694 (2016).
- [186] Giamarchi, T., & Le Doussal, P. *Moving glass phase of driven lattices*. Physical Review Letters **76**, 34083411 (1996).
- [187] Sheikhzada, A., & Gurevich, A. *Fragmentation of fast Josephson vortices and breakdown of ordered states by moving topological defects*. Scientific Reports **5**, 17821 (2015).
- [188] Golod, T., Iovan, A., & Krasnov, V. M. *Single Abrikosov vortices as quantized information bits*. Nature Communications **6**, 8628 (2015).
- [189] Chen, D. X., Moreno, J. J., Hernando, A., Sanchez, A., & Li, B. Z. *Nature of the driving force on an Abrikosov vortex*. Physical Review B **57**, 5059 (1998).
- [190] Rosenstein, B., Shapiro, I., & Shapiro, B. Ya. *Maximal persistent current in a type-II superconductor with an artificial pinning array at the matching magnetic field*. Physical Review B **81**, 064507 (2010).
- [191] Rosenstein, B., Shapiro, I., & Shapiro, B. Ya. *Transport current carrying superconducting film with periodic pinning array under strong magnetic fields*. Physical Review B **83**, 064512 (2011).

Bibliography

- [192] Zhu, B. Y., Marchesoni, F., Moshchalkov, V. V., & Nori, F. *Controllable step motors and rectifiers of magnetic flux quanta using periodic arrays of asymmetric pinning defects* Physical Review B **68**, 014514 (2003).
- [193] Zhu, B. Y., Marchesoni, F., & Nori, F. *Controlling the Motion of Magnetic Flux Quanta*. Physical Review Letters **92**, 180602 (2004).
- [194] Shklovskij, V. A., Sosedkin, V. V., & Dobrovolskiy O. V. *Vortex ratchet reversal in an asymmetric washboard pinning potential subject to combined dc and ac stimuli*. Journal of Physics: Condensed Matter **26**, 025703 (2014).
- [195] Shklovskij, V. A., & Dobrovolskiy O. V. *ac-driven vortices and the Hall effect in a superconductor with a tilted washboard pinning potential*. Physical Review B **78**, 104526 (2008).
- [196] Shklovskij, V. A., & Dobrovolskiy O. V. *Frequency-dependent ratchet effect in superconducting films with a tilted washboard pinning potential*. Physical Review B **84**, 054515 (2011).
- [197] Rodrigo, P. J., Eriksen, R. L., Daria, V. R., & Glückstad, J. *Interactive light-driven and parallel manipulation of inhomogeneous particles*. Optics Express **10** 26 (2002).
- [198] Shegai, T., Brian, B., Miljković, V.D., & Käll, M. *Angular Distribution of Surface-Enhanced Raman Scattering from Individual Au Nanoparticle Aggregates*. ASC Nano **5(3)**, 2036-2041 (2011).
- [199] Verduyn, D. et al. *Unidirectional Side Scattering of Light by a Single-Element Nanoantenna*. Nano Letters **13(8)**, 3843-3849 (2013).
- [200] Valev, V. K. et al. *Distributing the optical near-field for efficient field-enhancements in nanostructures*. Advanced Materials **24**, OP208-OP215 (2012).
- [201] Ivlev, B. I., Kopnin, N. B., & Maslova, L. A. *Dynamics of the resistive state of a superconductor*. Journal of Experimental and Theoretical Physics **78**, 1963-1978 (1980).
- [202] Ivlev, B. I., & Kopnin, N. B. *Electric currents and resistive states in thin superconductors*. Advances in Physics **33**, 47-114 (1984).
- [203] Maldonado, A., Vieira, S., & Suderow, H. *Supercurrent on a vortex core in 2H-NbSe₂: Current-driven scanning tunneling spectroscopy measurements*. Physical Review B **88**, 064518 (2013).

- [204] Berthod C. *Quasiparticle spectra of Abrikosov vortices in a uniform supercurrent flow*. Physical Review B **88**, 134515 (2013).
- [205] Gurevich, A. *Nonlocal Josephson electrodynamics and pinning in superconductors*. Physical Review B **46**, 3187(R) (1992).
- [206] Brun, C. et al. *Remarkable effects of disorder on superconductivity of single atomic layers of lead on silicon*. Nature Physics **10**, 444-450 (2014).
- [207] Yoshizawa, S. et al. *Imaging Josephson vortices on the surface superconductor $\text{Si}(111)-(\sqrt{7} \times \sqrt{3})\text{-In}$ using a scanning tunnelling microscope*. Physical Review Letters **113**, 247004 (2014).
- [208] Skocpol, W. J., Beasley, M. R., & Tinkham, M. *Phase-slip centers and nonequilibrium processes in superconducting tin microbridges*. Journal of Low Temperature Physics **16**, 145 (1974).
- [209] Kuznetsov, V. I., & Tulin, V. A. *Synchronization of high-frequency vibrations of slipping phase centers in a tin whisker under microwave radiation*. Journal of Experimental and Theoretical Physics **86**, 1364 (1998).
- [210] Wallraff, A. et al. *Quantum dynamics of a single vortex*. Nature **425**, 6954 (2003).
- [211] Wertheimer, M. R., & Gilchrist, J. G. *Flux jumps in type II superconductors*. Journal of Physics and Chemistry of Solids **28**, 2509 (1967).
- [212] Wördenweber, R. *Mechanism of vortex motion in high-temperature superconductors*. Reports on Progress in Physics **62**, 187-236 (1999).
- [213] Wördenweber, R., Hollmann, E., Schubert, J., Kutzner, R., & Panaitov, G. *Regimes of flux transport at microwave frequencies in nanostructured high- T_c films*. Physical Review B **85**, 064503 (2012).
- [214] Forgan, E. M. et al. *Measurement of vortex motion in a type-II superconductor: A novel use of the neutron spin-echo technique*. Physical Review Letters **85**, 3488 (2000).
- [215] Lee, J. U., Nordman, J. E., & Hohenwarter, G. *Josephson vortex flow in superconducting single crystal $\text{Bi}_2\text{Sr}_2\text{CaCu}_2\text{O}_x$* . Applied Physics Letters **67**, 1471 (1995).
- [216] Zotova, A. N., & Vodolazov, D. Y. *Photon detection by current-carrying superconducting film: A time-dependent Ginzburg-Landau approach*. Physical Review B **85**, 024509 (2012).

Bibliography

- [217] Zotova, A. N., & Vodolazov, D. Y. *Intrinsic detection efficiency of superconducting nanowire single photon detector in the modified hot spot model*. Superconductor Science and Technology **27**, 125001 (2014).
- [218] Lusche, R. et al. *Effect of the wire width on the intrinsic detection efficiency of superconducting-nanowire single-photon detectors*. Journal of Applied Physics **116**, 043906 (2014).
- [219] Hofherr, M. et al. *Time-Tagged Multiplexing of Serially Biased Superconducting Nanowire Single-Photon Detectors*. IEEE Transactions on Applied Superconductivity **23**, 2501205 (2013).
- [220] Engel, A. et al. *Tantalum nitride superconducting single-photon detectors with low cut-off energy*. Applied Physics Letters **100**, 062601 (2012).
- [221] Lara, A., Aliev F. G., Silhanek, A. V., & Moshchalkov V. V. *Microwave-stimulated superconductivity due to presence of vortices*. Scientific Reports **5**, 9187 (2015).
- [222] Mangold, M. et al. *Pulse repetition rate scaling from 5 to 100 GHz with a high-power semiconductor disk laser*. Optics Express **22**, 6099 (2014).
- [223] Schuller, J. A. et al. *Plasmonics for extreme light concentration and manipulation*. Nature Materials **9**, 193-204 (2010).
- [224] Davis, M. C. et al. *Manipulation of vortices by localized impurities in Bose-Einstein condensates*. Physical Review A **80**, 023604 (2009).
- [225] Libál, A., Reichhardt C., Jankó, B., & Olson Reichhardt, C. J. *Dynamics, Rectification, and Fractionation for Colloids on Flashing Substrates*. Physical Review Letters **96**, 188301 (2006).
- [226] Grier, D. G. *A revolution in optical manipulation*. Nature (London) **424**, 810 (2003).
- [227] Koss, B. A., & Grier, D. G. *Optical Peristalsis*. Applied Physics Letters **82**, 3985 (2003).
- [228] Lee, S.H., Ladovac, K., Polin, M., & Grier, D. G. *Observation of Flux Reversal in a Symmetric Optical Thermal Ratchet*. Physical Review Letters **94**, 110601 (2005).
- [229] Lee, S. H., & Grier, D. G. *Flux reversal in a two-state symmetric optical thermal ratchet*. Physical Review E **71**, 060102(R) (2005).

-
- [230] Babič, D., & Bechinger, C. *Noise-Enhanced Performance of Ratchet Cellular Automata*. Physical Review Letters **94**, 148303 (2005).
- [231] Babič, D., Schmitt, C., & Bechinger, C. *Colloids as model systems for problems in statistical physics*. Chaos **15**, 026114 (2005).
- [232] Yeo, J. et al. *Single Nanowire Resistive Nano-heater for Highly Localized Thermo-Chemical Reactions: Localized Hierarchical Heterojunction Nanowire Growth*. Small **10**, 5014 (2014).
- [233] Gross, et al. *Low-temperature scanning electron microscopy of superconducting thin films and Josephson junctions*. Reports on Progress in Physics **57**, 651 (1994).
- [234] Bartolf, H. et al. *Current-assisted thermally activated flux liberation in ultrathin nanopatterned NbN superconducting meander structures*. Physical Review B **81**, 024502 (2010).
- [235] Shmidt, V. V., & Mkrtychyan, G. S. *Vortices in type-II superconductors*. Advances in Physical Sciences **112**, 459-490 (1974).
- [236] Halperin, B. I., & Nelson, D. R. *Resistive transition in superconducting films*. Journal of Low Temperature Physics **36**, 599-616 (1979).
- [237] Ivlev, B. I., & Kopnin, N. B. *Resistive state of superconductors*. Journal of Experimental and Theoretical Physics - Letters **28**, 10 (1978).
- [238] Van de Vondel, J. et al. *Vortex core deformation and stepper motor behavior in a superconducting ratchet*. Physical Review Letters **106**, 137003 (2011).
- [239] Van Look, L. et al. *Shapiro steps in a superconducting film with an antidot lattice*. Physical Review B **60**, 10 (1999).
- [240] Van de Vondel, J. et al. *Self-organized mode-locking effect in superconductor/ferromagnet hybrids*. Physical Review B **79**, 054527 (2009).
- [241] Silhanek, A. V. et al. *Local probing of the vortex-antivortex dynamics in superconductor/ferromagnet hybrid structures*. Superconductor Science and Technology **24**, 024007 (2011).
- [242] Clem, J. R., & Berggren, K. K. *Geometry-dependent critical currents in superconducting nanocircuits*. Physical Review B **84**, 174510 (2011).

Bibliography

- [243] Bulaevskii, L. N., Graf, M. J., Batista, C. D., & Kogan, V. G. *Vortex-induced dissipation in narrow current-biased thin-film superconducting strips*. Physical Review B **83**, 144526 (2011).
- [244] Suderow, H., Brison, J. P., Marcenat, C., & Salce, B. *Thermal diffusivity and conductivity measurements for Si:P near the metal-insulator transition*. Journal of Physics: Condensed Matter **8**, 999-1009 (1996).
- [245] Berdiyrov, G. R., Milošević, M. V., & Peeters, F. M. *Spatially dependent sensitivity of superconducting meanders as single-photon detectors*. Applied Physics Letters **100**, 262603 (2012).
- [246] Vodolazov, D. Y., Elmuradov, A., & Peeters, F. M. *Critical currents of the phase slip process in the presence of electromagnetic radiation: Rectification for time asymmetric ac signal*. Physical Review B **72**, 134509 (2005).
- [247] Zotova, A. N., & Vodolazov, D. Y. *Photon detection by current-carrying superconducting film: A time-dependent Ginzburg-Landau approach*. Physical Review B **85**, 024509 (2012).
- [248] 4 GHz was the lowest frequency considered in this paper, but the stroboscopic resonances are expected to persist at lower frequencies as well.
- [249] Sahu, M. et al. *Individual topological tunnelling events of a quantum field probed through their macroscopic consequences*. Nature Physics **5**, 503-508 (2009).
- [250] Pekker, D., Shah, N., Sahu, M., Bezryadin, A., & Goldbart, P. M. *Stochastic dynamics of phase-slip trains and superconductive-resistive switching in current-biased nanowires*. Physical Review B **80**, 214525 (2009).
- [251] Chimenti, D. E., & Huebner, R. P. *Stroboscopic study of flux dynamics in superconductors during current-induced breakdown*. Solid State Communications **21**, 467-470 (1977).
- [252] Silhanek, A. V. et al. *Formation of stripelike flux patterns obtained by freezing kinematic vortices in a superconducting Pb film*. Physical Review Letters **104**, 017001 (2010).
- [253] Silin, V. P. *Pinning of Abrikosov-Josephson vortices*. Journal of Experimental and Theoretical Physics **110**, 741-755 (1996).
- [254] Silin, V. P. *Travelling small-scale Josephson vortices*. Journal of Experimental and Theoretical Physics **60**, 442-445 (1994).

- [255] Milošević, M. V., Kanda, A., Hatsumi, S., Peeters, F. M., & Ootuka, Y. *Local current injection into mesoscopic superconductors for the manipulation of quantum states*. Physical Review Letters **103**, 217003 (2009).
- [256] Milošević, M. V., & Peeters, F. M. *Vortex manipulation in a superconducting matrix with view on applications*. Applied Physics Letters **96**, 192501 (2010).
- [257] Jelić, Ž. L., Milošević, M. V., Van de Vondel, J., & Silhanek, A. V. *Stroboscopic phenomena in superconductors with dynamic pinning landscape*. Scientific Reports **5**, 14604 (2015).
- [258] Jelić, Ž. L., Milošević, & Silhanek, A. V. *Velocimetry of superconducting vortices based on stroboscopic resonances*. Scientific Reports **6**, 35687 (2016).
- [259] Ueno, K., Shimotami, H., Yuan, H., Ye, J. Kawasaki, M., & Iwasa, Y. *Field-Induced Superconductivity in Electric Double Layer Transistors*. Journal of the Physical Society of Japan **83**, 032001 (2014).
- [260] Glover, R. E., & Sherill, M. D. *Changes in superconducting critical temperature produced by electrostatic charging*. Physical Review Letters **5**, 248-250 (1960).
- [261] Takahashi, K. S. et al. *Local switching of two-dimensional superconductivity using the ferroelectric field effect*. Nature **441**, 195-198 (2006).
- [262] Caviglia, A. D. et al. *Electric field control of the LaAlO₃/SrTiO₃ interface ground state*. Nature **456**, 624-627 (2008).
- [263] Brun, C. et al. *Remarkable effects of disorder on superconductivity of single atomic layers of lead on silicon*. Nature Physics **10**, 444-450 (2014).
- [264] Yamada, M., Hirahara, T., & Hasegawa, S. *Magnetoresistance Measurements of a Superconducting Surface State of In-Induced and Pb-Induced Structures on Si(111)*. Physical Review Letters **110**, 237001 (2013).
- [265] Cudazzo, P., Profeta, P., & Continenza, A. *Low temperature phases of Pb/Si(111) and related surfaces*. Surface Science **602**, 747-754 (2008).
- [266] Brochard, S. et al. *Ab initio calculations and scanning tunneling microscopy experiments of the Si(111)- $\sqrt{7} \times \sqrt{3}$ -Pb surface*. Physical Review B **66**, 205403 (2002).

Bibliography

- [267] Eom, D., Qin, S., Chou, M. Y., & Shih, C. K. *Persistent Superconductivity in Ultrathin Pb Films: A Scanning Tunneling Spectroscopy Study*. Physical Review Letters **96**, 027005 (2006).
- [268] Qin, S., Kim, J., Niu, Q., & Shih, C. K. *Superconductivity at the Two-Dimensional Limit*. Science **324**, 1314-1317 (2009).
- [269] Özer, M. M., Thompson, J. R., & Weitering, H. H. *Hard superconductivity of a soft metal in the quantum regime*. Nature Physics **2**, 173 - 176 (2006).
- [270] Uchihashi, T. *Two-dimensional superconductors with atomic-scale thickness*. Superconductor Science and Technology **30**, 013002 (2017).
- [271] Brun, C., Cren, T., & Roditchev, D. *Review of 2D superconductivity: the ultimate case of epitaxial monolayers*. Superconductor Science and Technology **30**, 013003 (2017).
- [272] Buckel, V., & Hilsch, R. *Einfluß der Kondensation bei tiefen Temperaturen auf den elektrischen Widerstand und die Supraleitung für verschiedene Metalle*. Zeitschrift für Physik **138**, 109-120 (1954).
- [273] Anderson, P. W. *Theory of dirty superconductors*. Journal of Physics and Chemistry of Solids **11**, 26-30 (1959).
- [274] Goldman, A. M., & Markovic, N. *Superconductorinsulator transitions in the two-dimensional limit*. Physics Today **51**, 39-44 (1998).
- [275] Graybeal, J. M., & Beasley, M. R. *Localization and interaction effects in ultrathin amorphous superconducting films*. Physical Review B **29**, 4167-4169 (1984).
- [276] Haviland, D. B. et al. *Onset of superconductivity in the two-dimensional limit*. Physical Review Letters **62**, 2180-2183 (1989).
- [277] Guo, Y. et al. *Superconductivity modulated by quantum size effects*. Science **306**, 1915-1917 (2004).
- [278] Bao, X. Y. et al. *Quantum size effects on the perpendicular upper critical field in ultrathin lead films*. Physical Review Letters **95**, 247005 (2005).
- [279] Özer, M. M., Jia, Y., Zhang, Z., Thompson, J. R., & Weitering, H. H. *Tuning the quantum stability and superconductivity of ultrathin metal alloys*. Science **316**, 1594-1597 (2007).

- [280] Chiang, T. C. *Photoemission studies of quantum well states in thin films*. Surface Science Reports **39**, 181-235 (2000).
- [281] Dil, J. H., Kim, J. W., Kampen, T., Horn, K., & Ettema, A. R. H. F. *Electron localization in metallic quantum wells: Pb versus In on Si(111)*. Physical Review B **73**, 161308(R) (2006).
- [282] Orr, B. G., Jaeger, M. H., & Goldman, A. M. *Transition-Temperature Oscillations in Thin Superconducting Films*. Physical Review Letters **53**, 2046 (1984).
- [283] Paggel, J. J., Luh, D. A., Miller, T., & Chiang, T. C. *Electronic-Structure Dependence of the Electron-Phonon Interaction in Ag*. Physical Review Letters **92**, 186803 (2004).
- [284] Cren, T., Fokin, D., Debontridder, F., Dubost, V., & Roditchev, D. *Ultimate Vortex Confinement Studied by Scanning Tunneling Spectroscopy*. Physical Review Letters **102**, 127005 (2009).
- [285] Nishio, T. et al. *Superconducting Pb Island Nanostructures Studied by Scanning Tunneling Microscopy and Spectroscopy*. Physical Review Letters **101**, 167001 (2008).
- [286] Cren, T., Serrier-Garcia, L., Debontridder, F., & Roditchev, D. *Vortex Fusion and Giant Vortex States in Confined Superconducting Condensates*. Physical Review Letters **107**, 097202 (2011).
- [287] Nishio, T., Lin, S., An, T., Eguchi, T., & Hasegawa, Y. *Tip-induced excitation of a single vortex in nano-size superconductors using scanning tunneling microscopy*. Nanotechnology **21**, 465704 (2010).
- [288] Fischer, Ø. Kugler, M., Maggio-Aprile, I., & Berthod, C. *Scanning tunneling spectroscopy of high-temperature superconductors*. Reviews of Modern Physics, **27**, 353-419, (2007).
- [289] Serrier-Garcia, L. et al. *Scanning Tunneling Spectroscopy Study of the Proximity Effect in a Disordered Two-Dimensional Metal*. Physical Review Letters **110**, 157003 (2013).
- [290] Wei, C. M., & Chou, M. Y. *Theory of quantum size effects in thin Pb(111) films*. Physical Review B **66**, 233408 (2002).
- [291] Shanenko, A. A., Croitoru, M. D., & Peeters, F. M. *Oscillations of the superconducting temperature induced by quantum well states in thin metallic*

Bibliography

- films: Numerical solution of the Bogoliubovde Gennes equations*. Physical Review B **75**, 014519 (2007).
- [292] Hong, I. P. *Quantum Size Effects in Ultrathin Metallic Islands: a Scanning Tunneling Microscopy/Spectroscopy Study*. PhD thesis, EPFL Lausanne, Switzerland (2009).
- [293] Serrier-Garcia, L. et al. *Unpublished*.
- [294] Graugnard, E., & Lee, T. *TEM Pictures of STM Tips*. <http://www.physics.purdue.edu/nanophys/uhvstm/ptir-new3.html> (1999).
- [295] Serrier-Garcia, L. *Vortex confinés dans des nanostructures de Pb/Si(111) étudiés par microscopie à effet tunnel*. PhD thesis, University of Pierre and Marie Curie - Paris, France (2014).
- [296] Liu, J., Wu, X., Ming, F., Wang, K., & Xiao, X. *Superconductivity of individual Pb islands on Si(111): pseudogap, critical region, density of states, and island size*. Superconductor Science and Technology **26**, 085009 (2013).
- [297] Mel'nikov, A. S., & Vinokur, V. M. *Mesoscopic superconductor as a ballistic quantum switch*. Nature **415**, 60-62 (2002).
- [298] Winiecki, T., & Adams, C. S. *A Fast Semi-Implicit Finite-Difference Method for the TDGL Equations*. Journal of Computational Physics **179**, 127-139 (2002).
- [299] Douglas, J. *On the numerical integration of $u_{xx} + u_{yy} = u_t$ by implicit methods*. Journal of the Society of Industrial and Applied Mathematics **3**, 42-65 (1955).
- [300] Douglas, J. *Alternating direction methods for three space variables*. Numerische Mathematik **4**(1), 41-63 (1962).
- [301] Chang, M. J., Chow, L. C., & Chang, W. S. *Improved alternating-direction implicit method for solving transient three-dimensional heat diffusion problems*. Numerical Heat Transfer, Part B: Fundamentals **19**(1), 69-84, (1991).
- [302] Sadovskyy, I. A., Koshelev, A. E., Phillips, C. L., Karpeyev, D. A., & Glatz, A. *Stable large-scale solver for GinzburgLandau equations for superconductors*. Journal of Computational Physics **294**, 639-654 (2015).

Curriculum Vitae

Name: Željko L. Jelić

Date of birth: June 23, 1989

Nationality: Bosnia and Herzegovina (BiH)

Permanent address: Jovana Cvijića 29, 76230 Šamac, BiH

Current address: Rucaplein 131, 2610 Antwerpen, Belgium

E-mail: zeljko.jelic@uantwerpen.be

Education

- University of Liège/University of Antwerp 2013 - present
PhD student in *Experimental Physics of Nanostructured Materials and Condensed Matter Theory* groups
- Faculty of Electrical Engineering, University of Belgrade 2012 - 2013
Master degree in Electrical Engineering and Computer Science
Average grade: 10/10
- Faculty of Electrical Engineering, University of Belgrade 2008 - 2012
Bachelor degree in Electrical Engineering and Computer Science
Average grade: 9.02/10

Skills

- Languages:
Serbian (mother tongue), **English** (professional working proficiency), **German** (elementary proficiency), **Norwegian** (elementary proficiency)
- Programming:
Fortran (professional working proficiency), **C** (limited working proficiency),

C++ (limited working proficiency), **Julia** (elementary proficiency), **Python** (elementary proficiency)

- Scientific packages/programs:
Comsol, Visual Studio, MATLAB, Origin, Corel, Vegas, Latex, Microsoft Office

List of publications

- Embon, L., Anahory, Y., **Jelić, Ž. L.**, Lachman, E. O., Myasoedov, Y., Huber, M. E., Mikitik, G. P., Silhanek, A. V., Milošević, M. V., Gurevich, A., & Zeldov, E. *Imaging of super-fast dynamics and flow instabilities of superconducting vortices*. Nature Communications **8**, 85-95 (2017).
- **Jelić, Ž. L.**, Milošević, M. V., & Silhanek, A. V. *Velocimetry of superconducting vortices based on stroboscopic resonances*. Scientific Reports **6**, 35687 (2016).
- Adami, O. A., **Jelić, Ž. L.**, Xue, C., Abdel-Hafiez, M., Hackens, B., Moshchalkov, V. V., Milošević, M. V., Van de Vondel, J., & Silhanek, A. V. *Onset, evolution, and magnetic braking of vortex lattice instabilities in nanostructured superconducting films*. Physical Review B **91**, 134506 (2015).
- **Jelić, Ž. L.**, Milošević, M. V., Van de Vondel, J., & Silhanek, V. A. *Stroboscopic phenomena in superconductors with dynamic pinning landscape*. Scientific Reports **5**, 14604 (2015).
- **Jelić, Ž. L.**, Petrović, J., Matavulj, P., Melancon, J., Sharma, A., Zellhofer, C., & Živanović, S. *Modeling of the polymer solar cell with a P3HT:PCBM active layer*. Physica Scripta **162**, 14035 (2014).

Conferences

- **19th Symposium on Condensed Matter Physics**, Belgrade, Serbia (7th - 11th September 2015) - Poster entitled: *Stroboscopic phenomena in superconductors with dynamic pinning landscape*.
- **Advances in Studies of Superconducting Hybrids: Theory and Modeling vs Experiment**, Arcachon, France (16th - 19th May 2015) - Oral presentation entitled: *Influence of the dynamic pinning geometry on the stroboscopic phenomena in superconductors*.

- **Physics and Applications of Superconducting Hybrid Nano-Engineered Devices**, Santa Maria Di Castellabate, Italy (31st August - 3rd September 2014) - Poster entitled: *Dynamic vortex pinning*.

ξ

*Kad budeš prolazila pored tvrđave despotove...
Govorim ti, jer nisam još učio od prvih ljudi gospodarevog doma.*

*Zatočen sam
i govoriću ti.*

Nisi ostala u ulici zasutoj lišćem studentskih dana...

*Uhvatila si me za kosti, za mišiće prošlosti,
Kad bijah mlad, ili odveć star da te poznajem...*

Nego, muči me nešto.

Šta je to sa imenima kojima te nazivam?

Je li te to stepa zatočila u svom beskraju?

Jesi li to bila ti na poljima Rusije

Koja sam vidio jednom kada sam sanjao naše ime.

Ništa od toga, ništa od toga nije jasno Nebu.

To me muči...

Kako si urasla u ove nerve i

Procvjetala bojom jeseni?

Nego, ima još nešto, ξ.

A to me razuđuje u vremenima fizici znanim.

Vidio sam te jednom davno.

Sumnjao sam da si ti.

Vidio sam te u podnožju starog hrasta

Koji je rastao ispred moje zgrade

U Kotoru.

U jesen sam te gledao dok je

Lišće padalo pored tvojih kosa

Od kojih bijaše nebo.

Ćutiš?

Ne boj se...

Pa zar misliš da sad postoji

Nekakav bunar ili raskršće ili vodenica

U kojoj postoji nešto

Što će te ugristi?

Ne, ništa više ne obitava tamo,

Jer, evo, pojeli su me i zažalili.

Otrovao sam ih.

Marko Lješević